



**University of
Nottingham**

UK | CHINA | MALAYSIA

Development of a magnetic resonance imaging biomarker to improve prognostication in metastatic medulloblastoma

Miss Christine Angeline Mitoko

MRCS, MBBS

Thesis submitted to the University of Nottingham for the degree of
Doctor of Philosophy

June 2021



**Haydn Green Institute
for Innovation and
Entrepreneurship**



**University of
Nottingham**
Sir Peter Mansfield Imaging Centre

Abstract

Introduction Metastatic medulloblastoma (MB) manifests in one third of paediatric patients at diagnosis, conferring a poor prognosis. Our limited capacity to detect dissemination at diagnosis and disease recurrence however, results in the erroneous risk stratification of paediatric patients with MB, with serious subsequent prognostic implications.

Hypothesis Significantly correlated with metastasis and poor prognosis in other solid cancers, tumour-derived enzymes that facilitate their dissemination known as matrix metalloproteinases (MMPs) and specifically MMP-2 and MMP-9, were postulated to be potential biomarkers of metastasis in MB. We hypothesised that differential levels of functionally active MMP-2 and MMP-9, as expressed and secreted by a panel of primary and metastatic sub-grouped MB cell lines and patient tumours, would correlate with their propensity to metastasise. Once biologically characterised, these findings would be translatable, using our locally synthesised ¹⁹Fluorine-MMP-MRI biosensor, which would demonstrate an increase in the fluorine signal proportional to the concentration of the MMP-2/MMP-9 within the sample, as its substrate linker is cleaved from a paramagnetic gadolinium III-DOTA complex over time.

Methods Protein microarrays, western blotting and qRT-PCR were performed to determine the levels of MMP-2 and MMP-9 protein and gene expression in nine sub-grouped primary and metastatic MB cell lines. Levels of secreted functionally active MMP-2 and MMP-9 from

conditioned supernatants from the same MB cell lines and cerebrospinal fluid (CSF) from six paediatric patients with MB were assayed using gelatin zymography. Functional migration and invasion assays of 3-D cultured MB were performed to determine whether the detected levels of functionally active MMP-2 and MMP-9, would correlate to their migratory capacity and expected metastatic potential. The same samples were further examined using fluorescence resonance energy transfer (FRET) assays, to simulate and optimise the conditions for the biosensor experiments, prior to their imaging.

Results Our data strongly suggests that MMP-2 gene and protein is upregulated in metastatic MB cell lines. This was most evident in a matched pair of Group 4 MB where the recurrent cell line CHLA-01R-MED consistently expressed higher MMP-2 at all regulatory levels in comparison to its primary counterpart, CHLA-01-MED. This finding was also reflected in their increased migratory capacity in invasion assays. Zymography of MB patient CSF demonstrated significantly increased levels of functionally active MMP-2 in the recurrent samples; a finding resonated in our FRET assay experiments. ¹⁹Fluorine-MRI-MMP biosensor imaging demonstrated increased signal from the Fluorine moiety, following enzymatic degradation of the sensor by recombinant MMP-2 protein, demonstrating its capacity to detect the levels of functionally active MMP-2 and MMP-9 in MB patient cerebrospinal fluid and its potential as a clinically relevant imaging biomarker, once optimised.

Conclusions Levels of functionally active MMP-2 could prove to be a sensitive marker of metastasis in paediatric patients with medulloblastoma, at their initial diagnosis and ongoing disease surveillance. With further optimisation, we believe that our MMP-2 biosensor could become a useful adjunct as an intra-operative marker of residual metastatic cells, to enhance our limits of safe maximal resection.

Acknowledgements

While this PhD began as a dream, it became my most challenging and fulfilling reality, envisioned and supported by a few to whom I will be forever grateful. I would like to thank the Haydn Green Foundation and the International office at the University of Nottingham for granting me the international scholarship to actualize my dream.

To my supervisor Dr Beth Coyle, I am immensely grateful for your determination to see me through, especially when I lost sight of the possibilities. Thank you especially for the countless motivating meetings fuelled by your unending supply of great coffee. To my supervisor and neurosurgery, mentor Mr Donald Macarthur, thank you for your unrelenting support, encouragement and faith in my capabilities as a researcher and budding neurosurgeon. To my imaging supervisor Dr Henryk Faas, thank you for welcoming me into the incredible field of fluorine MR imaging and all the opportunities that it afforded me. To the best post-doc I could have imagined, Dr Franziska Linke, I am so grateful for all the teaching and time you invested in me. It has been an incredible pleasure to work with and learn from all of you.

To my school of medicine mentor, Mr David Humes, words escape me for the incredible gratitude I feel for your sage advice, encouragement and mentorship through some of the most challenging times of my PhD. To the Nottingham Neurosurgery team, thank you for welcoming me into the fold and making me feel at home. Special thanks to the Don Mr Ashpole, Mr Daren Subar, Mr Ravindra Nannapaneni, Ms Shazia Javed,

Ms Beverley Cheserem, Dr Obwanga and Mr Andrew Adelaide, for helping to expand my horizons of what I thought I could achieve.

To my CBTRC, SPMIC and Rad. Sci. families who enriched my PhD journey in so many ways, thank you all for being so welcoming. I am especially grateful to the wonderful friends and esteemed colleagues with whom I was incredibly proud to work with and learn from. Hannah, Alice, Macha, Sophie and Louisa, thank you for the laughs, love and incredible friendship, it meant so much.

My heartfelt gratitude to my rock Sam, thank you for supporting every crazy idea and every ridiculous ambition. Your steadfast love has seen me through so much and I truly appreciate you. Thank you to my wonderful and inspiring parents Dr Grace Ohayo-Mitoko and Mr Micah Haydn Mitoko, whose love and sacrifice kept me going, and my siblings Micah and Tryphosa, whose unbelievable support kept me soaring. To Uncle Lazarus and Aunty Nelly Amayo, thank you for your love and constant encouragement; and to Moji, Rachel and Solomon, thank you for giving me a home away from home. To Kui, Minan, Georgina and Yvonne whose unwavering friendship over the years has seen me through so much, I thank you. To the incredible God I serve, I am forever in awe of you and so grateful. Lastly, to the loved ones who wished to but were not able to see this day, Grandpa Gordon Ohayo, Uncle Chief Oruka and Aunty Margaret Radier, I dedicate this thesis to you. I hope I made you proud.

Contents

Development of a magnetic resonance imaging biomarker to improve prognostication in metastatic medulloblastoma	I
Abstract	II
Acknowledgements	V
List of Figures	XIII
List of Tables	XXI
List of Abbreviations	XXVI
Chapter 1. Introduction	1
Introduction	2
1.1 Epidemiology	2
1.2 Pre-disposing risk factors to MB	4
1.3 Clinical presentation	7
1.4 Pathological classification of MB	9
1.5 Risk stratification of paediatric patients with MB	18
1.6 Clinical management of paediatric MB	20
1.7 Metastasis and Recurrence in Medulloblastoma	25
1.7.1 The brain tumour microenvironment	29
1.8 Leptomeningeal metastasis	36
1.9 Candidate biomarkers of metastasis	43
1.10 Matrix Metalloproteinases as biomarkers of Metastasis	48
1.11 Molecular Magnetic Resonance Imaging	56
Chapter 2.	63
Materials and Methods	63
Materials and Methods	64
2.1 Cell culture	64
2.1.1 Procurement of cell lines	64
	VII

2. 1.2 Sub-culture of cell lines	65
2.2 Preparation of 2-D cultured medulloblastoma cell line samples for gelatin zymography, gene and protein expression from the same cell population	68
2.2.1 Preparation of cell pellets for molecular analysis	68
2.3 Experimental set-up for Gelatin Zymography	71
2.3.2 Preparation of conditioned medium for zymography, ELISA and protease/protease inhibitor arrays	71
2.4 Investigating the MMP-2 and MMP-9 gene expression in medulloblastoma cell lines	77
2.4.3 MMP-2 Primer optimisation	81
2.4.4 MMP-9 Primer optimisation	83
2.5 MMP-2 and MMP-9 protein expression in medulloblastoma cell lines	86
2.7 3-D cell culture	91
2.7.3 Determining which assay dye most accurately detected invasive MB cells	94
2.8 Drug treatments	95
2.9 19F-Magnetic Resonance Imaging of MMPs using an enzymatic degradable biosensor	96
Chapter 3.	98
Biological characterisation of matrix metalloproteinases in paediatric medulloblastoma	98
3.1 Chapter outline	99
3.2 Aims and hypotheses	101
3.3 Elucidating protein biomarkers of metastasis in matched primary and recurrent MB cell lines	102
3.3.1 Differentially expressed analytes in matched primary (D425-Med) and metastatic (D458-Med) Group 3 cell lines	104
3.3.2 Differentially expressed analytes in matched primary (CHLA-01-Med) and recurrent (CHLA-01R-Med) Group 4 cell lines	109

3.4 MMP-2 gene expression in medulloblastoma cell lines	116
3.5 MMP-9 gene expression in medulloblastoma cell lines	117
3.6 MMP-2 protein expression in medulloblastoma cell lines	118
3.6 MMP-9 protein expression in medulloblastoma cell lines	122
3.7 Gelatin zymography for the detection of functionally active MMP-2 and MMP-9 in medulloblastoma cell lines	125
3.7.1 Optimisation of Gelatin Zymography	126
3.7.2 Gelatin zymography detection of pro- and active- MMP-2 and MMP 9 from medulloblastoma cell lines	128
Summary	132
Chapter 4	134
Functional characterisation of matrix metalloproteinases in 3-D models of medulloblastoma	134
4.1 Chapter outline	135
4.2 Aims and Hypotheses	138
4.3 The effect of 3-dimensional spheroid culture of medulloblastoma cell lines on their secreted levels of functionally active MMP-2 and MMP-9	141
4.3.1 Generation of medulloblastoma spheroids	141
4.3.2 The effects of variations in the tumour microenvironment on the levels of functionally active MMP-2 and MMP-9 secreted by medulloblastoma	144
4.3.3 Effects of pharmacological inhibition of MMP-2 and MMP-9 on the migration patterns of 3D SHH medulloblastoma spheroids seeded on collagen IV matrices	155
4.4 Migration of Group 3 and 4 medulloblastoma cell lines through trans-well assays	172
4.4.1 Choosing the right transwell barrier	173

4.4.2 The effect of pharmacologic inhibition of MMP-2 and MMP-9 on the rate of transwell invasion across a collagen IV/Laminin I barrier	176
4.4.4 Comparison of transwell invasion assays of matched primary and metastatic Group 3 and Group 4 cell lines across a collagen IV/Laminin I barrier	178
4.5 Summary	181
Chapter 5	183
Validation of MMPs as prognostic biomarkers in tissue and CSF from paediatric patients with primary and metastatic medulloblastoma	183
5.1 Chapter outline	184
5.2 Objectives and hypothesis	185
5.3 Liquid biopsy, handling and storage of cerebrospinal fluid samples from paediatric medulloblastoma patients	186
5.4 Results	192
5.4.1 Investigating the epigenetic and genetic landscape of matrix metalloproteinases and their inhibitors	192
5.4.2 Gelatin zymography of cerebrospinal fluid from patients with primary and recurrent medulloblastoma	196
5.4 Summary	218
Chapter 6	220
Towards the radiological characterisation of matrix metalloproteinases in biological samples using our ¹⁹Fluorine-MMP-MRI biosensor	220
6.1 Chapter outline	221
6.2 Objectives and Hypothesis	224
6.3 Results	226

6.3.1 FRET Optimisation experiments	226
6.4 ¹⁹ Fluorine MRI MMP-2/MMP-9 biosensor experiments	241
6.4.1 Biosensor optimisation experiments and proof of principle	241
	242
6.4.2 Biosensor detection of functionally active MMP-2 and MMP-9 in concentrated cell supernatant	243
6.4 Summary	245
Chapter 7. Discussion	246
7.1 Background and rationale	247
7.2 The elucidation of a biomarker of increased metastatic potential in MB.	251
7.3 Biological characterisation of MMP-2 and MMP-9 in 2-D cultured sub-grouped MB cell lines	253
7.4 Functional characterisation of matrix metalloproteinases in 3-D models of medulloblastoma	256
7.5 The effect of pharmacological inhibition of MMP-2 and MMP-9 on the patterns of migration and invasion of 3-D cultured MB	261
7.6 Validation of MMPs as prognostic biomarkers in paediatric MB patient samples	265
7.7 Improving the risk stratification of paediatric patients with MB using our ¹⁹ Fluorine-MMP-MRI biosensor	269
7.8 Proposals for future work	272
7.9 Concluding statement	273
References	274
Appendices	285
PhD Project outputs	296
Conferences	297

Published conference abstracts	297
Post-graduate prizes	298
Presentations	298
Poster Presentations	299

List of Figures

Figure 1.1 Clinical, genetic, molecular and histopathological characteristics of paediatric medulloblastoma	3
Figure 1.2 Histological subtypes of MB	11
Figure 1.3 The WNT signalling pathway showing consequences of its activation.	13
Figure 1.4 SHH signalling and interactions with the PI3K/AKT/MTOR and PKA pathways	15
Figure 1.5 Overview of the structural differences in the composition of the blood-brain barrier at anatomically distinct regions of the brain.....	33
Figure 1. 6 CSF flow through the ventricles and around the brain.....	35
Figure 1. 7 Stages of carcinogenesis in which matrix metalloproteinases are involved.	52
Figure 1.8 The anatomically and physiologically distinct primary and metastatic niches in medulloblastoma.	55
Figure 1.9 Our locally synthesised 19-Fluorine MMP-MRI probe	61
Figure 2.1 Schematic workflow of the main methods described in this thesis.	70
Figure 2.2 Analysis of the concentrations (ng/ μ l) of RNA extracted from sub-grouped MB cell lines.	78
Figure 2.3 Results from confirmation experiments of MMP-2 primer efficiency.	82
Figure 2.4 Gradient PCR for MMP-9 primer	84

Figure 2.5 Results from primer efficiency experiments on GAPDH primer.	85
Figure 2.6 Graphical representation of the stepwise incremental protein concentrations of the Bradford reagent standard curve.....	87
Figure 3.1 Protease and protease inhibitor microarrays of conditioned supernatant following 48hrs of culture of the matched Group 3 medulloblastoma.	103
Figure 3.2 Densitometry of protease and protease inhibitor microarrays of the matched Group 3 medulloblastoma.	108
Figure 3.3 Protease and protease inhibitor microarrays of conditioned supernatant following 48hrs of culture of the Group 4 medulloblastoma primary A. (CHLA-01-Med) and metastatic B. (CHLA-01R-Med) cell lines.	111
Figure 3.4 Densitometry of protease and protease inhibitor microarrays of the matched Group 4 medulloblastoma cell lines.	114
Figure 3.5 MMP-2 gene expression by qRT-PCR of 9 sub-grouped medulloblastoma cell lines.....	117
Figure 3.6 MMP-2 protein expression by Western blotting of cell lysates from 10 sub-grouped medulloblastoma cell lines (n=5).	119
Figure 3.7 Levels of secreted MMP-2 protein as detected with the total MMP-2 Quantikine ELISA immunoassay (R&Dsystems).....	120
Figure 3.8 Levels of secreted MMP-2 protein as detected with the total MMP-2 Quantikine ELISA immunoassay (R&Dsystems).....	122

Figure 3.9 MMP-9 protein expression by Western blotting of 9 sub-grouped 2-D cultured medulloblastoma cell lines alongside a control cell line (H1-NSC).....	123
Figure 3.10 Gelatin zymography of supernatant from a panel of 9 medulloblastoma sub-grouped cell lines.....	130
Figure 4.1 Growth of medulloblastoma spheroids	142
Figure 4.2 Spheroid culture in neurosphere medium and on top of a collagen IV matrix.....	143
Figure 4.3 Levels of functionally active MMP-2 and MMP-9 from initial SHH and Group 3 MB spheroid experiments.	145
Figure 4.4 The effect of SHH spheroid culture on a hyaluronan-based matrix on the secreted levels of functionally active MMP-2 and MMP-9.	146
Figure 4.5 Levels of functionally active MMP-2 and MMP-9 secreted by DAOY spheroids migrating across different matrices.....	147
Figure 4.6 Levels of functionally active MMP-2 and MMP-9 secreted by DAOY spheroids migrating across different matrices.....	148
Figure 4. 7 Schematic diagram of 3-dimensional hydrogel culture of medulloblastoma	150
Figure 4. 8 Gelatin zymography of supernatant from 3-D embedded medulloblastoma cell lines.....	151

Figure 4.9 Generation of ONS-76 wild type TP53 and ONS-76 dnp53 spheroids.....	152
Figure 4.10 Zymography of supernatant from SHH MB spheroid and macrophage culture.....	153
Figure 4. 11 Chemical structure of Doxycycline Hyclate.....	156
Figure 4.12 Gelatin zymography of 72hr conditioned supernatant from 10µM and 100µM Doxycycline treated spheroids alongside matched DAOY and ONS-76 spheroids cultured in their usual neurosphere medium.....	157
Figure 4.13 DNA methylation profiling of TIMP-1 in normal cerebellum and sub-grouped medulloblastoma.	158
Figure 4. 14 Kaplan Meier survival analyses of MB patient gene expression data of TIMP-1, -2, -3, and -4.....	162
Figure 4.15 72 hour treatment of SHH MB spheroids with 25nM and 50nM concentrations of TIMP-1 and TIMP-2 recombinant proteins...	164
Figure 4. 16 Representative gelatin zymogram of supernatant from ONS-76 spheroids after 72 hour rTIMP-1 and rTIMP-2 treatment at 25 and 50 nanomolar concentrations.	165
Figure 4.17 Volumetric comparison of SHH MB spheroids following 24-72 hours of TIMP-1 50nM treatment alongside media and vehicle controls.....	167
Figure 4.18 DAOY Coll. IV migration assay.....	169
Figure 4.19 ONS-76 Collagen IV migration assay	170

Figure 4.20 UW228-3 Collagen IV migration assay.....	171
Figure 4.21 24 hour invasion assays of an aggressive Group 3 cell line through different barrier coatings.....	175
Figure 4.22 PrestoBlue cytotoxicity experiment in 2-dimensional culture of HD-MB03 Group 3 MB cells treated with varying concentrations of rTIMP-1	177
Figure 4.23 Effect of rTIMP-1 treatment on the invasive capacity of HD-MB03 cells (n=3)	178
Figure 4.24 Invasion assays (n=3) of matched primary and metastatic Group 3 (D425-Med and D458-Med) cell lines.	179
Figure 4.25 Invasion assays (N=3) of matched primary and metastatic Group 4 (CHLA-01-MED and CHLA-01R-MED) cell lines.	180
Figure 5.1 Perivascular flow of CSF through the glymphatic system.	187
Figure 5.2 Correlation of DNA methylation patterns and resulting gene expression of MMP-2, MMP-9 and EMMPRIN in normal cerebellum (na) compared to MB patient samples using the R2 Genomic Visualisation database.....	194
Figure 5.3 Correlation of DNA methylation patterns of TIMP-1 and TIMP-2 with their resulting gene expression in MB patients from the Cavalli dataset, as analysed on the R2 Genomics and Visualisation platform.	196

Figure 5.4 Patient 1: T1 weighted post-contrast pre-operative (yellow-outlined) and post-operative (green-outlined) magnetic resonance imaging.....	201
Figure 5.5 T1-weighted post-contrast magnetic resonance imaging of patient 2.....	203
Figure 5.6 T1-weighted post-contrast magnetic resonance imaging of patient 3.....	206
Figure 5.7 T1-weighted post-contrast magnetic resonance imaging of patient 4.....	208
Figure 5.8 T1-weighted post-contrast magnetic resonance imaging of patient 5.....	210
Figure 5.9 T1-weighted post-contrast magnetic resonance imaging of patient 6.....	213
Figure 5.10 Levels of functionally active MMP-2 and MMP-9 within cerebrospinal fluid from matched primary and recurrent MB paediatric patients.....	214
Figure 5.11 Serial cerebrospinal fluid samples from Patient 6 in whom surgical resection of his primary tumour was performed prior to sample 6 [1] and recurrence detected at 6 [2]......	215
Figure 6.1 Representative diagram demonstrating the shared mechanisms of FRET assay (A) and our ¹⁹ F MRI MMP-2/MMP-9 biosensor (B).....	224

Figure 6. 2 FRET Assay of recombinant MMP-2 (0.61ng/μl) in Acetonitrile solutions.	229
Figure 6.3 FRET assay of different amounts of recombinant MMP-2 protein (Peprotech) in different percentage concentrations of acetonitrile.	229
Figure 6.4 FRET assay of different amounts of recombinant MMP-2 protein (Peprotech) in different percentage concentrations of acetonitrile..	231
Figure 6.5 FRET assay of column concentrated supernatant from 48 hour culture of ONS-76 medulloblastoma cells.....	232
Figure 6.6 . FRET assay of column concentrated supernatant from 48 hour culture of HD-MB03 (Group 3 metastatic) medulloblastoma cells.	233
Figure 6. 7 FRET assay of column concentrated supernatant from 48 hour culture of paired Group 3 primary-D425-Med and metastatic D458-Med medulloblastoma cells..	234
Figure 6. 8 FRET assay of column concentrated supernatant from 48 hour culture of paired Group 4 primary-CHLA-01-Med and metastatic CHLA-01R-Med medulloblastoma cells.....	235
Figure 6. 9 FRET assay of the SHH MB cell line ONS-76 (wt p53) in black and ONS-76 (dnp53) in red.	236
Figure 6. 10 FRET assay of column concentrated supernatant following 48-hour culture of ONS-76 medulloblastoma cells.	237

Figure 6. 11 FRET assay of naïve CSF samples from Patient 1 at their first presentation (primary) and following growth of the residual tumour.	238
Figure 6. 12 FRET assay of naïve CSF samples from Patient 2 at the first recurrence of their MB (recurrence) and following relapsed MB.	239
Figure 6. 13 FRET assay of naïve CSF samples from Patient 3 at recurrence of their MB (recurrence) and following relapsed MB.....	239
Figure 6. 14 FRET assay of naïve CSF samples from Patient 4 at his first presentation with MB (primary) and recurrence of their disease.	240
Figure 6.15 19-Fluorine MMP2/MMP-9 biosensor optimisation experiments.....	242
Figure 6.16 19-Fluorine MRI MMP-2/MMP-9 imaging of concentrated cell supernatant	244
Figure 7.1 Schematic diagram of the stepwise development of an imaging biomarker	250
Figure 7.2 Schematic diagram of the 3-D models used.....	257
Figure 7.3 Typical MRI appearances of the four MB subgroups.....	270

List of Tables

Table 1. 1 Hereditary syndromes and germline mutations that predispose to MB.....	4
Table 1.2 Recurrently mutated chromatin-regulating genes implicated in MB. Table from (Northcott, Jones et al. 2012).....	6
Table 1.3 Improved risk stratification of medulloblastoma in paediatric patients over 3 years of age. Taken from (Ramaswamy, Remke et al. 2016, Juraschka and Taylor 2019)	20
Table 1.4 Summary of the re-classification of MB in the 2016 World Health Organisation Classification of CNS tumours (Louis, Perry et al. 2016).	39
Table 2.1 Characteristic of the panel MB cell lines used.*Matched pairs of primary and recurrent cell lines (Ivanov, Coyle et al. 2016).....	66
Table 2.2 Separating gel mix.....	74
Table 2.3 Stacking gel mix	74
Table 2.4 RNA Nanodrop table showing quantities of RNA from MB cell lines	79
Table 2.5 Reagents and volumes required to be added to RNA and dH ₂ O for cDNA synthesis	80
Table 2.6 MMP-2 (human) gene primer sequence	81
Table 2.7 MMP-9 (human) gene primer sequence	83

Table 2.8 Bradford assay standards with increasing BSA concentration	86
Table 2.9 Bradford assay results once exported into pre-filled Excel file	87
Table 2.10 Neurosphere medium	91
Table 2.11 Comparison of technical differences between Calcein-AM© and PrestoBlue© fluorescent dyes	94
Table 3.1 Differentially expressed proteases in matched Group 3 primary (D425-Med) and metastatic (D458-Med) medulloblastoma cell lines.	104
Table 3.2 Differentially expressed protease inhibitors in matched Group 3 primary (D425-Med) and metastatic (D458-Med) medulloblastoma cell lines.	106
Table 3. 3 Differentially expressed proteases in matched Group 4 primary (CHLA-01-Med) and recurrent (CHLA-01R-Med) medulloblastoma cell lines.	112
Table 3.4 Differentially expressed protease inhibitors in matched Group 4 primary (CHLA-01-Med) and recurrent (CHLA-01R-Med) medulloblastoma cell lines.	113
Table 3.5 Gelatin zymography optimisation experiments	127
Figure 4.1 Growth of medulloblastoma spheroids	142

Figure 4.2 Spheroid culture in neurosphere medium and on top of a collagen IV matrix.	143
Figure 4.3 Levels of functionally active MMP-2 and MMP-9 from initial SHH and Group 3 MB spheroid experiments.	145
Figure 4.4 The effect of SHH spheroid culture on a hyaluronan-based matrix on the secreted levels of functionally active MMP-2 and MMP-9.	146
Figure 4.5 Levels of functionally active MMP-2 and MMP-9 secreted by DAOY spheroids migrating across different matrices.	147
Figure 4.6 Levels of functionally active MMP-2 and MMP-9 secreted by DAOY spheroids migrating across different matrices.	148
Figure 4. 7 Schematic diagram of 3-dimensional hydrogel culture of medulloblastoma Medulloblastoma cell lines were seeded in a pure hyaluronan (HA) hydrogel and established in extended culture with media changes performed every 48 hours.	150
Figure 4. 8 Gelatin zymography of supernatant from 3-D embedded medulloblastoma cell lines.....	151
Figure 4.9 Generation of ONS-76 wild type TP53 and ONS-76 dnp53 spheroids.....	152
Figure 4.10 Zymography of supernatant from SHH MB spheroid and macrophage culture.....	153
Figure 4. 11 Chemical structure of Doxycycline Hyclate.....	156

Figure 4.12 Gelatin zymography of 72hr conditioned supernatant from 10µM and 100µM Doxycycline treated spheroids alongside matched DAOY and ONS-76 spheroids cultured in their usual neurosphere medium.....	157
Figure 4.13 DNA methylation profiling of TIMP-1 in normal cerebellum and sub-grouped medulloblastoma.	158
Figure 4. 14 Kaplan Meier survival analyses of MB patient gene expression data of TIMP-1, -2, -3, and -4.....	162
Figure 4.15 72 hour treatment of SHH MB spheroids with 25nM and 50nM concentrations of TIMP-1 and TIMP-2 recombinant proteins...	164
Figure 4. 16 Representative gelatin zymogram of supernatant from ONS-76 spheroids after 72 hour rTIMP-1 and rTIMP-2 treatment at 25 and 50 nanomolar concentrations.	165
Figure 4.17 Volumetric comparison of SHH MB spheroids following 24-72 hours of TIMP-1 50nM treatment alongside media and vehicle controls.....	167
Figure 4.18 DAOY Coll. IV migration assay.....	169
Figure 4.19 ONS-76 Collagen IV migration assay	170
Figure 4.20 UW228-3 Collagen IV migration assay	171
Figure 4.21 24 hour invasion assays of an aggressive Group 3 cell line through different barrier coatings.....	175

Figure 4.22 PrestoBlue cytotoxicity experiment in 2-dimensional culture of HD-MB03 Group 3 MB cells treated with varying concentrations of rTIMP-1	177
Figure 4.23 Effect of rTIMP-1 treatment on the invasive capacity of HD-MB03 cells (n=3)	178
Figure 4.24 Invasion assays (n=3) of matched primary and metastatic Group 3 (D425-Med and D458-Med) cell lines.	179
Figure 4.25 Invasion assays (N=3) of matched primary and metastatic Group 4 (CHLA-01-MED and CHLA-01R-MED) cell lines.	180
Table 5.1 Comparison of electrolyte content of CSF and plasma.....	188
Table 5.2 Expected cellular counts in cerebrospinal fluid (Termini, Neman et al. 2014).	189
Table 5. 3 Characteristics of CSF sampled from paediatric patients with medulloblastoma	197
Table 5.4 Characteristics of paediatric medulloblastoma patients.	216
Table 6. 1 Results from centrifugal column concentration of MB cell line supernatants.....	227

List of Abbreviations

APC	Adenomatous polyposis coli
ATM	Ataxia telangiectasia mutated
$\alpha 9\beta 1$	Alpha-9 Beta 1 integrin
BBB	Blood-brain barrier
BCSFB	Blood-CSF barrier
BLM	Bloom syndrome
B-catenin1	Beta-Catenin 1 gene
bFGF	Human recombinant fibroblastic growth factor basic
BRCA2	Breast cancer gene
CCL 4/5/12	Chemokine ligand 4, 5 or chemokine ligand receptor-12
CDK6	Cyclin-dependent kinase 6
CEST	Chemical exchange saturation transfer
C-MET	aka tyrosine-protein kinase or hepatocyte growth factor receptor
CREBBP	CREB binding protein
CSF	Cerebrospinal fluid
DDB	Damage specific DNA binding protein
DMEM	Dulbecco's modified Eagle Medium

DVL	Dishevelled Segment Polarity Protein
ECM	Extracellular matrix
EGF	Human recombinant epidermal growth factor
EGFR	Epidermal growth factor receptor
EMMPRIN	Extracellular matrix metalloproteinase inducer
EP300	E1A Binding protein
ERBB2	Epidermal growth factor b2 receptor tyrosine kinase
ERCC	Excision repair 1, Endonuclease non-catalytic subunit
FANCA-W	Fanconi anaemia complementation group A-W
FAP	Familial adenomatous polyposis
GF11/ GF11B	Growth differentiation factor 11/B
GLI2	GLI family zinc finger 1, 2 or 3
GSTA5	Glutathione S-transferase alpha
GSK3β	Glycogen Synthase Kinase 3 Beta
IGF-R	Insulin-like growth factor receptor
KDM6A	Lysine demethylase 6A
MB	Medulloblastoma
MEM	Modified Eagle Medium
MLH	MutL Homolog 1

MMP	Matrix metalloproteinase
MRS	Magnetic Resonance Spectroscopy
MSH	Melanocyte stimulating hormone
MT-MMPs	Membrane type matrix metalloproteinases
MYC	MYC proto-oncogene/ bHLH transcription factor
MYCN	MYCN proto-oncogene transcription factor
NBN	Nibrin
NF-κB	Nuclear factor kappa B
OTX2	Orthodenticle homeobox 2
PALB2	Partner and localiser of BRCA2
PDGFRα	Platelet derived growth factor receptor alpha
PLGF	Placental growth factor
PMS2	Postmeiotic segregation increased 2
POLH	DNA polymerase eta
PTCH1	Patched 1
SHH	Sonic Hedgehog
SMARCA4	SWI/SNF related, matrix associated, actin dependent regulator of chromatin, subfamily a, member 4
SMO	Smoothed, Frizzled Class Receptor

SNCAIP	Synuclein alpha interacting protein
SPARC	Secreted protein Acidic and Cysteine rich
STAT3	Signal transducer and activator of transcription 3
SUFU	Suppressor of fused homolog
P53/TP53	Tumour suppressor gene p53
TERT	Telomerase reverse transcriptase
TGF-β	Transforming growth factor- β
TIMPs	Tissue inhibitors of metalloproteinases
TNF	Tumour necrosis factor
TWIST1	Twist related protein 1
VEGF	Vascular endothelial factor
WNT	Wingless
XPA	Xeroderma pigmentosum complementation group A
XPC	Xeroderma pigmentosum complementation group C
YAP1	Yes associated protein 1

Chapter 1. Introduction

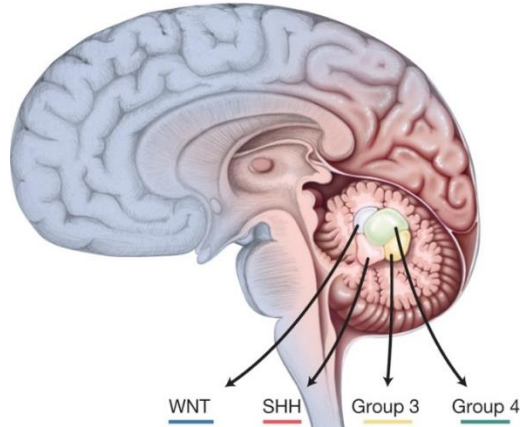
Introduction

1.1 Epidemiology

Since its debut as the small round blue cell tumour of the cerebellum described by Cushing and Bailey a century ago, medulloblastoma (MB) has remained the most common malignant brain tumour in children, accounting for one-fifth of all paediatric brain tumours (Ramaswamy and Taylor 2017). Owing to its embryonal origins, MB predominantly affects children within their first decade of life, with a bimodal peak of incidence between the ages of 1-4 years and 5-9 years old (Millard and De Braganca 2016, Juraschka and Taylor 2019).

Given its reported annual incidence of five cases per million children, MB is considered a rare condition, with a slight preponderance for males [male to female ratio of 1.7:1]. While it can occur in adulthood, it is incredibly infrequent with an incidence of 0.05 cases per 100,000 adults, and will usually present before the age of 40 years (Millard and De Braganca 2016, Juraschka and Taylor 2019).

While 75% of MB patients are reported to survive up to 5 years following their initial diagnosis (Orr 2020), progress in genetic and molecular pathology have highlighted prognostic implications of the molecular subgroup of the patient's tumour. This is due to their distinct epidemiological and clinical characteristics, including the age groups most commonly affected as well as the frequency of metastasis and recurrence in each subgroup as demonstrated in the Figure 1.1.



Subgroup		WNT	SHH	Group 3	Group 4
Clinical Characteristics	% of Cases	10	30	25	35
	Age at Diagnosis				
	Gender Ratio (M:F)	1:1	1:1	2:1	3:1
	Anatomic Location				
	Histology	Classic, Rarely LCA	Desmoplastic, Classic, LCA	Classic, LCA	Classic, LCA
	Metastasis at Diagnosis (%)	5-10	15-20	40-45	35-40
	Recurrence Pattern	Rare; Local or metastatic	Local	Metastatic	Metastatic
	Prognosis	Very good	Infants good, others intermediate	Poor	Intermediate
Molecular Characteristics	Proposed Cell of Origin	Progenitor cells in the lower rhombic lip	Granule precursors of the external granule layer	Neural stem cells	Unipolar brush cells
	Recurrent Gene Amplifications	-	<i>MYCN</i> <i>GLI1</i> or <i>GLI2</i>	<i>MYC</i> <i>MYCN</i> <i>OTX2</i>	<i>SNCAIP</i> <i>MYCN</i> <i>OTX2</i> <i>CDK6</i>
	Recurrent SNVs	<i>CTNNB1</i> <i>DDX3X</i> <i>SMARCA4</i> <i>TP53</i>	<i>PTCH1</i> <i>TERT</i> <i>SUFU</i> <i>SMO</i> <i>TP53</i>	<i>SMARCA4</i> <i>KBTD4</i> <i>CTDNBP1</i> <i>KMT2D</i>	<i>KDM6A</i> <i>ZMYM3</i> <i>KTM2C</i> <i>KBTD4</i>
	Cytogenetic Events Gain Loss	6	3q, 9p 9q, 10q, 17p	1q, 7, 18 8, 10q, 11, 16q i17q	7, 18q 8, 11p, X i17q
	Other Recurrent Genetic Events	-	-	<i>GF11</i> and <i>GF11B</i> enhancer hijacking	<i>PRDM6</i> , <i>GF11</i> , and <i>GF11B</i> enhancer hijacking

Age: Infant Child Adult

Figure 1.1 Clinical, genetic, molecular and histopathological characteristics of paediatric medulloblastoma (Ivanov, Coyle et al.). MB was recently determined to exist as four distinct molecular subgroups, each with varying 5-year overall survival- Wingless (WNT>95%), Sonic hedgehog (SHH-75%), Group 3 (50-60%) and Group 4 (75%) as shown above. Images from (Northcott, Buchhalter et al. 2017, Juraschka and Taylor 2019)

1.2 Pre-disposing risk factors to MB

1.2.1 Genetic mutations

Genomic advances in the biological heterogeneity of MB led to the consensus that it exists as four molecularly defined subgroups: Wingless (WNT), Sonic hedgehog (SHH), Group 3 and Group 4 MB. While hereditary syndromes associated with aberrant signalling in the developmental WNT and SHH pathways are responsible for less than 5% of MB (Millard and De Braganca 2016), the increased prevalence of MB in patients with hereditary cancer predisposing syndromes, led to the discovery of shared germline genetic mutations, that are involved in MB aetiology or drive MB metastatic behaviour (Table 1. 1). Genetic mutations in MB seem to occur most frequently in the WNT (β -CATENIN1) and SHH (PTCH1, SUFU and TP53) subgroups (Roussel and Stripay 2018, Northcott, Robinson et al. 2019).

Table 1. 1 Hereditary syndromes and germline mutations that predispose to MB.

TP53, PTCH1, SUFU, APC, PALB2 and BRCA2 genes were the most cited to significantly increase the risk of developing MB. Adapted from (Northcott, Robinson et al. 2019)

Predisposing hereditary conditions	Germline genetic mutations involved
Gorlin syndrome	PTCH1, SUFU
Li-Fraumeni syndrome	TP53
Familial adenomatous polyposis syndrome	APC
Fanconi anaemia	FANCA-W, PALB2, BRCA2
Curry-Jones syndrome	SMO
Greig cephalopolysyndactyly syndrome	GLI3
Bloom syndrome	BLM
Constitutional mismatch repair deficiency	MSH2, MSH6, MLH1, PMS2
Ataxia telangiectasia	ATM
Nijmegen breakage syndrome	NBN
Rubinstein-Taybi syndrome	CREBBP, EP300
Xeroderma pigmentosum	DDB2, ERCC1, ERCC2, ERCC3, ERCC4, ERCC5, POLH, XPA, XPC

1.2.2 Epigenetic regulation

Epigenetics relates to the regulation of gene expression without changes to the DNA sequences or genome (Roussel and Stripay 2018). The significance of epigenetic regulation in the pathogenesis of MB has become indisputable, given the detection of the several subgroup-specific epigenetic alterations, some of which have been correlated to more aggressive MB phenotypes (Northcott, Robinson et al. 2019). As succinctly described by Zou et al, 'epigenetic regulators serve as oncogenes or tumour suppressors in a context-dependent manner across the distinct subtypes of MB' (Zou, Poore et al. 2020), effecting activation of the former or suppression of the latter (Roussel and Stripay 2018).

While these epigenetic alterations encompass changes in DNA methylation, histone modifications, non-coding micro- and long RNAs, the most commonly implicated in MB development, are concerned with chromatin remodelling, with almost 50% of MBs demonstrating altered chromatin-regulating genes (Northcott, Robinson et al. 2019). In addition, anomalous methylation patterns in the histones H3K4 and H3K27 exist in all MB subgroups (Roussel and Stripay 2018). Of the 4 MB subgroups, Group 3 and Group 4 are most frequently associated with metastasis at diagnosis and early recurrence in comparison to SHH and WNT (Northcott, Robinson et al. 2019). The relative infrequency of mutations in Group 3 and 4 MB (Table 1.2) therefore remains a

conundrum, and led to the emerging notion that their increased metastatic potential is due to underlying epigenetic dysregulation (Roussel and Stripay 2018).

Table 1.2 Recurrently mutated chromatin-regulating genes implicated in MB. Table from (Northcott, Jones et al. 2012)

Gene	Somatic mutation (%)	Subgroup affected	Function of affected gene
<i>MLL2</i>	5.8	WNT and SHH	H3K4 methyltransferase
<i>SMARCA4</i>	5.8	WNT and Group 3	Chromatin remodeller
<i>KDM6A</i>	5.2	Group 4	H3K27me2 and H3K27me3 demethylase
<i>MLL3</i>	2.6	Group 3 and Group 4	H3K4 methyltransferase
<i>BCOR</i>	2.0	SHH	Transcriptional repressor
<i>CHD7</i>	1.9	Group 3 and Group 4	Chromatin remodeller
<i>LDB1</i>	1.6	SHH	Transcriptional regulator
<i>CREBBP</i>	1.3	WNT and SHH	HAT
<i>ZMYM3</i>	1.3	Group 4	Associated with HDAC complex
<i>ARID1B</i>	1.2	WNT and SHH	Chromatin remodeller
<i>EYA4</i>	1.2	None	Histone phosphatase
<i>EP300</i>	1.0	SHH	HAT
<i>TRRAP</i>	1.0	None	Associated with HAT complex
<i>KDM4C</i>	1.0	Group 3 and Group 4	H3K9me3 and H3K36me3 demethylase
<i>CTR9</i>	<1.0	NA	Associated with RNA Pol II activity
<i>TLK2</i>	<1.0	NA	Modulates chromatin assembly
<i>SETD2</i>	<1.0	NA	H3K36 methyltransferase
<i>TAF1</i>	<1.0	NA	Component of TFIID–RNA Pol II complex
<i>KDM1A</i>	<1.0	NA	H3K4me1, H3K4me2 and H3K9 demethylase
<i>KDM5A</i>	<1.0	NA	H3K4me2 and H3K4me3 demethylase
<i>BRCA2</i>	<1.0	NA	Regulates DNA double-strand break repair
<i>CTCF</i>	<1.0	NA	Chromatin binding and remodelling factor
<i>REST</i>	<1.0	NA	Recruits histone demethylases and HDACs
<i>HDAC9</i>	<1.0	NA	Histone lysine deacetylase

1.2.3 Other factors

While no geographical or ethnicity related factors have been identified to increase the risk of developing MB, high birth weight was purported by Harder et al. in 2008, to be a pre-disposing factor to developing MB following a systematic review of 8 published studies reporting an odds

ratio of 1.27 [confidence interval 1.02-1.60] (Massimino, Biassoni et al. 2016).

1.3 Clinical presentation

As MB commonly presents within the first decade of life with non-specific symptoms that could be attributable to a vast array of differential diagnoses, it results in diagnostic delays and consequently, treatment provision. While this delay to diagnosis has improved from a median of 12-13 weeks in 2007 to 6.5 weeks more recently following the introduction of clinical guidelines aiding diagnosis of brain tumours in children, more work is needed to improve MB patient outcomes (HeadSmart:-Be-Brain-Tumour-Aware 2015).

The clinical presentation of a paediatric patient with MB varies according to the patient's age and the anatomical location of the tumour. The rapidly growing nature of medulloblastoma results in presentation with either cerebellar symptoms due to its anatomical location, and/or obstruction of the cerebrospinal fluid (CSF) pathways due to invasion into or compression of the fourth ventricle, resulting in obstructive hydrocephalus. While the former could present with cranial nerve palsies, reduced coordination, muscle tone, stability and disturbances in motor function and gait; the latter frequently presents with headaches, nausea and vomiting, cognitive impairment in school-going children, developmental delay in infants or in extremis (Kumar, Liu et al. 2020).

As the patient's age at diagnosis determines how they clinical present, it can result in a delay to diagnosis. Considering the non-specific manner in which infants may present, as well as the fact that their open cranial sutures (from infancy up to 18 months of age) can accommodate the increasing intracranial pressure, their MB may manifest as insidious gradual increments in their head circumference, which may not be detected as quickly as other symptoms. Paediatric patients with MB may also present with symptoms suggestive of metastatic dissemination including back pain, urinary or bowel disturbance, or focal radiculopathies (Northcott, Robinson et al. 2019, Kumar, Liu et al. 2020).

Following referral to a tertiary neurosurgery centre for thorough clinical assessment, the child with suspected medulloblastoma will have diagnostic and staging magnetic resonance imaging (MRI) of their entire neuroaxis for anatomical localisation of their tumour and exclusion of macroscopic metastases. A multidisciplinary team then considers the patient's demographics, clinical assessment and imaging before recommending a treatment plan. This would include a combination of neurosurgery for the excisional biopsy of the tumour and decompression of the posterior fossa, adjuvant chemotherapy for systemic control of metastases and craniospinal irradiation for the treatment and prevention of leptomeningeal macrometastases. This multimodal therapeutic approach to medulloblastoma has culminated in a substantial reduction in mortality, but has incurred significant morbidity in similar proportions,

borne by the survivors of this devastating disease (Dufour, Beaugrand et al. 2012, Ramaswamy and Taylor 2017).

1.4 Pathological classification of MB

1.4.1 Histopathological classification of MB

Historically, the sole method used for grading medulloblastoma was the histopathological examination of resected MB tumour specimens. The World health organisation (WHO) designates tumours to Grade I, II III or IV, reflecting the scale of histological divergence of the tumour from its cells of origin. All MB histological variants are designated to be grade IV tumours due to their 'cytologically malignant, mitotically active and necrosis-prone' appearances coupled with their associated poor outcomes (Louis, Ohgaki et al. 2007).

Previous editions of the WHO classification of central nervous system (CNS) tumours included 'medulloblastoma with myogenic differentiation/ medullomyoblastomas', an MB phenotype described in any histological MB exhibiting rhabdomyoblast-like appearances (small round cells with desmin, myoglobin and myosin immunopositivity) (Louis, Ohgaki et al. 2007). This descriptor along with another, 'medulloblastoma with melanocytic differentiation/ melanocytic medulloblastoma', were omitted from the most recently published WHO classification in 2016 (Louis, Ohgaki et al. 2007, Louis, Perry et al. 2016). Of the 5 remaining histologically distinct MB phenotypes, desmoplastic/nodular

(Ramaswamy, Remke et al. 2016) and large cell/ anaplastic (LCA) variants were combined, due to their similar metastatic behaviour.

1.4.1.1 Classic MB

Up to 80% of MB exhibit classic histology denoted by densely packed tissue consisting of small round blue cells with large hyperchromatic nuclei and scanty cytoplasm as shown in Figure 1.2 (Kumar, Kumar et al. 2017). While majority of WNT MB demonstrate classic histology, this morphology is also observed in 40-45% of SHH and in a smaller proportion of Group 3 and 4 MB (Northcott, Robinson et al. 2019).

1.4.1.2 Desmoplastic/Nodular MB

While most MB demonstrating the desmoplastic nodular (DN) histological subtype are SHH MB, it is observed in 30-35% of tumours in this subgroup (Northcott, Robinson et al. 2019) and is characterised by round nodules enveloped by reticulin fibres (Figure 1.2) resulting in a firm tissue architecture (Kumar, Kumar et al. 2017).

1.4.1.3 Medulloblastoma with extensive nodularity (MBEN)

Phenotypically similar to its DN histological counterpart, this variant is observed in 1-2% of all MB. These tumours with highly neuronally differentiated phenotypes consist of round cells with low mitotic indices (Figure 1.2) and are frequently observed in infants (Kumar, Kumar et al. 2017).

1.4.1.4 Large cell/ Anaplastic

Heralding a poor prognosis, this histological subtype is defined by large cells with significant nuclear pleomorphism and prominent nucleoli with scanty cytoplasm (Figure 1.2). High proliferative rates signified by their high mitotic indices and frequent associations with necrosis are characteristic (Kumar, Kumar et al. 2017).

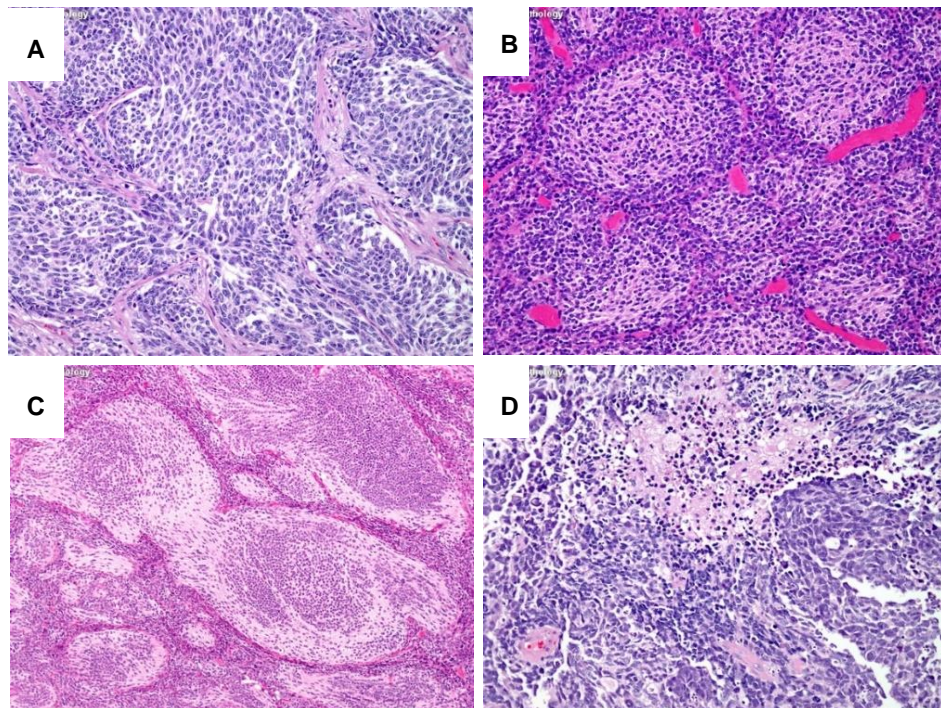


Figure 1.2 Histological subtypes of MB

The four main histological variants in MB are demonstrated following haematoxylin and eosin staining of MB tumour samples. A. Classical MB is denoted by the small round blue cells. B. Desmoplastic/Nodular MB is characterised by densely packed nodular tissue, enveloped by reticulin fibres. C. MB with extensive nodularity is characterised by pale islands of uniformly round cells surrounded by fibrillary tissue. D. Anaplastic MB demonstrating irregular large hyperchromatic nuclei with scanty cytoplasm. (Images from <https://www.webpathology.com/>- accessed November 2020.

1.4.2 Molecular classification of MB

1.4.2.1 Wingleless Medulloblastoma (WNT)

Emerging from the dorsal brainstem, WNT tumours are postulated to originate from progenitor cells of the lower rhombic lip (Northcott, Jones et al. 2012). With more than 95% of patients with WNT tumours having an overall survival of 10 years, WNT has been identified as the subgroup conferring the best outcome in children with medulloblastoma, following the standard management of surgical resection, chemotherapy and craniospinal irradiation (Ramaswamy, Remke et al. 2016). It is the least frequently occurring subgroup of all the medulloblastoma subtypes (10%) and is incident in males and females in equal proportions, with a propensity for affecting children over 3 years of age (Northcott, Jones et al. 2012).

Up to 90% of WNT tumours harbour missense mutations in the β -catenin1 gene located on chromosome 3, which manifests as the upregulation of the β -catenin WNT signalling pathway, a key regulator of stem cell pluripotency (Holgado, Guerreiro Stucklin et al. 2017). Diagnostic techniques used to identify β -catenin 1 mutation and establish WNT tumour subgrouping include DNA methylation profiling, gene expression profiling and sequencing as well as by immunohistochemistry. In addition, up to 80% of WNT tumours exhibit monosomy 6, a pathognomonic finding in this subgroup. The excellent prognosis associated with WNT tumours could be as a result of their

typically stable genomes. This could also explain the low likelihood of metastasis and recurrence observed in patients with WNT tumours (Holgado, Guerreiro Stucklin et al. 2017, Ramaswamy and Taylor 2017). Other mutations implicated in the tumorigenesis of WNT tumours include DDX3X observed in 50%, SMARCA4 in a 25% and TP53 mutations in 13% of WNT tumours (Holgado, Guerreiro Stucklin et al. 2017). WNT tumours also tend toward classic histological appearance, with majority of medulloblastoma previously categorised as classical medulloblastoma, being identified as WNT in molecular nature (Northcott, Jones et al. 2012).

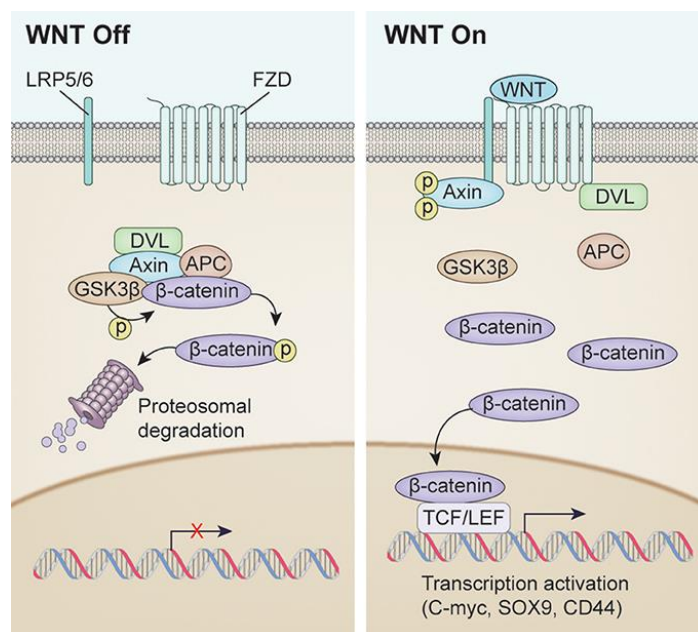


Figure 1.3 The WNT signalling pathway showing consequences of its activation.

Following nuclear translocation of β -catenin1, its phosphorylation in the absence of the **WNT** ligand results in breakdown of proteasomes (left), while in the presence the bound **WNT** ligand, activation of the pathway occurs, resulting in perpetual transcription of genes implicated in MB metastasis such as C-MYC, SOX9 and CD44. Image from (McCord, Mukoyama et al. 2017).

1.4.2.2 Sonic Hedgehog (SHH) MB

Derived from multiple progenitors including cerebellar granule neuron precursors, sub-ventricular zone neural stem cells and cochlear nuclei (Northcott, Jones et al. 2012), SHH tumours are so named due to their possession of somatic nucleotide variants and mutations in drivers of the sonic hedgehog pathway (a pathway involved in cerebellar development). These drivers culminate in upregulation of the SHH pathway, as observed in approximately 90% of SHH medulloblastoma (Ramaswamy, Remke et al. 2016). Demographically, SHH tumours constitute 30% of medulloblastoma and preferentially occur in infants and in adulthood with a slight male preponderance (Northcott, Jones et al. 2012).

The most commonly identified mutations are inactivating mutations in PTCH1 in 23.3% and SUFU in 13.5% (Holgado, Guerreiro Stucklin et al. 2017). These mutations inactivate these genes, both being negative regulators of the SHH pathway. Mutations in the PI3K pathway in SHH tumours have also been identified to negate SUFU function and thereby result in increased SHH signalling. In addition, mutations resulting in the activation of SMO in 14.3% are also postulated to result in increased SHH pathway activity. A small proportion of SHH medulloblastoma are reported to harbour MYCN and GLI2 amplicons, while 40% of SHH tumours harbour mutations in the TERT promoter, the latter resulting in

dysfunctional cellular proliferation (Ramaswamy, Remke et al. 2016, Holgado, Guerreiro Stucklin et al. 2017, Ramaswamy and Taylor 2017).

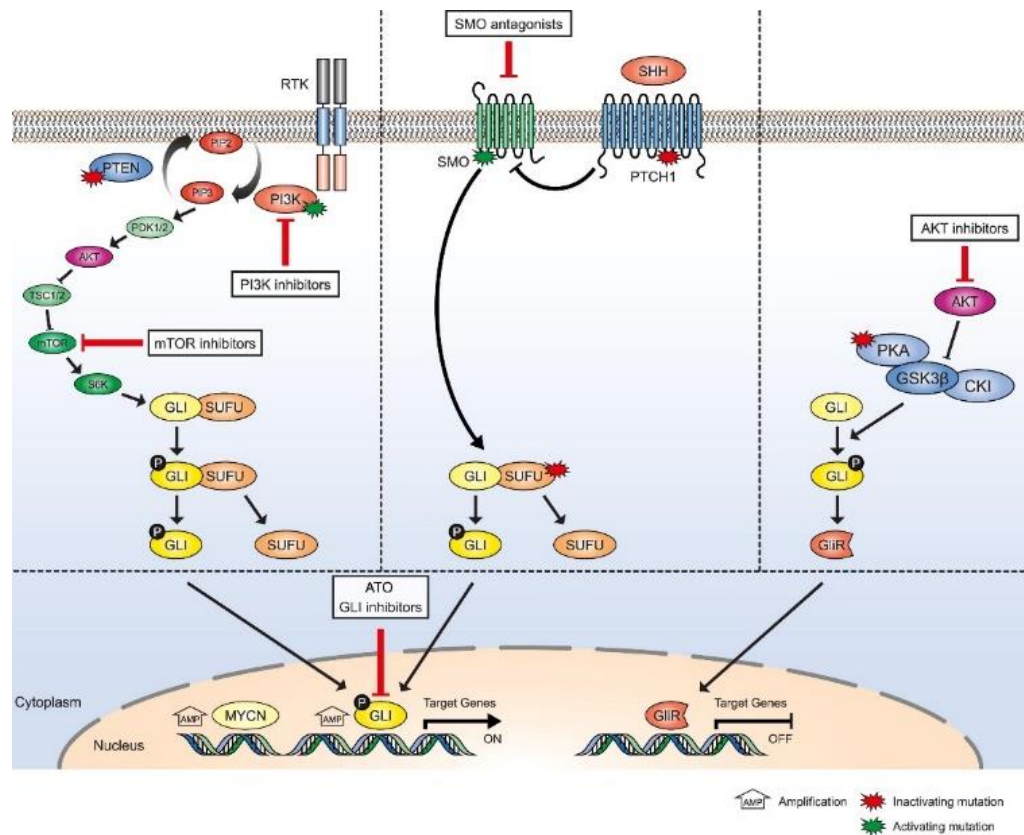


Figure 1.4 SHH signalling and interactions with the PI3K/AKT/MTOR and PKA pathways

Mutations in the genes above have been implicated in the pathophysiology of SHH-MB, due to their amplification or alterations in their activation (green-activated, red-inactivated). These changes culminate in primed oncogenes such as GLI proteins, which exert canonical effects downstream, driving SHH-MB tumours. Image from (Kool, Jones et al. 2014)

The most widely accepted prognostic indicator of SHH tumours are mutations in the tumour suppressor gene, TP53. Recognised to occur sporadically as well as in association with germline syndromes such as Li Fraumeni, SHH tumours harbouring this mutation have been determined to be high risk by the WHO, especially when associated with

classical or large cell/anaplastic histology. SHH-TP53 mutant tumours are most common in patients over 3 years of age and are associated with significantly poorer outcomes compared to their counterparts without TP53 mutations (Louis, Perry et al. 2016, Ramaswamy, Remke et al. 2016).

SHH medulloblastoma present with metastases in 15-20% (Northcott, Jones et al. 2012) and tend to recur within the resection margins of the primary tumour, a finding that appears to be distinct to this subgroup (Ramaswamy, Remke et al. 2016). With 5 year survival depicted at 75% (Northcott, Jones et al. 2012), SHH tumours are often considered to confer intermediate prognosis (Louis, Perry et al. 2016). Though all histological variants may be seen in SHH, they commonly exhibit desmoplastic/nodular histology (Northcott, Jones et al. 2012).

[1.4.2.3 Group 3](#)

Group 3 medulloblastoma tumours confer the worst prognosis with an overall 5-year survival of approximately 50% (Louis, Perry et al. 2016, Ramaswamy, Remke et al. 2016). Worse still, approximately half of these patients will have metastasis at diagnosis, culminating in an even poorer clinical outcome (Northcott, Jones et al. 2012, Holgado, Guerreiro Stucklin et al. 2017). This is especially evident in the approximate 20% of patients with Group 3 tumours that exhibit recurrent MYC amplifications (Ramaswamy, Remke et al. 2016, Holgado, Guerreiro Stucklin et al. 2017). At recurrence, Group 3 tumours often present with

dissemination throughout the neuroaxis, without radiological evidence of disease in the original resection cavity (Ramaswamy, Remke et al. 2016).

Identified in 25% of WNT tumours, mutations in the SMARCA4 gene are the most frequently implicated genetic mutation in Group 3 medulloblastoma (Holgado, Guerreiro Stucklin et al. 2017). Similar to group 4, group 3 tumours demonstrate significant genomic instability with multiple structural variations including isochromosome 17q, as well as recurrent deletions in the long arms of chromosomes 10, 11 and 16 and the short arm on chromosome 17, and genetic amplicons that play key roles in the TGF- β and NF- κ B signalling pathways. These aberrations culminate in a highly unstable genome. In addition, 40% of group 3 tumours exhibit activation and overexpression of the oncogenes GFI1A or GFI1B and OTX2 amplicons. Demographically, group 3 occurs more frequently in males with a predilection for presenting in infants and young children (Northcott, Jones et al. 2012, Holgado, Guerreiro Stucklin et al. 2017).

[1.4.2.4 Group 4](#)

Group 4 medulloblastoma is the most frequently occurring subgroup, with a strong predilection for males (M: F=3:1) and occurs most frequently in children and adolescents (Northcott, Jones et al. 2012, Ramaswamy, Remke et al. 2016). Commonly identified chromosomal abnormalities in group 4 tumours are also shared with group 3 as alluded to previously,

including isochromosome 17q and amplifications in MYCN and cyclin-dependent kinase 6 (CDK6). Though occurring at a lower frequency than is observed in WNT and SHH tumours, 10% of group 4 tumours exhibit recurrent single nucleotide variants in the histone demethylase gene, KDM6A. Group 4 tumours may also possess SNCA1P duplications and loss of the long arms on chromosome 10 (Northcott, Jones et al. 2012, Ramaswamy, Remke et al. 2016).

Similar to group 3 tumours, group 4 medulloblastoma present with dissemination throughout the neuroaxis, with no radiological evidence of recurrent tumour at the previous site of the primary as is observed with SHH medulloblastoma (Holgado, Guerreiro Stucklin et al. 2017, Ramaswamy and Taylor 2017). As group 3 and 4 tumours harbour similar chromosomal anomalies, tend to occur in the midline and behave in a similar fashion at recurrence, it is possible that these subgroups exploit similar metastatic mechanisms. Group 4 medulloblastoma are the second most likely subgroup to present with metastasis which is observed in 35-40% of these patients (Northcott, Jones et al. 2012).

1.5 Risk stratification of paediatric patients with MB

From Cushing's discovery of better survival outcomes in children with MB following tumour resection compared to biopsy, the volume of $<1.5\text{cm}^3$ of residual tumour burden has remained an important prognostic predictor. In addition, the patient's age at diagnosis as well as the presence and extent of metastatic disease, are considered to be the

clinically significant risk factors when paediatric patients with MB are stratified to either average or high risk (Juraschka and Taylor 2019).

Following the pioneering work in adjuvant craniospinal irradiation for management of paediatric medulloblastoma by Paterson et al. in 1953, the previously assigned 'hopeless' prognosis of surgically resected medulloblastoma was transformed into a 3-year 60% survival (Paterson and Farr 1953). The subsequent introduction of adjuvant chemotherapy, culminated in the current 5 year survival rates of 70-80% in patients stratified to the average risk category, while in the less fortunate high risk patients, 5 year survival is given as 60-65% (Juraschka and Taylor 2019).

Infantile MB carries a particularly poor prognosis as below the age of three, paediatric patients suffer unacceptable complications from irradiation of the neuro-axis. For this reason, radiation-sparing treatment regimens are utilised in this age group and produce good outcomes in those without metastases at diagnosis and with either WNT or SHH-MBs (Yeo, Margol et al. 2019).

Since the discovery of the molecular heterogeneity in MB, better risk stratification models have been proposed (Table 1.3) , that take this as well as other genetic characteristics observed in more aggressive disease into account (Juraschka and Taylor 2019). Furthermore, the recent discovery of 8 molecular subtypes of Group 3 and 4 MB with differential cytogenetic, demographic and metastatic characteristics has

further refined our ability to prognosticate medulloblastoma patients (Sharma, Schwalbe et al. 2019).

Risk Category	Low Risk	Standard Risk	High Risk	Very High Risk
Survival (%)	>90	75-90	50-75	<50
Subgroup, clinical and molecular characteristics	Non-metastatic	Non-metastatic, <i>TP53</i> WT and no <i>MYCN</i> amplification	One or both: • Metastatic • <i>MYCN</i> amplification	<i>TP53</i> Mutation
	Non-metastatic and Chromosome 11 loss	Non-metastatic and no <i>MYC</i> amplification		Metastatic
			Non-metastatic and no chromosome 11 loss	Metastatic

Table 1.3 Improved risk stratification of medulloblastoma in paediatric patients over 3 years of age. Taken from (Ramaswamy, Remke et al. 2016, Juraschka and Taylor 2019)

1.6 Clinical management of paediatric MB

1.6.1 Surgical resection

The goals of neurosurgical intervention in MB are to obtain tissue for histomolecular diagnosis, reduce the tumour burden as much as is safely possible (maximal safe resection) and relieve hydrocephalus- the obstruction of the CSF flow through the ventricular system due to invasion or compression of the fourth ventricle by the cerebellar tumour (Menyhárt and Győrffy 2020). As they tend to grow in the midline cerebellar vermian region, Group 3 and 4 MB are most likely to be associated with obstructive hydrocephalus. While the volume of residual tumour burden $>1.5\text{cm}^3$ (also considered subtotal resection-STR) is considered a high risk stratifier, complications associated with standard and radical surgical resection such as cerebellar mutism, neurocognitive, motor and sensory deficits plague paediatric MB survivors (COG 2018).

Furthermore, studies investigating the prognosis of MB patients following near-total resection versus gross-total resection of their tumours, found no progression-free nor overall survival benefit, thus the neurosurgical consensus is of maximal safe resection (Juraschka and Taylor 2019).

If emergency management of obstructive hydrocephalus is required prior to resection of the tumour, an external ventricular drain is placed under image guidance through a burr hole (surgical window created in the skull) and into the ventricles for CSF diversion. If still required following surgery, this can be internalised by insertion of a ventriculo-atrial, ventriculo-pleural or ventriculoperitoneal shunt, the cranial portion of which is inserted through a frontal or parietal burr hole into the lateral ventricle. The distal portion is tunneled through subcutaneous tissues and inserted into the atria, pleural or peritoneal cavities. Risks of these procedures include infection, bleeding, injury to surrounding structures, pneumothoraces, seizures and shunt/drain displacement and malfunction (COG 2018).

While resection of primary MB is the mainstay of treatment, surgical intervention at recurrence or relapse is only performed on candidates selected by a multi-disciplinary team. This is due to the high risk nature of these operations as well as the poor prognosis associated with disease recurrence (Juraschka and Taylor 2019). Improved overall survival has been reported in the patient cohort in whom re-resection of their disease at relapse is performed (Hill, Richardson et al. 2020).

1.6.2 Radiotherapy

Traditionally, radiation therapy provided as external beam photon irradiation, is offered to two risk-stratified groups, ideally 4 weeks following resection of their tumour, provided the patient has recovered with a well-healed operative wound. These are average and high-risk paediatric patients aged ≥ 3 -5 years. Infants and children younger than 3 years are typically offered radiation-sparing treatment regimens due to their increased susceptibility to treatment related complications (Menyhárt and Gyórfy 2020).

Average and high-risk stratified patients older than 3 years of age are usually designated to receive a total of 54-55.8 grays (Gy) including a boost to the operative site. A further dose of 23.4 Gy of photon therapy is administered to the entire neuroaxis of average-risk patients and escalated to 36-39.6 Gy in the high-risk group (Menyhárt and Gyórfy 2020).

While radiotherapy dose-reducing strategies are being explored for paediatric patients with WNT sub-grouped MB, de-escalation of craniospinal irradiation regimes for other patients has been shown to result in poorer outcomes in comparison to the standard (Menyhárt and Gyórfy 2020). Furthermore, delays of more than 4 weeks post-operatively to the initiation of adjuvant radiotherapy correlate with poor outcomes in overall survival (Menyhárt and Gyórfy 2020).

Technological advances resulting in improved radiotherapy planning, modulating of intensity and hyperfractionation (2 doses/day) of regimes, as well as newer techniques of proton-based radiotherapy have led to better side-effect profiles with reduced irradiation of healthy tissue. These measures culminated in better quality of life in these patients with decreased rates of hearing loss (Juraschka and Taylor 2019, Menyhárt and Gyórfy 2020).

1.6.3 Chemotherapy

At present, there are multiple ongoing clinical trials into various combinations of multi-agent chemotherapy and subgroup specific immunotherapy regimes in MB. However, the current consensus for radiation-sparing regimens in infants and children younger than 3 years of age, prescribes either a high-dose chemotherapy regimen incorporating vincristine, cyclophosphamide, etoposide and cisplatin with subsequent stem cell rescue known as the CCG-99703 protocol; or a regimen incorporating intrathecal (delivered via Ommaya reservoir) Methotrexate alongside parenteral methotrexate, vincristine, cyclophosphamide and cisplatin (Menyhárt and Gyórfy 2020).

In the average and high-risk patients, 6-8 weeks of adjuvant intensive chemotherapy regimens consisting of cyclophosphamide, cisplatin and vincristine are instigated following weekly intravenous vincristine during radiotherapy, resulting in 85% 5-year overall survival (OS) in the former

and 70% 5-year OS in the latter group. While the regimens used in high-risk patients with disseminated disease are often variable, they can receive additional boosts of craniospinal irradiation to metastatic sites (Juraschka and Taylor 2019, Menyhárt and Győrffy 2020).

1.6.4 Complications of MB treatment

While the multimodal therapy of MB has improved patient OS and progression-free survival in all risk groups, each therapeutic approach is associated with unavoidable adverse effects. In addition, these effects may be compounded further by subsequent therapies. Hence the need for robust risk-stratification methods to enable tailored regimens that maximise treatment efficacy and minimise concomitant neuro-cognitive and psychosocial complications.

Notwithstanding the common complications associated with neurosurgery under general anaesthetic in the paediatric population, up to 25% MB patients develop posterior fossa syndrome (PFS) also known as cerebellar mutism (CMS). This presents in a delayed fashion post-operatively, with mutism, emotional lability and hypotonia, alongside bulbar symptoms and brainstem dysfunction (Jabarkheel, Amayiri et al. 2020). Published risk factors for development of this syndrome include younger patients at diagnosis and large tumours in the midline (Jabarkheel, Amayiri et al. 2020).

While radiotherapy has been correlated with increased rates of cataracts, stroke and radiation-induced tumours in MB survivors, cytotoxic chemotherapy can cause reno-, oto- hepato- and neuro-toxicity as well as blood and urinary tract malignancies (COG 2018). For surviving MB patients, the ensuing neurocognitive, hormonal, developmental and psycho-social effects of these life-saving therapies heavily impact their quality of life, highlighting the need for personalised therapy (Millard and De Braganca 2016, Juraschka and Taylor 2019).

1.7 Metastasis and Recurrence in Medulloblastoma

Metastasis and recurrence account for more than 95% of paediatric patients with MB who succumb to their disease (Menyhárt and Györfly 2020). Metastasis is defined by the dissemination or spread of cancer cells from their original location to other sites. Most theories regarding the mechanisms of metastasis converge upon the idea that metastasis begins with mutations in a select population of cells- cancer stem cells (CSCs), wherein they develop mutations in their oncogenes and tumour suppressor genes, enabling their differentiation into several clones resulting in tumour heterogeneity (Pavelic, Sedic et al. 2011). Genomic studies have proven that while the molecular subgroup of the MB is preserved at metastasis, recurrence and relapse, alterations in the genetic mutations of surviving clones occur. This is observed at high frequencies in gene pathways such as TP53, especially within SHH-MBs (Menyhárt and Györfly 2020). This is thought to explain why targeted

chemotherapy regimens fail or why recurrence may occur despite previously established effectual cytotoxic chemotherapy and radiotherapy regimes (Pavelic, Sedic et al. 2011, Steeg, Camphausen et al. 2011).

Cancer stem cells have similar characteristics to normal stem cells including their autonomous growth, pluripotency and capacity to maintain clonal expansion (Pavelic, Sedic et al. 2011). In addition, their activation and functioning depends on the very pathways that facilitate self-renewal in normal stem cells, namely the WNT/Beta-catenin and Hedgehog signalling pathways as well as the Notch and PTEN pathways (Pavelic, Sedic et al. 2011). In both WNT and Sonic Hedgehog medulloblastoma, upregulation of these pathways are thought to play a major role in the initiation and propagation of tumours belonging to these medulloblastoma subgroups (Holgado, Guerreiro Stucklin et al. 2017).

Metastasis of brain tumours can be categorised into either parenchymal or leptomeningeal metastasis (Steeg, Camphausen et al. 2011), wherein the circulating tumour cells inhabit these anatomically and metabolically diverse microenvironments (Boire, Brastianos et al. 2020). The former occurs when tumour cells disseminate from the location of the primary tumour and invade the adjacent substance of the brain tissue, while the latter occurs when tumour cells invade and colonize the cerebrospinal fluid pathways and the meninges covering the brain and spinal cord (Steeg, Camphausen et al. 2011). In medulloblastoma, the latter is more

common and occurs with highest frequency in Group 3 and 4 tumours which tend to arise in the midline cerebellar area, circumscribing the fourth ventricle (Ramaswamy, Remke et al. 2016, Holgado, Guerreiro Stucklin et al. 2017, Kralik, O'Neill et al. 2017). In contrast to Group 3 MB patients in whom recurrence of their disease occurs early in the disease progression, recurrence in Group 4 MB presents later and incurs better survival outcomes following relapsed disease (Menyhárt and Györfy 2020).

For metastases to occur, it is believed that the acquisition of mesenchymal gene expression promotes loss of epithelial contacts between cells of the primary tumour. Subsequent interactions with the tumour microenvironment facilitate and precede tumour cell migration, enabling the extravasation (or intravasation) of tumour cells into the vasculature, a possible route of spread of metastatic medulloblastoma cells to the rest of the neuroaxis (Steeg, Camphausen et al. 2011, Kralik, O'Neill et al. 2017). Studies of brain metastases from aggressive breast cancers have demonstrated that interactions between the tumour cells and brain milieu enable their metastatic cells to adapt morphologically and via their β 1 integrins, adhere and invade the vascular basement membranes (Steeg, Camphausen et al. 2011).

While the brain is well recognised to be immune privileged due to the robust blood-brain barrier and specialised 'glymphatic' network of perivascular pathways that facilitate transport of metabolic solutes and

waste to the cervical lymphatics; both these routes provide possible means by which circulating tumour cells (CTCs) may reach their preferred metastatic niche (Boire, Brastianos et al. 2020). These CTCs are postulated to mimic leucocyte mechanisms of migrating across these tight barriers, in addition to manipulating their surrounding cellular and acellular brain tumour microenvironments, causing these previously tight blood-brain and blood-CSF barriers to become leaky and conducive to their permeation (Boire, Brastianos et al. 2020).

Additionally, histological examination of metastatic brain parenchyma have revealed features of inflammation, with activation of astrocytes and microglia. Thus disruption of the blood-brain barrier by inflammatory mediators such as interleukin-6 secreted by activated microglia and the more recently implicated cytokine C3, reduce its integrity and in theory could facilitate intravascular access of tumour cells (Steeg, Camphausen et al. 2011, Boire, Zou et al. 2017).

For migrating cancer cells to metastasize to the brain, they must be capable of adapting to the unfamiliar surroundings. Most brain metastases originate from primary tumours outside of the neuroaxis and are thought to gain entry by breaking down the blood-brain barrier. However in the case of medulloblastoma, haematogenous, perivascular and leptomeningeal routes result in nodular and laminar leptomeningeal metastases in Group 3 and 4 MB, whereas SHH MB tend to recur within the primary site of disease (Boire, Brastianos et al. 2020). These

preferred metastatic niches within the MB subgroups suggest subgroups specific differences in their interactions with the tumour microenvironment.

The increasing prominence of the role of the tumour microenvironment plays in the progression on metastasis and recurrence in cancer warrants a closer look at the unique milieu that is the brain tumour microenvironment (Boire, Brastianos et al. 2020)

1.7.1 The brain tumour microenvironment

1.7.1.1 The cellular microenvironment

This unique microenvironment constitutes cells found only in the neuroaxis as well as a tightly regulated extracellular environment. These include astrocytes and oligodendrocytes as well as neurons and microglia, the latter being the resident immune cells. While neuronal secretion of glutamate and factors such as the brain neurotrophic factor have been shown to support growth of gliomas, reactive astrocytes and activated microglia have been reported to interact with primary and metastatic tumour cells through paracrine signalling; culminating in the production of a microenvironment that is conducive to cell migration (Schulz, Salamero-Boix et al. 2019).

Endothelial cells, components of all brain vasculature have also been shown to interact and respond to tumour-derived factors that drive neo-angiogenesis such as vascular endothelial growth factor (VEGF).

Furthermore, their central role in the integrity, function and permeability of the blood-brain and blood-CSF barriers necessitates their consideration in the brain tumour microenvironment (Morad and Moses 2019).

1.7.1.2 The Blood-brain barrier and regional differences in its cellular architecture

The blood-brain barrier (BBB) can be regarded as a highly selective multi-level structure that acts as an anatomical and physiological protective barricade between the periphery and the brain (Abbott, Rönnbäck et al. 2006). Anatomically, it has been characterised to consist of endothelial tight junctions between the capillary endothelial cells which are enveloped by the astrocytic foot processes and reinforced by the capillary basement membrane as well as pericytes (contractile connective tissue cells), glia limitans (comprised by astrocytic end-feet) and microglia. Various laminin isoforms, type IV collagen, proteoglycans and fibronectin are some of the constituents of the basal lamina of the BBB. Physiologically, the blood-brain barrier restricts molecular and cellular transport into the brain by specific active and facilitated diffusion of substances necessary for neuronal function. This is beneficial as it is thought to reduce the pathological spread of infective organisms, immune cells and circulating cancer cells (Abbott, Rönnbäck et al. 2006, Steeg, Camphausen et al. 2011, Mastorakos and McGavern 2019).

The brain and spinal cord are housed within coverings called meninges, the first of which are a dual layer of dura mater, between which venous sinuses and lakes are situated. Dural-based vasculature tend to be capacious, fenestrated vessels that lack tight junctions. The second layer the avascular arachnoid mater measures approximately 200 microns thick, and is comprised of a dual squamous epithelium layer with a laminin $\alpha 5$ rich basal lamina. The pia mater is adherent to the brain parenchyma and constitutes of laminin $\alpha 1$ basement membrane as well as fibroblast-like cells. Unlike the subarachnoid mater, the pia mater lacks tight junctions (Mastorakos and McGavern 2019).

The vast majority of arteries supplying the brain are enclosed within the cerebrospinal fluid filled subarachnoid space, the space between the arachnoid and pia maters. From here, they enter into the brain parenchyma enveloped within the glia limitans and pia mater, creating perivascular spaces between their walls and the pia. The aforementioned pial fenestrations enable fluid and molecule movement through the subpial (perivascular), pial and subarachnoid space (Mastorakos and McGavern 2019).

In physiological circumstances, the glia limitans that envelope the parenchymal surfaces of the brain and spinal cord are permeable to substances of 0.8-70kDa, while larger molecules up to 2000kDa are housed within the perivascular space. The 20nm gaps within the glia limitans and the negatively charged basal lamina are said to be the

decisive determinants of fluid and molecule exchange between the interstitial and cerebrospinal fluid (Mastorakos and McGavern 2019).

The function of the BBB has been shown to be impaired by inflammatory and coagulation cascade mediators, neurotransmitters such as glutamate, free radicals, endothelin-1 and nitric oxide to name a few. A growing body of evidence suggests that these mediators may provide the mechanistic routes by which metastatic cells circumvent this protective barricade to invade the neuroaxis and lead to leptomeningeal metastases (Abbott, Rönnbäck et al. 2006, Boire, Zou et al. 2017, Mastorakos and McGavern 2019).

Regional variations in its composition have been observed to correlate with the functions of the specific anatomical region of the brain. At sites such as the choroid plexus and circumventricular organs (Figure 1.5), the BBB is specialised to suit their physiological functions. The main difference is the paucity of tight junctions in the endothelia lining their vasculature, enabling easier access of molecules and inflammatory mediators from the systemic circulation into the brain. Circumventricular organs such as the subfornical organ, area postrema and vascular organ of the lamina terminalis play important homeostatic roles that require a direct communication to the systemic vasculature as well as others that secrete hormones into the systemic circulation for example the posterior pituitary and pineal gland (Mastorakos and McGavern 2019).

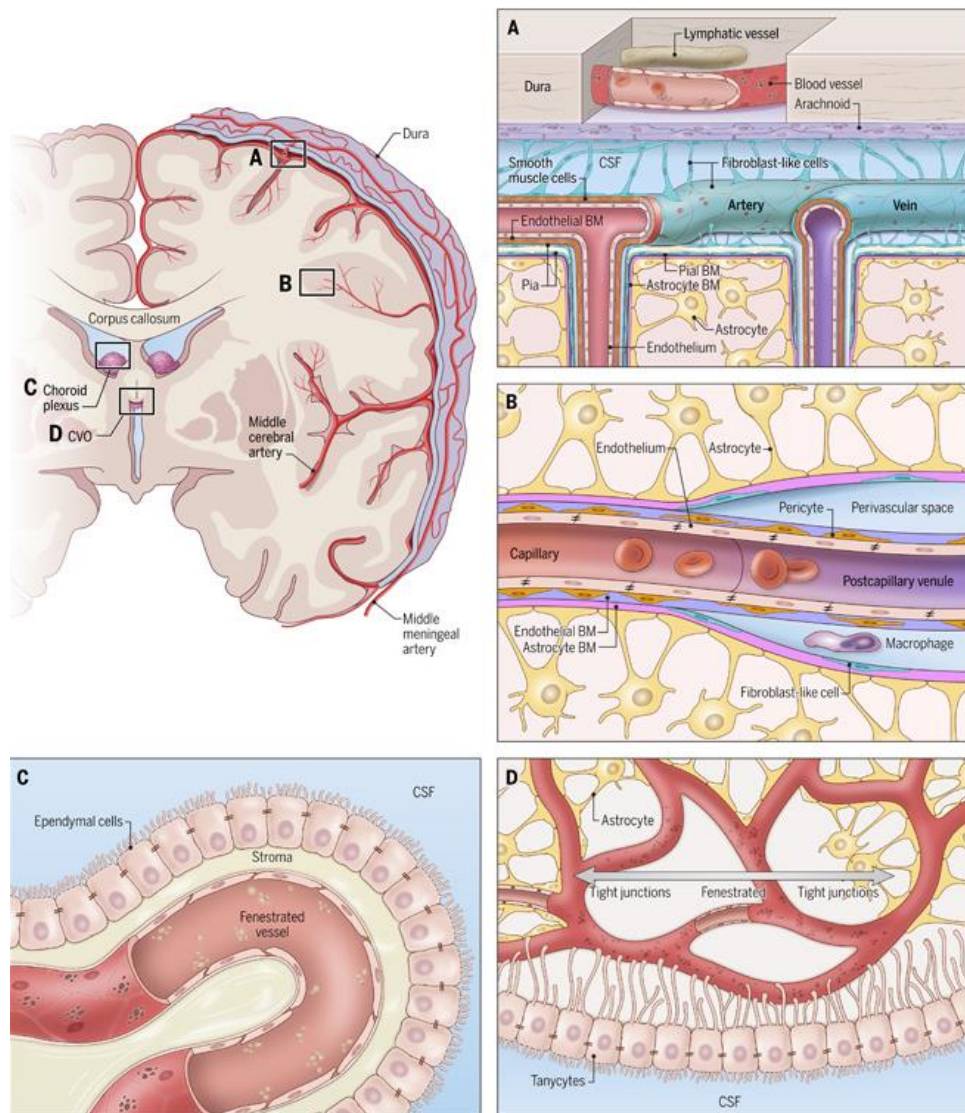


Figure 1.5 Overview of the structural differences in the composition of the blood-brain barrier at anatomically distinct regions of the brain.

A. Meningeal vasculature. As shown, blood vessels within the dura are fenestrated allowing direct communication with the systemic circulation, in contrast to blood vessels within the arachnoid space whose tight junctions prevent diffusion of large molecules or free fluid exchange between the dura and systemic vasculature. B. As the subarachnoid blood vessels enter the parenchyma and become parenchymal capillaries, they are enveloped by pia and glia limitans from the end-feet of astrocytic foot processes. C. Specialised choroid plexus vasculature lacking tight junctions enable the secretion of CSF into the ependymal lining D. Vascular architecture of periventricular organs showing fenestrated capillaries within but tight junctions between the tancytes that line their exterior CSF facing surface. Image taken from (Mastorakos and McGavern 2019)

1.7.1.3 The leptomeninges, cerebrospinal fluid and the blood-CSF barrier

The leptomeninges are comprised of the two innermost membranous layers covering the surfaces of the brain and spinal cord; the pia mater that adheres to the surfaces of the brain and spinal cord and the subarachnoid mater above it (Steeg, Camphausen et al. 2011). Between the pia and subarachnoid layers is the subarachnoid space which is filled with cerebrospinal fluid (CSF), an acellular, low solute fluid secreted by specialised choroid plexus epithelium, into the lateral, third and fourth ventricles (Boire, Zou et al. 2017). While the fenestrated endothelia of the choroidal vessels lack tight junctions and glia limitans, they are lined by ependymal cells, which have tight junctions and form the ventricular walls. This allows diffusion of proteins from the systemic circulation into the choroid capillaries, further passage into the ventricles is limited by the ependyma (Mastorakos and McGavern 2019).

The ventricles are a low pressure, ependymal-lined cavities within which the cerebrospinal fluid circulates. From its genesis in the choroid plexus, it flows through the lateral ventricles through the foramen of Munro into the third ventricle, passing into the cerebral aqueduct into the fourth ventricle, which sits just anterior to the cerebellum as shown in Figure 1. 6. Traversing through the medial Magendie and lateral Lushka foramina, the CSF continues to flow into the basal cisterns and around the spinal cord.

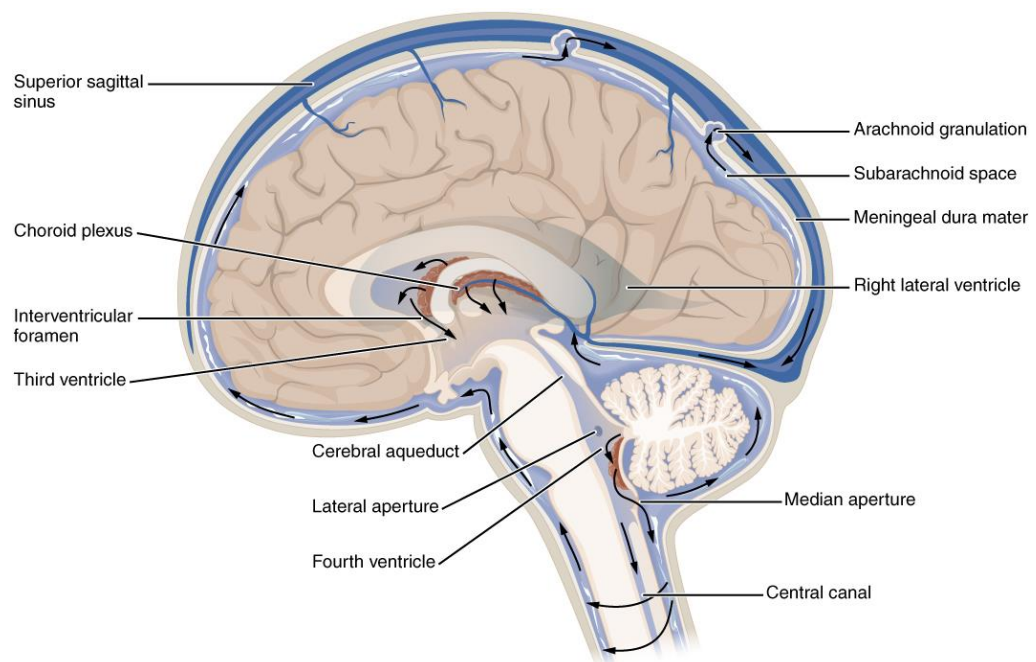


Figure 1. 6 CSF flow through the ventricles and around the brain

Once secreted by the choroid plexus in the lateral ventricle, it flows into the third ventricle through the interventricular foramen, down the cerebral aqueduct and into the fourth ventricle. This is the point at which a medulloblastoma within the cerebellum could invade or compress the fourth ventricle causing obstructive hydrocephalus. Image taken from <http://cnx.org/content/m46719/1.3/>, 2013 (OpenStaxCollege 2013)

While it was historically thought that all CSF was reabsorbed at the arachnoid granulations on the superior cortical surface of the subarachnoid mater, recent MRI tracer studies have demonstrated paravascular flow of ISF/CSF along brain vasculature as it penetrates the subarachnoid space into the pia mater (Vinje, Eklund et al. 2020). The perivascular CSF enables transport of solutes to the interstitium and metabolic waste away from the extracellular space, which it accesses via aquaporin-4 (AQP-4) channels between glial cell foot-processes. This perivascular fluid proceeds above basal lamina of parenchymal then

leptomeningeal arteries. CSF drainage is postulated to occur at the arachnoid granulations and into the venous superior sagittal sinus from where it proceeds to enter the peripheral circulation, as well as via the paravenous outflow into cervical lymphatics (Vinje, Eklund et al. 2020). This may be the course by which primary brain tumours disseminate to extra-neural sites (Boire, Zou et al. 2017).

Furthermore, the co-localisation of antigen presenting cells within the perivascular spaces and in close proximity to leptomeningeal vasculature, the choroid plexus and subarachnoid space; highlights their role in maintaining the brain's immune privilege but may also implicate them in the tumour-immune system interactions observed in primary and metastatic microenvironments that propagate metastasis (Mastorakos and McGavern 2019) .

1.8 Leptomeningeal metastasis

Several mechanisms by which leptomeningeal metastases may occur have been proposed. Direct invasion of the glia limitans by cancer cells within the brain parenchyma, venous access through the Bateson's venous plexus and entry via the choroid epithelium are some of the plausible routes of dissemination of cancer cells into the leptomeningeal space (Boire, Zou et al. 2017). Enzymatic degradation of the glia limitans has also been proposed, following the tumour mediated activation of

astrocytes and microglia at the perivascular spaces (Mastorakos and McGavern 2019).

Furthermore, the continuity of the subarachnoid space allows free movement of cancer cells within the CSF which can then invade the pia mater and establish focal metastases, visible as focal nodular enhancement on spinal MRI contrast-enhanced images or drop/nodular metastases on the surface of the spinal cord (Kralik, O'Neill et al. 2017). While the continuity of the subarachnoid space may present advantageous routes for chemotherapeutic drug delivery as has been used in the intrathecal administration of antibiotics, it also raises questions regarding how the metastatic cells are able to survive within the dynamic, deficient environment that is the constantly replenished cerebrospinal fluid environment (Boire, Zou et al. 2017).

In a recently published paper it was postulated that complement C3 secreted into the cerebrospinal fluid by circulating metastatic cells within the subarachnoid space, binds to its receptor at the epithelial surface of the choroid plexus, triggering disruption of the choroid epithelium (Boire, Zou et al. 2017). As this epithelium is responsible for the bulk of secretion of cerebrospinal fluid into the lateral and third ventricles, the blood-brain barrier here is physiologically deficient compared to other regions of the brain, making it a possible route by which breast and lung cancer metastatic cells gain access to the neuroaxis. Once in the CSF pathways, it is plausible that these cancer stem cells can survive in the

cerebrospinal fluid long enough to invade the leptomeninges, the brain and spinal cord. This might explain the significant mortality associated with leptomeningeal metastases, with the natural history of this complication of disseminated cancer culminating in death within 6-8 weeks in untreated individuals (Boire, Zou et al. 2017).

Boire et al. identified two distinct populations of metastatic tumour cells following intra-arterial injection of metastatic lung and breast cancer cells in immunocompromised mice. Those that established leptomeningeal metastases were biologically determined to be specifically aggressive towards invading the leptomeninges with distinct phenotypic and transcriptomic profiles to the cells that invaded the brain parenchyma (Boire, Zou et al. 2017).

1.8.1 Current methods employed in the diagnosis of metastasis recurrence and prognostication in MB

Patients with metastatic medulloblastoma are classified into four categories using Chang's operative classification ranging from: no cytological/radiological evidence of metastases (M0), cytological evidence of tumour cells in cerebrospinal fluid (M1), nodular metastases within the intracranial subarachnoid spaces or ventricles (M2), metastases within the spinal subarachnoid space (M3) and extraneural metastases (M4)(Dufour, Beaugrand et al. 2012).

Given the propensity for leptomeningeal metastasis in MB, the current clinical methods of detection at diagnosis and recurrence are less than accurate in their determination of metastatic disease. Considering the impact that this has on the prognostication of children with medulloblastoma, safe and minimally-invasive detection methods with better accuracy are needed to correctly identify patients for whom escalated doses of craniospinal irradiation or chemotherapy would be most appropriate (Bennett, Ashmawy et al. 2017). The WHO staging of medulloblastoma shows the current staging of MB according to molecular and histological diagnosis (Louis, Perry et al. 2016).

Table 1.4 Summary of the re-classification of MB in the 2016 World Health Organisation Classification of CNS tumours (Louis, Perry et al. 2016).

Genetic profile	Histology	Prognosis
WNT-activated	Classic	Low risk, common in most WNT-MB
	Large cell/ Anaplastic	Uncertain clinicopathological significance
SHH-activated TP53-mutant	Classic	Uncommon, high risk tumour
	Large cell/ Anaplastic	High risk, prevalent in patients 7-17 years old
	Desmoplastic/Nodular	Uncertain clinicopathological significance
SHH-activated TP53-wild type	Classic	Standard/ Average risk
	Large cell/ Anaplastic	Uncertain clinicopathological significance
	Desmoplastic/Nodular	Low risk in infants, prevalent in adults and infants
	Extensive nodularity	Low risk in infants
Group 3	Classic	Standard/ Average risk
	Large cell/ Anaplastic	High risk
Group 4	Classic	Standard/ Average risk, common in Group 4-MB
	Large cell/ Anaplastic*	Uncertain clinicopathological significance

To streamline prognostication in patients with tumours that metastasise to the leptomeninges, a response assessment in neuro-oncology (RANO) working group defined standardised methods and criteria by which leptomeningeal disease can be diagnosed. They proposed three main domains which when combined, would give the best chance of accurate prognostication of disease for appropriate treatment assignment. These domains included a full neurological examination to exclude symptoms secondary to leptomeningeal MB deposits; contrast enhanced magnetic resonance imaging of the entire neuroaxis at 1.5 or 3-tesla scanners; and cerebrospinal fluid cytology usually performed 10-14 days post-operatively (Bennett, Ashmawy et al. 2017, Chamberlain, Junck et al. 2017). These assessments should be performed in a timely fashion; the brain and spinal MRI pre-operatively to avoid artefacts associated with surgical manipulation and cerebrospinal fluid cytology within 10-14 days post-operatively to avoid detection of iatrogenic dissemination of medulloblastoma cells at surgery (Bennett, Ashmawy et al. 2017).

Dufour et al. found that patients with nodular metastases had better survival rates compared to those who had either cytological evidence of medulloblastoma cells in CSF or laminar metastases. Both CSF cytological analysis and spinal MRI used in the detection of disseminated medulloblastoma have limited sensitivity and specificity in this regard (Kralik, O'Neill et al. 2017). Post-mortem CSF analysis of patients with

leptomeningeal metastatic disease confirmed by histology, revealed a positive CSF result in only 59% (Kralik, O'Neill et al. 2017). Additionally, spinal MRI at the clinical strength of up to three Tesla (1.5-3T) has limited spatial resolution especially when compounded with artefact from patient movement, CSF flow and lack of specialist neuro-radiological expertise. Thus, the determination of patients with metastases in the absence of macroscopic radiologically detectable disease remains a challenge. Hence, more sensitive MRI techniques that can detect disseminated disease at diagnosis and surveillance are required to improve the prognostication of patients with medulloblastoma. This in turn, would enable the identification of patients at highest risk, in whom it would be justified to administer high dose craniospinal irradiation for treatment and control of their metastatic disease (Holgado, Guerreiro Stucklin et al. 2017, Kralik, O'Neill et al. 2017).

Another factor that has greatly improved prognostication of medulloblastoma patients is its re-classification from the histological variants to the molecularly defined subgroups WNT, Sonic Hedgehog (SHH), Group 3 and Group 4 medulloblastoma. Genomic studies have revealed prognostic correlations for each subgroup and identified disparate clinical phenotypes in the age groups they frequently affect, their metastatic profiles and even where they arise anatomically, within the posterior fossa. Though further work into their characterisation is needed, clear evidence from molecular profiling of WNT tumours has

consistently shown it to be the subgroup with the most favourable prognosis, while Group 3 tumours tend to be more aggressive and most likely to recur (Holgado, Guerreiro Stucklin et al. 2017, Ramaswamy and Taylor 2017). Even so, clinical practice presently advocates the indiscriminate provision of craniospinal irradiation where the patient is older than 3 years of age. As such, adverse effects from the high doses of radiotherapy remain high in the surviving patients who suffer from long term neurocognitive deficits, neuroendocrine dysfunction and secondary radiation-induced malignancies (Ramaswamy, Remke et al. 2016, Holgado, Guerreiro Stucklin et al. 2017).

The Royal College of radiologists advocate MRI as the gold standard for diagnosis and surveillance of paediatric brain tumours, due to its excellent safety profile and good spatial resolution. Its non-invasive nature allows for its use in the diagnosis and monitoring of treatment response, in patients who would otherwise come to harm from the effects of accumulated ionising radiation, especially in paediatric patients who would be particularly susceptible (Manias, Gill et al. 2017).

However, due to the limited availability, long duration of acquisition and high cost of MRI, contrast-enhanced computed tomography (CT) is sometimes used to diagnose paediatric brain tumours and metastases within the neuroaxis. Unlike MRI, CT scanning exploits the differential absorption and consequently transmission of ionising radiation through tissues of varying density to produce contrast. Given the recognised risk

of carcinogenesis associated with the forms of ionising radiation employed in imaging modalities such as computed tomography (CT) and positron emission tomography (PET), MRI is advantageous as it permits the detection of micrometastases (<5mm in diameter) with less bone derived artefact, superior soft tissue contrast and minimal propensity to instigate carcinogenesis (due to lack of ionising radiation as is the case in CT imaging). All three modalities require administration of exogenous contrast for vascular enhancement of the tumour, a characteristic thought to occur due to disruption of the BBB that is believed to occur more so in aggressive tumours (Goo and Ra 2017).

Unfortunately, both contrast agents used in the respective modalities- Gadolinium in MRI and Niopam in CT imaging, are associated with adverse effects including allergic reactions, anaphylaxis, nephrotoxicity and accumulation within soft tissues. For these reasons, development of safer, equally effective contrast agents are required or the development of molecular magnetic resonance imaging techniques that can negate or minimise the amount of exogenous contrast agents. Newer contrast agents using chelated paramagnetic oxide nanoparticles or activatable 'smart' probes may fulfil this purpose, albeit with different potential adverse effects (Carril 2017).

1.9 Candidate biomarkers of metastasis

Biomarkers of metastasis, by definition, must be quantifiable biological, molecular, genomic, histologic, physiological or radiological signals that

reliably indicate the presence, advancement or resurgence of disseminated cancer (O'Connor, Aboagye et al. 2017). For use in clinical practice, imaging biomarkers of metastases must be reproducible, readily accessible, cost-beneficial and adequately specific and sensitive for the detection of the desired target, in this case, brain metastases (O'Connor, Aboagye et al. 2017).

The development of an imaging biomarker that is compatible with clinical 3-Tesla MRI scanners would be ideal, for the detection of neuroaxial metastases and the exclusion of recurrence during disease monitoring. Furthermore, such a biomarker could be used intra-operatively, to determine the invasive margins of MB tumours, to guide targeted resection of these tumour populations. Considering the increasing evidence that safe maximal resection of medulloblastoma in paediatric patients is superior to radical resection, due to the ensuing adverse effects of the aforementioned strategy, chief being cerebellar mutism syndrome (Thompson, Hielscher et al. 2016).

Though characteristic subgroup specific metastatic signatures are yet to be discovered, a number of proteomic and genomic markers have been proposed to correlate with increased metastatic potential (Steeg, Camphausen et al. 2011, Gu, Chen et al. 2017). Based on the well accepted premise of metastasis requiring interactions between the tumour cells and their immediate microenvironment to establish a nurturing niche, a number of mediators involved in the epithelial to

mesenchymal transformation theory have been accorded significance and demonstrated to change during the process (Termini, Neman et al. 2014). Notable suspects include the chemokine ligands CCL5, CCL4 and its receptor CCL12 as well as WIP1, the latter being implicated in the SHH pathway (Northcott, Jones et al. 2012). Other proteomic studies have implicated $\alpha 9\beta 1$ integrin (a transmembrane receptor that facilitates cell migration), SPARC (a cysteine-enriched matrix protein) and PDGFR α (Platelet derived growth factor α that functions as a mitogen for mesenchymal cells) as facilitators of metastasis in medulloblastoma (Gu, Chen et al. 2017).

Astrocytes that normally play a supportive role to glial cells in the brain have been implicated in the facilitation of a pro-metastatic niche by secreting factors such as TWIST1, BCL21 and GSTA5 when activated (Termini, Neman et al. 2014). These factors have been shown to increase survival of metastatic cells (Termini, Neman et al. 2014). Given that metastasis is a pro-inflammatory state, a number of inflammatory mediators have been correlated with metastasis including cytokine-C3 that has the propensity to disrupt the blood brain barrier. Other mediators that have the propensity to disrupt the blood-brain barrier (BBB) include interleukins (1, 6, 8), tumour necrosis factor (TNF) and transforming growth factor- β (TGF- β), the latter demonstrated to be upregulated in leptomeningeal metastases (Steeg, Camphausen et al. 2011, Boire, Zou et al. 2017).

For established metastases, cultivation of the site of metastasis requires neo-angiogenesis to satisfy the increased oxygen demand associated with the more metabolically active metastatic cells (Termini, Neman et al. 2014). Vascular endothelial factor (VEGF-A) has been demonstrated to correlate with the radiological detection of melanoma metastases to the brain (Steeg, Camphausen et al. 2011). Monoclonal antibodies to VEGF such as Bevacizumab are already in clinical use and VEGF receptor antagonists are undergoing clinical validation to assess their efficacy in impeding metastatic progression. Through inhibitory pre-clinical experiments, other mediators proposed to alter the progression of brain metastases include Epidermal growth factor receptor (EGFR) and Signal transducer and activator of transcription 3 (STAT3) (Steeg, Camphausen et al. 2011).

Specific to the MB molecular subgroups, nuclear expression of β -catenin1 in WNT tumours, SUFU (a key negative regulator in the hedgehog pathway) and mutant TP53 expression in SHH, and MYC amplification in both Group 3 and 4 tumours, have all been postulated to correlate with their subgroup-specific metastatic potential, as reflected in the new WHO prognostic criteria (Louis, Perry et al. 2016). Further mediators postulated to play key roles in the invasion of medulloblastoma include ERBB2, IGF-1R, c-MET and placental growth factor (PLGF), which all appear to be upregulated in metastatic medulloblastoma models (Gu, Chen et al. 2017). Proteomic analysis of a matched pair of

primary and metastatic Group 4 medulloblastoma cell lines revealed increased expression of YAP1 and MMP-2 in the metastatic cell line compared to its counterpart (Gu, Chen et al. 2017).

Though seemingly exhausted in cancer research, matrix metalloproteinases and their regulators have resurfaced as interesting modulators of the metastatic neural niche (Termini, Neman et al. 2014, Isaacson, Jensen et al. 2017). Extracellular Matrix metalloproteinase inducer (EMMPRIN) is an MMP associated glycoprotein that has been shown to be upregulated in medulloblastoma compared to normal cerebellar tissue and has been correlated to higher metastatic type, more aggressive histological variants and poor tumour differentiation in medulloblastoma; factors that commonly signify poorer prognoses (Chu, Chen et al. 2011).

With the exception of the aforementioned very recent publication by Gu et al. 2017, the majority of the research investigating the differential expression of MMPs in medulloblastoma was performed prior to its molecular subgrouping and therefore according to the histological variants (Vince, Herbold et al. 2001, Ö., B. et al. 2004, Bhoopathi, Chetty et al. 2011). This mandates a fresh look at the functional activity as well as the gene and protein expression of MMPs in the different molecular subgroup of medulloblastoma.

1.10 Matrix Metalloproteinases as biomarkers of Metastasis

1.10.1 Introduction

The significance of the role played by interactions between cancer cells and their microenvironment in the progression and dissemination of metastatic disease have borne fluctuating scientific interest in matrix metalloproteinases over the years. With over 23 different matrix metalloproteinases identified in the human genome (Shimoda and Khokha 2017), the gelatinases MMP-2 and MMP-9 are the most commonly correlated MMPs with metastasis of solid cancers including medulloblastoma (Ö., B. et al. 2004, Bhoopathi, Chetty et al. 2011).

Overexpression of matrix metalloproteinases has been closely related to the staging and consequently predicted clinical outcomes of patients with disseminated cancer (Isaacson, Jensen et al. 2017). Moreover, where MMP upregulation is detected, multiple studies have demonstrated augmented neo-angiogenesis, cellular growth and migration, lymphatic spread of tumour cells and increased risks of recurrence (Isaacson, Jensen et al. 2017). Thus, if differentially expressed between the molecular subgroups of medulloblastoma, MMPs could provide a potential biomarker that may correlate with their differential metastatic potentials.

MMPs are zinc and calcium endopeptidases with domains which consist of a generic region and a modifiable catalytic domain that is specific to

their preferred substrates (Kessenbrock, Plaks et al. 2010). They can either be bound to the cell membranes of inflammatory cells as in the case of membrane-type MMPs or be secreted from the cytosol into the extracellular matrix where their activation enables their functions as modulators of the extracellular matrix (Kessenbrock, Plaks et al. 2010, Isaacson, Jensen et al. 2017).

MMPs are synthesised as zymogens i.e. as inactive proenzymes that require activation by a number of mediators through interaction with the zinc-cysteine catalytic domains (Ö., B. et al. 2004). Though most MMPs are believed to be activated in the extracellular space, there is evidence that cytosolic activation also occurs especially concerning MMP-2 (Isaacson, Jensen et al. 2017).

MMPs can be categorised by the specific substrates that they hydrolyse. The characterised MMPs include the aforementioned Gelatinases (MMP-2 and MMP-9), the Collagenases (MMP-1, MMP-8, MMP-13), the Stromelysins (MMP-3, -10, -11), the Matrilysins (MMP-7, MMP-26) and those bound to the surface of the cell membrane (MTMMP-14, -15, -16, -17, -24 and -25) (Isaacson, Jensen et al. 2017).

1.10.2 Regulation of Matrix Metalloproteinases

The multilevel regulation of matrix metalloproteinases ensures a tightly controlled homeostatic tumour microenvironment. For instance, pro-MMP-2 (Gelatinase A) is secreted and exported to the cell membrane

surface, where upon fusing with it, is activated by chelating with another activated membrane-bound metalloproteinase MMP-14. In addition to activating each other, the regulated function of matrix metalloproteinases is also dependent upon the presence of tissue inhibitors of metalloproteinases (TIMPs 1-4). These can impose both positive and negative regulation of various MMPs through complex formation, rendering the affected MMP active or inactive according to the desired effect (Ö., B. et al. 2004, Isaacson, Jensen et al. 2017, Shimoda and Khokha 2017).

In addition to the mechanisms of regulation previously alluded to such as zymogen activation, MMP regulation has been characterised at the genomic and proteomic levels, at their transcellular exocytosis via membrane bound vesicles (Shimoda and Khokha 2017), their inhibition by TIMPS and complex formation with other MMPs (Isaacson, Jensen et al. 2017). Even more enthralling, is their recognised overexpression at each stage of carcinogenesis in many solid cancers (Isaacson, Jensen et al. 2017). Their widespread regulation and mechanisms of action have stimulated their consideration as targets for modulation of metastatic progression in cancers and culminated in the experimental investigations using exogenous MMP inhibitors. This was demonstrated in a study where Bhoopathi et al. who showed that inhibition of MMP-9 expressed by a SHH medulloblastoma cell line- DAOY cells, resulted in their integrin β 1-mediated apoptosis (Bhoopathi, Chetty et al. 2011). Further work into

the development of specific targets of MMP inhibitors, for disruption of metastasis is warranted.

1.10.3 Functions of Matrix Metalloproteinases

MMPs have been widely documented to perform functions distinct to their modulation of extracellular matrix components. In fact, only a fifth of MMPs have been characterised to undertake matrix remodelling, while the majority are implicated in regulating cellular growth, proliferation and inflammation by the hydrolysis of growth factors, their receptors and modulating immune mediators such as cytokines. Thus MMPs appear to play key roles in homeostasis, tissue healing, embryogenesis and organ development, further highlighting their prominence in most bodily processes (Isaacson, Jensen et al. 2017).

MMPs have been implicated in the facilitation of every stage of carcinogenesis from enabling loss of cell-to-cell connections allowing tumour cells to migrate through 'pathways of least resistance' within the extracellular matrix. Some theories put forward the role of MMPs in maintaining the stiffness of the ECM according to physiological or pathological need can impede or promote invasion or migration of tumour cells. In addition, MMPs have been shown to promote the production and maintenance of pro-inflammatory mediators that facilitate essential mechanisms of metastasis including stimulating the synthesis and

expression of angiogenic, proliferative and migratory factors (Isaacson, Jensen et al. 2017).

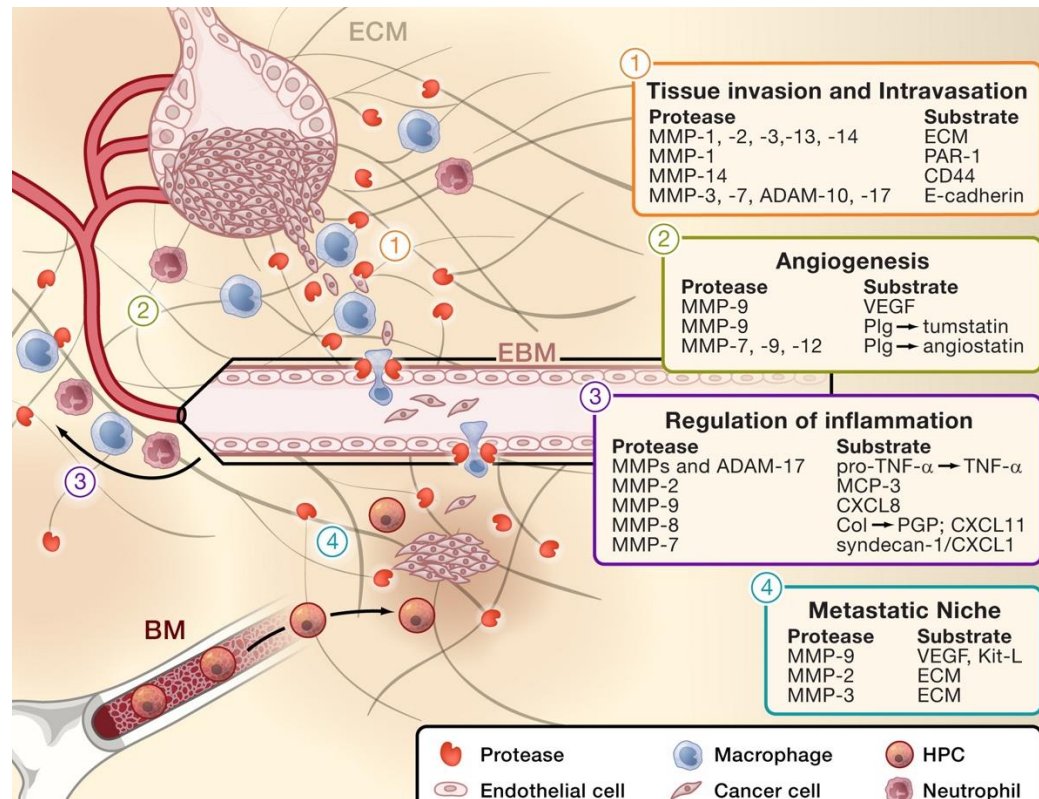


Figure 1. 7 Stages of carcinogenesis in which matrix metalloproteinases are involved. As important modulators of the extracellular matrix in physiology and cancer, MMPs originating from tumour cells and their surrounding cellular microenvironment, digest matricellular substrates, releasing factors that prime the metastatic niche as well as create a more conducive milieu promoting migration, metastasis and intravascular invasion (Kessenbrock, Plaks et al. 2010).

1.10.4 MMPs as biomarkers of metastasis and prognosis in Medulloblastoma

To evaluate their potential as prognostic markers of metastasis and staging in various cancers, several studies have investigated their expression in different bodily fluids by various techniques including

immunohistochemistry, genomic analysis using real time PCR (qPCR), protein expression quantification by Immunoblotting, ELISA and Gelatine Zymography (Isaacson, Jensen et al. 2017).

As alluded to previously, several MMPs have been characterised to be upregulated in metastatic liquid biopsies from patients with cancer, by a 10-fold incremental MMP expression compared to healthy controls. These levels have also been shown to relate significantly with the staging of the patient's disease, and more importantly have been associated with increased risk of brain metastases as seen with aggressive breast cancer. This pathological overexpression of MMPs has been postulated to accord medulloblastoma cells with chemo- and radio-resistance, thereby promoting their dissemination and recurrence (Ganji, Nalla et al. 2011). Consequent features of worsened survival, increased propensity to metastasize and invade locally as well as poorer tumour differentiation are seen, all of which correlate with increasing metastatic potential of the tumour cells (Ö., B. et al. 2004, Isaacson, Jensen et al. 2017).

The most commonly implicated MMPs in medulloblastoma metastasis are MMP-1, -2, 9 and -13. MMP-1 in particular has been implicated in increasing endothelial permeability, making intravasation of metastatic cells and their haematogenous spread thereafter, much easier. In preparation of sites for metastases, MMPs are postulated to enable shedding of cellular CD44, enabling metastatic cell attachment to the

new niche for establishment of new metastases (Isaacson, Jensen et al. 2017).

Remarkably, MMP-9 is often preferentially associated with the cell membranes of cancer cells and is postulated to exert its effects in cellular proliferation, growth and angiogenesis (Isaacson, Jensen et al. 2017). In addition, MMP-2 and MMP-9 proteins have been detected within extracellular vesicles of malignant liquid biopsies from patients with aggressive ovarian and breast cancer (Shimoda and Khokha 2017). Furthermore, tumour cell derived membrane type 1-MMP activates MMP-2 and has also been shown to exert functions in the hydrolysis of gelatin and collagen type 1. This suggests that MT1-MMPs work in synergy with MMP-2 to create paths for migration of cells along these routes. There is little evidence regarding the overexpression of these gelatinases in CSF from patients with brain metastases, which presents an exciting opportunity for further research. It is plausible that metalloproteinase-containing endovascular vesicles cultivate new niches within the leptomeningeal space, thereby enhancing survival of the metastatic cells. Surface transport of highly concentrated metalloproteinases on extracellular vesicles such as exosomes and microvesicles promote shedding of anchoring proteins in the receptive cells following their incorporation, promoting free movement and invasion of these cells, as well as cultivating sites for neo-angiogenesis (Shay, Lynch et al. 2015, Shimoda and Khokha 2017).

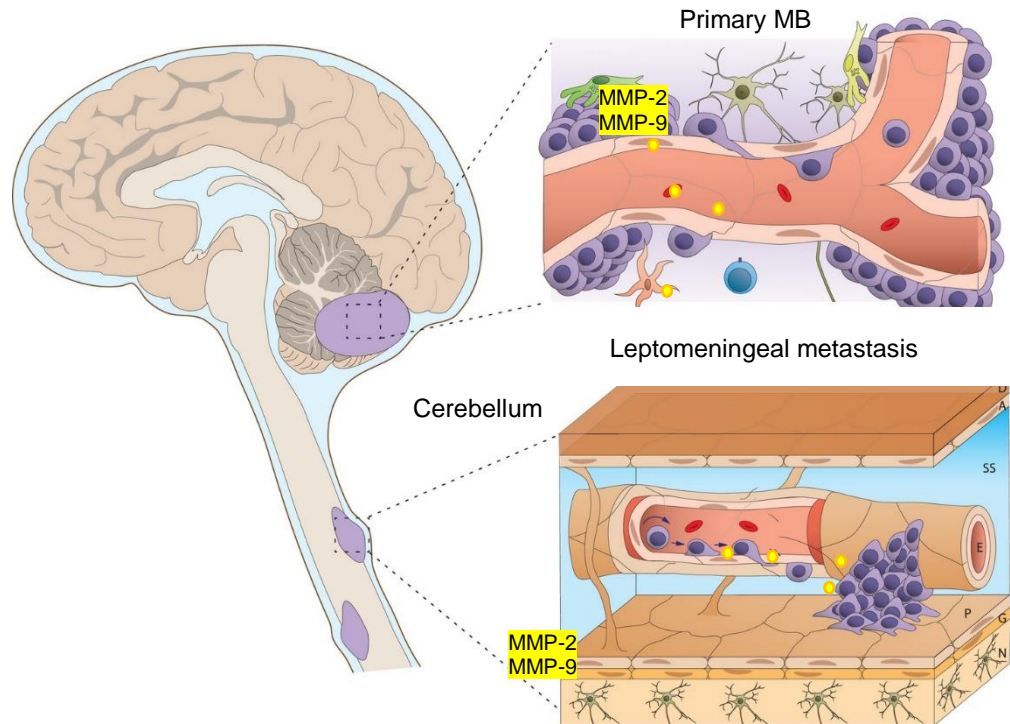


Figure 1.8 The anatomically and physiologically distinct primary and metastatic niches in medulloblastoma.

Emanating from the cerebellum (the top purple area) the primary MB tumour microenvironment consists of the cellular (astrocytes, oligodendrocytes, neurons, microglia and macrophages) and the extracellular matrix, rich in hyaluronan and proteoglycans. This nutrient-rich and supportive milieu create a conducive pro-migratory niche, that enables cancer stem cells to eventually leave the primary tumour and permeate brain vasculature, through defective BBB. Upon reaching the leptomeninges, circulating tumour cells are thought to acclimatise to their new sparse surroundings, by secreting immune mediators e.g. MMP-2 and MMP-9 themselves or through paracrine signalling to endothelial, immune and ependymal cells, rendering the BBB and blood-CSF barriers to become permeable to enriching factors. The now replenished metastatic cells then settle into their primed niche as nodular or laminar metastatic leptomeningeal coatings. [D] dura mater, [A] Arachnoid mater, [P] Pia mater, [SS] subarachnoid space, [E] endothelial cells, [G] glia limitans, [N] neurons, [BM] basement membrane. Image adapted from (Van Ommeren, Garzia et al. 2020).

1.11 Molecular Magnetic Resonance Imaging

1.11.1 Introduction

Advances made in understanding the molecular mechanisms of medulloblastoma through genomic and proteomic analyses have been paralleled by achievements in the field of translational imaging, with the emergence of molecular magnetic resonance imaging. Even so, analogous to the delayed assimilation of molecular subgrouping of medulloblastoma into clinical practice, few pre-clinical techniques have been integrated into the mainstream. Most attribute this to the existence of imaging modalities of equal standard, the increased need for specialist radiological expertise, scarcity of resources within the national health system and limited availability of equipment required (Haris, Yadav et al. 2015).

Magnetic resonance imaging exploits the natural magnetism derived from the precession of charged unpaired protons that can be excited by absorbing energy from a radiofrequency pulse, targeted to their specific resonance frequency. Following excitation within an external magnetic field, these protons achieve higher energy states and return to their stable state, emitting the absorbed energy, which is then detected and transduced into an image by a number of processes.

The strength of the signal from the emitted electromagnetic energy is determined by the proton density of the sample or tissue being imaged,

thus signal strength is achieved by the characteristic molecular and proton density of the specific tissue (Panigrahy and Blüml 2009). This can be further augmented by 'weighting' the image to improve spatial resolution, applying further radiofrequency pulses or altering their duration, or by administering intravenous contrast agents composed of paramagnetic metals such as gadolinium, which amplify vascular enhancement. In clinical practice, intolerance to the contrast agents used, limit their use and necessitate their replacement with sensitive nuclear magnetic resonance (NMR) modalities that negate the need for exogenous contrast. Two such techniques include ^1H Magnetic Resonance Spectroscopy (^1H -MRS) and diffusion-weighted imaging (DWI) (Blüml, Margol et al. 2015, Goo and Ra 2017).

1.11.2 Magnetic Resonance Spectroscopy

Magnetic Resonance Spectroscopy (MRS) is a well-established NMR technique that allows for direct evaluation of the metabolite profiles of tissues and cells, thus depicting the metabolic microenvironment. It is preferred to mass spectrometry, as MRS allows for *in vivo* detection of the metabolite profiles of tumours *in situ* (Haris, Yadav et al. 2015, Manias, Gill et al. 2017).

MRS has been demonstrated to be useful in predicting clinical outcomes based upon metabolite profiles that have been correlated with aggressive tumours. Recently, it has been employed to differentiate

medulloblastoma subgroups in patient samples, by using a 5-metabolite discriminator (Blüml, Margol et al. 2015). Blüml et al 2015 demonstrated accurate sub-group differentiation of 30 medulloblastoma tumours by correlating their differential spectra of creatine, myo-inositol, taurine, aspartate and lipid 13 (Blüml, Margol et al. 2015). The ease with which MRS can be performed in the clinical setting enabled its translation. Though important, the determination of medulloblastoma subgroup of a patient's tumour is not sufficient for the determination of its metastatic potential and is consequently inadequate for the complete prognostication of their disease (Holgado, Guerreiro Stucklin et al. 2017, Ramaswamy and Taylor 2017). Thus, other non-invasive, translational imaging modalities are required to address this problem.

MRS is also limited in its portrayal of the tumour environment at a molecular level due to its poor resolution for detection of low concentration metabolites. In addition, a phenomenon referred to as 'resonance frequency overcrowding' prevents the identification of individual spectra of metabolites that have similar resonance frequencies. Moreover, the detection of many metabolites will be affected by uncontrollable factors such as basal metabolic activity, presence of oxidative stress, age and any simultaneous physiological or pathological processes that may alter the metabolite concentrations. Thus, it is difficult to distinguish whether alterations in metabolite concentrations are solely due to the presence of the tumour (Rae 2014).

Even so, proton magnetic resonance spectroscopy (^1H MRS) has been shown to successfully predict the aggressiveness of tumours by evaluating the ratios of endogenous metabolites detected, to produce spectra of increased amplitude compared to those expressed by normal tissue. For example, the Choline (Cho): N-acetylaspartate (NAA) ratio has been used in the staging of astrocytomas and gliomas, while the Cho: Creatine ratio has been used to differentiate low-grade gliomas from normal brain tissue. Choline compounds such as phosphocholine have also been correlated with malignant transformation of several solid cancers including breast and ovarian carcinoma (Haris, Yadav et al. 2015).

1.11.3 Diffusion-weighted imaging MRI

Diffusion weighted magnetic resonance imaging (DWI-MRI) is an advanced technique that quantitatively portrays characteristics of tumours and metastases that correlate with increased metastatic potential. These include parameters such as cellularity and associated vasogenic oedema, vascularity and proliferation. It does so by measuring the diffusion of water within a tissue at a molecular level, producing a value known as the 'apparent diffusion co-efficient' (ADC) which inversely correlates with the cellularity of a given tumour. Consequently, the ADC value of MB tumours is typically low in comparison to normal tissue, due to their higher cellularity (Manias, Gill et al. 2017).

In addition to use in cancer, DWI-MRI also helps the clinician to distinguish between infective cavities and high-grade tumours, which on conventional MRI would not be easily established. As such, it forms a part of the newer multiparametric MRI protocols for the diagnosis and surveillance of patients with brain tumours and prognostication of metastatic disease (Sawhani, Patel et al. 2020).

1.11.4 MMP-2 and MMP-9 as Imaging Biomarkers using ¹⁹F MRI Enzymatic Probes

In the quest for developing MR Imaging biomarkers, biomarker studies in cancer have used activatable enzymatic probes as contrast agents to enhance MRI sensitivity and specificity (Carril 2017). ¹H enzymatic probes have been the most frequently published agents to demonstrate increased activity of enzymes thought to play significant roles in carcinogenesis and metastasis. Examples of previously investigated enzymes including tyrosine kinases, caspase-3, caspase-7 and β -Galactosidase, the latter of which has also been used with fluorine probes (Carril 2017).

As previously mentioned, standard MRI techniques target the differential resonance frequencies of protons attached to different molecules within soft tissue. As ¹H is highly prevalent in the human body, its high background signal confers high signal-to-noise ratios (SNRs) as well as low specificity. For this reason, ¹⁹F MR imaging with similar natural abundance to ¹H provides acceptable sensitivity but is advantageous

because most fluorine in the body exists as a stable isotope. Therefore, any resulting MR signal is derived from the probe given, while the low background signal of endogenous fluorine, affords enhanced specificity (Carril 2017).

For use as enzymatic biomarkers, we wish to quantify the levels of MMP-2 and MMP-9 in our medulloblastoma cell line supernatants and correlate the resulting differences in signal strengths to the patterns of functional MMP-2 and -9 activity from our biological assays.



Figure 1.9 Our locally synthesised 19-Fluorine MMP-MRI probe

Our locally synthesised Fluorine-MMP MRI biosensor allows for the dynamic quantification of MMP-2 and MMP-9. Cleavage of the MMP specific substrate results the increased distance between the fluorine moiety and gadolinium DOTA complex. Due to the previously paramagnetically shielded fluorine moiety by the chelate, the resulting increased distance between them results in a proportionally stronger fluorine signal (Faas, Krupa et al. 2019).

Similar to other ^{19}F -MRI enzymatic probes, our MMP-biosensor consists of the fluorine-containing moiety, which upon excitation with its specific radiofrequency pulse delivers the signal, the paramagnetic Gd III-bound DOTA-complex and the peptide substrate which links the other two constituents. Therefore in the presence of MMP-2/MMP-9, cleavage of the gelatin peptide linker results in ^{19}F -MRI signal (Carril 2017).

Building upon the strides achieved in understanding the mechanisms of metastasis using genomic profiling, we aim to characterise differentially expressed proteins that correlate the behaviour of different metastatic medulloblastoma cell lines and enable detection of potential indicators of poorer prognosis and disease dissemination.

To this end, we plan to identify biomarkers of metastasis that can predict the metastatic behaviour of medulloblastoma and are detectable on safe translational MRI techniques, to better stratify patients at highest risk of metastatic and recurrent disease, who would benefit most from the more aggressive multimodal therapeutic strategies. We are initially investigating Matrix Metalloproteinases (MMPs), enzymes implicated in tumorigenesis and at every stage of metastasis, to ascertain whether they are differentially expressed between different metastatic medulloblastoma cell lines. We hope to detect and correlate these biological analyses using MRI-MMP biosensors, a novel technique which would allow for the real-time *in vivo* determination of the metastatic potential of a medulloblastoma to spread or recur.

Chapter 2.

Materials and Methods

Materials and Methods

2.1 Cell culture

All medulloblastoma cell lines used in the subsequent 2-D and 3-D experiments are indicated in Table 2.1, with brief details of the clinical history pertaining to the patient donors from whom the cell lines were derived. The cells were obtained from sub-cultures previously defrosted by fellow colleagues, to reduce the time taken for the cell lines to recover and establish their respective proteome in culture. Cell culture was undertaken in aseptic conditions and all equipment decontaminated with 70% IMS thoroughly prior to use to reduce the risk of infection.

2.1.1 Procurement of cell lines

The group 4 matched primary and recurrent medulloblastoma cell lines CHLA-01-MED (ATCC[®]CRL-3021) and CHLA-01R-MED (ATCC[®]CRL-3034) were kindly donated by Professor Geoff Pilkington (University of Portsmouth, UK) while the group 3 cell line HD-MB03 was kindly donated by Dr Till Milde (DKFZ, Heidelberg, Germany). The cell line D283 Med, categorised as intermediate Group 3/4 medulloblastoma was purchased from ATCC (ATCC[®]HTB-185[™]) as was the DAOY SHH cell line (ATCC[®]HTB-186[™]). The cell lines ONS-76 (a wild type p53 cell line as well as its counterpart with and a dominant negative TP53 ONS-76, were gifted by Annette Künkele (Charité Universitätsmedizin, Berlin) and Dr Professor Silber (University of Washington, Seattle) kindly donated the

UW228-3 cell line. The primary of the matched Group 3 cell lines pair, D425-Med, was kindly donated by Marcel Kool (DKFZ, Heidelberg) and its metastatic counterpart D458-Med, by John R. Silber (University of Washington, Seattle). The neural stem cells used as controls in the western blotting experiments were FB83 were derived from human foetal tissue obtained via a Joint MRC/Wellcome Trust grant (#099175/Z/12/Z), and H1-NSC a kind gift from a colleague from Dr Ruman Rahman's team at the CBTRC.

2. 1.2 Sub-culture of cell lines

2.1.2.1 Adherent cell lines

The FB83, DAOY, UW228-3 and ONS-76 cell lines were cultured in treated flasks (Eppendorf/Corning) as per our lab's local standard operating procedures. Cell supernatants were aspirated and the adherent 70-80% confluent cells, washed with 10 mL of HBSS (Gibco, 14170) prior to dissociation from the flask bottom with 2mL of 1X Trypsin-EDTA (Sigma, LH-SIG2044) and then allowed to incubate at 37°C in 5% CO₂ for 5 minutes. Following confirmed dissociation into single cells by microscopy, 3 mL of the required medium was added to the flask to inactivate the trypsin. The resulting 5mL cell suspension was transferred to a clean labelled falcon as well as a further 5mL of media used to wash the flask to obtain residual cells. A dilution of 1:3 or 1:5 of cell suspension: fresh media was then added to a new T75 treated flask (Eppendorf/Corning).

Table 2.1 Characteristics of the panel MB cell lines used. *Matched pairs of primary and recurrent cell lines (Ivanov, Coyle et al. 2016)

MB Cell lines	Molecular subgroup & TP53 status	Patient demographics + clinical information	Mx according to Chang's criteria	2-D In vitro culture phenotype	Recommended 2-D culture medium	3-D In vitro culture phenotype	References
DAOY	SHH: TP53 mutated	4 year old male	M0 : Primary MB cell line	Adherent	Dulbecco's Modified Eagle Medium (DMEM; Fisher Scientific 11574446) supplemented with 10% foetal bovine serum (FBS; HyClone, SH30541.03).	Tight spheroids	Jacobsen et. al., 1985
ONS-76	SHH: TP53 wild-type	2 year old female with 3cm midline vermis tumour	M2 : metastases to right pre-pontine cistern	Adherent	RPMI 1640 with L-glutamine (Sigma, R8758)+10% FBS(HyClone)	Tight spheroids	Yamada et al., 1989 Shimizu et al., 1991
ONS-76	SHH: dnp53	2 year old female with 3cm midline vermis tumour	M2 : metastases to right pre-pontine cistern	Adherent	RPMI 1640 with L-glutamine (Sigma, R8758)+10% FBS(HyClone) supplemented with 1% puromycin	Tight spheroids	
UW228-3	SHH: TP53 mutated	9 year old female with contrast enhancing midline cerebellar vermis tumour	M0 : Primary MB cell line	Adherent	DMEM/F12 +15% FBS + 1% L-glutamine +1% sodium pyruvate	Tight spheroids	Keles et al., 1995 Künkele et al., 2012
CHLA-01-MED*	Group 4: TP53 wild-type	8 year old male, primary tumour	M0 : Primary MB tumour (but had neuroaxial dissemination at diagnosis-M3)	Suspension	DMEM/F-12 medium (Fisher Scientific 11520396) supplemented with 2% B-27 supplement (Gibco, 17504044), 20 ng/mL recombinant human epidermal growth factor (EGF; Gibco, PHG0315), and 20 ng/mL recombinant human basic fibroblast growth factor (FGF; Gibco, PHG0266).	N/A	Xu et al., 2015
CHLA-01R-MED*	Group 4: TP53 wild-type	8 year old male, recurrent tumour	M2 : Recurrent metastatic cells from pleural fluid	Suspension			
D283 Med	Group 3: TP53 wild-type	6 year old male	M2 : Peritoneal metastasis and malignant ascites	Semi-adherent	Dulbecco's Modified Eagle Medium (DMEM; Fisher Scientific 11574446) supplemented with 10% foetal bovine serum (FBS; HyClone, SH30541.03).	N/A	Friedman et al., 1985
D425-Med*	Group 3: TP53 mutated	5 year old male	M0 : Primary MB cell line	Semi-adherent			Bigner et al., 1990
D458-Med*	Group 3: TP53 wild-type		M+ Metastatic	Semi-adherent			
HD-MB03	Group 3: TP53 wild-type	3 year old male, midline 4 th ventricle and vermis	M3 : Spinal metastasis at diagnosis	Semi-adherent	RPMI 1640 with L-glutamine (Sigma, R8758)+10% FBS(HyClone)	Loose spheroids	Milde et al., 2012

2.1.2.2 Semi-adherent cell lines

The semi-adherent medulloblastoma group 3 cell lines D425-Med, D458-Med, D283-Med and the HD-MB03 cells and were cultured in treated T75 or T25 flasks (Eppendorf/Corning). Firstly, cell suspensions were transferred into the respective labelled falcons and retained. As with the adherent cells, following a wash with 10mL of HBSS, the semi-adherent cells were incubated with 1X Trypsin-EDTA in the same incubator conditions as before. 7mL of the required media was added to inactivate the trypsin and the resultant mixture added to the previously removed cell suspension. As HD-MB03 cells grew faster than the D283 Med cells, they were split in 1:5 and 1:3 respectively with fresh media every 48-72 hours.

2.1.2.3 Suspension cultured cell lines

The paired group 4 cell lines CHLA-01-MED and CHLA-01R-MED were cultured in non-treated T75 or T25 flasks (Eppendorf). In suspension culture, the primary CHLA-01-MED formed more clusters and appeared to proliferate more rapidly requiring a slightly harsher split compared to its recurrent counterpart, CHLA-01R-MED. As per ATCC recommendations, the cells were always sub-cultured in 25% of their previously conditioned medium, with 75 % of fresh media which was prepared weekly, due to its growth factor constituents (table 5). Once

weekly, the cell suspensions were centrifuged at 100g for 7 minutes and re-suspended in the aforementioned ratio of conditioned: fresh media.

2.2 Preparation of 2-D cultured medulloblastoma cell line samples for gelatin zymography, gene and protein expression from the same cell population

The preparation of matched cell pellets and supernatant samples from a panel of nine medulloblastoma cell lines was performed, to reduce the effects of any confounding technical or environmental factors that would be difficult to control.

Figure 2.1 demonstrates a schematic of how this was performed. Prior to their use in any experiments, mycoplasma infections were excluded on a regular basis and cell viability confirmed using PrestoBlue blue reagent (ThermoFisher, A13261). The PrestoBlue was diluted in medium (1 in 5 dilution) and added to cells within black-walled 96 well plates. After an hour's incubation at 37°C in the dark, fluorescence was quantified using our FLUOstar microplate reader (BMG, labtech).

2.2.1 Preparation of cell pellets for molecular analysis

Following removal of the conditioned medium from the adherent cell lines, 1XTrypsin-EDTA was used to detach the cells and thereafter inactivated with the respective cell line growth medium, resulting in a cell suspension. For the semi-adherent cell lines, the conditioned medium containing cells in suspension was transferred to a clean labelled

Eppendorf and the remaining cells trypsinised with 1XTrypsin-EDTA, which was inactivated with the respective media and added to the cells already in suspension.

All cell suspensions including the group 4 cell lines that required no prior preparation as they grow in suspension, were thereafter subjected to centrifugation at 100g for 7 minutes. The supernatants were removed and the resulting cell pellets re-suspended in 1 mL of PBS and re-centrifuged in the same conditions. The excess PBS was removed with a 1mL pipette with care not to disperse the pellet and the cell pellets snap frozen in liquid nitrogen before storage into the -80°C freezer.

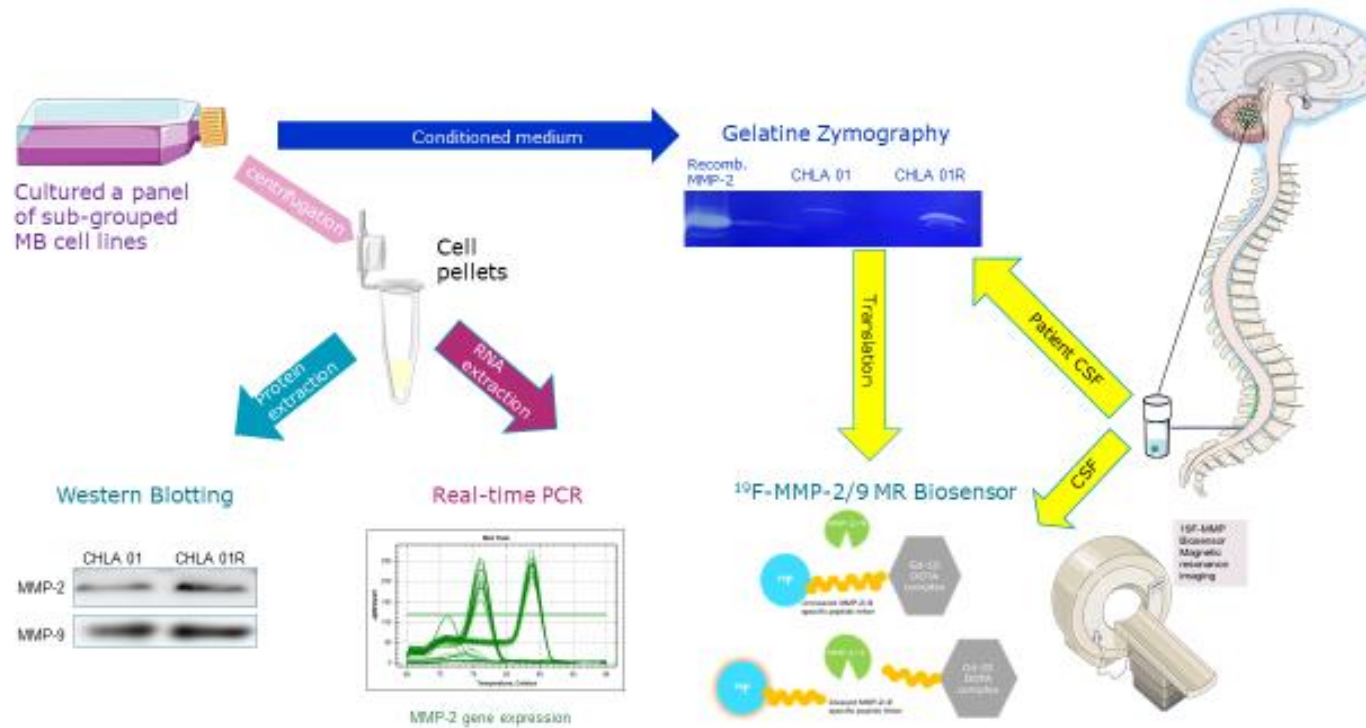


Figure 2.1 Schematic workflow of the main methods described in this thesis. RNA and protein were extracted from the same cell pellets to enable comparison of the gene and protein expression of the same cell population from each MB cell line. The supernatant aspirated prior to cell harvest was first split into two following centrifugation and the same volume used in zymography and concentrated for biosensor experiments.

2.3 Experimental set-up for Gelatin Zymography

2.3.1 Controls

For the initial zymogram experiments, concentrated Foetal Bovine Serum (FBS, HyClone) was used as a positive control to assess for technical validity. Once a positive zymogram was obtained, the positive controls used were Recombinant human MMP-2 (Peprotech, 420-02) and Recombinant human MMP-9 (R&D systems, 911-MP-010). Both were re-constituted according to the instructions received from the respective companies. As the signal from the latter seemed to obscure adjacent wells on the zymogram, a further Recombinant human MMP-9 was obtained from Abcam (Ab168863). As serum (FBS) had produced a positive signal in the first optimisation zymography experiments, the respective serum-containing culture media were loaded in equal volumes as the supernatant samples and used as further positive controls.

2.3.2 Preparation of conditioned medium for zymography, ELISA and protease/protease inhibitor arrays

2.3.2.1 Cell counting

For each experiment, the same cell number of each cell line were seeded into their respective flasks and conditioned medium collected 48 hours after culture in 37°C, 5% CO₂ conditions. From the resulting cell suspensions after trypsin-mediated detachment and washing of residual

cells with 7mL of required media for both semi-adherent and adherent cells lines, 10µl of this was added to 10µl of Trypan blue and cells counted on either an EVE™ Automated Cell Counter (Nanotech) or manually using a haemocytometer and clicker.

For the paired group 4 cell lines growing as clusters and single cells in suspension culture, dissociation into single cells was achieved by centrifuging an aliquot of the cell suspension at 100g for 7 minutes and extracting the supernatant. The resulting cell pellet was thereafter re-suspended 10X in Accutase cell detachment solution (AT104-500) in a ratio of 1:5 of Accutase to the volume of the aliquot taken for cell counting. This mixture was then re-suspended 10X, incubated for 10 minutes and re-suspended again 10X before 10µL was added to an equal volume of the trypan blue and cells counted on an EVE™ Automated Cell Counter (Nanotech) or manually using a haemocytometer and clicker.

For each cell suspension, trypan blue mixture was mixed by pipetting up ten times and 10µL of the mixture loaded to the EVE counting slides. After insertion of the slide, the default cell counting mode was selected and a live cell count per mL obtained. This was used to calculate the required volume of cell suspension of the respective cell lines, required for the seeding of 5×10^6 cells in the respective flasks. The volume of required media was then added to the flasks and incubated at 37°C, 5% CO₂ conditions for 48 hours.

487 hours later, MB cell suspensions obtained as described in the manner detailed in the preceding cell culture section were centrifuged first at 800 rpm, then at 1500rpm each for 7 minutes.

2.3.3 Preparation of SDS Polyacrylamide Zymogram gel

To prepare the gelatine constituent of the separating zymogram gel, a 5mL solution of (3mg/mL) of Gelatine (Sigma, G1890) was completely dissolved in distilled water by gentle warming in a water bath at 37°C. Once fully dissolved, it was cooled completely by incubating at 4°C and filtered prior to use.

To prepare the 3% Gelatin impregnated SDS-PAGE gel, the reagents were added as per Table 2 and vortexed for 10 seconds prior to pouring the separating gel mix into a clean 1mm spacer (Biorad). This was allowed to set 1 hour after which the stacking gel was made. A thin layer of 70% IMS was overlaid above the separating gel mix to ensure it set in a straight line.

The stacking gel was made by adding the following components (Table 3), mixing by vortex for 10 seconds and pipetting it onto the separating gel, once 70% IMS layer had been removed with filter paper.

Table 2.2 Separating gel mix

Chemicals	Volume
3% Gelatin (Sigma, G1890)	5ml
Distilled H ₂ O	1ml
1.5M Tris/HCl pH 8.8	3.8ml
10% SDS (MP Biomedicals, 194831)	150µl
Acrylamide/bis solution (30%) (Sigma, A3699)	5mL
TEMED (Sigma, T7024)	15µl
10% APS	150µl

Table 2.3 Stacking gel mix

Chemicals	Volume
Distilled H ₂ O	3.9ml
0.5M Tris/HCl pH 6.8	320µl
10% SDS	50µl
Acrylamide/bis solution (30%) (Sigma, A3699)	750µl
TEMED (Sigma, T7024)	5µl
10% APS	80µl

The stacking gel set after 90 minutes and the gel cassettes covered with a damp paper towel and stored within a plastic sealed bag at 4°C for at least 1-2 hours prior to use. For best results, gels and the supernatant samples were used within 7 days to prevent expiry of the gelatine and maximise the MMP-2 and -9 signal obtained from the samples.

2.3.4 Zymography buffer components

The solutions used in the zymography technique were made according to buffer constitution instructions kindly advised by our postdoctoral research fellow, Dr Franziska Linke. The constituents of the buffers used were as follows; 10X running buffer: 25mM Tris Base (X), 192 mM Glycine and 0.1% SDS; the 2X sample buffer: 0.5M Tris-HCl pH. 6.8, 10% SDS, 25% Glycine and 1% Bromophenol blue (Santa Cruz, E0807); 10XRenaturing buffer: 2.5% Triton-X-100 (Sigma, T8787) and the Developing buffer was procured from Biorad, 161-0766. The Coomassie Blue staining solution was made up as a 0.5% Coomassie R-250 (ThermoScientific, 20278) solution in 10% Acetic acid and 40% methanol, while the de-staining solution was 40% Methanol and 10% Acetic acid in distilled water.

2.3.5 Loading and running the gel

Following a 48-hour incubation at 37°C and 5% CO₂, the supernatant from each MB cell line, was removed and twice centrifuged at 100g for 7 mins to exclude any cell debris. Cell supernatant samples were collected within a week of the zymography being performed. 30µL of each supernatant and control sample were mixed with an equal volume of 2X sample buffer (SB) and 20µL of this was loaded with a Hamilton pipette into each well. The gel was run at a constant voltage of 125V until the loading buffer had reached the junction between the stacking and

separating gel and with the electricity off, a further 20 μ L of the sample/control:2XSB solution was added and the gel allowed to run until the sample buffer ran off the gel. To allow for the best separation, the gel was electrophoresed for a further 15-20 minutes before being removed from the gel cassettes and washed in renaturing buffer for 1 hour under slight agitation at room temperature. The renaturing buffer was then replaced with developing buffer and the gel washed for a further 30 minutes. After this step, the developing buffer wash was replaced and the gel incubated at 37°C for 18 hours (2D) and 24 hrs (3D).

After the appropriate incubation time, the gel was thrice washed in deionised water with gentle agitation at room temperature and thereafter submerged in the coomassie blue staining solution for 15 minutes. The gel was then placed in de-staining solution for up to 2 hours or until clear bands of digested gelatin were visible on the blue background of the gel. Images of the gel were then acquired either by scanning the gel within a sealed, transparent plastic case or with a phone camera. The images were then imported into Image J and semi-quantitative determination of MMP-2 and MMP-9 functional activity thereafter determined by densitometry (see Appendix).

2.4 Investigating the MMP-2 and MMP-9 gene expression in medulloblastoma cell lines

Real-time polymerase chain reaction (qRT-PCR) is a technique that enables the sensitive quantification of a gene's expression in multiple samples simultaneously. A primer sequence specific to the gene of interest initiates the transcription of the gene within the double stranded cDNA template of the sample being examined. Optimal conditions created by cyclical temperature variations programmed in the real-time PCR cycler, result in amplification of the DNA product until the reaction is stopped. Addition of a fluorescent dye such as SYBR Green I (Biorad) that binds to double stranded DNA, results in an increasing fluorescence signal that is proportional to the quantity of the amplified DNA product of interest. The continuous fluorescence signal is detected with time and plotted graphically. To improve validity of the experiment, the quantification of a gene that is expressed by all the samples being compared, is performed alongside that of the gene of interest and the latter normalised according to the former, known as the housekeeping gene. For these experiments, the Glyceraldehyde-3-phosphate dehydrogenase (GAPDH) gene was used.

2.4.1 RNA extraction

A panel of nine sub-grouped medulloblastoma cell lines were cultured in their normal media for 48 hours in 5% CO₂ at 37°C and cell pellets containing approximately 2.5X10⁶ cells were obtained and frozen down at -80°C. RNA extraction using the Nucleospin© RNA plus (Fisher) kit was performed simultaneously on all cell pellet samples designated for the same experiment. RNA quality and concentrations were quantified using a Nanodrop machine Table 2.4.

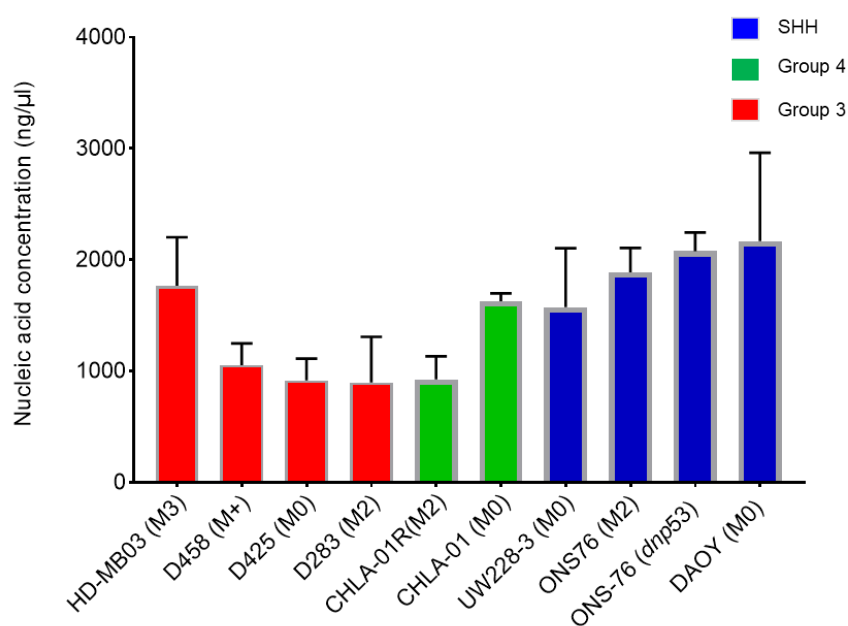


Figure 2. 2 Analysis of the concentrations (ng/ µl) of RNA extracted from sub-grouped MB cell lines.

Brackets indicate paired Group 3 and Group 4 cell lines. While the paired Group 3 cell lines D425 (primary) and D458 (metastatic) demonstrated similar quantities of RNA from the same number of cells, the Group 4 primary cell line CHLA-01 produced higher quantities of RNA than its metastatic counterpart.

Table 2.4 RNA Nanodrop table showing quantities of RNA from MB cell lines

Cell line samples	Nucleic Acid Conc. (ng/μl)	260/280	260/230
DAOY	3039.8	2.16	2.04
DAOY	1480.8	2.14	2.16
DAOY	1977.4	2.12	2.16
ONS76	1931.3	2.12	2.14
ONS-76	1364.6	2.19	2.12
ONS-76	2179.8	2.12	2.07
ONS-76	1716.4	2.14	2.1
ONS-76	1723.4	2.12	2.21
ONS-76 dnp53	2269.5	2.1	2.18
ONS-76 dnp53	2002.9	2.11	2.22
ONS-76 dnp53	1959.6	2.1	2.05
UW228-3	1199.3	2.15	2.15
UW228-3	2180.3	2.1	2.04
UW228-3	1345.7	2.13	2.02
CHLA-01	783.5	2.15	2.1
CHLA-01	1548.4	2.16	1.98
CHLA-01	1667.6	2.13	2.04
CHLA-01R	1230	2.17	2.02
CHLA-01R	877.8	2.12	2.04
CHLA-01R	799.1	2.11	2.18
CHLA-01R	798.5	2.15	2.07
D283	606.5	2.07	2.07
D283	1187.4	2.14	2.12
D425	1141	2.1	2.2
D425	821.7	2.08	2.16
D425	787.8	2.07	2.19
D458	1355.7	2.15	2.1
D458	786.4	2.11	2.08
D458	1095.3	2.11	2.22
D458	993.3	2.1	2.2
D458	940.7	2.1	2.26
D458	1150.3	2.14	2.15
HDMB03	1783.4	2.15	2.04
HDMB-03	2162.8	2.15	2.1
HD-MB03	1153	2.13	2.23
HD-MB03	1947.5	2.13	2.13

Once the quality and concentration of the eluted RNA from each sample was confirmed, they were stored at -80°C or transcribed into cDNA, the beginning blocks for the real-time PCR experiments.

2.4.2 cDNA synthesis

RNA samples for cDNA synthesis were defrosted on ice and diluted to a concentration of 1µg/mL of RNA before being combined with the reagents as indicated in Table 2.5.

Table 2.5 Reagents and volumes required to be added to RNA and dH2O for cDNA synthesis

cDNA synthesis reagent	Volume for 1 reaction (µl)
Random primers 250ng/µl (Invitrogen, 48190-011)	1
dNTPs 10mM (Bioline, BIO-39044)	1
5X First Strand Buffer (Invitrogen 18080093)	4
DTT 0.1M (Invitrogen 18080093)	1
**SuperScript III Reverse Transcriptase (Invitrogen 18080093)	1

The samples were then heated up in a thermocycler on an automated program that heated the samples to 25°C for 5 minutes, 50°C for 45 minutes and lastly 70 °C for 15 mins. The resulting cDNA was stored at -20 °C.

2.4.3 MMP-2 Primer optimisation

The MMP-2 primer sequence used for the PCR experiments was a kind gift from a collaborator, Professor Anna Grabowska (University of Nottingham). The primer sequence was then confirmed to have suitable properties on searchable free online software programs, Oligocalc © and Oligoanalyzer©.

Table 2.6 MMP-2 (human) gene primer sequence

Matrix metalloproteinase 2 (MMP-2), Gelatinase A	GCCTTTAACTGGAGCAAAAACAA	TCCATTTTCTTCTTCACCTCATTG
--	-------------------------	--------------------------

2.4.3.1 Determining the annealing temperature of the MMP-2 primer

Gradient polymerase chain reaction (PCR) experiments were performed to determine the optimal annealing temperature of the MMP-2 primer in Table 3.2. Positive and negative cDNA samples were tested alongside a no template control (NTC) at five different temperatures i.e. 57.1 °C, 58.1 °C, 59.6 °C, 60.2 °C, and 62.2 °C, to obtain a temperature gradient. After adding the same volume of a master mix containing SYBR green I (Biorad), forward and reverse MMP-2 primers (see table 3.2) and PCR grade water, the samples were centrifuged prior to incubation in a thermocycler and a pre-set program run as detailed in the methodology chapter of this thesis. Once synthesised, equal volumes of the PCR products were loaded into the wells of an agarose gel alongside a DNA

ladder of 100 base pairs and allowed to run for 30-45 minutes at 120V until good band separation was achieved.

The MMP-2 primer product length was approximately 98 base pairs at the optimal annealing temperature of 60 °C. Once the primer efficiency of the MMP-2 primer was determined by a fellow student, Hannah Jackson, confirmation experiments were performed and the MMP-2 primer efficiency determined to be 99.6%.

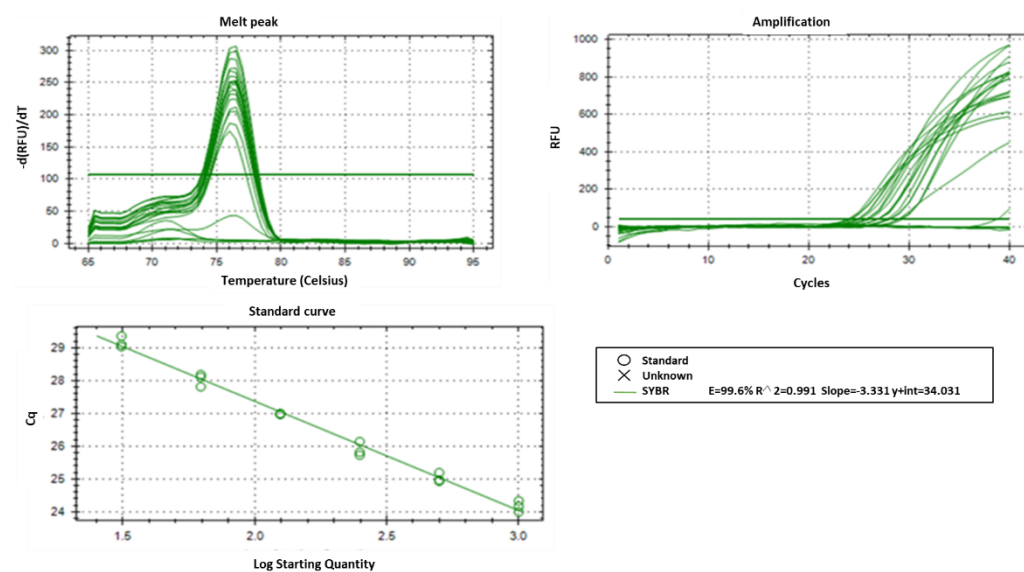


Figure 2.3 Results from confirmation experiments of MMP-2 primer efficiency. A. Melt peak shows a single product above the threshold and smaller peaks of secondary products below. **B.** Amplification plots of the SYBR Green I fluorescence at different levels of DNA concentration. **C.** Indicates good pipetting technique, as all values were either superimposed or proximal to each other.

A panel of nine sub-grouped medulloblastoma cell lines were cultured in their normal media for 48 hours in 5% CO₂ at 37°C and cell pellets obtained for RNA extraction and subsequent cDNA synthesis. RNA extraction was performed using the Nucleospin® RNA plus (Fisher, cat.

74098450) and cDNA synthesised as described in chapter 2 of this thesis. Real time PCR experiments using SYBR green I (Biorad) were performed and results normalised to the expression of GAPDH, to enable comparison of MMP-2 gene expression of each MB cell line.

2.4.4 MMP-9 Primer optimisation

To date, five MMP-9 primers were tested and failed at either the Gradient PCR stage or at the primer efficiency experiments. Unfortunately, during the time of the experiments, substantial equipment problems were experienced that prevented return to testing further MMP-9 primers.

The most successful MMP-9 primer tested, was a sequence also donated as a kind gift from a collaborator, Professor Anna Grabowska (University of Nottingham).

Table 2.7 MMP-9 (human) gene primer sequence

Matrix metalloproteinase 9 (MMP-9), Gelatinase B	GCCTTTAACTGGAGCAAAAACAA	TCCATTTTCTTCTTCACCTCATTG
--	-------------------------	--------------------------

2.4.4.1 Determining the annealing temperature of the MMP-9 primer

Following the same procedure as that performed for the MMP-2 primer, a gradient PCR experiment (

Figure 2.3) for the MMP-9 primer sequence above was performed.

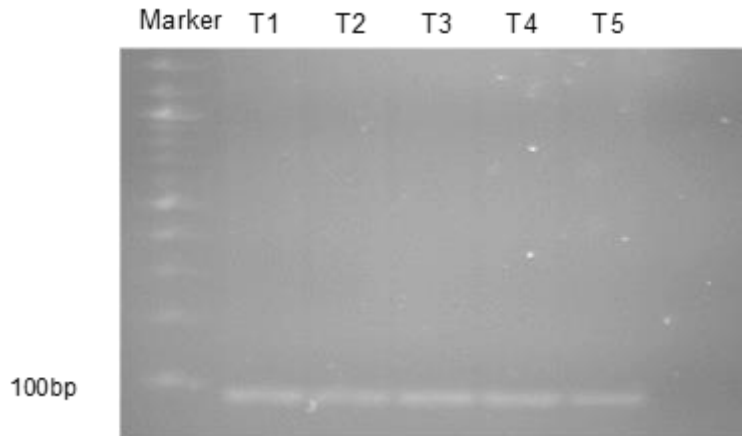


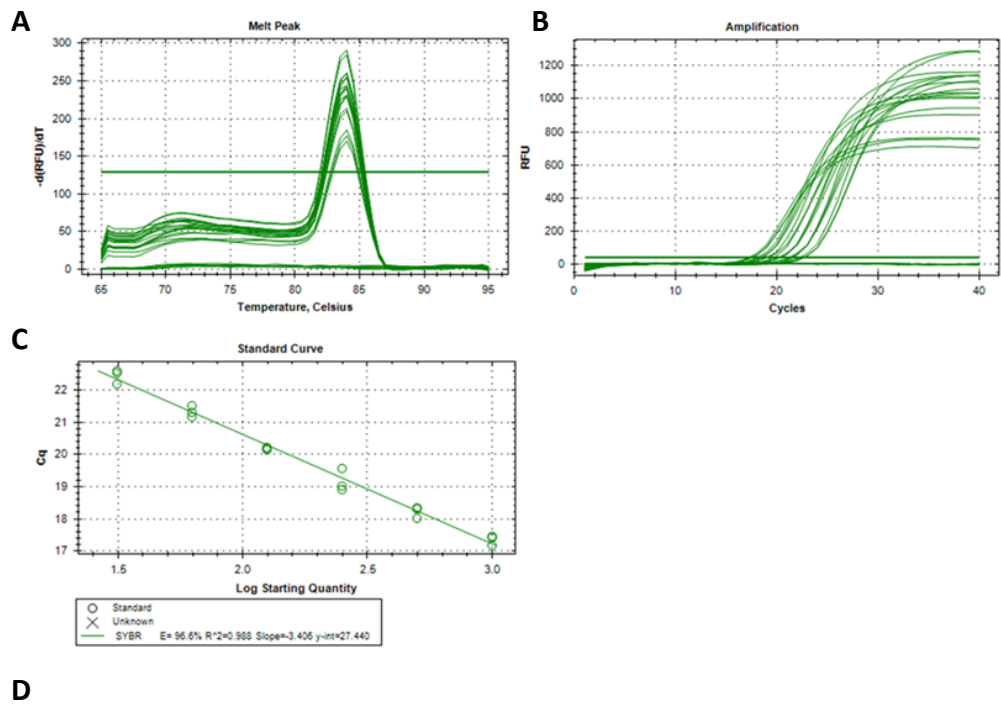
Figure 2.4 Gradient PCR for MMP-9 primer (Table 3.3) optimisation showing a PCR product at approximately 100 base pairs with equally strong signals at all 5 temperatures tested. From left to right T1= 57.1 °C, T2=58.1 °C, T3=59.6 °C, T4= 60.2 °C, and T5= 62.2 °C.

2.4.4.2 MMP-9 Primer efficiency experiments

Having been previously demonstrated to express MMP-9 (ref), cDNA from the DAOY cell line was selected to confirm primer efficiency of the MMP-9 sequence in table 3.3. Several challenges were encountered and further experiments modified to surmount them. However, due to limited time, MMP-9 gene expression experiments were not taken further.

To confirm correct experimental technique, the experiments were first performed using primers from the housekeeping gene, GAPDH. As it is a routinely used primer, it was optimised by previous PhD students in our lab. These results were then used as a benchmark, to compare the results from the MMP-9 primer efficiency experiments. A dilution series of cDNA was performed and the resulting GAPDH gene expression quantified. As shown in fig 3.15, a single product was obtained in the melt

peak curve and clear sample amplification plots from the samples with decreasing cDNA content within the samples.



GAPDH (housekeeping gene)	F: ATGTCGTCATGGGTGTGAA	R: GTCTTCTGGGTGGCAGTGAT
---------------------------	------------------------	-------------------------

Figure 2.5 Results from primer efficiency experiments on GAPDH primer.

A. Melt peak shows a single product above the green line (threshold) which shows no other DNA products or primer dimers were obtained. B. Amplification of the SYBR Green I fluorescence at different levels of DNA concentration. C. indicates good pipetting technique as all values were either superimposed or proximal to each other. D. GAPDH sequence

Detailed efforts to further optimise this and published MMP-9 primers were unsuccessful.

2.5 MMP-2 and MMP-9 protein expression in medulloblastoma cell lines

2.5 Determination of relative protein concentration using Bradford assay

For the calculation of relative protein content of the samples loaded on the gel, a Bradford assay was performed using the Protein Assay Dye Reagent concentrate (Biorad, 500-0006) This was diluted 1:4 in distilled water to the volume required depending on the number of samples to be tested (1mL/sample). A 0.2% solution of Bovine serum albumin (Sigma-Aldrich, A7906) was used to prepare the required standards shown in Table 2.8 below.

Table 2.8 Bradford assay standards with increasing BSA concentration

Solution	Concentrations of BSA ($\mu\text{g}/\text{mL}$)							
	0	1	5	10	15	20	30	40
BSA (μL)	0	0.5	2.5	5	7.5	10	15	20
Protein Assay Dye (μL)	1000	999.5	997.5	995	992.5	990	985	980
Total Volume (mL)	1	1	1	1	1	1	1	1

These were then loaded onto a pre-planned 96-well flat bottomed plate along with similar volumes of supernatant samples (Eppendorf). Once the protein content of the samples was visually determined to be in the range of the Bradford assay standards, the plate was inserted into the plate reader (FLUOstar Omega, BMG Labtech) and the Bradford assay program on Omega selected. The results were then exported into a pre-filled Excel file, resulting in Table 2.9 and graph shown in

Figure 2.6 Graphical representation of the stepwise incremental protein concentrations of the Bradford reagent standard curve.

Table 2.9 Bradford assay results once exported into pre-filled Excel file

BSA standard	1st absorbance	2nd absorbance	3rd absorbance	average	BSA standard	Subtract blank	from linear equation	from linear equation	protein concentration (ug/ul)	vol for 20ug (ul)
Blank	0.276	0.274	0.257	0.269	0	0.000				
1	0.29	0.289	0.291	0.29	1	0.021				
5	0.328	0.326	0.335	0.329667	5	0.061				
10	0.377	0.382	0.391	0.383333	10	0.114				
15	0.438	0.44	0.448	0.442	15	0.173				
20	0.48	0.484	0.492	0.485333	20	0.216				
30	0.57	0.583	0.586	0.579667	30	0.311				
40	0.661	0.658	0.658	0.659	40	0.390				
D283 media	0.483	0.508	0.5	0.497	D283 med	0.228	0.240	15.088	7.544	2.651
D283 supern.	0.435	0.443	0.442	0.44	D283 supe	0.171	0.183	11.503	5.752	3.477
CHLA media	0.409	0.405	0.41	0.408	CHLA med	0.139	0.151	9.491	4.745	4.215
CHLA 01 supern	0.386	0.405	0.397	0.396	CHLA 01 st	0.127	0.139	8.736	4.368	4.579
CHLA 01R sup.	0.362	0.376	0.382	0.373333	CHLA 01R	0.104	0.116	7.310	3.655	5.472
HDMB03 media	0.405	0.401	0.413	0.406333	HDMB03 r	0.137	0.149	9.386	4.693	4.262
HDMB03 sup	0.529	0.543	0.531	0.534333	HDMB03 s	0.265	0.277	17.436	8.718	2.294

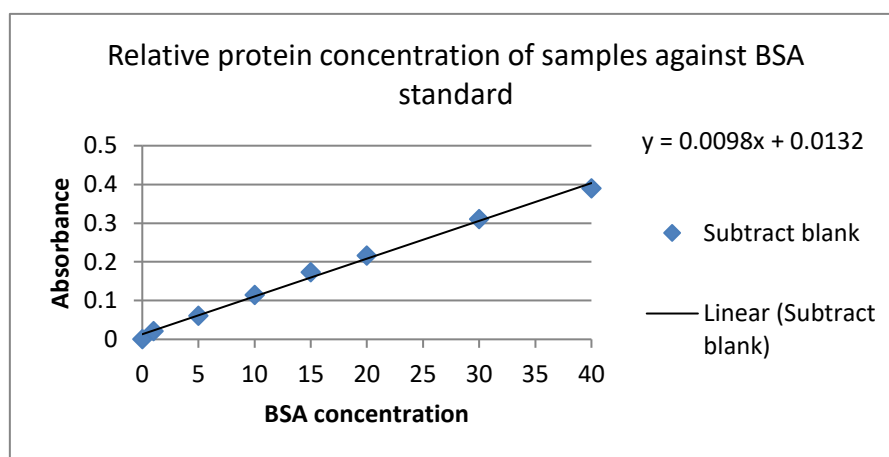


Figure 2.6 Graphical representation of the stepwise incremental protein concentrations of the Bradford reagent standard curve.

2.6.1 Western blotting

To determine the baseline differential MMP-2 protein expression in isogenic primary and medulloblastoma cell lines, equal amounts of protein lysates were examined using western blotting. Briefly, equal amounts of protein from each cell line as determined in Bradford assays, were agitated with equal volumes of 4X sample buffer containing β -mercaptoethanol and loaded into 1.5mm wells of 10% sodium dodecyl sulphate polyacrylamide gels (SDS-Page). The gels were electrophoresed within running buffer at 40 milliamps until adequate separation of the protein ladder was observed. The separated proteins were then transferred from the gels onto polyvinylidene difluoride (PVDF) membranes which were dried for 15 minutes before being blocked in 5% bovine serum albumin in TBS-T for 1 hour. The membrane was then incubated with 10mls of 1:1000 primary anti-rabbit MMP-2 antibody (Cell signalling; #4022) diluted in the blocking solution for 18 hours at 4°C. The next day, the membrane was washed in TBS-T before and after being incubated with the secondary anti-rabbit antibody at 1:1000 concentration in 5% BSA for 1 hour at room temperature. After incubation with horseradish peroxidase (HRP) solution and ECL solution, the membranes were imaged using chemiluminescence (LAS 4000 mini Biomolecular imager, GE Healthcare) and image J densitometry used to quantify the differential levels of MMP-2 protein in each cell line (see appendix).

2.6.2 Enzyme Linked Immunosorbent Assays [ELISA]

ELISA experiments were mainly used to determine what role the storage conditions of supernatants and CSF would exert on the levels of MMP-2 protein detectable. The Quantikine total MMP-2 immunoassay kit (R&D systems; MMP200) was used to detect the MMP-2 levels within cell supernatants to determine the optimal storage conditions for CSF.

A standard of MMP-2 concentrations was prepared by its serial dilution to give a standard curve for comparison to, when read by a plate reader. Reagents were added to the same volume of samples to be investigated and a substrate solution added last to the sample was observed to change colour depending upon the MMP-2 concentration within the sample. Results were then extrapolated from the correlated optical density to the MMP-2 standards and concentrations of our samples given.

2.6.3 Protease and protease inhibitor arrays

Forty-eight hour conditioned cell supernatants were prepared as previously described and tested immediately after being harvested, using a Human Protease/Protease inhibitor Array kit (R&D Systems; ARY025). Reagents and buffers required were all provided within the kit and used according to the volumes and times described within their manual. Briefly, nitrocellulose membranes were placed into a multi-well plastic dish and incubated in the provided blocking buffer for an hour on a shaker

at room temperature. During this time, samples for analysis were diluted to a volume of 1.5ml with array buffer 6, with the addition of 15µl of either the protease or protease inhibitor detection antibody cocktails. The membranes were then incubated in the supernatant/array buffer 6 solution overnight at 4°C. The next day, in a manner similar to western blotting, the membranes were thrice-washed before being incubated with 2mL of Streptavidin-HRP. Further washing with the washing buffer was done after 30 minutes of incubation and array detection assessed using chemiluminescence, as previously described.

Array correlates were localised using the transparent overlay templates provided and quantified using a publicly available macro for analysis of protein arrays (see appendix). Densitometry performed on Image J was then used to compare the relative protease and protease inhibitor expressions within the supernatant samples, with normalisation to the mean of the reference controls on each membrane. Graphs were created on Graphpad prism.

2.6.4 Fluorescence Resonance energy transfer (FRET)

As previously employed in the optimisation of our MRI-MMP biosensor, FRET assays were used to explore specific factors prior to imaging with the biosensor which is expensive. Equal volumes of supernatant derived from samples with the same initial seeded cell numbers, were pipetted into corning, black-bottom 96 well plates, along with fluorescently

quenched DQ gelatin and reaction buffer. The presence of MMP-2/MMP-9 within the supernatant sample would degrade the fluorescent quenched gelatin, resulting in increasing fluorescence with time, as detected by our FLUOstar Omega plate reader (BMG labtech) and plotted using graph pad prism.

2.7 3-D cell culture

SHH cell lines DAOY, ONS-76 and UW228-3 were the main cell lines cultured as unicellular spheroids. Using a protocol for the development of a spheroid MB model that was optimised by a colleague Dr Sophie Roper, the optimal cell densities of each cell line, were seeded within ultra-low attachment round bottom plates (Corning, 7007) and left to aggregate over 96 hours in 200µl of freshly prepared neurosphere medium. These cell lines formed tight spheroids, which could be safely transferred with 100µl of their older medium, to ECM coatings on flat-bottomed 96 well plates with 100µl of fresh neurosphere medium, prepared every 7 days. This practice helped to ensure that the added factors remained active within the medium (recipe in Table 2.10).

Table 2.10 Neurosphere medium

For 50ml neurosphere medium	Volume required
DMEM/F-12	48.5mL
B-27 supplement (Gibco, 17502048)	1mL
N-2 supplement (Gibco 17502048)	500µl
Heparin [2µg/ml] (Stem Cell Technologies, 07980)	125µl
EGF [20ng/ml] (Gibco PHG0315)	10µl
FGF [10ng/ml] (Gibco PHG0266)	5µl

2.7.1 Spheroid migration across a Collagen IV matrix

Day 4 generated spheroids of approximately ~300µm diameter, were transferred along with 100µl of their original neurosphere medium onto a dry 20µl coating of 10µg/mL of collagen IV (Cultrex mouse, 3400-010-01) after the 96 well plate was washed with HBSS. A further 100µl of fresh medium was added and daily imaging of the migrating spheroids was performed using a camera (Canon, DS126431) attached to a brightfield microscope (Olympus, CKX41) at X4 and X10 magnifications. Images were calibrated using a graticule photographed at the same magnification and a macro designed by a predecessor Dr Ivanov (see appendix) was used to quantify spheroid volume. This was then analysed on excel and presented graphically using GraphPad prism.

2.7.2 Spheroid and macrophage co-culture

The spheroid-macrophage co-cultures were performed by Dr Sophie Roper with macrophages gifted by Dr Luisa Martinez-Pomares group. Briefly, macrophages delivered in 24-well ultra-low attachment plates on ice were trypsinised then harvested before being twice centrifuged at 300g for 5mins. The pellet was washed in neurosphere medium and centrifuged as before twice more. Optimal cell densities of DAOY *mut* p53, ONS-76 dnp53 and ONS-76 *wt.* p53 cells were seeded in ultra-low attachment plates (Corning, 7007) with macrophages in ratios of 1:1 ratio, 1:0.5 and 1:0.25 by Dr S. Roper (Roper 2019) and zymogram

experiments of the resulting 72hr conditioned supernatants performed as demonstrated in Figure 4.10.

2.7.3 Transwell-migration assays

Having been demonstrated by a colleague, Dr Macha Aldighieri to migrate through uncoated trans-well inserts with pores measuring 8µm in diameter (Greiner Bio-One Thincert, 662638), invasion assays of Group 3 and Group 4 MB cell lines were performed, to determine their differential capacities for invasion through a collagen IV/Laminin I matrix. Further details of the optimisation work are available here (Aldighieri 2020). The collagen coatings were performed in the same manner described for the spheroid migration assays. Once completely dried in the cell culture hood and immediately prior to seeding the MB cells, 50µl of 100µg/µl of Laminin I mouse (Cultrex, 3400-010-02) was added and left for an hour before being aspirated.

To create a chemokine gradient towards which MB cells would move, cell lines were cultured in 2% FBS for 24 hours prior to counting 10^4 viable cells for loading in the upper chamber in 2% FBS, with 10% FBS in the 24 plate receptacle. Invasion was permitted for 48 hours following which the remaining cell suspension within the transwell were aspirated and invaded cells dissociated from the bottom receptacle-facing surface of the transwell by incubating them in 1X cell dissociation solution (CDS) at 37°C for 1 hour.

2.7.4 Determining which assay dye most accurately detected invasive MB cells

While the assay had thus far been optimised using Calcein AM[®] for the quantification of the invaded HD-MB03 cells, initial experiments testing the slower growing metastatic Group 3 and 4 cell lines D458-Med and CHLA-01R-Med respectively resulted in reduced accuracy in detection of cell numbers below 2.5×10^4 . Therefore comparative standard curves using 50,000 and 100,000 HD-MB03 cells were used, and PrestoBlue[®] compared to Calcein-AM[®]. Table 2.11 summarises their key distinctive features.

Table 2.11 Comparison of technical differences between Calcein-AM[®] and PrestoBlue[®] fluorescent dyes

Characteristics	Calcein-AM [®]	PrestoBlue [®]
Assay type	Dye uptake, live assay + self-quenching	Resazurin based; live assay Colorimetric
Cell permeability	Cell-permanent	Cell-permanent
Incubation	1 hour	10 minutes- 2 hours
Sensitivity	Unreported	10-12 cells/well
Phenol red compatible	Affects assay sensitivity	Yes
Detection method	Absorbance/Fluorescence	Absorbance/Fluorescence
Excitation/Emission	485/520	535-560/590-615
Assay duration	Cell-dep. <2-4hrs	<72hrs

As demonstrated in the appendix section of this thesis, the accuracy of detection of cell populations less than 2.5×10^4 was better in the PrestoBlue[®] standard curves compared to those for Calcein-AM[®], at both 50,000 cells and 100,000 cells; with the co-efficient of determination (R²)

of 0.9993 and 0.9752 for PrestoBlue 50,000 and 100,000 cells respectively; against those attained with Calcein-AM[®]. Subsequent experiments were performed using PrestoBlue[®] to increase the validity of the results attained.

2.8 Drug treatments

2.8.1 3-D cultured MB treatments with recombinant Tissue inhibitors of matrix metalloproteinases (TIMPs) TIMP-1, TIMP-2 and Doxycycline

The recombinant TIMP-1 (Peprotech; 410-01) and TIMP-2 (Peprotech; 410-01) proteins were reconstituted to 10 μ M stock solutions in sterile cell-culture grade water and aliquots made and stored at -20°C as specified by Peprotech. The required volumes were then added to give final concentrations of 10nM, 25nM, 50nM and 100nM, used in the 3-D experiments.

Doxycycline a general metalloproteinase inhibitor, was obtained from Sigma (D9891). A fresh stock of 1mM concentration was made by dissolving the white powder in sterile cell-culture grade water to give a yellow-green solution, which was gently warmed for 5 minutes in a 37°C hot water bath and filtered. This solution was freshly prepared for each experiment.

As sterile cell-culture grade water was used for reconstitution of each of these MMP inhibitors, the same was used as the vehicle control in all experiments.

2.9 ¹⁹F-Magnetic Resonance Imaging of MMPs using an enzymatic degradable biosensor

The activatable enzymatic ¹⁹-fluorine MRI MMP biosensor used was locally synthesised through a collaboration between the Sir Peter Mansfield Imaging Centre and the Centre for Biomolecular Sciences at the School of Chemistry, University of Nottingham. It consists of a ¹⁹-fluorine (¹⁹F) moiety that is linked to a gadolinium III-DOTA complex by a substrate specific to MMP-2/MMP-9 (Faas, Krupa et al. 2019). Biological samples of column concentrated (X30) conditioned supernatant from HD-MB03, CHLA-01-MED and CHLA-01R-MED were separately tested by addition of 5µl of the samples to 600µl of the biosensor contained within 5mm nuclear magnetic resonance (NMR) tubes that were housed in a customised sample holder. 2D transverse gradient echo and ultra-short echo time sequences were performed using a Bruker Avance III 14.1 tesla spectrometer with an inner ¹⁹F coil, at room temperature and later at 37°C. Prior to testing the biological samples, they were stored at -80°C, transferred on dry ice to the scanner, and were slowly thawed immediately prior to the sample being added. Over the 18-hour experiment, spectroscopy demonstrated the initial peak of the biosensor at -64ppm. Once complete, results were analysed with the Igor Pro7 program. Prior to each experiment, the functional activities of the samples were confirmed in zymography and FRET experiments. Further details of the biosensor experiments are available in this recently published paper (Faas, Krupa et al. 2019).

2.10 Statistical analyses

GraphPad Prism 8 software (<https://www.graphpad.com/scientific-software/prism/>) was used to create, analyse and perform one-way ANOVA or paired t-test statistical analyses on all graphs where specified.

2.11 Fluorescence resonance energy transfer (FRET) assays

Fresh cell supernatants were firstly prepared by adding equal volumes from each cell line into Vivaspin (Vivaspin 20-50,000 MWCO, SLS VS2032) columns. These were centrifuged at 4000g for 40 minutes at 4°C. The EnzCheck™ Gelatinase/Collagenase Assay kit (ThermoFisher Scientific, E12055) was used for all experiments. 100µL of 1:2 dilutions of the resulting concentrates were added to the 80 µL of reaction buffer and 20 µL of fluorescence quenched (DQ) gelatin provided within the kit within a black-walled 96-well plate (Brandtech). Bottom reads on a FLUOstar Omega plate reader (BMG labtech) at absorption maxima~495nm and emission maxima ~515nm of fluorescence were recorded following digestion of the DQ gelatin over 24 hours and presented graphically using GraphPad Prism 8 software. 100µL of undiluted naïve CSF samples from patients 1-6 were examined in similar experiments.

Chapter 3.
**Biological characterisation of matrix
metalloproteinases in paediatric
medulloblastoma**

3.1 Chapter outline

Metastasis is recognised as the predominant cause of mortality in paediatric patients with medulloblastoma (MB). As it is detected at diagnosis in 30%-45% of paediatric patients, it is considered to be an early event in the disease progression (Juraschka and Taylor 2019, Menyhart, Giangaspero et al. 2019). While the emergence of biological heterogeneity within MB improved our understanding of the disease, it most importantly highlighted sub-group specific distinctions in their frequency of metastasis, their propensities for nodular or laminar metastasis, and anatomical sites of recurrence, whether local or distant to the primary tumour (Ramaswamy, Remke et al. 2013, Zapotocky M 2017)

Further compounding the problem, the current methods used to detect MB dissemination are suboptimal, with negative neuroaxial magnetic resonance imaging observed in 30-70% and negative cerebrospinal fluid cytology in up to 50% of patients with leptomeningeal disease, necessitating their combined application. Thus more quantitative and validated techniques that more accurately determine the metastatic status and treatment response in paediatric patients with medulloblastoma, pre-operatively and at surveillance, are essential to improving our provision of personalised therapy (Chamberlain, Soffiatti et al. 2014).

While the molecular subgroups remain unchanged at recurrence (Ramaswamy et al. 2013), a paucity in studies investigating recurrent disease due to limited surgical resection and liquid biopsies in the affected patient population, has led to the unfounded notion that primary and metastatic medulloblastoma are biologically similar. This has culminated in failed clinical trials, in which genes and proteins upregulated in the primary tumour are designated as therapeutic targets in metastatic disease and administered to these patients (Wu, Northcott et al. 2012).

The limited data from the few studies of matched primary and metastatic medulloblastoma tumours available, have highlighted that the latter are frequently derived from the clonal selection of populations of the primary tumour with certain metastatic virulence characteristics. Furthermore, their molecular, genetic and proteomic signatures are distinct, which could in part account for the poor treatment response in paediatric patients who present with disease recurrence, when therapies previously administered at diagnosis are given (Ramaswamy, Remke et al. 2013). Examples of these include transcriptional modifications in the TP53 gene and pathway, which are frequently observed between SHH primary and recurrent tumours, and enrichment in extracellular matrix associated gene sets in Group 4 recurrent tumours (Wu, Northcott et al. 2012).

3.2 Aims and hypotheses

As extracellular matrix gene sets were shown to be enriched in matched metastatic Group 4 MB tumours (Wu, Northcott et al. 2012), it was postulated that these genes would be a pragmatic starting point. It was hypothesised that the balance between the proteases and their respective inhibitors would best account for the differential metastatic potential between the primary and recurrent cell lines. Similarly, a matched pair of Group 3 cell lines were also compared due to their increased propensity to metastasise at an earlier stage from smaller primary tumours (Mata-Mbemba, Zapotocky et al. 2018). To this end, the aims of this chapter were as follows:

1. To elucidate the expression of biomarkers of increased metastatic potential, through protease and protease inhibitor microarray experiments, comparing conditioned supernatant samples from matched primary and recurrent medulloblastoma cell lines.
2. To investigate gene and protein expression of the identified differentially expressed candidate proteins using real time PCR and western blotting in a wider panel of cell lines. Levels and functional activity of secreted proteins will also be examined using ELISA and Gelatin Zymography respectively.

It was postulated that the levels of functional activity of the candidate proteases would be higher in metastatic and recurrent MB cell lines, and would therefore provide a valid, measurable molecular signature that could potentially be worthy of translation into the clinic and designated as a prognostic biomarker of metastasis in MB.

3.3 Elucidating protein biomarkers of metastasis in matched primary and recurrent MB cell lines

To elucidate potential prognostic biomarkers in metastatic medulloblastoma, the relative expression levels of protease and protease inhibitors (R&D systems) were detected from conditioned supernatant from matched primary and metastatic MB cell lines. 5×10^6 cells of the primary Group 3 cell line, D425-MED and its metastatic counterpart D458-MED and the same number of the matched primary and metastatic Group 4 cell lines CHLA-01-MED and CHLA-01R-MED respectively, were cultured in their usual growth medium in 5% CO₂ at 37°C for 48 hours. The resulting cell suspensions were twice centrifuged at 100g for 7 minutes, to obtain cell free supernatant and hence reduce the potential for inadvertent cellular protein detection. The analytes that were notably differentially expressed between matched cell lines are shown in Table 3.1 and Table 3.2. An image of the Proteome Profiler Array obtained for the Group 3 matched pair are shown (Figure 3.1).

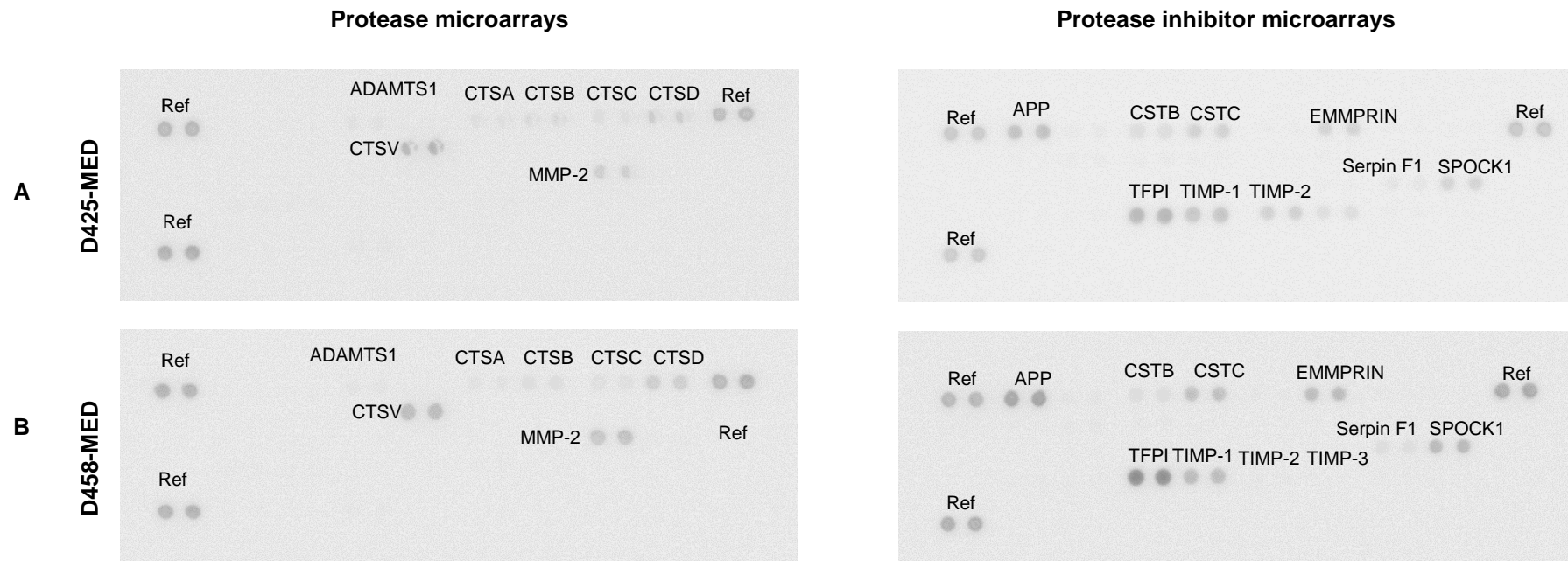


Figure 3.1 Protease and protease inhibitor microarrays of conditioned supernatant following 48hrs of culture of the matched Group 3 medulloblastoma **A. primary (D425-Med)** and **B. metastatic (D458-Med)** cell lines. The cell lines were cultured in the same media and experiments performed simultaneously. An overlay provided within the protease and protease inhibitor array kit (R&D systems) was used to locate the analytes as shown following 15 minutes of chemiluminescence exposure. The signal intensity of each analyte was normalised to the reference (ref) intensities on the respective membrane and their densitometry determined using a microarray plugin from image J software.

3.3.1 Differentially expressed analytes in matched primary (D425-Med) and metastatic (D458-Med) Group 3 cell lines

All membranes were exposed to chemiluminescence for a period of 15 minutes. Each analyte signal was quantified using a protein array analyser macro from image J software and the resulting densitometry (see appendix) determined relative to internal reference controls allowing analytes that were notably differentially expressed between matched cell lines to be identified (Table 3.1 and Table 3.2).

Table 3.1 Differentially expressed proteases in matched Group 3 primary (D425-Med) and metastatic (D458-Med) medulloblastoma cell lines.

Proteases	D425-Med (Primary)	D458-Med (Metastatic)	% Increase in D458-Med
Cathepsin B	0.153	0.159	3.73
Cathepsin D	0.286	0.394	27.3
Cathepsin V	0.607	0.763	20.5
Kallikrein 5	0.001	0.021	95.0
MMP-2	0.255	0.592	56.9
MMP-3	0.010	0.027	62.9

As shown in Table 3.1, Kallikrein 5 (KLK5) was the most highly upregulated protease in the metastatic Group 3 cell line in comparison to its primary counterpart. Kallikreins are serine proteases that are involved in modulating the extracellular matrix. Their overexpression has been

correlated to poorer outcomes in lung, pancreatic and head and neck squamous cell cancers. Interestingly, upregulated KLK5 expression as seen in the Group 3 metastatic cell line, has been correlated with increased mortality in urothelial bladder carcinoma (Tailor, Kodeboyina et al. 2018) and worse patient outcomes in ovarian cancer (Borgono and Diamandis 2004).

MMP-2 and MMP-3 expression was increased by 56.9% and 62.9% respectively, in the Group 3 metastatic cell line D458-Med. Both matrix metalloproteinases have been implicated in multiple hallmarks of metastasis, including tissue invasion, intravasation and preparation of the metastatic niche (Kessenbrock, Plaks et al. 2010).

The metastatic Group 3 cell line D458-Med also demonstrated increased expression of the cysteine proteases, cathepsins B, D and V as shown in Table 3.1. When activated, these proteases remodel the extracellular matrix, releasing chemokines that promote migration and invasion of tumour cells. Cathepsin B in particular has been shown to degrade the endogenous tissue inhibitors of metalloproteinases (TIMPs), resulting in increased MMP activity independent of levels of MMP expression (Olson and Joyce 2015).

While the profile of protease expression between the matched Group 3 cell lines were within similar ranges, the expression levels of protease inhibitors in the metastatic Group 3 cell line D458-Med, was significantly

lower than those observed in its primary counterpart. The most significant changes are shown in Table 3.2 as fold decreases from the expression levels detected in the supernatant of the primary Group 3 cell line D425-Med.

Table 3.2 Differentially expressed protease inhibitors in matched Group 3 primary (D425-Med) and metastatic (D458-Med) medulloblastoma cell lines.

Protease inhibitors	D425-Med (Primary)	D458-Med (Metastatic)	Fold decrease in D458-Med
APP	1.09	1.15E-04	9554
Cystatin A	0.081	3.31E-06	24308
Cystatin B	0.467	1.45E-05	32219
Cystatin C/3	0.633	5.86E-05	10796
Cystatin E/M/6	0.035	4.90E-07	71578
EMMPRIN/CD147	0.667	6.14E-05	10861
Serpin F1	0.165	1.10E-05	14986
SPOCK 1	0.516	5.65E-05	9137
TFPI-2	1.69	6.30E-05	26810
TIMP-1	0.818	3.05E-05	26805
TIMP-2	0.525	3.83E-07	1372159

Being the endogenous inhibitors of cysteine proteases-cathepsins, the downregulation of cystatins A, B, C and E occurs in the metastatic Group 3 cell line (Table 3.2,

Figure 3.2), resulting in unchecked cathepsin activity. SPOCK1 is an isoform of the SPARC (secreted protein acidic and rich in cysteine) protein family that has been shown to be upregulated in cancers where it promotes proliferation, metastasis and invasion. However, as seen in Table 3.2, it is downregulated in the metastatic Group 3 cell line, D-458-Med, a common finding in brain tumours. This conundrum is in part postulated to be dependent on their concentrations which determine whether their overall effects are pro-metastatic and anti-migratory (Gerarduzzi, Hartmann et al. 2020).

Meanwhile, TFPI-2 (tissue factor pathway inhibitor 2) is a protein that inhibits tissue factor, plasmin and kallikreins all of which when inhibited, result in the downregulation of activated MMP-2 protein levels. It is therefore unsurprising that its secreted levels are much higher in the primary Group 3 cell line D425-Med in comparison to the metastatic line D458-Med (Table 3.2, Figure 3.2).

Significant downregulation of the tissue inhibitors of metalloproteinases (TIMPs) -1, -2 and -3 is also observed in the metastatic cell line D458-Med (Figure 3.2), suggesting a pro-metastatic niche in its secretome, as a result of the unopposed actions of the upregulated MMPs and other proteases aforementioned.

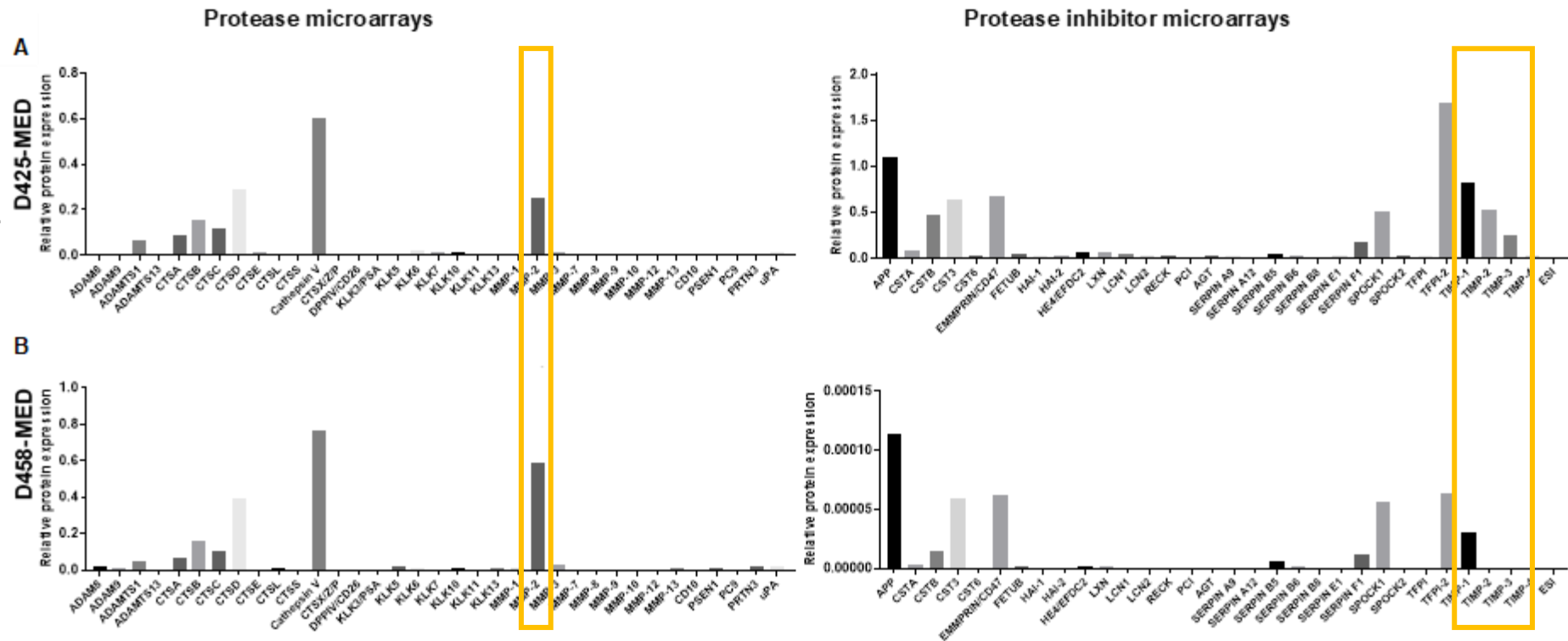


Figure 3.2 Densitometry of protease and protease inhibitor microarrays of the matched Group 3 medulloblastoma A. primary (D425-Med) and B. metastatic (D458-Med) cell lines. Analytes were quantified using an Image J plugin. While their levels of protease expression were comparable, the metastatic cell line secreted significantly less protease inhibitors resulting in disproportionate protease activity. Surprisingly, no detectable MMP-9 signal was observed in this screening experiment.

3.3.2 Differentially expressed analytes in matched primary (CHLA-01-Med) and recurrent (CHLA-01R-Med) Group 4 cell lines

An image of the Proteome Profiler Array obtained for the Group 4 matched pair is shown in Figure 3.3. Each signal was then quantified using a protein array analyser macro from image J software and the resulting densitometry determined relative to internal reference controls allowing analytes that were notably differentially expressed between matched cell lines to be identified.

In comparison to the expression profile of proteases and protease inhibitors in the matched Group 3 cell lines, more differentially expressed analytes were detected in the matched Group 4 pair. As demonstrated in Table 3. 3 and Figure 3.4, the kallikreins and matrix metalloproteinases were the most upregulated proteases in the recurrent Group 4 cell line CHLA-01R-Med compared to its primary counterpart. CHLA-01R-Med also depicted increased MMP-1 and MMP-2 expression by 90.7% and 97.3% respectively from the levels detected in the primary Group 4 cell line, as well as upregulated levels of more MMPs (-3,-7, -8, -10 and -12) compared to the Group 3 metastatic cell line D458-Med, in which MMP-2 was upregulated by 56.9%. This suggests that MMPs could play a more pivotal role in progression in Group 4 medulloblastoma in comparison to Group 3 MBs.

The Group 4 metastatic cell line also exhibited higher levels of kallikreins (KLKs) which have been reported to digest plasminogen to plasmin (Dong, Loessner et al. 2014), one of the key activators of pro-MMP-2. CHLA-01R-MED demonstrated 4-29X higher levels of kallikreins -6, -7 and -10 compared to its primary counterpart. In addition, cathepsins B and C were also overexpressed in the metastatic line CHLA-01-R-Med by 78.9% and 54% respectively.

The most striking decrease in the levels of protease inhibitors secreted in the metastatic compared to its primary counterpart, were the tissue inhibitors of metalloproteinase 1 (TIMP-1) with almost no TIMP-1 detected in the metastatic cell line (Table 3.4, Figure 3.4). Additionally, SPOCK2 expression was downregulated to a similar degree as were cystatin D (CST6) and B (CSTB).

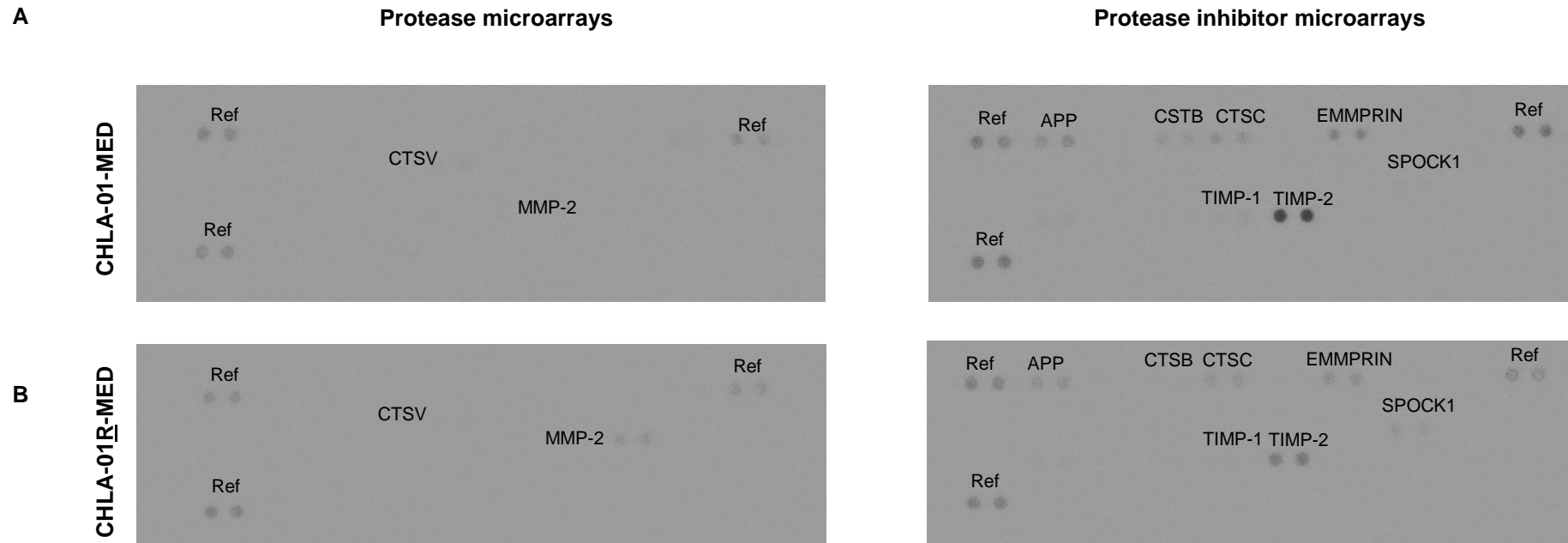


Figure 3.3 Protease and protease inhibitor microarrays of conditioned supernatant following 48hrs of culture of the Group 4 medulloblastoma primary **A. (CHLA-01-Med)** and metastatic **B. (CHLA-01R-Med)** cell lines. The cell lines were cultured in the same serum-free media and experiments performed simultaneously. The intensity of each dot was normalised to the reference (ref) dots on the respective membranes and their intensity was determined using a microarray plugin from image J software. An overlay provided within the protease and protease inhibitor array kit (R&D systems) was then used to locate the analytes as shown.

Table 3. 3 Differentially expressed proteases in matched Group 4 primary (CHLA-01-Med) and recurrent (CHLA-01R-Med) medulloblastoma cell lines.

Proteases	CHLA-01-Med (Primary)	CHLA-01R-Med (Metastatic)	% Increase in CHLA-01-Med
Cathepsin B	0.007	0.034	78.9
Cathepsin C	0.016	0.034	54.0
Cathepsin S	0.034	0.072	52.9
Cathepsin V	0.059	0.084	30.2
Kallikrein 5	0.015	0.039	62.5
Kallikrein 7	0.021	0.096	78.4
Kallikrein 10	0.015	0.118	87.7
Kallikrein 11	0.004	0.109	96.0
Kallikrein 13	0.003	0.085	96.6
MMP-1	0.015	0.157	90.7
MMP-2	0.014	0.516	97.3
MMP-3	0.016	0.119	86.6
MMP-7	0.003	0.016	81.8
MMP-8	0.009	0.019	55.0
MMP-10	0.016	0.027	42.4
MMP-12	0.021	0.052	58.7

As shown in Table 3.4, the group 4 pair demonstrated decreased levels of Serpins A9, A12, B5, B6 B8 and E1 in the recurrent cell line, CHLA-01R-MED. Recognised to inhibit angiogenesis, the reduced expression of these protease inhibitors would likely promote unregulated angiogenesis in the metastatic Group 4 cell line.

Table 3.4 Differentially expressed protease inhibitors in matched Group 4 primary (CHLA-01-Med) and recurrent (CHLA-01R-Med) medulloblastoma cell lines.

Protease inhibitors	CHLA-01-Med (Primary)	CHLA-01R-Med (Metastatic)	Fold Decrease in CHLA-01R-Med
CSTA	0.025	0.007	3.77
CSTB	0.168	0.012	13.6
CST6	0.029	0.000	0.029
EMMPRIN/CD147	0.545	0.515	1.06
Serpin A9	0.066	0.024	2.69
Serpin A12	0.064	0.028	2.29
Serpin B5	0.070	0.022	3.10
Serpin B6	0.070	0.037	1.90
Serpin B8	0.097	0.035	2.79
Serpin E1	0.057	0.036	1.57
SPOCK 1	0.056	0.025	2.25
SPOCK 2	0.055	0.000	0.055
TIMP-1	0.077	0.000	0.077
TIMP-2	2.422	1.442	1.68

Having been shown to correlate with aggressiveness, higher grade and poor patient outcome in multiple solid cancers (Isaacson, Jensen et al. 2017), it was hypothesised that matrix metalloproteinases (MMPs), a large proportion of the proteases involved in modulation of the tumour microenvironment, would be upregulated in the metastatic compared to the primary MB cell lines. As they have been widely demonstrated to be instrumental in metastasis, MMP-2 and MMP-9 were thought to be the most likely of the extracellular proteases, to be amplified in the metastatic/recurrent MB counterparts (Isaacson, Jensen et al. 2017)

Homeostasis of the tumour microenvironment is a complex and dynamic landscape in which matricellular proteins such as matrix metalloproteinases, released into the extracellular matrix may not be as strictly controlled as in physiological conditions. As alluded to earlier, the very concentrations and co-localisations of these matricellular proteins may determine their context specific effects. To complicate issues further, the pathways of expression or upregulation of pro-metastatic factors may also activate pathways with opposing effects. Thus, it would be presumptuous to conclude that increased secretion of matrix metalloproteinases would be the sole mechanism that results in the increased metastatic potential in the recurrent Group 3 and 4 cell lines.

Therefore, to gain a comprehensive understanding of the landscape of metalloproteinases and their inhibitors in promoting metastasis in medulloblastoma, their multi-level regulation at the gene and protein

expression, as well as functional activity was investigated, to determine the point of upregulation in the metastatic cell lines.

3.4 MMP-2 gene expression in medulloblastoma cell lines

To investigate the gene expression of MMP-2 in a panel of 9 sub-grouped medulloblastoma cell lines, real time PCR experiments using SYBR green I were performed and results normalised to their relative expression of GAPDH, to enable comparison of MMP-2 gene expression between the different MB cell lines.

As shown in Figure 3.5, MMP-2 gene expression varied between and within the subgroups. While the highest MMP-2 gene expression was observed in the most aggressive cell lines within each subgroup, HD-MB03 in Group 3, DAOY and ONS in SHH and CHLA-01R-Med in Group 4, there was a statistically significant increase in MMP-2 gene expression in the metastatic Group 4 cell line, CHLA-01R-Med, compared to its primary counterpart ($p=0.0215$). The low levels of MMP-2 gene expression in the metastatic Group 3 cell lines, D458-Med and D283 was unexpected, but could be in part due to their extraneural origins.

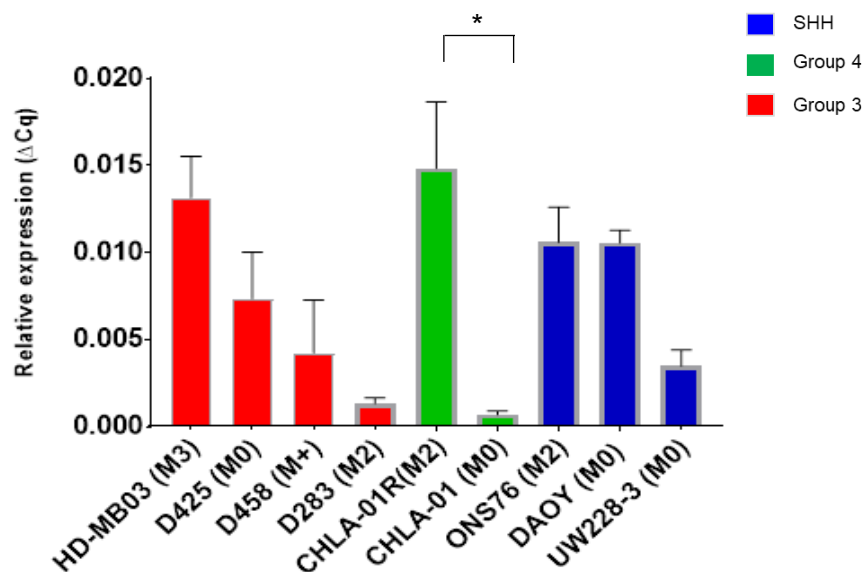


Figure 3.5 MMP-2 gene expression by qRT-PCR of 9 sub-grouped medulloblastoma cell lines. For each cell line, the mean of the quantitation cycles of MMP-2 expression was normalised to that of GAPDH expression and analysed using Graphpad prism. *indicates the statistically significant difference in the gene expression of MMP-2 between the primary and recurrent Group 4 cell lines. (ANOVA; $p=0.0215$) Error bars represent SD.

3.5 MMP-9 gene expression in medulloblastoma cell lines

While the multilevel regulation of MMP-9 was attempted, the MMP-9 gene expression in the MB cell lines could not be determined due to multiple failed primers, substantial equipment problems and time constrains.

3.6 MMP-2 protein expression in medulloblastoma cell lines

To determine the baseline differential MMP-2 protein expression in isogenic primary and medulloblastoma cell lines, protein extraction was performed from the same cell pellets used in the MMP-2 gene expression experiments. Equal amounts of protein were examined using western blotting as described in detail in the methodology section of this thesis. Image J densitometry was performed on the resulting chemiluminescent images to quantify the differential levels of MMP-2 protein expressed by each cell line.

As shown in Figure 3.6, the protein expression in the control neural stem cell line H1-NSC was present but at very low levels, supporting the hypothesis that MMP-2 is constitutively expressed. Though the differential MMP-2 protein expression between the paired Group 3 cell lines D425-Med (M0) and D458-Med (M+) as well as the paired Group 4 cell lines CHLA-01-Med (M0) and CHLA-01R-Med (M2) did not reach statistical significance, the metastatic cell lines expressed considerably more MMP-2 protein. This result was in contrast to the pattern of gene expression in the Group 3 pair, where the primary cell line D425-Med exhibited higher MMP-2 gene expression than its metastatic counterpart. The highest MMP-2 protein expression was observed in the metastatic ONS-76 (*wt p53*) cell line, in stark contrast to the ONS-76 *dnp53*, in which the p53 gene was knocked down.

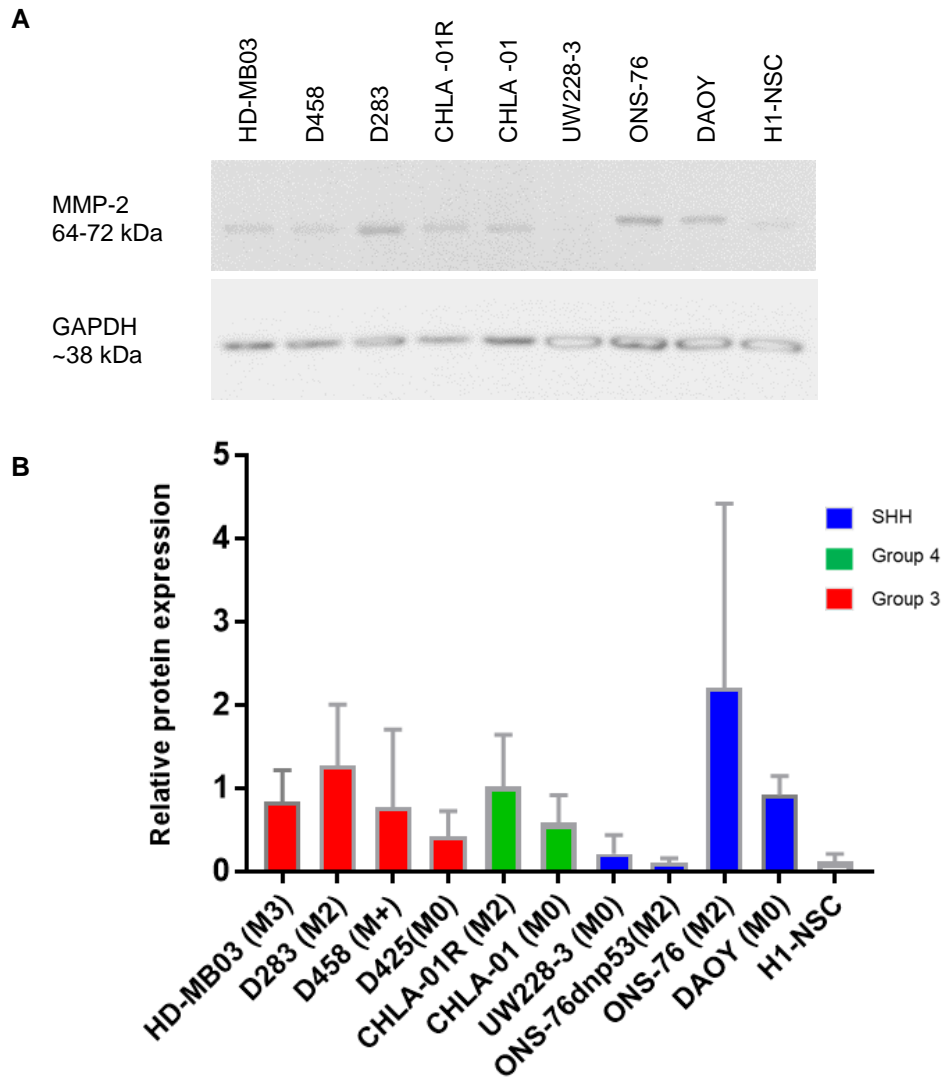


Figure 3.6 MMP-2 protein expression by Western blotting of cell lysates from 10 sub-grouped medulloblastoma cell lines (n=5). **A.** Representative western blot of 8 MB cell lines alongside a foetal stem cell control H1-NSC. **B.** MMP-2 protein expression was normalised to expression of the housekeeping protein, GAPDH and plotted in Graphpad prism as shown above. Error bars indicated standard deviations from the mean (SD).

This suggests that an intact tumour suppressor p53 gene may be essential to the gene transcription and therefore protein expression of MMP-2. This is supported by the finding that the MMP-2 promoter inhabits a binding site for TP53 (Bian and Sun 1997).

Having determined the relative protein expression between the MB cell lines, their levels of secreted MMP-2 protein into conditioned media was investigated. Briefly, supernatant from 5×10^6 cells of 6 MB cell lines was harvested following 48 hours of incubation in their respective optimal culture medium in 5% CO₂, 37°C. After centrifugation at 100g for 7 minutes, the supernatant samples were snap frozen, stored at -80 °C and slowly de-frosted on ice immediately prior to the experiment. The Quantikine ELISA Total MMP-2 immunoassay kit from R&D systems (cat. MMP200) was used to quantify the levels of total MMP-2 protein detectable within each cell line's conditioned medium.

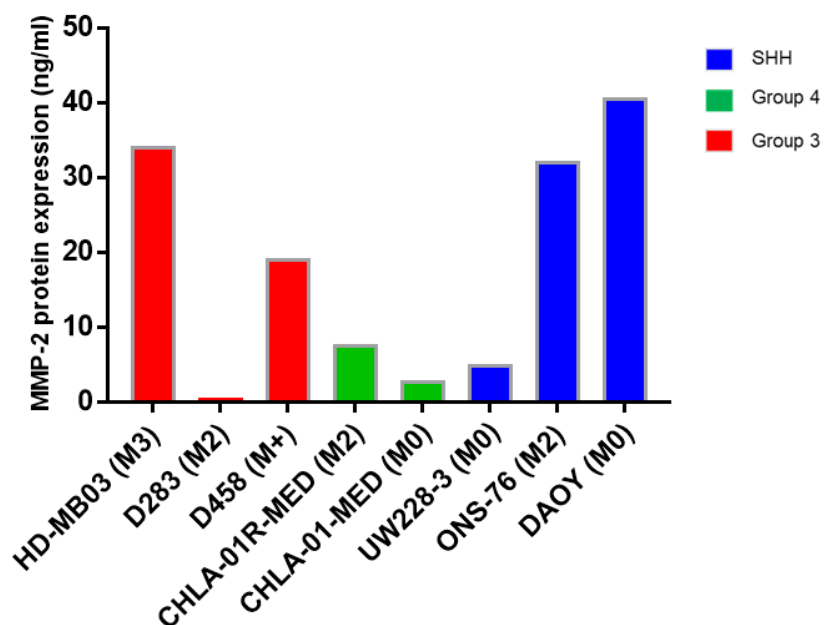


Figure 3.7 Levels of secreted MMP-2 protein as detected with the total MMP-2 Quantikine ELISA immunoassay (R&Dsystems). Screening ELISA experiments were performed to determine whether the MB cell lines secreted differential levels of MMP-2 into their conditioned medium, following a 48 hour incubation in 37°C and 5% CO₂ conditions. The resulting protein levels were compared to MMP-2 standards ranging from 0.5ng/mL to 32ng/mL of MMP-2 protein and quantified using a microplate reader.

As shown in Figure 3.7, the levels of secreted MMP-2 protein follow a similar pattern as that observed for gene expression of the same MB cell lines (see Figure 3.5). Notably, the Group 4 metastatic cell line CHLA-01R-Med appeared to secrete 2.7 times more MMP-2 protein compared to the primary CHLA-01-Med. However, as these experiments were not repeated, this data supported the likelihood that the levels of MMP-2 protein secreted by each MB cell line might be detectable using Gelatin Zymography.

To determine the best storage conditions for the supernatant and later, patient cerebrospinal fluid that would maximise the functional activity of the MMP-2 and MMP-9 therein, ELISA experiments were performed on supernatants harvested from the Group 4 paired cell lines that were stored at 4°C for 7-day intervals. As shown in

Figure 3.8, levels of MMP-2 protein secretion from the metastatic group 4 cell line CHLA-01R-Med, decreased in a stepwise manner over the 2-week period, but at all times, secreted between 5-10 times the amount of MMP-2 protein detected in its primary counterpart.

Following this experiment, supernatant and patient cerebrospinal fluid destined for zymography experiments were snap frozen in liquid nitrogen, stored at -80°C and thawed on ice immediately prior to experimentation, to maximise the functional activity of the MMP-2 and MMP-9 within the samples.

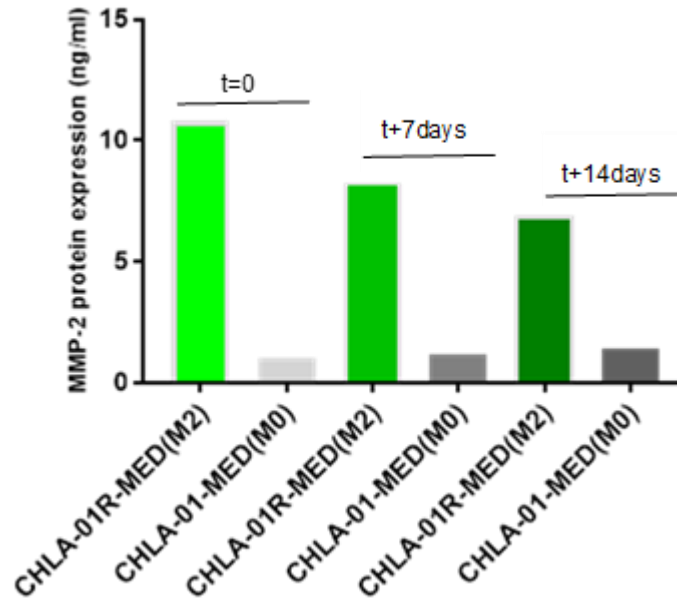


Figure 3.8 Levels of secreted MMP-2 protein as detected with the total MMP-2 Quantikine ELISA immunoassay (R&Dsystems). Screening ELISA experiments were performed to determine whether the paired Group 4 MB cell lines secreted differential levels of MMP-2 into their conditioned medium, following a 48hour incubation in 37°C and 5% CO₂ conditions. The resulting protein levels were compared to MMP-2 standards ranging from 0.5ng/mL to 32ng/mL of MMP-2 protein and quantified using a microplate reader, in a similar manner as the prior experiment.

3.6 MMP-9 protein expression in medulloblastoma cell lines

MMP-9 has been shown to play a substantial role in multiple facets of the metastatic process including angiogenesis by catalysing the release of vascular endothelial growth factor (VEGF) from the extracellular matrix, as well as priming the metastatic niche by activating cancer associated immune cells and astrocytes to release pro-metastatic factors that further modulate the tumour microenvironment (Shimoda and Khokha 2017, Cacho-Diaz, Garcia-Botello et al. 2020).

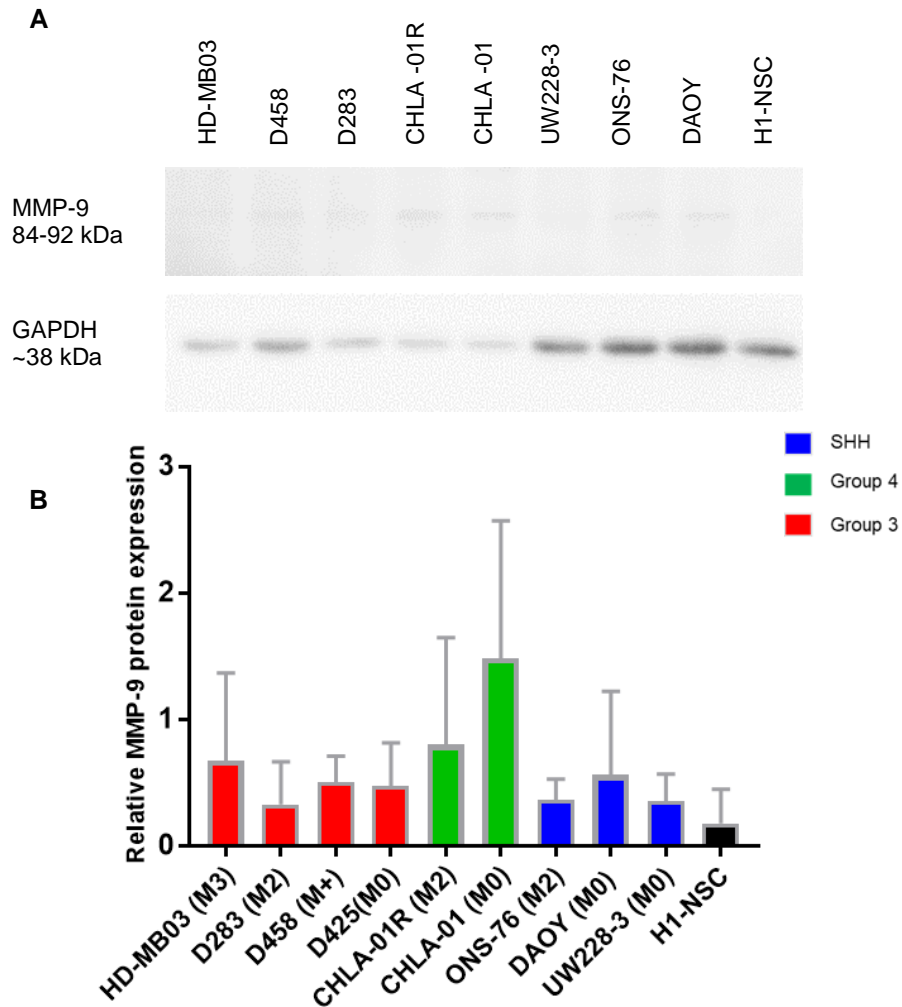


Figure 3.9 MMP-9 protein expression by Western blotting of nine sub-grouped 2-D cultured medulloblastoma cell lines alongside a control cell line (H1-NSC). A. Representative western blot of (n=4) MMP-9 and GAPDH (housekeeping protein) expression in MB. **B.** Image J densitometry of MMP-9 protein expression normalised to expression of the housekeeper, GAPDH and plotted in GraphPad prism as shown above.

As one of the most commonly implicated MMPs in metastatic tumours including medulloblastoma, it was felt that a further look at the protein expression of MMP-9 in MB would be worthwhile, in spite of their low expression at the genetic level. This was determined by performing western blotting experiments in the same manner as was described for

MMP-2. The main differences were that the concentration of the MMP-9 primary antibody (Cell Signalling #13667) used was 1:500 diluted in 5% BSA, twice that of MMP-2. In addition, ECL signal fire elite (Cell signalling, 12757P) a stronger chemiluminescence imaging solution, was used to maximise the signal intensity obtained.

MMP-9 protein expression varied between the medulloblastoma cell lines with considerable variation within the replicates of the sample. This was postulated to be as a result of the low overall protein expression of MMP-9 in MB in comparison to their MMP-2 protein expression. As primary cell lines appeared to express similar MMP-9 protein to their metastatic counterparts, it seemed unlikely that MMP-9 protein expression could serve as a robust biomarker of metastasis.

While perturbing the gene and protein expression of MMP-2 and MMP-9 in the primary and metastatic medulloblastoma cell lines suggested that MMP-2 may serve as a robust biomarker at protein levels in matched recurrent cell lines, their secretion into the tumour microenvironment represented by their conditioned supernatant, was thought to be the most physiologically relevant. This is because of the observation that the specific biological roles played by MMPs is determined by their localisation (Kessenbrock, Plaks et al. 2010). This enables their strict homeostasis in a vast array of physiological and pathological states including carcinogenesis and metastasis. Thus in their roles as modulators of the microenvironment, the levels of functionally active

MMP-2 and MMP-9 secreted into the MB cell supernatants were examined using gelatin zymography.

3.7 Gelatin zymography for the detection of functionally active MMP-2 and MMP-9 in medulloblastoma cell lines

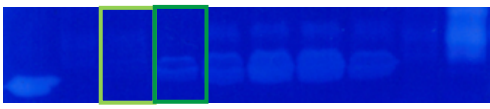
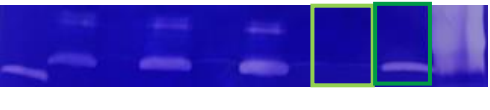
While MMP-2 and MMP-9 are regulated at multiple levels, a key determinant of specific role is dependent upon their localisation within the intracellular or extracellular compartments. This enables their wide range of functions including extracellular matrix remodelling, lysosomal digestion of microbes and preparation of the metastatic niche. In these different contexts, their effects can vary based on their cellular source i.e. tumour cells, endothelial cells, tumour-associated immune cells or astrocytes for example, as well as the physiological or pathological situation (Kessenbrock, Plaks et al. 2010). While majority of MMPs are secreted, some such as MMP-2 are both membrane-bound and secreted within exosomes which are nanometre-sized, membrane-bound vesicles that are thought to be involved in autocrine and paracrine signalling between tumour cells, their cellular microenvironment and their distant pre-metastatic niche (Shay, Lynch et al. 2015). As such, investigating the levels of functionally active, secreted MMP-2 and MMP-9 in the supernatants of the MB cell lines, may provide a pertinent indicator of their metastatic potential.

Gelatin zymography is a gel electrophoresis technique in which the levels of the zymogens and their active forms can be detected by their enzymatic digestion of gelatin incorporated into the gel. Having not previously been performed in our lab, optimisation of the technique for the detection of pro- and active MMP-2 and MMP-9 in the MB cell line supernatants was necessary.

3.7.1 Optimisation of Gelatin Zymography

With the exception of the 10X zymography development buffer (Biorad, 1610766), all other material were made up in the lab. **Table 3.5** shows the steps taken in the optimisation of this technique. Annotations of the reasons resulting in experimental technical failure and the resolutions at each stage were annotated alongside each zymogram. As shown in **Table 3.5** zymograms A and B were the first two unsuccessful experiments with no detectable evidence of functional MMP2 or MMP9 activity despite using concentrated FBS, a well-established, strongly positive control. This technical challenge was addressed by re-constituting the assay buffers according to the aforementioned instructions in the methods and storing the gel buffers at 4°C. With slight modifications to the order in which the reagents were incorporated into the Gelatin-SDS-PAGE mixture, positive results were obtained as shown in zymograms C through F.

Table 3.5 Gelatin zymography optimisation experiments

Zymogram	Altered experimental conditions	Main result
<p>A</p> <p style="text-align: right;">FBS</p> 	<p>Gel thickness: 1.5 mm Volume of sample loaded: 20 µL Staining time: 1 hour De-staining time: 1 hour</p>	<p>Technical failure</p>
<p>B</p> <p style="text-align: right;">FBS</p> 	<p>Gel thickness: 1.5 mm Volume of sample loaded: 20 µL Staining time: 1 hour De-staining time: 2 hours</p>	<p>Technical failure</p>
<p>C</p> <p style="text-align: right;">FBS</p> 	<p>Gel thickness: 0.75 mm Volume of sample loaded: 20 µL Staining time: 30 mins De-staining time: 45 mins</p>	<p>Successful but overflow of FBS into other adjacent wells</p>
<p>D</p> <p style="text-align: right;">FBS</p> 	<p>Gel thickness: 0.75 mm Volume of sample loaded: 20 µL Staining time: 30 mins De-staining time: 45 mins</p>	<p>Successful but contamination of FBS into other adjacent wells. This was the first experiment in which supernatant from the matched primary CHLA-01-Med (lime green) and metastatic (dark green) cell lines were loaded.</p>
<p>E</p> <p>MMP-2 MMP-9</p> 	<p>Gel thickness: 1.0 mm Volume of sample loaded: 40 µL Staining time: 30 mins De-staining time: 45 mins</p>	<p>Successful, clear lane separation of different loaded samples with introduction of Hamilton pipette for more accurate loading of gel</p>
<p>F</p> <p>MMP-2 MMP-9</p> 	<p>Gel thickness: 1.0 mm Volume of sample loaded: 40 µL Staining time: 15 mins De-staining time: 90 mins</p>	<p>Successful with better contrast between digested gelatin and Coomassie blue-stained background</p>

The cosmetic appearances of the zymograms was improved by incubating the gels for a shorter period of 15 minutes in the 0.5% coomassie blue staining solution (zymograms E and F) and longer incubation in the de-staining solution. This was postulated to be due to the binding affinity of the freshly made staining solution. In addition, the accuracy of loading conferred by using a Hamilton pipette (Hamilton, 80600) instead of using the standard pipettes was greatly enhanced as the slim needle easily accessed the bottoms of the wells within the 1mm/0.75mm gels, in comparison to the standard pipette tips with a considerably larger diameter.

The optimal gel thickness of 1mm allowed for easier manipulation compared to the 0.75mm gels which were fragile, especially on handling and transfer between the various buffers. When compared to the 1.5mm gel spacers commonly used in Western Blotting, poor penetration of the renaturing and developing buffer due to the thicker gel may have prevented the activation of MMP-2 and MMP-9 proteins expressed by the cell supernatants in these particular gels.

3.7.2 Gelatin zymography detection of pro- and active-MMP-2 and MMP 9 from medulloblastoma cell lines

5×10^6 cells of each cell line were cultured in their optimal media and incubated for 48 hours in 5% CO₂ at 37°C. Following cell dissociation of the adherent and semi-adherent cell lines, the cell suspensions were

twice centrifuged at 100g for 7 minutes to obtain cell-free supernatant. These samples were either snap frozen and stored at -80 °C or used immediately in zymography experiments. A key important difference between zymography and western blotting is that the samples in the former are not denatured to enable their enzymatic functions by preserving their 3-dimensional structures. After gel electrophoresis of the loaded samples, the gels were incubated in renaturing buffer on a rocker for 1 hour at room temperature, before incubation in zymogram developing buffer (Biorad, 1610766) overnight. After washing the gels in dH₂O, they were stained in a 0.5% coomassie blue solution for 15 minutes and de-stained for 2 hours. Zymograms were photographed and quantified using Image J densitometry.

As shown in Figure 3.10, the highest levels of MMP-2 were seen in the metastatic cell lines with the exception of D283. Within each subgroup, the cell lines with the highest metastatic status secreted the highest levels of functionally active MMP-2. While the difference in active MMP-2 detected in the Group 3 matched pair (primary D425-Med and metastatic D458-Med cell lines) was not statistically significant, the difference between the levels detected in the Group 4 matched pair, CHLA-01-Med (primary) and CHLA-01R-Med (metastatic) cell achieved statistical significance ($p=0.022$).

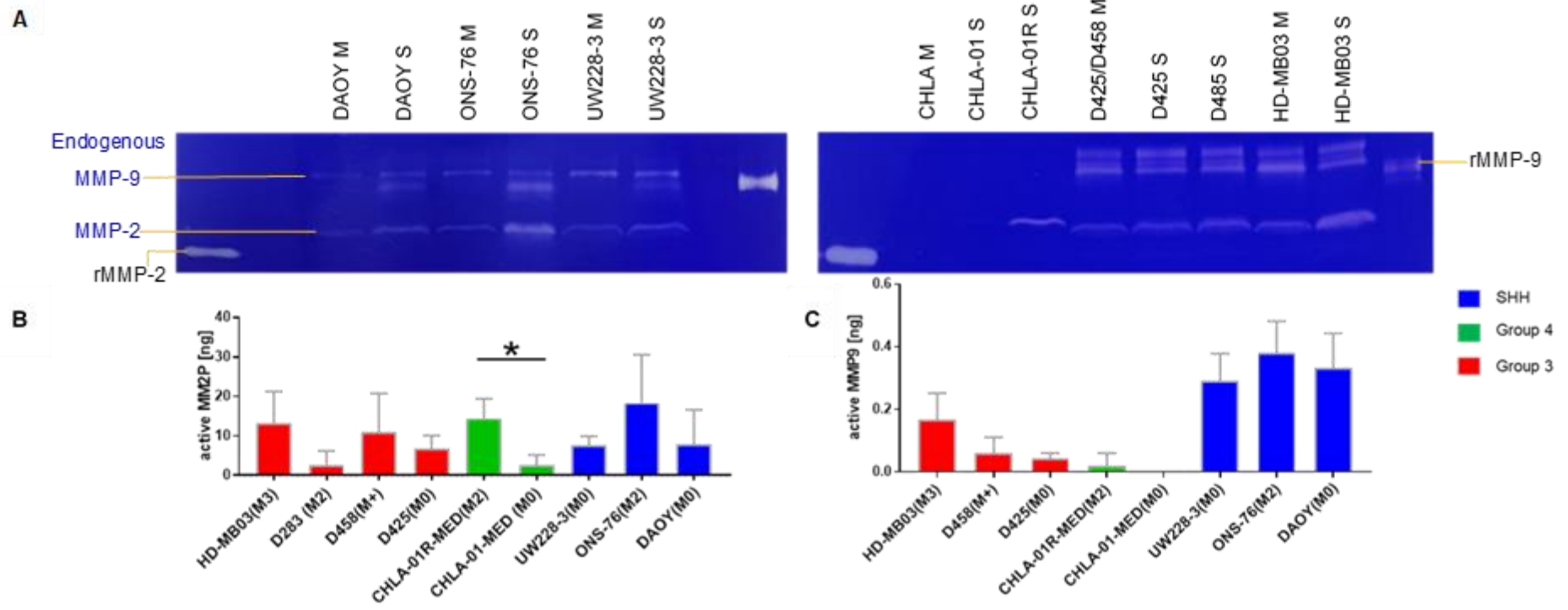


Figure 3.10 Gelatin zymography of supernatant from a panel of 9 medulloblastoma sub-grouped cell lines **A**. Representative zymograms showing endogenous MMP-2 and MMP-9 signals alongside equal volumes of their respective media controls. Image J densitometry was performed to determine the differential levels of functionally active MMP-2 (**B**) and MMP-9 (**C**) signal compared to that derived from known concentrations of the recombinant MMP proteins. (* ANOVA; $p=0.022$)

In keeping with the low levels of MMP-9 expression observed at both gene and protein levels, the levels of functionally active MMP-9 secreted by the medulloblastoma cell lines 100 times less than the levels of MMP-2. As depicted in Figure 3.10 the highest levels of functionally active MMP-9 were observed in the SHH cell lines, in contrast to the pattern seen in the protein expression from the same lines. In addition, while the matched Group 4 cell lines CHLA-01-Med (M0) and CHLA-01R-Med expressed comparable levels of MMP-9 to those seen in HD-MB03, their levels of secreted MMP-9 were significantly low and undetectable in the primary cell line.

These results suggest that functionally active MMP-2 is secreted by all medulloblastoma cell lines and is present at much higher levels in the extracellular compartment in comparison to levels of active MMP-9. These results suggest that functionally active MMP-2 may be the most clinically relevant biomarker in predicting the metastatic potential of medulloblastoma. As both are detectable using gelatin zymography, this technique was taken forward for the determination of whether levels of functionally active MMP-2 in cerebrospinal fluid from paediatric patients with MB, would best correlate with their tumours' metastatic potential.

Summary

- ❖ Screening protease and protease inhibitor microarray experiments used to elucidate potential biomarkers of increased metastatic potential in medulloblastoma cell lines, revealed an imbalance in the secretion of proteases in the primary Group 3 (D425-Med) and Group 4 (CHLA-01-MED) cell lines in comparison to the scarcity of protease inhibitors in their respective metastatic counterparts. This likely results in a tumour microenvironment that is more conducive to migrating metastasizing tumour cells.
- ❖ The most striking differences involved the levels of MMP-2 secreted by the recurrent cell lines, thus further determination of its potential as a valid and robust prognostic biomarker was performed. While the secretion levels of MMP-9 were less dramatic, it is well-documented to be highly expressed at the invasive margins of solid tumours as well as play a synergistic role with MMP-2. We therefore proceeded to focus on these proteases.
- ❖ At the level of gene expression, MMP-2 was expressed at higher levels in the metastatic MB cell lines, especially in the Group 4 recurrent cell line CHLA-01R-MED in comparison to its primary counterpart. The pattern of MMP-9 expression appeared more

complicated, likely due to the low expression levels in MB cell lines.

- ❖ Given its enzymatic functions, ELISA experiments were performed to determine the optimal storage and handling of the supernatant samples from the MB cell lines and patient cerebrospinal fluid. A stepwise reduction in the MMP-2 protein was detected by ELISA in the matched Group 4 MB cell lines, emphasizing the importance of storage of the samples at -80°C.
- ❖ The levels of functional activity as determined using gelatin zymography further confirmed the higher levels of functionally active MMP-2 in the recurrent Group 4 cell line (CHLA-01R-MED) compared to the primary, while similar levels of MMP-2 and MMP-9 were observed in the Group 3 matched pair. The highest levels of MMP-9 were secreted by the most aggressive group 3 cell line and the SHH cell lines, suggesting subgroup specific differences in the multi-level regulation of MMP-2 and MMP-9.

Chapter 4

Functional characterisation of matrix metalloproteinases in 3-D models of medulloblastoma

4.1 Chapter outline

Though metastasis has remained the leading cause of mortality and morbidity in paediatric patients with medulloblastoma (MB), its precise mechanisms are poorly understood. This is in part due to the inaccessibility of biological samples from paediatric patients with advanced disease, in whom surgical intervention would be unethical and detrimental to their survival. For this reason, the development of relevant translational biological models in which the mechanisms of medulloblastoma dissemination can be examined, is invaluable to our understanding of metastatic disease.

While aspects of the pathophysiology of MB metastasis can be investigated in animal models, they are expensive, and have limited survival; at times curtailing the study duration to less than that required to establish disseminated disease. In addition, the animals are often immune suppressed, which impedes the elucidation of interactions between the host immunological response and disseminating tumour cells, a key feature of the tumour microenvironment (Van Ommeren, Garzia et al. (2020). Considering the increasing evidence of the fundamental role played by the tumour milieu in all aspects of metastasis and drug resistance (Boire, Brastianos et al. 2019, Morad and Moses 2019), 3-dimensional models present an exciting opportunity in which the interactions between MB and aspects of their *in vivo* tumour microenvironment, can be recapitulated and explored.

While the molecular subgrouping of MB is maintained at relapse (Ramaswamy, Remke et al. 2013), there are subgroup-specific distinctions in their preferred sites of recurrence and morphology of metastases. SHH MB tumours preferentially arise within the cerebellar hemispheres and recur locally in nodular metastases, whereas the midline cerebellar Group 3 and 4 medulloblastoma tend to metastasise to the leptomeninges, where they radiologically appear as laminar and laminar-nodular metastases respectively (Zapotocky M 2017). These inherent differences may also extend to their primary and metastatic tumour microenvironments, which may explain the Group 4 MB predilection for suprasellar metastases, or why greater immune cell infiltration is observed in SHH tumours (Zapotocky M 2017, Mata-Mbemba, Zapotocky et al. 2018, Van Ommeren, Garzia et al. 2020).

Thus, cancer cells can adapt the biochemical, physical and immunological properties of their microenvironments, to secure their survival in their chosen pre-metastatic niche by various mechanisms (Cacho-Diaz, Garcia-Botello et al. 2020). Through reciprocal interactions, disseminating metastatic cells modulate their milieu by secreting growth factor liberating proteases, chemokines and immune mediators, enabling their evasion from immune detection and initiating signalling pathways that augment their proliferation, motility and survival (Novak and Kaye 2000). Dysregulation of MMP-2 and MMP-9 secretion or functional activity could contribute to these pro-metastatic cascades.

Constituents of the brain tumour microenvironment include cells such as neurons, astrocytes, microglia, endothelia and macrophages, as well as non-cellular components embedded within the extracellular matrix (ECM) (Van Ommeren, Garzia et al. 2020).

The ECM of the brain is defined by the parenchymal interstitial matrix in which glycosaminoglycans (GAGs) such as hyaluronan and proteoglycans like tenascin C are present in abundance, as well as the basal lamina that encapsulates the vascular endothelium and is mainly composed of collagen IV, laminin and fibronectin. The ubiquity of hyaluronan in the brain ECM facilitates its role as a key anchor of many matricellular proteins and modulator of cell migration. This may explain its higher prevalence within the brain tumour microenvironment in comparison to normal brain, where its overexpression is advantageous to migrating tumour cells (Richard, Kortei et al. 2020). In addition, its receptors CD44 and receptor for hyaluronan-mediated motility (RHAMM), have been detected at higher expression levels and observed to co-localise with MMP-2 and -9 at the invasive margins of gliomas, breast and other solid tumours (Novak and Kaye 2000, Yu, Chen et al. 2017, Richard, Kortei et al. 2020, Toole 2020).

This observation could support the theory that CD44-mediated activation of MMP-9 (Novak and Kaye 2000) and subsequent activation of MMP-2 at the leading edge of metastasizing tumours, could result in digestion of collagen IV in the basal lamina, disrupting the blood-brain barrier and

initiating the haematogenous dissemination of MB cells (Novak and Kaye 2000, Boire, Zou et al. 2017). The re-modelling of the tumour microenvironment initiated by the hyaluronan-CD44 dependent MMP-9 activation, may also result in the concomitant release of previously sequestered pro-angiogenic factors (Bauvois 2012), culminating in neo-angiogenesis and further permeability of the blood-tumour barrier, a phenomenon radiologically observed in Group 3 MB which also express higher levels of angiogenesis-related genes (Thompson, Keir et al. 2017).

As shown in chapter 3 of this thesis, MB cells secrete functionally active MMP-2 and MMP-9 that may enable them to remodel their microenvironment by modifying the stiffness of the extracellular matrix, as well as liberating growth factors and chemokines that drive their proliferation, migration and invasion. As the experiments performed thus far concerned medulloblastoma cells cultured in 2-dimensional methods, it was postulated that their secreted proteome would be altered in 3-dimensional culture, in a manner that would better recapitulate the *in vivo* setting.

4.2 Aims and Hypotheses

Therefore, to explore the effects that different aspects of the tumour microenvironment may exert on the levels of functionally active MMP-2 and MMP-9 secreted by medulloblastoma cells, 3-dimensional culture

models that replicated interactions between MB and their architectural or cellular milieu were used. Aims for this chapter were as follows:

- 1) To better re-capitulate the tumour microenvironment of SHH MB micrometastases, a spheroid model was employed. The SHH MB spheroids were generated over 96 hours and on day 4 seeded on top of collagen IV and hyaluronan-based matrices, alongside media controls; and their levels of functionally active MMP-2 and MMP-9 correlated to their migration across the matrices. It was hypothesised that the increased cell-cell interactions within the spheroids, as well as their adhesion to and the presence of a digestible extracellular matrix protein, would result in higher levels of secreted functionally active MMP-2 and MMP-9, which would correlate with their extent of migration across the matrices.

- 2) To determine whether the migration of SHH spheroids across extracellular matrices was MMP-2/-9 dependent, pharmacologic inhibition using recombinant tissue inhibitor of metalloproteinases 1 (TIMP-1), TIMP-2 and Doxycycline, was used to inhibit the tumour-derived functionally active MMP-2/MMP-9. Sequential imaging of the spheroids was then performed every 24 hours over a 48-72-hour period. It was postulated that the extent of migration would be limited following MMP-2 and MMP-9 inhibition.

- 3) To explore the effect that immune cell infiltration may have on the levels of functionally active MMP-2 and MMP-9 secreted by medulloblastoma, SHH spheroids were co-cultured with macrophages. The supernatants were thereafter harvested, and levels of functionally active MMP-2 and MMP-9 determined by gelatin zymography.
- 4) To determine whether the observed differential levels of functionally active MMP-2 and MMP-9 secreted by the matched primary and metastatic Group 3 (D425-Med and D458-Med) and Group 4 cell lines (CHLA-01-MED and CHLA-01R-MED) would correlate with their invasiveness in a 3-D model of the basal lamina, transwell invasion assays were performed. It was thought that the increased levels of functionally active MMP-2 and MMP-9 secreted by the matched primary and recurrent cell lines, would correlate with their invasive capacity.
- 5) To explore the effect of hyaluronan on the levels of functionally active MMP-2 and MMP-9 secreted by MB cell lines, conditioned supernatants from SHH, Group 3 and Group 4 medulloblastoma were examined using gelatin zymography, following the 3-D culture embedded within a hyaluronan-based hydrogel. It was postulated that the presence of hyaluronan would result in increased levels of both MMP-2 and MMP-9 secretion.

4.3 The effect of 3-dimensional spheroid culture of medulloblastoma cell lines on their secreted levels of functionally active MMP-2 and MMP-9

4.3.1 Generation of medulloblastoma spheroids

To ascertain whether 3-D culture of MB cell lines would impact their secretion of MMP-2 and MMP-9, a spheroid model optimised in MB by a former PhD colleague, Dr Roper was used (Roper 2019). SHH cell lines, which form an adherent monolayer in 2-D culture, formed tight spheroids within 24 hours of seeding, while the Group 3 cell lines, which were semi-adherent in 2-D culture, produced very loose spheroids in 3-D. Meanwhile, the matched pair of Group 4 cell lines that were cultured in suspension did not form suitable spheroids, despite forming a mixture of large cell clusters and single cells in suspension culture. Thus, it appeared that the MB cell line phenotype in 2-D culture gave some indication of the cell lines predicted suitability for the spheroid model (Kramer, Walzl et al. 2013, Roper 2019).

MB spheroids with an approximate diameter of 300µm were generated 96 hours after seeding (

Figure 4.1 A). While initial experiments included the Group 3 cell line HD-MB03, its loose spheroids resulted in unacceptable variation in subsequent functional assays in which the transfer of these delicate structures was required. As such they were excluded from further

spheroid work. The initial 7-day experiments (involving HDMB-03 cells) of spheroid culture within serum-free neurosphere media versus seeded **A** on top of a Collagen IV matrix are shown in Figure 4.2.

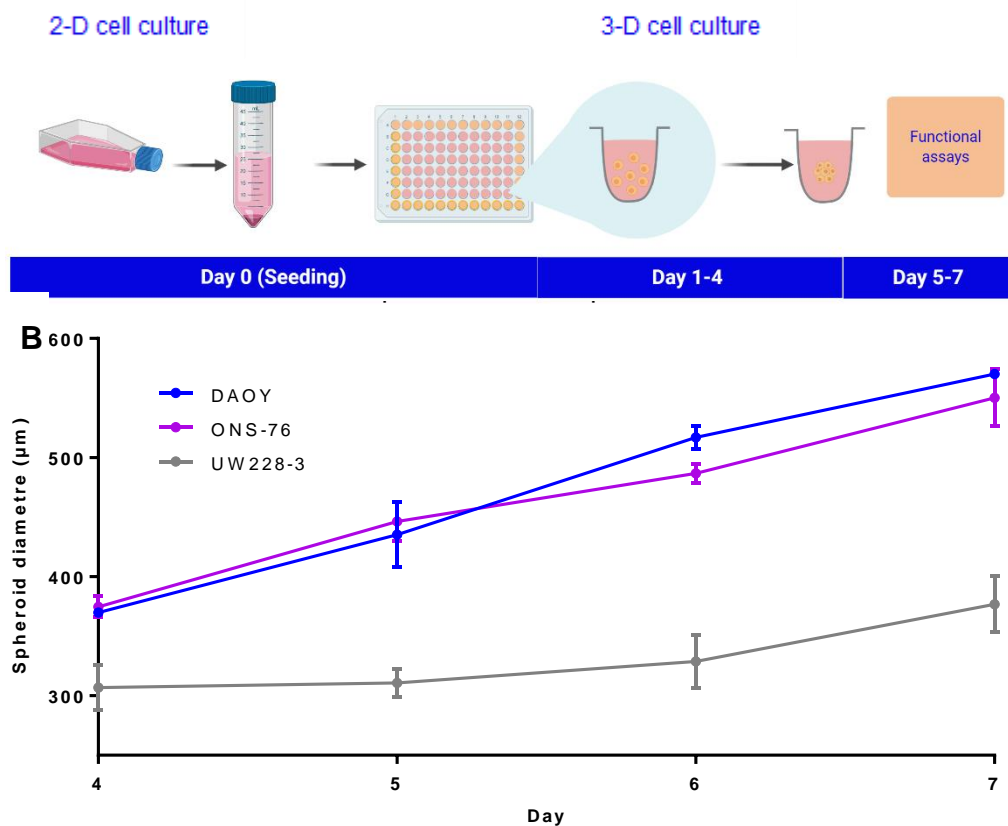


Figure 4.1 Growth of medulloblastoma spheroids

A. Schematic showing the generation of medulloblastoma spheroids.

The previously optimised cell seeding densities of each cell line as determined by Dr S. Roper were seeded into ultra-low attachment plates and allowed to grow for 72 hours. On day 4, the spheroids were ~300µm in diameter and therefore suitable for functional experiments. Image created with BioRender.com.

B. Graphical representation of the growth of the SHH spheroids over 72 hours from Day 4 to Day 7. Spheroid volume was measured using an image J macro designed by a previous lab colleague Dr Ivanov and plotted within Graphpad prism from day 4 to day 7. While DAOY and ONS-76 cell lines remained spherical at Day 7, the UW228-3 spheroids began to adopt an ovoid phenotype from day 4 onwards. All spheroids measured over 300 µm at the beginning of the experiment and continued to grow over the 72 hours period.

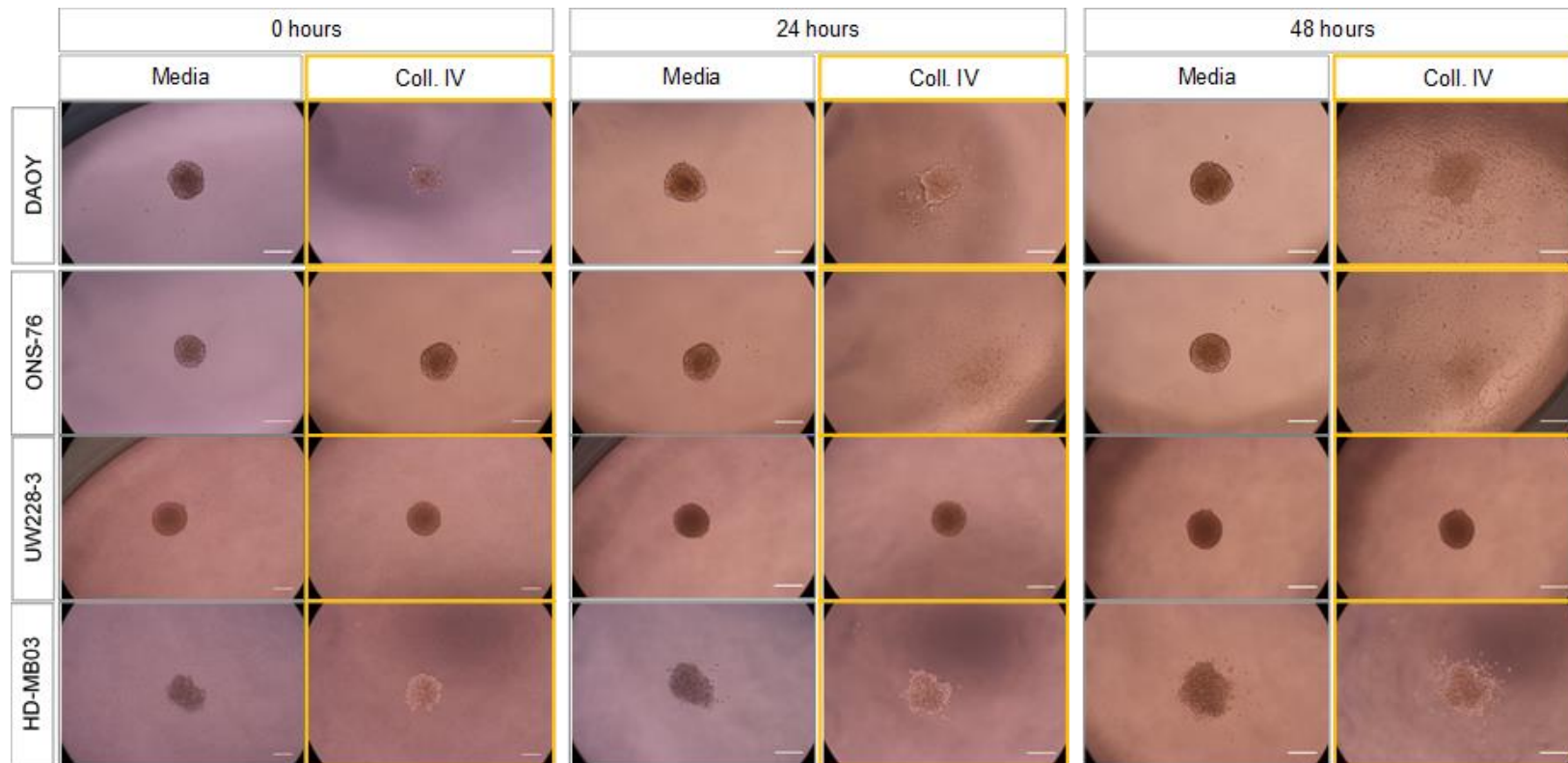


Figure 4.2 Spheroid culture in neurosphere medium and on top of a collagen IV matrix. As shown above, all except HD-MB03 form spherical spheroids. When seeded onto a collagen IV coating, all except UW228-3 began to migrate across the matrix within the first 24 hours (Scale bar=300µM)

4.3.2 The effects of variations in the tumour microenvironment on the levels of functionally active MMP-2 and MMP-9 secreted by medulloblastoma

4.3.2.1 3-D spheroid culture of MB spheroids on top of a Collagen IV matrix

To determine whether the culture of SHH and Group 3 spheroids on various extracellular matrix components would stimulate higher levels of secreted functionally active MMP-2 and MMP-9; DAOY, ONS-76, UW228-3 and HD-MB03 spheroids were seeded on top of collagen IV-coated 96 well plates. Fresh serum-free neurosphere medium was then added and the spheroids allowed to migrate for 72 hours, following which images as shown in Figure 4.2 were taken, and conditioned supernatant harvested for gelatin zymography. A representative zymogram is shown in Figure 4.3. At 48 hours, the intensity of the MMP-2 signal modestly increased in all the cell lines seeded on the collagen IV matrix in comparison to their media-cultured counterparts as shown in Figure 4.3 B (i). Only DAOY and ONS-76 spheroids secreted detectable levels of functionally active MMP-9 at 48 hours, with increased signal observed in those seeded onto the collagen IV matrix (Figure 4.3 B (ii)). While the levels of functionally active MMP-2 and MMP-9 were easily detectable after 48 hour conditioned supernatant from 2-D culture of the MB cell lines (Figure 3.10), this duration was extended to 72 hours to improve

MMP-2 and MMP-9 signal intensity from spheroid 48 hr conditioned media as shown in **Figure 4.3A**.

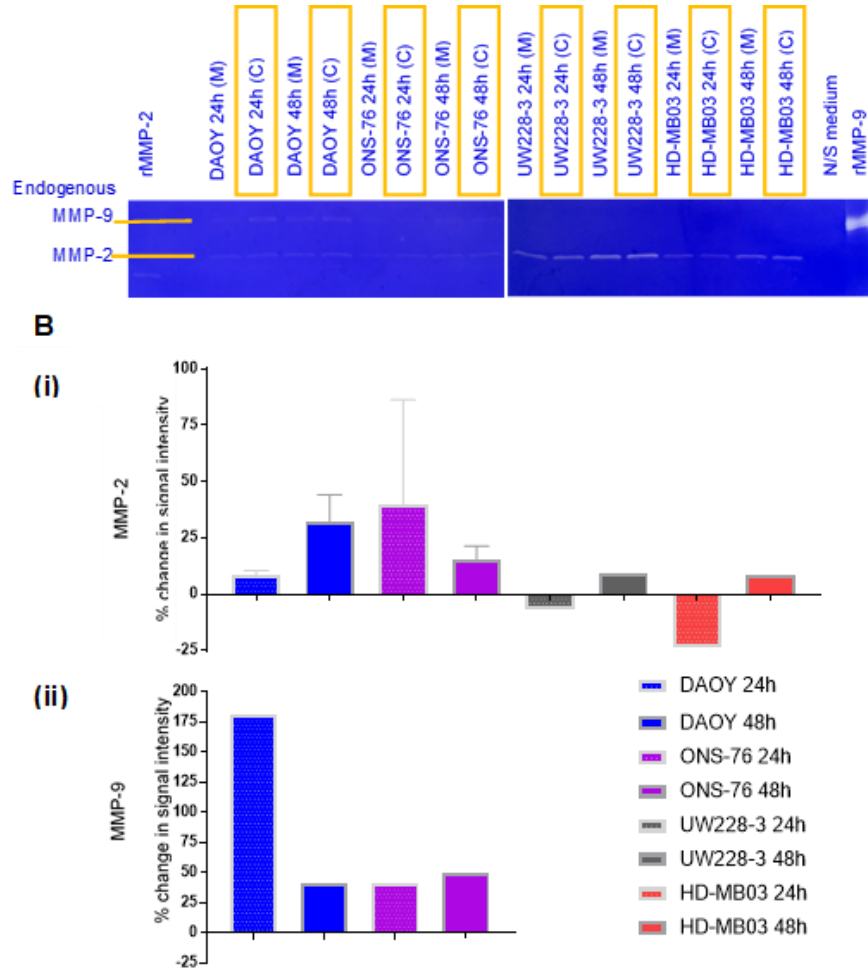


Figure 4.3 Levels of functionally active MMP-2 and MMP-9 from initial SHH and Group 3 MB spheroid experiments.

A. Gelatin zymograms of conditioned supernatant following 48 hour culture of MB SHH and Group 3 MB spheroids on top of a collagen IV coating (10µg/mL). 15µl of each sample were loaded alongside serum-free neurosphere media (N/S medium) and recombinant MMP-2 (rMMP-2) and MMP-9 (rMMP-9) controls and the resulting percentage change in signal intensity quantified with Image J densitometry where detectable. (M)-Media, (C)-collagen IV

B. Graphical representation of the percentage change in the signal intensity of detectable MMP-2 (i) and MMP-9 (ii) secreted by spheroids cultured for 48 hours in neurosphere media versus on top of a collagen IV matrix. As shown, n=3 experiments for DAOY and ONS-76 spheroids demonstrated consistently higher MMP-2 in the collagen cultured spheroids at 24 and 48 hours, while UW228-3 and HD-MB03 showed MMP-2 levels lower than the media controls at 24 hours but more MMP-2 at 48 hours. MMP-9 signals from 48-hour spheroid collagen cultures were not always demonstrable thereby preventing replicated experiments.

4.3.2.2 3-D spheroid culture of SHH spheroids on top of a hyaluronan based hydrogel

To explore the effect of a hyaluronan (HA) microenvironment on the levels of secreted functionally active MMP-2 and MMP-9 from medulloblastoma, day 4 DAOY and ONS-76 spheroids were seeded by Dr S. Roper (Roper 2019), on top of a hyaluronan-based matrix (Hystem[®]) along with different combinations of extracellular protein components. The spheroids were incubated in neurosphere medium for 72 hours before their supernatant was extracted, centrifuged and stored at -80°C, allowing for simultaneous zymography experiments to be performed, as shown below.

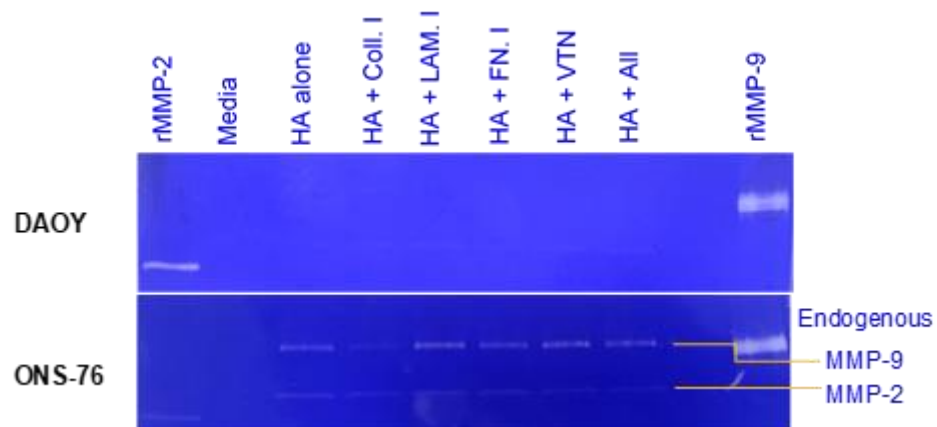


Figure 4.4 The effect of SHH spheroid culture on a hyaluronan-based matrix on the secreted levels of functionally active MMP-2 and MMP-9.

Day 4 DAOY and ONS-76 spheroids were seeded on top of a customisable 1% hyaluronan hydrogel (Hystem[®]) combined with different matricellular protein combinations to final concentrations of 50 µg/mL-as optimised by our post-doctoral fellow, Dr Franziska Linke. Equal volumes of 72 hr conditioned supernatant were examined with gelatin zymography. Zymograms shown above were representative of n=2 experiments, with ONS-76 spheroids MMP-9 signal intensity more visible than MMP-2 while DAOY MMP-9 signal was difficult to detect. HA-hyaluronan, Coll. I-collagen I, LAM I-laminin I, FN.I-fibronectin I, VTN-vitronectin.

While DAOY spheroids migrated to similar extents across all matrix combinations (Roper 2019), their differential levels of functionally active MMP-2 ($p=0.0004$) and MMP-9 ($p=0.0333$) were statistically significant following ANOVA analysis of replicated experiments ($n=2$) as shown in below.

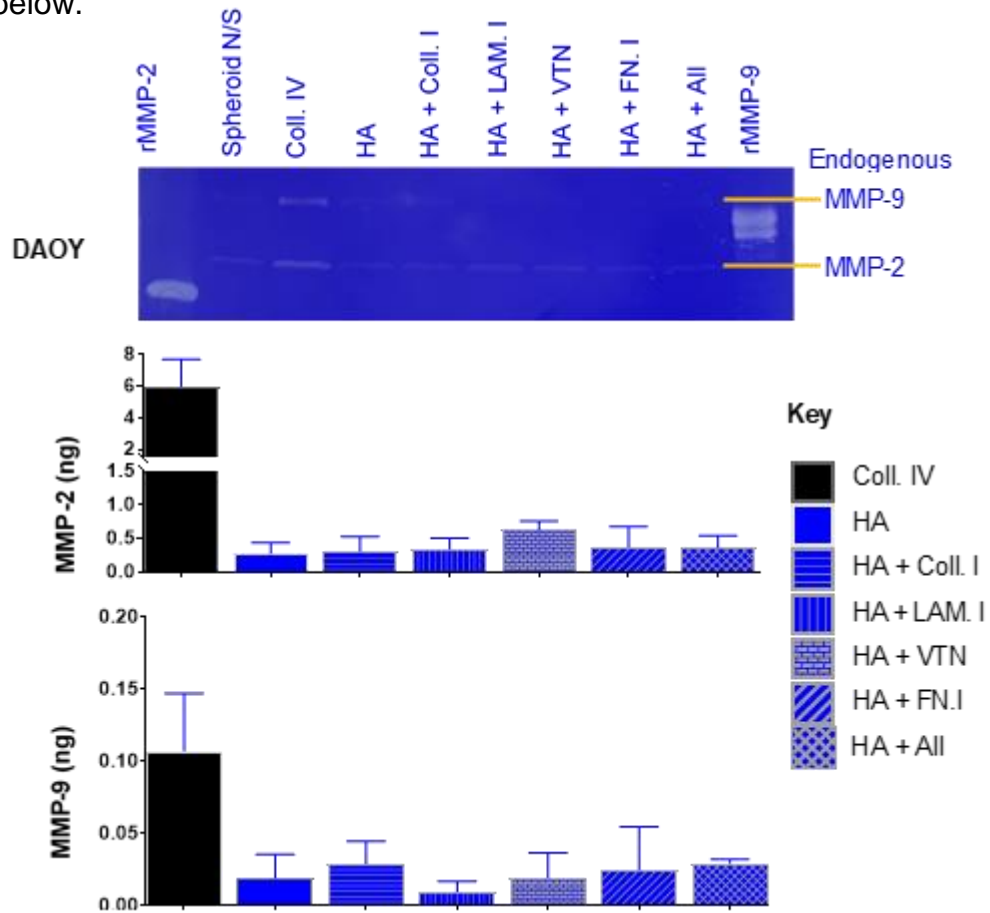


Figure 4.5 Levels of functionally active MMP-2 and MMP-9 secreted by DAOY spheroids migrating across different matrices.

DAOY spheroids were generated and after 96 hours, seeded on top of either collagen IV ($10\mu\text{g/mL}$) or 1% hyaluronan hydrogel alone or supplemented with collagen I, laminin I, vitronectin, fibronectin or a combination of 1% hyaluronan supplemented with the latter 4 factors to resulting concentrations of $50\mu\text{g/mL}$, and allowed to migrate for 72 hours. Conditioned supernatant was harvested and gelatin zymography performed as shown ($n=2$). Image J densitometry was used to determine the MMP-2 and MMP-9 content of each sample relative to loaded controls of MMP-2 ($3.33\text{ng}/\mu\text{l}$) and MMP-9 (1:100 of $6.66\text{ng}/\mu\text{l}$), and analysed using GraphPad prism. DAOY spheroids migrating across a collagen IV matrix secreted the highest MMP-2 and MMP-9 levels.

Similarly, ONS-76 spheroids migrated across all matrix combinations, but exhibited the most dramatic migration pattern on hyaluronan supplemented with fibronectin (Roper 2019). While the differential levels of functionally active MMP-2 and MMP-9 secreted by the ONS-76 spheroids cultured on the various were not statistically significant, the highest levels of MMP-9 seemed to emanate from ONS-76 spheroids on HA hydrogels supplemented with laminin I or vitronectin (Figure 4.8).

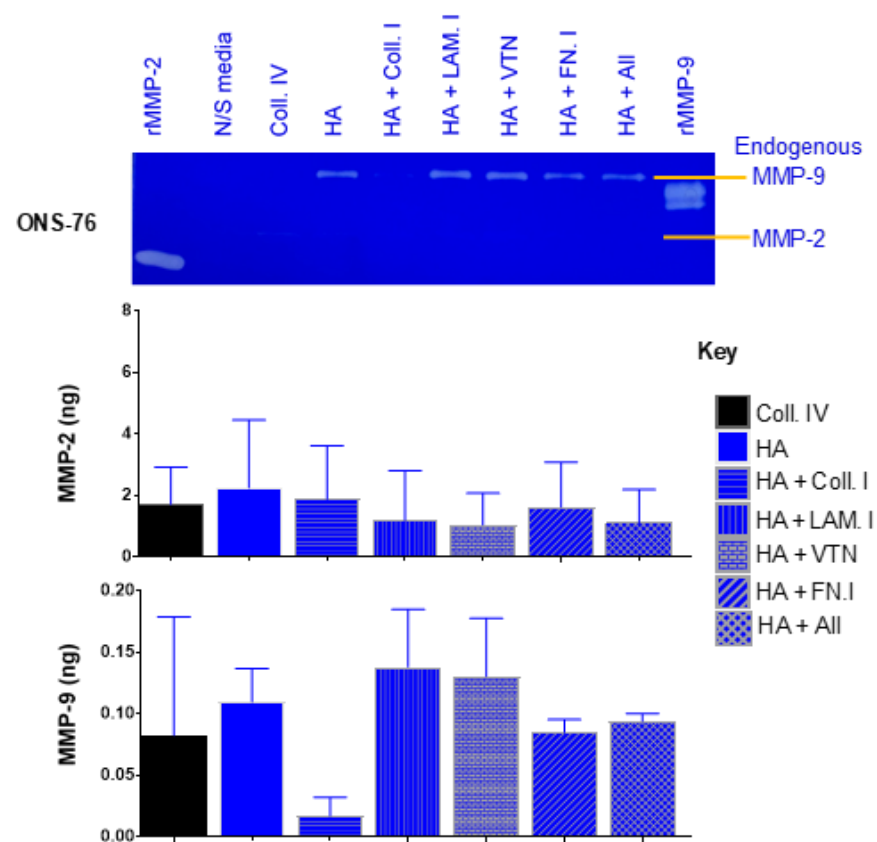


Figure 4.6 Levels of functionally active MMP-2 and MMP-9 secreted by DAOY spheroids migrating across different matrices.

Following 72 hour migration of ONS-76 spheroids across pure collagen IV (10µg/mL), pure 1% hyaluronan or hyaluronan (HA) supplemented with collagen I, laminin I, fibronectin I, vitronectin or a combination of all 4 factors, supernatant was examined using gelatin zymography as shown and analysed using image J densitometry and ANOVA statistical test on Graphpad prism. The strongest MMP-9 signal intensities were apparent in the HA + laminin I and HA + vitronectin matrix cultured ONS-76 spheroids.

Further experiments to explore this differential secretion of functionally active MMP-2 and MMP-9 from SHH MB cultured on different ECM components and conditions are required to make definitive conclusions. While DAOY and ONS-76 spheroids migrated across each representative ECM surface, they were not found to be invasive when embedded within pure or supplemented hyaluronan based hydrogels ([Roper 2019](#)). We therefore explored whether hyaluronan-embedded single MB cells would secrete stronger levels of functionally active MMP-2 and MMP-9.

4.3.2.3 The effect of 3-dimensional culture of medulloblastoma cell lines embedded in a Hyaluronan hydrogel on their secreted levels of functionally active MMP-2 and MMP-9

MB cells were embedded within a pure hyaluronan hydrogel by our post-doctoral fellow, Dr Franziska Linke. Forty-eight hour conditioned media was harvested after 20 days of extended culture and examined using gelatin zymography.

Figure 4. 7 demonstrates a schematic of the experiments performed.

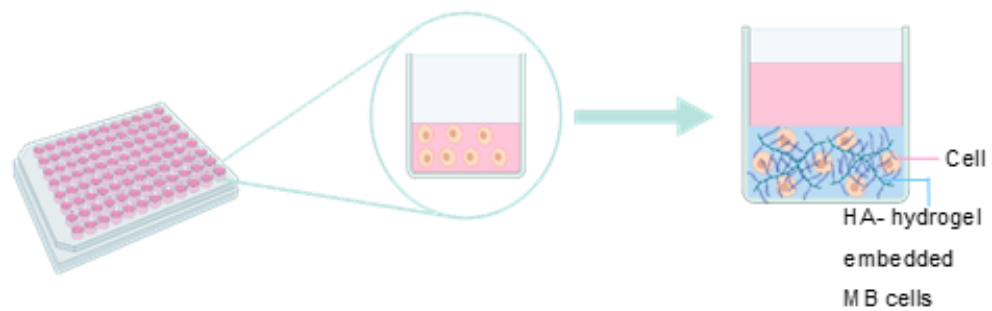


Figure 4. 7 Schematic diagram of 3-dimensional hydrogel culture of medulloblastoma Medulloblastoma cell lines were seeded in a pure hyaluronan (HA) hydrogel and established in extended culture with media changes performed every 48 hours. Supernatant from embedded 20-day old cells was centrifuged and their levels of functionally active MMP-2 and MMP-9 examined using gelatin zymography. Image created with BioRender.com

As shown in Figure 4.8, the levels of functionally active MMP-2 and to a lesser extent MMP-9 expressed by the MB cell lines embedded within the pure hyaluronan gel, are drastically stronger than those previously seen from their 2-D cultured counterparts (Figure 3.10). This is especially clear when the initial numbers of seeded cells are considered, i.e. less than 1000 cells per well in the hydrogel compared to the 5 million cells seeded in the 2-D cultures.

In comparison to the signal intensity (Figure 4.8) of the functionally active MMP-2 and MMP-9 detected in the supernatants derived from the 2-D monolayer cultures of 5×10^6 MB cells, higher levels of functionally active MMP-2 and MMP-9 were derived from considerably fewer cells embedded within the hyaluronan hydrogel. While the concomitant optimisation of this hyaluronan-based hydrogel 3-D model prevented

replicate experiments, this data suggests that the encapsulation and interactions with components of their extracellular matrix, may stimulate their increased secretion of MMP-2 and MMP-9 from medulloblastoma.

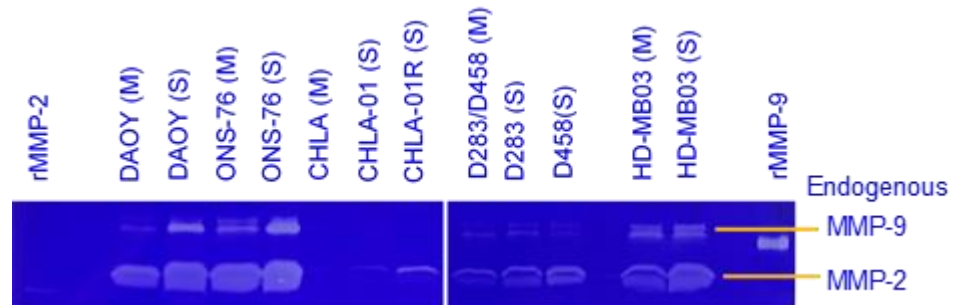


Figure 4. 8 Gelatin zymography of supernatant from 3-D embedded medulloblastoma cell lines.

Equal volumes of 48-hour conditioned supernatant (S) from 20 day hydrogel embedded medulloblastoma cells were loaded alongside serum containing media (M) controls into a gelatin impregnated SDS-gel and examined for their levels of functionally active MMP-2 and MMP-9 using zymography. Reference controls of recombinant MMPs (rMMPs) loaded were 33.3ng of rMMP-2 and 0.66ng of rMMP-9 in this experiment. As shown, the signal intensity of MMP-2 and MMP-9 from the embedded cells are comparable to those from millions of single MB 2-D cultured cells.

4.3.2.4 Investigating the effect of spheroid and macrophage co-culture and p53 status of SHH medulloblastoma on their secreted levels of functionally active MMP-2 and MMP-9

In addition to being the MB subgroup with the highest immune cell infiltration, the p53 status in SHH medulloblastoma is a well-known prognostic indicator as highlighted by the WHO (Louis, Perry et al. 2016) While we primarily sought to evaluate whether co-culture with macrophages would increase the levels of functionally active MMP-2 and MMP-9 secreted by the tumour spheroids, the availability of spheroid

forming SHH cell lines with different p53 statuses and previously published data suggesting p53 regulates MMP-2 activation at the transcriptional level, drove us to explore whether the p53 gene status would have any effect upon the secreted levels of functionally active MMP-2 and MMP-9 from SHH spheroid-macrophage co-cultures.

To this end, previously optimised cell densities of DAOY *mut* p53, ONS-76 *dnp53* and ONS-76 *wt.* p53 were co-cultured with macrophages graciously donated by Dr Luisa Martinez-Pomares group (see Methods 2.7.2). Tumour cells were seeded in ultra-low attachment plates (Corning, 7007) with macrophages in ratios of 1:1 ratio, 1:0.5 and 1:0.25 by Dr S. Roper (Roper 2019) and zymogram experiments of the supernatants performed as demonstrated in Figure 4.10.

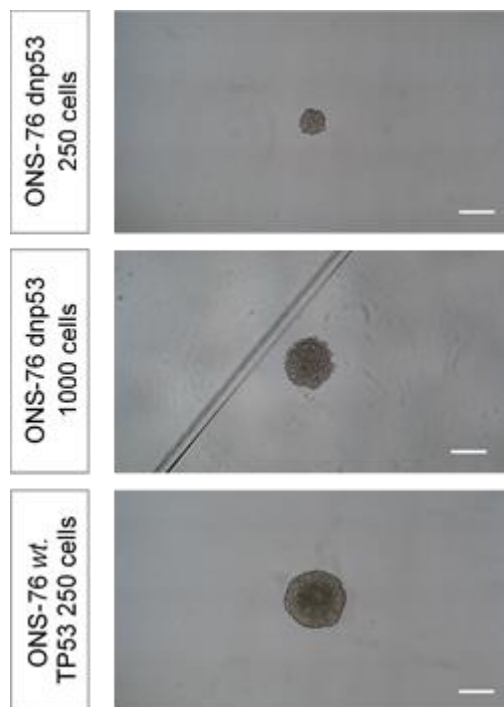


Figure 4.9 Generation of ONS-76 wild type TP53 and ONS-76 *dnp53* spheroids.

To generate spheroids of approximately 300µm diameter at day 4, 1000 ONS-76 *dnp53* cells were required in comparison to 250 cells of the wild type p53 counterpart. As shown, the resulting in the ONS-76 *wt.* TP53 spheroid was much tighter in appearance with a more well-defined outline. Scale bar=300µm

While the doubling time in 2-D culture of ONS-76 *dnp53* was similar to that of its *wt.* p53 counterpart, more than 4 times the number of *dnp53* ONS-76 cells were required to obtain spheroids of suitable size as shown in Figure 4.8. In addition, the ONS-76 *dnp53* spheroids secreted less functionally active MMP-2 compared to its wild-type p53 counterpart, suggesting that an intact p53 gene is necessary for MMP-2 secretion (Figure 4.10).

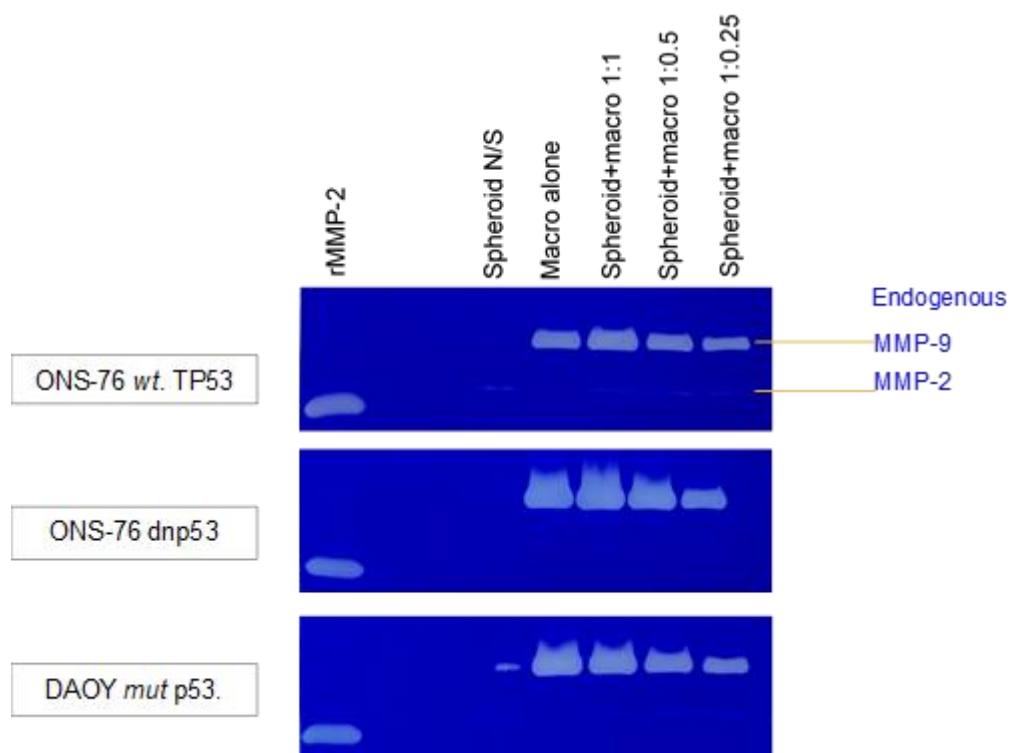


Figure 4.10 Zymography of supernatant from SHH MB spheroid and macrophage culture

Equal volumes of supernatant following 72-hour co-culture of macrophages in the ratios given above to the respective cell lines were examined using gelatin zymography. Surprisingly, in the absence of macrophages, little to no MMP-9 signal was seen in any of the spheroid supernatants with the exception of possible artefact in the DAOY sample. In the co-culture samples, the MMP-2 signal appeared to emanate predominantly from the spheroids while the MMP-9 signal appeared to be proportional to the ratio of macrophages cultured with the MB cell lines.

As depicted in Figure 4.10, the levels of functionally active MMP-2 signal remained constant between the MB spheroids of the same cell line irrespective of whether macrophages were added, suggesting the secreted MMP-2 was mainly tumour-derived. The MMP-2 signal intensity was easily detectable in the supernatant from the DAOY and ONS-76 *wt.* p53 spheroids but substantially reduced in the ONS-76 *dnp53* spheroids. This data supports findings from the earlier works of Bian and Sun, 1997 that demonstrated p53 regulation of MMP-2 at the transcriptional level.

Meanwhile, the MMP-9 signal intensities decreased in a manner proportional to the ratio of macrophages seeded within the co-cultured spheroids. While preliminary, this exciting data suggests that majority of the functionally active MMP-9 in the SHH MB tumour microenvironment originates from the tumour cellular microenvironment. As both MMP-2 and MMP-9 have been correlated with increased invasive capacity in MB, it is possible that these paracrine interactions with surrounding tumour associated immune cells, may be an additional mechanism by which SHH MB metastasize, given their predominance for immune cell infiltration (Margol AS 2015). Further work is needed to elucidate the autocrine and paracrine signalling involved in the medulloblastoma: immune cell interface, and determine their resulting effects on migration and invasion through functional assays.

4.3.3 Effects of pharmacological inhibition of MMP-2 and MMP-9 on the migration patterns of 3D SHH medulloblastoma spheroids seeded on collagen IV matrices

Choosing an appropriate matrix metalloproteinase inhibitor

To determine whether the migration of SHH spheroids across ECM coatings would be altered by inhibition of their secreted MMP-2 and MMP-9, we selected a synthetic MMP inhibitor (MMPI) Doxycycline (Figure 4. 11) (Li K 2020), to test alongside human recombinant forms of the endogenous tissue inhibitors of metalloproteinases (TIMPs).

4.3.3.1 Medulloblastoma spheroid treatment with Doxycycline Hyclate

Doxycycline is a well-tolerated tetracycline antibiotic that inhibits MMPs by chelating their calcium and zinc ions, key co-factors that enable their functional activity. As Vandenbroucke et al reported that the IC₅₀ at which *in vitro* MMP-2 inhibition is achieved was 56µM, a range of concentrations centred around this figure, were trialled to ascertain which effectively inhibited the secreted MMP-2 and MMP-9 from the spheroids but did not result in concomitant toxicity (Vandenbroucke RE 2014, Laronha H 2020).

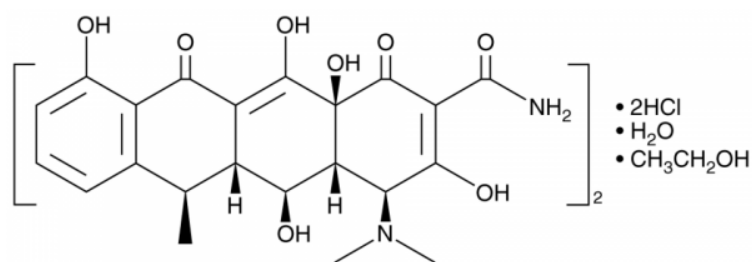


Figure 4. 11 Chemical structure of Doxycycline Hyclate

(Image from <https://www.biomol.com/products/chemicals/antibiotics/doxycycline-hyclate-cay14422-1-accessed> 19/10/20)

Day 4 DAOY, ONS-76 and UW228-3 spheroids were then treated with freshly re-constituted Doxycycline at 10 μ M, 25 μ M, 50 μ M and 100 μ M concentrations over a 72-hour period. After photomicrographs were captured, the supernatants were harvested and examined for the secreted levels of functionally active MMP-2 and MMP-9 from the respective spheroids and compared to their matched controls, using gelatin zymography as shown in Figure 4.12.

Replicated experiments of all three SHH cell line spheroids were performed and their supernatants examined with gelatin zymography to determine the lowest effective concentration of Doxycycline that inhibited the secreted MMP-2 and MMP-9, without conferring spheroid toxicity. However, it soon became evident that above concentrations of 10 μ M, the spheroids looked less viable after 24 hours and began to disintegrate by 48 hours. On the other hand, the data demonstrated that complete inhibition of the spheroid-derived MMP-2 and MMP-9 only occurred at the highest concentration of Doxycycline, 100 μ M (Figure 4.12). Due to

these high toxicities, doxycycline was found unsuitable for functional studies and instead recombinant TIMPs were favoured for further MMP inhibition experiments. Additional data from the Doxycycline experiments are given in the appendix section of this thesis.

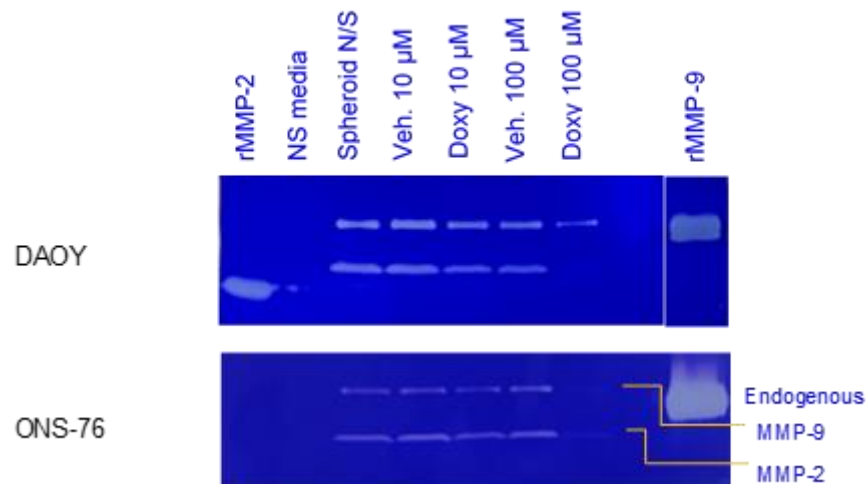


Figure 4.12 Gelatin zymography of 72hr conditioned supernatant from 10µM and 100µM Doxycycline treated spheroids alongside matched DAOY and ONS-76 spheroids cultured in their usual neurosphere medium.

Day 4 DAOY, ONS-76 and UW228-3 spheroids were cultured in neurosphere media (spheroid N/S) or neurosphere media supplemented with sterile water (vehicle) or Doxycycline at 10 µM and 100 µM concentrations. Gelatin zymography of the 72hr supernatant from spheroids treated as described, demonstrated Doxycycline 100 µM inhibited both spheroid-derived gelatinases but at the cost of spheroid viability.

4.3.3.2 Medulloblastoma spheroid treatment with recombinant TIMP-1 and TIMP-2

In physiological states, homeostasis between the levels of MMPs and TIMPs modulates the extracellular environment. In cancer however, many authors attribute the unchecked migration, invasion and cultivation of new metastatic niches to the disequilibrium of this pathway, resulting

in disproportionate upregulation of MMPs in comparison to TIMPs (Li K 2020), as demonstrated in the protease/protease inhibitor array experiments in Chapter 3 of this thesis. This pattern was also suggested by data from DNA methylation profiling of 276 MB and 8 normal cerebellar samples from the Hovestadt dataset analysed on the R2 Genomic Analysis and Visualisation platform (<http://r2.amc.nl>).

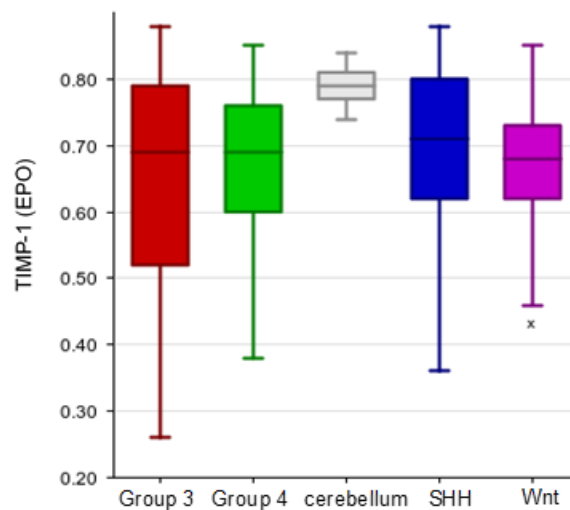


Figure 4.13 DNA methylation profiling of TIMP-1 in normal cerebellum and subgrouped medulloblastoma.

DNA from fresh frozen and paraffin-embedded samples of normal cerebellum and medulloblastoma from the Hovestadt dataset was examined using the Illumina 450K methylation array and resulting TIMP-1 gene methylation data accessed and analysed on the R2 Genomic Analysis and Visualisation platform. Box and whisker plots representing each group are shown with the median and interquartile ranges demonstrated. One way ANOVA analysis demonstrated statistical significance ($p=0.015$) of the TIMP-1 hypomethylation in the MB samples in comparison to the cerebellum.

The 4 members of the TIMP family TIMP-1, -2, -3 and -4, form irreversible inhibitory complexes with MMPs in 1:1 stoichiometric ratios via non-covalent mechanisms (Laronha H 2020, Raeeszadeh-Sarmazdeh M 2020). While TIMP-1 and -3 are physiologically inducible, TIMP-2 is

constitutively expressed. In addition to their inhibition of most MMPs, TIMPs have also been shown to inhibit other matricellular proteases such as disintegrin metalloproteinases (O'Connor, Aboagye et al.). (Jackson, Defamie et al. 2017).

Following their secretion into the extracellular matrix, the actions of TIMPs and where they exert them, is determined by their glycosylation and interactions with largely non-protease ligands (Table 4. 1). TIMP3 is the only member that remains integrated within the extracellular matrix as a result of its glycosylation (Jackson, Defamie et al. 2017). Conversely, the extracellular levels of the other TIMPs and non-glycosylated TIMP-3, are regulated by their endocytosis which is facilitated by proteins such as plasma α 2-macroglobulin and low density lipoprotein receptor-related protein (LRP-1), when the TIMPs are bound to zymogen forms of the MMPs (Jackson, Defamie et al. 2017).

Table 4.1 summarises their other key features. While the TIMP-1: MMP-9 complex impedes the activation of pro-MMP-9 and mediates its elimination from the tumour microenvironment; the complex formed between TIMP-2 and MMP-2, in the presence of MMP-14, results in the activation of pro-MMP-2 (Raeeszadeh-Sarmazdeh M 2020). Thus, the resulting effects of TIMPs can be contradictory to what they are initially assumed to be. The understanding of the effects of TIMPs in the tumour microenvironment is further complicated by their ability to initiate, induce and trigger proliferative, migratory and survival pathways that culminate in a pro-metastatic environment (Jackson, Defamie et al. 2017).

Table 4. 1 Summary of key features of TIMPs 1-4. Table adapted from ([Jackson, Defamie et al. 2017](#)).

Feature	TIMP-1	TIMP-2	TIMP-3	TIMP-4
Molecular weight (kDa)	21	22	22	22
Amino acid residues	184	194	188	194
Co-localisation	Soluble and cell surface	Soluble and cell surface	Extracellular matrix and cell surface	Soluble and cell surface
MMP inhibition	All*	All	All	Most
Pro-MMP binding	proMMP-9	proMMP-2	proMMP-2 proMMP-9	proMMP-2
Non-protease binding ligands	CD63 LRP1 β 1 integrin	α 3 β 1 integrin LRP1	EFEMP1 VEGFR2 AGTR1	
Clinical correlations of altered TIMP expression in other cancer types	Overexpressed in breast, brain, lung renal, pancreatic, gastric, pancreatic, colorectal, endometrial and skin cancers	Equivocal expression in most cancers	Downregulated in most cancers	Equivocal expression in most cancers

To gain an indication into which TIMP would most effectively inhibit the MB spheroid-derived MMP-2 and MMP-9, survival analyses of their gene expression from the publically available Cavalli dataset of 763 MB patients, were performed using the R2 genomic analysis and visualisation platform (<http://r2.amc.nl>). Over 10 years of survival data was available in 612 fresh frozen primary MB samples as shown in Figure 4.14.

In contrast to other tumours including glioblastoma (Jackson, Defamie et al. 2017), high gene expression of TIMP-1 in medulloblastoma conferred a statistically significant survival benefit [$p=0.011$], as shown in the Kaplan Meier curves below, albeit in a select proportion-3.27% of MB patients. While the survival analyses for TIMP-2 also demonstrated a statistically significant survival advantage of high TIMP-2 expression, this difference was much less compared to that of TIMP-1. As shown by the Kaplan Meier curves for TIMP-3 and TIMP-4, neither proved to be statistically significant within this patient dataset. We therefore chose to trial both recombinant forms of TIMP-1 and TIMP-2 to ascertain which would most effectively inhibit the endogenous MMP-2 and MMP-9 secreted by the spheroids.

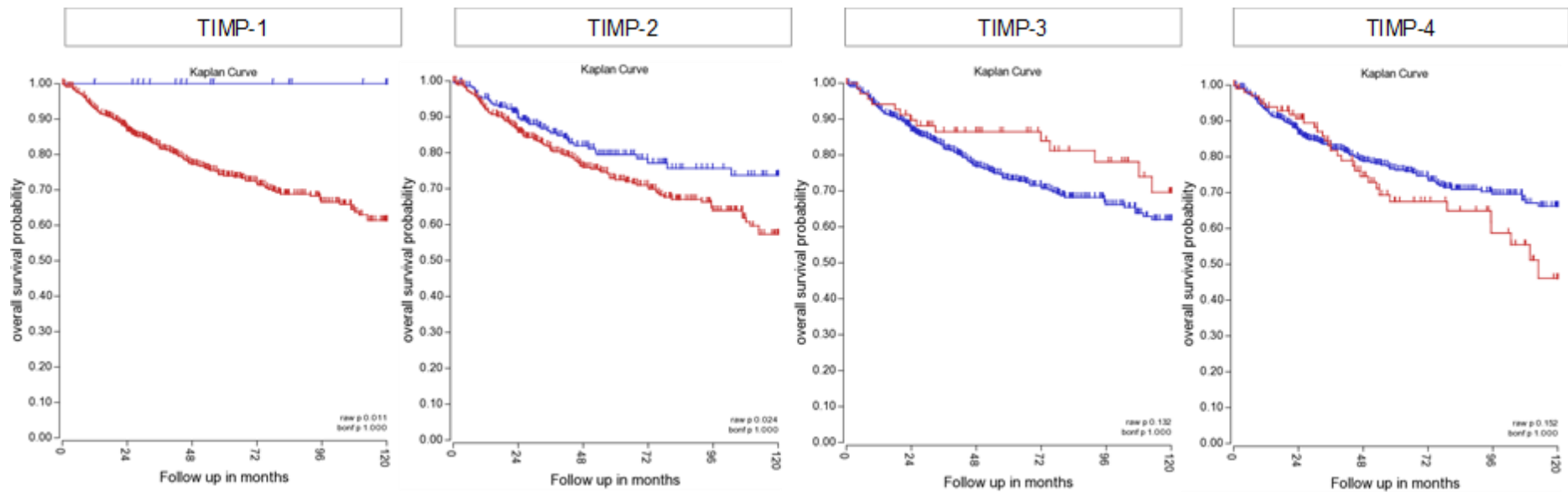


Figure 4. 14 Kaplan Meier survival analyses of MB patient gene expression data of TIMP-1, -2, -3, and -4.

RNA extracted from a total of 612 fresh-frozen medulloblastoma patient samples in the Cavalli dataset was hybridised by Affimetrix array profiling and the gene expression of all TIMPs were quantified and correlated to survival data of the same patients (Cavalli, Remke et al. 2017). The most striking difference in survival was observed in the MB patient samples with high TIMP-1 expression, followed by TIMP-2. As the Kaplan Meier curves for high and low gene expression of TIMP-3 and TIMP-4 intersect, the resulting effect is not statistically significant and therefore unlikely to be clinically relevant.

To recapitulate the complexity of the MMP-TIMP *in vivo* interactions, SHH MB spheroids were generated as previously described and treated with different nanomolar concentrations of recombinant TIMP-1 and TIMP-2 proteins over a 72-hour period. Their phenotype, levels of functionally active gelatinases and growth were thereafter examined with microscopy, gelatin zymography and volumetric analyses, respectively. Initial experiments were performed using recombinant TIMP-1 and TIMP-2 at 10nM and 100nM concentrations, which were based on previous publications (Junseo Oh 2004, Stetler-Stevenson 2008). At 10nM TIMP-1 and TIMP-2 treatments, there was very little detectable change in the signal intensity of the DAOY, ONS and UW228-3 spheroid-derived MMP-2 and MMP-9; while at 100nM, spheroid viability was affected. These experiments were therefore repeated using 25 and 50 nanomolar concentrations of TIMP-1 and TIMP-2 as shown in Figure 4.15.

DAOY, ONS-76 and UW228-3 spheroids remained viable following 72 hours of treatment with the recombinant TIMP-1 and TIMP-2 proteins at both 25nM and 50nM concentrations. Since TIMP-1 strongly inhibited both MMP-2 and MMP-9 as confirmed in the gelatin zymography of ONS-76 treated spheroids (Figure 4.18), and did not appear to result in concomitant activation of either gelatinase, it was decided that it would be the best endogenous MMP inhibitor to determine whether inhibition of MMP-2 and MMP-9 would alter the extent or pattern of migration of the SHH MB spheroids across the collagen IV matrices.

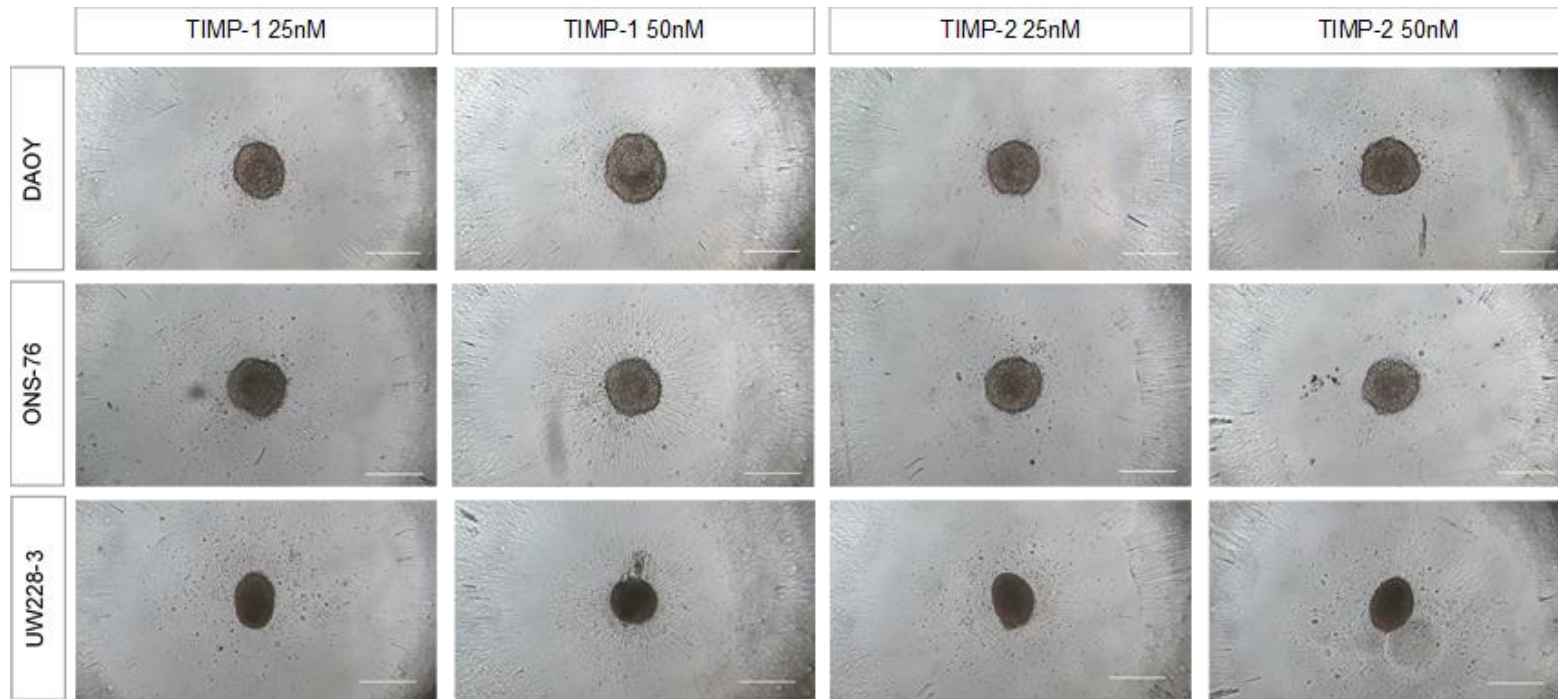


Figure 4.15 72-hour treatment of SHH MB spheroids with 25nM and 50nM concentrations of TIMP-1 and TIMP-2 recombinant proteins.

As shown above, the spheroids remained viable following TIMP-1 and TIMP-2 treated spheroids at the given concentrations over the 72 hours period. With the exception of UW228-3 which adopted an ovoid shape after 4-5 days following their generation, DAOY and ONS-76 remained spherical throughout the 72-hour drug treatments. Scale bar=300microns

As 72-hour conditioned supernatant from ONS-76 spheroids demonstrated high levels of functionally active MMP-2 and MMP-9, ONS-76 spheroids were used to determine the right TIMP-1 inhibitor concentrations and treated with recombinant TIMP-1 at 10, 25, 50 and 100nM concentrations. A representative zymogram is shown in Figure 4.18.

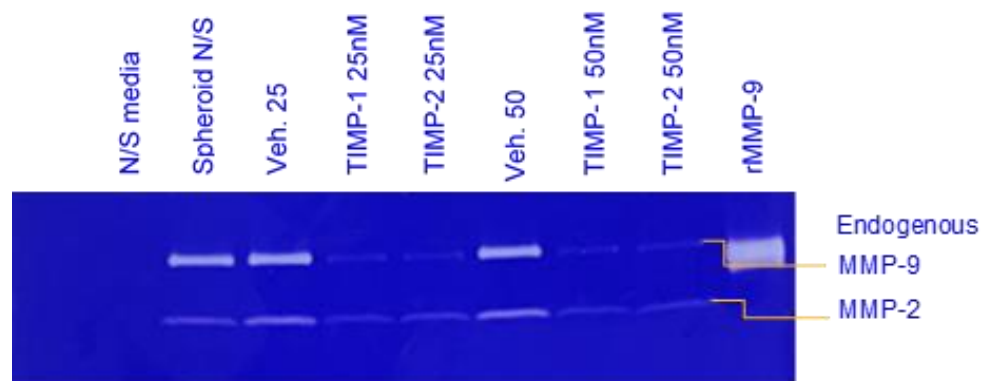


Figure 4. 16 Representative gelatin zymogram of supernatant from ONS-76 spheroids after 72-hour rTIMP-1 and rTIMP-2 treatment at 25 and 50 nanomolar concentrations.

As shown in the zymogram, the MMP-2 and MMP-9 signal intensities within the supernatant harvested from ONS-76 spheroids treated with both rTIMP-1 and rTIMP-2 at both concentrations of 25 and 50nM were drastically reduced in comparison to their corresponding vehicle treated counterparts. Interestingly, the MMP-2 and MMP-9 signal intensities in the vehicle-treated spheroids were stronger than the media controls. As both rTIMP-1 and rTIMP-2 appeared to inhibit the ONS-76 spheroid derived MMP-2 and MMP-9 to a similar extent, rTIMP-1 was selected for future experiments to reduce the possibility of inadvertent MMP-2 activation with recombinant TIMP-2 treatments.

As shown in Figure 4.17, volumetric analyses of the DAOY, ONS-76 and UW228-3 spheroids demonstrated their continual cell proliferation and viability over the 72-hour course of TIMP-1 50nM treatment. In addition, gelatin zymography (Figure 4.19) and densitometry of replicated ONS-76 experiments treated with both rTIMP-1 and rTIMP-2 at concentrations of 25nM and 50nM confirmed that rTIMP-1 and rTIMP-2 had a similar inhibitory effect at both concentrations. At 25nM, rTIMP-1 treatment resulted in a mean 64.0% decrease in MMP-2 signal and a mean 88.2% decrease in the MMP-9 signal, compared to its vehicle control. At the same concentration, rTIMP-2 treatment resulted in a 60.9% decrease and a 92% decrease in functionally active MMP-2 and MMP-9, respectively. At 50nM, a similar pattern of reduced MMP-2 and MMP-9 signal intensities were detected in the supernatant from both TIMP treatments.

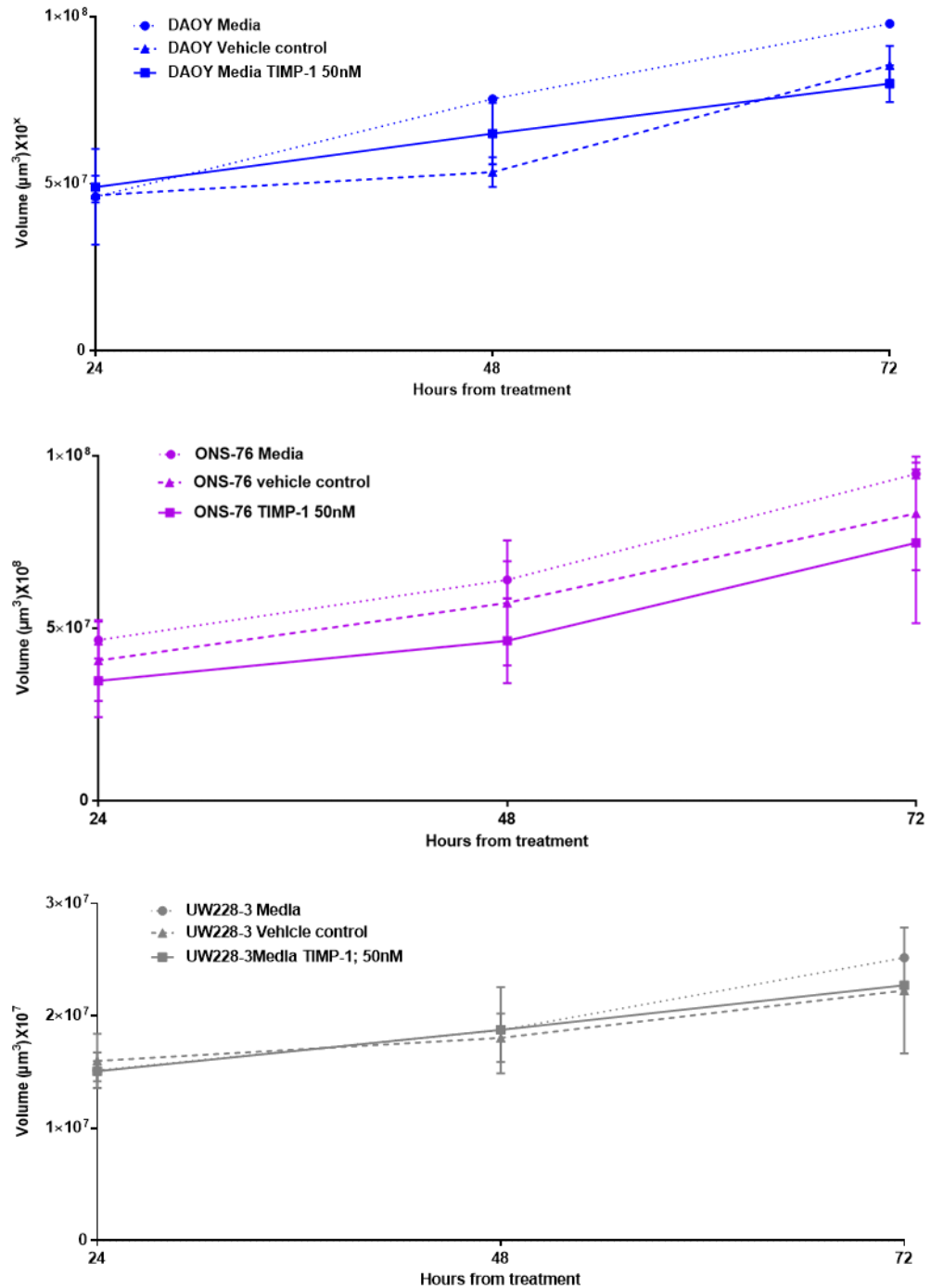


Figure 4.17 Volumetric comparison of SHH MB spheroids following 24-72 hours of TIMP-1 50nM treatment alongside media and vehicle controls.

Volumetric analysis of DAOY (A), ONS-76 (B) and UW228-3 (C) spheroids were cultured for 72 hours in either the standard neurosphere media (media), vehicle control or TIMP-1 50nM treated media. The spheroids remained viable and continuously grew over the duration of the 72 hour treatment with TIMP-1 at 50nM n=4.

To determine whether treatment with recombinant TIMP-1 (rTIMP-1) would affect SHH spheroid migration across a collagen IV matrix, DAOY, ONS-76 and UW228-3 spheroids were generated in the usual fashion and seeded onto a collagen IV matrix with fresh pure neurosphere media or neurosphere media supplemented with the vehicle (sterile water) or rTIMP-1 50nM.

Figure 4.18 shows the effect of rTIMP-1 treatment on DAOY cell migration across the collagen IV matrix. In comparison to media and vehicle treated controls, there are fewer areas of confluent collective migration seen in the rTIMP-1 treated spheroids over the 72-hour period. Whereas in ONS-76, rTIMP-1 treatment did not appear to have any effect on the extent of migration as shown in Figure 4.19. However, the rTIMP-1 treated ONS-76 spheroid appeared to be slower to disseminate across the collagen IV as by 24 hours, its vehicle counterpart had migrated to the extent that a central spheroid body was not visible. On the other hand, UW228-3 spheroids that seldom migrate over collagen IV matrices, did not demonstrate any overt changes in their phenotype following treatment with rTIMP-1 (Figure 4.18-Figure 4,20).

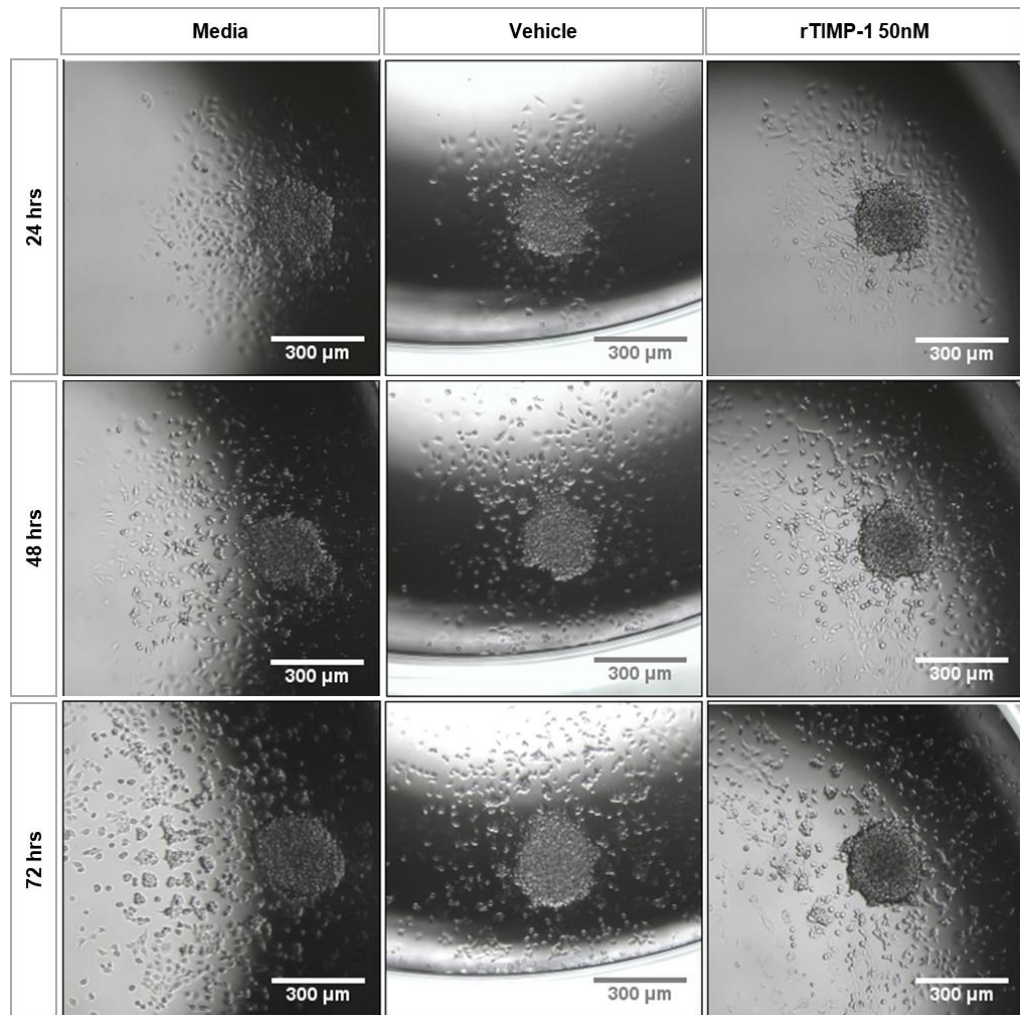


Figure 4.18 DAOY Coll. IV migration assay

At 24 and 48 hours, the extent of migration across the collagen IV matrix appeared restricted in the rTIMP-1 treated DAOY spheroids compared to the media and vehicle controls. This effect appeared to be lost at 72 hours where the DAOY cells had migrated from the central spheroid body beyond the microscopy field of view, similar to the migration seen in the media and vehicle controls.

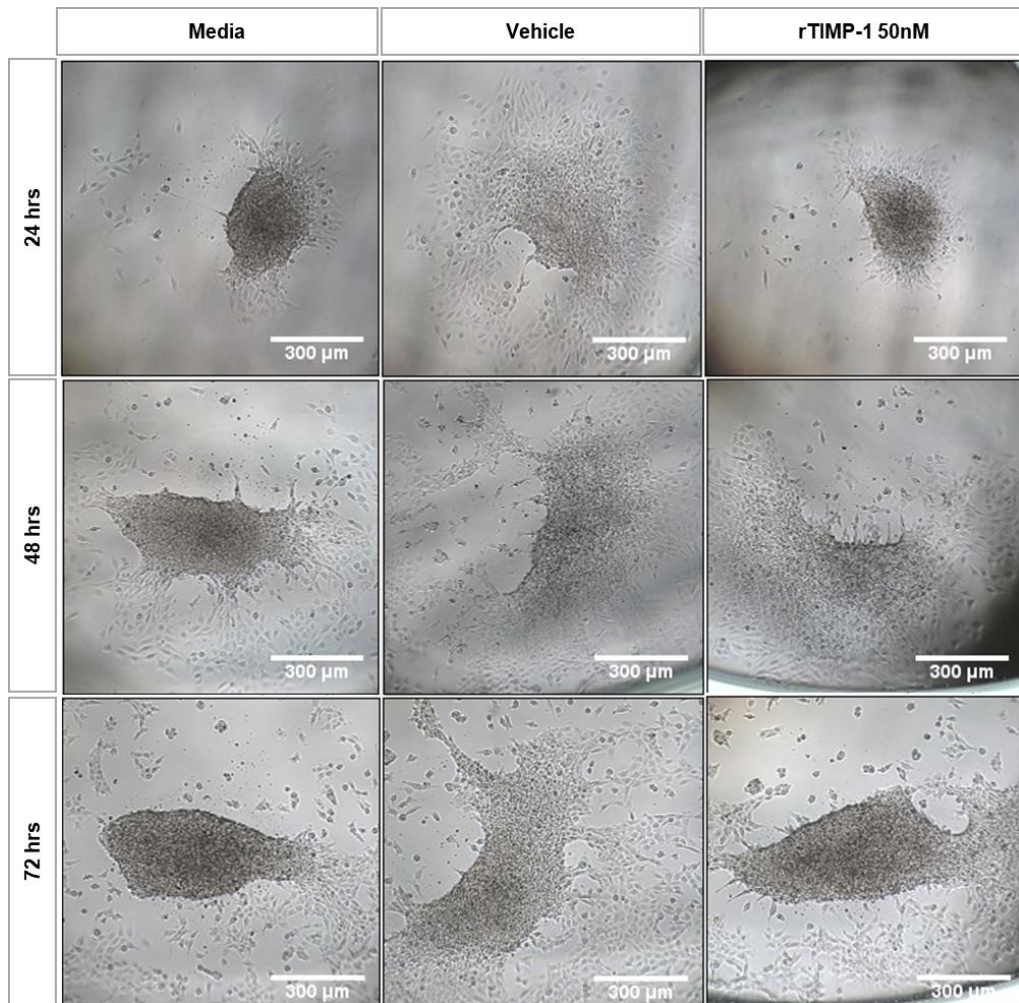


Figure 4.19 ONS-76 Collagen IV migration assay

While the ONS-76 spheroid appeared to favour a collective mode of migration across the collagen IV matrices, in comparison to the DAOY spheroids, rTIMP-1 treatment did not appear to modify their extent or pattern of migration.

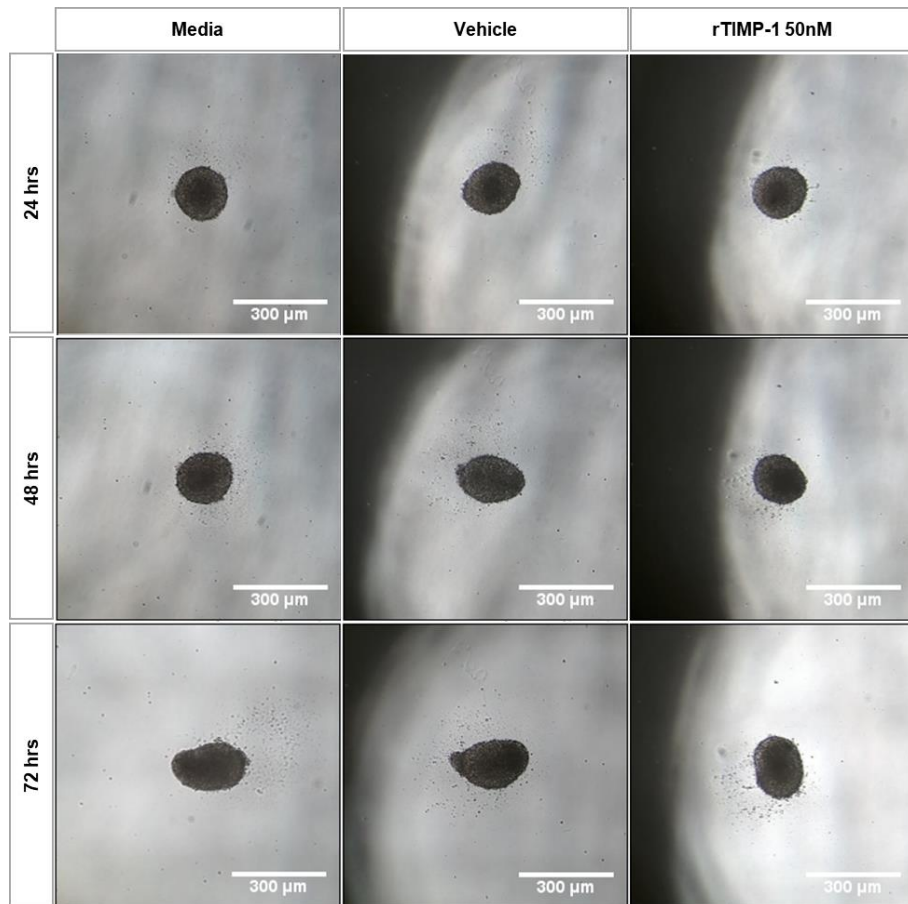


Figure 4.20 UW228-3 Collagen IV migration assay

In contrast to DAOY and ONS-76 spheroids, single cell migration was inconsistently observed in UW228-3 spheroids after 48 hours of seeding on top of the collagen IV matrix. In comparison to the other SHH spheroids, UW228-3 were the only cell line whose morphology changed over 7 days of culture. However when seeded on Collagen IV matrices, the migrating single cells appeared to emerge from the polar ends of the ovoid spheroids.

This data suggests that rTIMP-1 mediated MMP-2 and -9 inhibition, may cause cells to adapt their migratory mechanisms in an autocrine manner that circumvents the need for increased secretion of functionally active MMP-2 and MMP-9; or that MMPs are not essential to the spheroid migration across a collagen IV matrix, hence their inhibition had little observable effect.

4.4 Migration of Group 3 and 4 medulloblastoma cell lines through trans-well assays

While the spheroid migration model sufficiently demonstrated the migratory patterns of 3 SHH cell lines across a collagen IV matrix, it proved unsuitable for the correlation of their respective secretion levels of functionally active MMP-2 and MMP-9 to their expected metastatic potential, due to the presence of many confounding factors including the ECM components the spheroids were seeded upon, and the finding that their extent of migration was unaffected by TIMP-1 mediated inhibition of their secreted gelatinases.

While this conundrum may mimic the complex and dynamic *in vivo* tumour microenvironment, we postulated that a different 3-D invasion model may be more suitable to answer our question. As migration across a matrix will depend heavily on cell adhesion to the matrix it can occur by protease-independent mechanisms. However, invasion through a matrix necessitates proteolysis and consequent re-modelling of the barrier environment (Kramer, Walzl et al. 2013)

Having been recently shown to metastasize to the leptomeninges via haematogenous and CSF routes (Boire, Zou et al. 2017), the transmigratory capacity of MB cells across the BBB would be an important consideration especially in Group 3 and 4 MB, which disseminate further from their primary tumour cavity (Zapotocky M 2017). The transwell assay is a validated *in vitro* model, used to investigate the transmigratory

capacity of cancer cells through perforated wells with pores measuring less than 10µm. At this pore diameter, cancer cells commonly of 20µm, must actively migrate through the pores towards a chemokine. Additionally, coatings of different permutations of basal lamina proteins can be applied, to recapitulate the *in vivo* cell adhesion interactions that allow the invading cancer cells to anchor to the basement membrane, prior to their protease mediated transmigration into the brain vasculature (Justus, Leffler et al. 2014). Thus, to recapitulate the BBB, the permutation of ECM proteins had to be determined.

While *ex vivo* basement membranes originating from peritoneal and placental tissues have been used to investigate the transmigration of other tumour types (Touboul, Lis et al. 2013), the unique features of the BBB render these substitutes inadequate for determination of migration and invasion of medulloblastoma.

4.4.1 Choosing the right transwell barrier

While hyaluronan is most predominant component of the cerebellar parenchyma (Novak and Kaye 2000), collagen IV and laminin isoforms constitute the bulk of the basal lamina, a layer of the BBB formed by two layers distinguished by their cells of origin and laminin-isoform components. The endothelial derived basal lamina contains laminin 111 and -211 while its parenchymal counterpart is constituted by laminin -411 and -511 isoforms (Ferro, Heilshorn et al. 2020).

Although synthetic substitutes such as Matrigel© which contain collagen IV, laminin and other proteoglycans found in basal lamina have been

used in previously described BBB models, these polymers do not produce the endogenous architectural structures that would limit their permeation by disseminating tumour cells. Thus, collagen IV and laminin I isoforms that more closely recapitulated the *in vivo* basal lamina backbone were employed in the following experiments (Ferro, Heilshorn et al. 2020).

As collagen I is a commonly employed barrier in published trans-well migration models due to its scaffold structure, experiments were set up to determine whether the MB invasive capacity would be altered in the presence of a collagen I gel barrier in comparison to a collagen IV coating (Figure 4.21).

Building upon work done by a colleague Dr Macha Aldighieri in the optimisation of this transwell assay (Aldighieri 2020), initial experiments using the most aggressive Group 3 MB metastatic cell line available in our lab, HD-MB03 were performed, to determine the optimal trans-well coating for the investigation of the migratory and invasive capacities of matched primary and recurrent Group 3 (D425-Med and D458-Med) (and Group 4 (CHLA-01-Med and CHLA-01R-Med) MB cell lines. As Dr Aldighieri had already demonstrated a barrier function using collagen IV and collagen IV/laminin transwell coatings in her work, this was not tested further.

As shown in Figure 4.21, 25% of seeded HD-MB03 cells invaded within 24 hours with no significant differences observed between the different trans-well coatings used. The Group 3 medulloblastoma cell line used

had a doubling time of approximately 48 hours, therefore to minimise the confounding effects of concomitant proliferation, a shorter duration of 24 hours for invasion was used for these initial experiments.

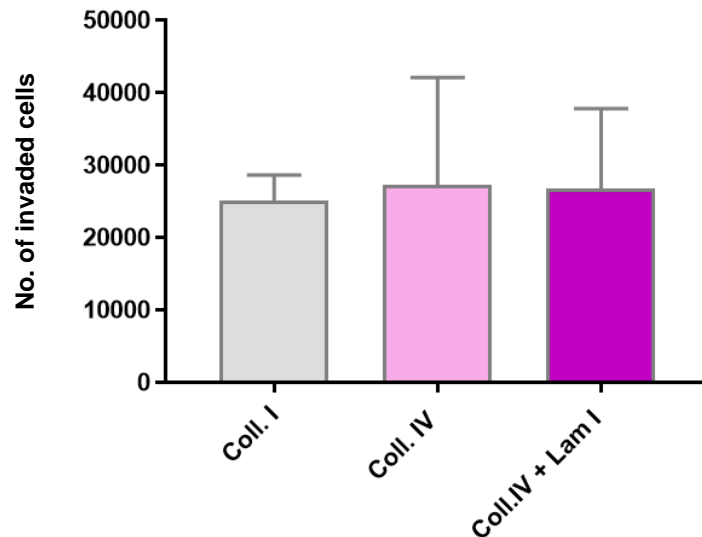


Figure 4.21 24 hour invasion assays of an aggressive Group 3 cell line through different barrier coatings.

100,000 HD-MB03 cells were seeded into trans-wells and allowed to invade through Collagen I (1.5mg/mL), Collagen IV (10µg/mL) and Collagen IV (10µg/mL)/Laminin I (100 µg/mL) coatings (n=3). Invaded cells were dissociated and numbers determined using a Presto blue® standard curve. Similar proportions of seeded HD-MB03 cells invaded through the three transwell coatings.

As similar numbers of HD-MB03 cells invaded through the different transwell coatings (Figure 4.21) and collagen IV/laminin I are well described in the literature as key components of the basal lamina (Hoarau-Véchet J et al, 2014), this combination transwell coating was adopted for all subsequent transwell invasion experiments, to recapitulate invasion through the BBB-a key step in the haematogenous dissemination of MB to the leptomeninges.

4.4.2 The effect of pharmacologic inhibition of MMP-2 and MMP-9 on the rate of transwell invasion across a collagen IV/Laminin I barrier

Having observed that rTIMP-1 treatment of SHH MB spheroids had little effect on the extent of migration of SHH spheroids across extracellular matrices (Figure 4.18, Figure 4.19 and Figure 4.20), it was postulated that TIMP-1 may alter the invasive potential of the aggressive Group 3 HD-MB03 cells. However as previous rTIMP-1 experiments were performed on 3-dimensional spheroid cultures, baseline confirmation of the viability of 2-d cultured cells treated with rTIMP-1 50nM was necessary, to ensure that any changes in the levels of secreted MMP-2 and MMP-9 would be due to the pharmacological inhibition by TIMPs rather than cytotoxicity. To this end, PrestoBlue© was added to matched HD-MB03 cell populations following 72 hours of rTIMP-1 treatment, at 10nM, 25nM, 50nM and 100nM concentrations, alongside vehicle controls Figure 4.22.

As shown in Figure 4.22, HD-MB03 cell viability was preserved in the replicate rTIMP-1 treatments at 25nM, 50nM and 100nM concentrations.

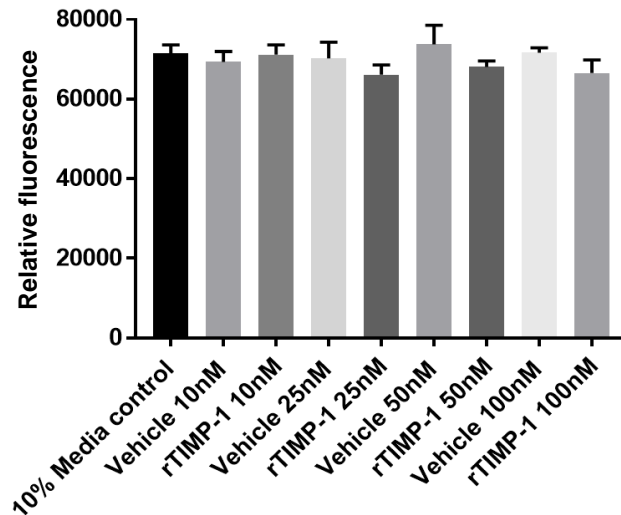


Figure 4.22 PrestoBlue cytotoxicity experiment in 2-dimensional culture of HD-MB03 Group 3 MB cells treated with varying concentrations of rTIMP-1

In comparison to the media control, less than 10% reduction in cell viability was observed after rTIMP-1 treatment of HD-MB03 cells.

Equal numbers of HD-MB03 cells were treated with rTIMP-1 for 48 hours and allowed to invade for 24 hours (Figure 4.23). Interestingly, rTIMP-1 treatment of the Group 3 HD-MB03 cells did not significantly alter their invasive capacity and in the case of Collagen IV trans-well assays, it appeared to slightly increase their migration through the Collagen IV matrix as seen in Figure 4.23. While unexpected, these findings could be due to the effect of increased secreted levels of MMP-2 and MMP-9 stimulated by the presence of their substrate collagen IV, which may counteract the inhibitory effects of rTIMP-1. As observed in the spheroid rTIMP-1 migration experiments, the rTIMP-1 may also cause the cells to adapt to MMP-independent invasion mechanisms.

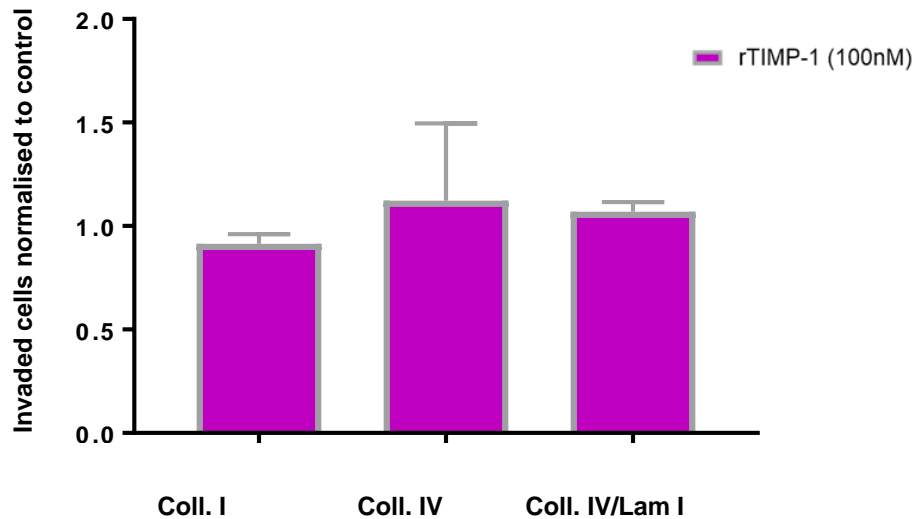


Figure 4.23 Effect of rTIMP-1 treatment on the invasive capacity of HD-MB03 cells (n=3)

Following 48 hours of pre-treatment with rTIMP-1 at 100nM, 100,000 HD-MB03 cells were seeded into trans-wells and allowed to invade through Collagen I, Collagen IV and Collagen IV/Laminin I coatings. The number of rTIMP-1 treated cells that invaded through the barriers were normalised to the numbers of vehicle controls for each corresponding trans-well coating and analysed using GraphPad prism. One-way ANOVA analysis of the mean revealed no statistically significant differences between the three transwell coatings.

4.4.4 Comparison of transwell invasion assays of matched primary and metastatic Group 3 and Group 4 cell lines across a collagen IV/Laminin I barrier

To determine whether the secreted levels of functionally active MMP-2 and MMP-9 would correlate with the postulated increased invasive potential of metastatic Group 3 and Group 4 medulloblastoma, trans-well invasion assays of the matched primary and metastatic Group 3 (D425-Med and D458-Med) and Group 4 (CHLA-01-MED and CHLA-01R-MED) cell lines were performed. As these cell lines are less aggressive

(as denoted by the origin from lower graded M status tumours) and had longer doubling times in comparison to HD-MB03, the duration allowed for the invasion assays was doubled to 48 hours.

As demonstrated in Figure 4.24, nearly a third of the seeded cells from the matched primary and metastatic Group 3 (D425-Med and D458-Med) cell lines invaded through the Collagen IV/Laminin I matrix, over 48 hours. This finding correlated well with the detected levels of functionally active MMP-2 and MMP-9 by gelatin zymography, which were comparable (Figure 3.10).

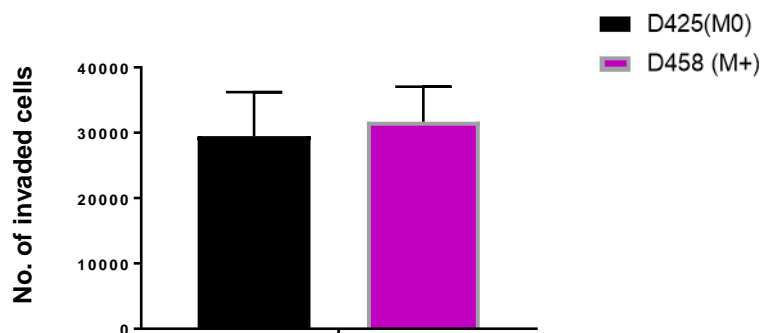


Figure 4.24 Invasion assays (n=3) of matched primary and metastatic Group 3 (D425-Med and D458-Med) cell lines.

Equal cell numbers were seeded into trans-wells coated with Collagen IV/Laminin I and incubated for 48 hours. Invaded cells were dissociated and numbers determined using a Presto blue[®] standard curve (n=3) and analysed using Graphpad prism. As shown, the matched primary and metastatic Group 3 cell lines appeared to have similar invasive capacity.

When equal cell numbers of the matched Group 4 primary and metastatic (CHLA-01-MED and CHLA-01R-MED) cell lines were seeded, a statistically significant difference ($p < 0.05$) in the invasive capacity was

observed as shown in Figure 4.23. While a third of the original number of primary cells invaded across the Collagen IV/Laminin I matrix, almost 50% of the number of metastatic cells invaded within the same 48-hour period. This increased invasive capacity in the metastatic Group 4 cell line CHLA-01R-Med compared to its primary counterpart mirrored the previously demonstrated pattern of increased levels of functionally active MMP-2 in the metastatic Group 4 cell line.

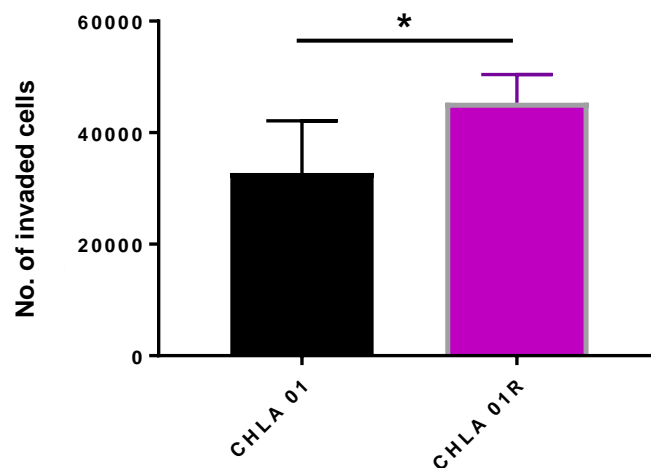


Figure 4.25 Invasion assays (n=3) of matched primary and metastatic Group 4 (CHLA-01-MED and CHLA-01R-MED) cell lines.

Equal cell numbers were seeded into trans-wells coated with Collagen IV/Laminin I and incubated for 48 hours. Invaded cells were dissociated and numbers determined using a Presto blue® standard curve. The difference in the numbers of invaded cells between the primary and recurrent Group 4 cell lines was statistically significant. (n=3+SD t-test*=p<0.05)

These replicate invasion assays appeared to correlate with the differential levels of secreted MMP-2 and MMP-9 by the matched Group 3 and Group 4 cell lines, supporting the hypothesis that the levels of functionally active MMP-2 and MMP-9 could be predictive of the metastatic and invasive potential of medulloblastoma cell lines.

4.5 Summary

In conclusion, the data from the 3-D functional assays of SHH, Group 3 and Group 4 medulloblastoma suggest that:

- ❖ A hyaluronan-rich tumour microenvironment may stimulate increased levels of secreted functionally active MMP-2 and MMP-9 from embedded medulloblastoma cells.
- ❖ The spheroid model proved to be an optimal model for the elucidation of the SHH spheroid migration across a range of extracellular matrices, and their secreted levels of functionally active MMP-2 and MMP-9 in each condition. Interestingly, when seeded on a hyaluronan matrix, the *wtp53* SHH ONS-76 cell line consistently secreted higher levels of MMP-2 and MMP-9 compared to its *p53 mutant* SHH counterpart DAOY when both were seeded on top of Collagen IV. The converse was seen in the *mut.p53* SHH cell line DAOY, which secreted higher levels of MMP-2 and MMP-9 when seeded on top of the collagen IV compared to hyaluronan. This may be as a result of their differential HA/collagen IV receptor densities. It was also observed that the levels of secreted functionally active MMP-2 and MMP-9 increased when the spheroids were cultured on top of a matrix compared to neurosphere medium.
- ❖ While the mode of migration across the matrix may be altered following endogenous MMP-2 and MMP-9 inhibition with TIMPs (as seen in the case of DAOY), the extent of migration was not altered by the TIMP-1

mediated MMP-2/-9 inhibition. This suggests that, as *in vivo*, the tumour cells adapt their migratory behaviour/mechanisms to circumvent the MMP inhibition as seen in the change of collective to more single cell migration in ONS-76 spheroids; or that migration across a matrix does not depend upon proteolysis (Dauth, Grevesse et al. 2016).

- ❖ A collagen IV/Laminin I transwell invasion model demonstrated that the invasive capacities of the MB cell lines that secreted higher levels of functionally active MMP-2 and MMP-9, correlated with their differential invasive capacities. This pattern was clearly demonstrated in the matched primary and recurrent Group 4 cell lines (CHLA-01-MED and CHLA-01R-MED) but was not as distinctive in the Group 3 matched primary and recurrent cell lines (D425-Med and D458-Med).

Chapter 5

**Validation of MMPs as prognostic
biomarkers in tissue and CSF from
paediatric patients with primary and
metastatic medulloblastoma**

5.1 Chapter outline

From epigenetic regulation to zymogen activation, the multiple regulatory checkpoints of matrix metalloproteinases, ensure that their levels of activity are strictly controlled in a physiological context, whereas in patients with aggressive primary and metastatic brain tumours, this homeostasis is lost, resulting in higher than normal expression of matrix metalloproteinases (Friedberg, Glantz et al. 1998). Several authors suggest that this may increase the invasive capacity of the tumour cells and therefore the potential for recurrence in these patients (Vihinen and Kahari 2002). In chapters 3 and 4, by exploring the biological characterisation of matrix metalloproteinases -2 and -9 in primary and metastatic medulloblastoma cell lines, I demonstrated that their levels of functionally active MMP-2 and MMP-9 best correlated with their metastatic potential. For this reason, the levels of functionally active MMP-2 and MMP-9 in CSF samples from paediatric patients with primary, metastatic or recurrent medulloblastoma (defined as relapsed disease following previous recurrence) were determined, using gelatin zymography.

Due to the selective nature of the intact blood-CSF-barrier, the proportion of the tumour-derived MMP-2 and MMP-9 detectable in the patient serum would likely be negligible and therefore undetectable. In addition, the wide range of physiological and pathophysiological systemic functions in which MMPs are involved, would render difficulty in the determination of whether any detectable functionally active MMP-2/MMP-9 levels, were

derived from the circulating medulloblastoma cells or non-specific systemic inflammation. For these reasons, cerebrospinal fluid sampling was determined to be the most sensitive method for the determination of tumour associated levels of functionally active MMP-2 and MMP-9 (Bonner, Bornhorst et al. 2018).

5.2 Objectives and hypothesis

Considering the newer theories that suggest that the mechanisms of metastatic spread from the primary brain tumour to the leptomeninges may involve both haematogenous and cerebrospinal fluid dissemination, we hypothesised that:

1. Epigenetic changes in medulloblastoma occur and may contribute to their increased levels of MMP-2 and MMP-9 gene expression in comparison to normal cerebellum
2. Increased levels of functionally active MMP-2 and MMP-9 within the tumour secretome i.e. patient CSF, will reflect the metastatic capacity of the tumour, either in its capability for upregulation of functionally active MMP-2/ MMP-9, or manipulating its microenvironment by paracrine mechanisms that stimulate microglia, immune and endothelial cells to release active MMP-9 (Kessenbrock, Plaks et al. 2010).

To facilitate easier adoption and clinical translation of our work, we examined samples as they had been routinely obtained and stored in the current clinical manner i.e. cerebrospinal fluid biopsy via day 14 post-operative lumbar puncture, and investigated whether handling and storage of CSF may affect our results. Once the levels of MMP-2 and MMP-9 have been demonstrated to be detectable using laboratory techniques, it was postulated that this would increase the likelihood of their successful radiological detection using our imaging biosensor.

5.3 Liquid biopsy, handling and storage of cerebrospinal fluid samples from paediatric medulloblastoma patients

Cerebrospinal fluid (CSF) is largely produced and secreted from the choroid plexus, a network of modified ependymal capillaries, located in the lateral, third and fourth ventricles of the brain. It represents a modified part of the blood-brain-barrier (sometimes referred to as the blood-CSF barrier) through which cerebrospinal fluid is produced at an approximate rate of 0.3ml/minute in the adult brain (Greenberg and Arredondo 2001). CSF production is thought to be physiologically controlled by sympathetic and parasympathetic outflow, the former innervating α and β 2 adrenoceptors, thereby stimulating vasoconstriction or vasodilatation of the vascular supply to the choroid plexus (Damkier, Brown et al. 2013)

There is emerging evidence of a 'glymphatic' system in the brain, a network of low resistance perivascular channels through which CSF from the subarachnoid space flows alongside arteries and arterioles penetrating the pia into the brain parenchyma. Once in the interstitium, solute exchange between CSF and interstitial fluid occurs, before the CSF permeates the basal lamina of capillaries and proceeds to the perivenular spaces from where it is drained via the cervical lymphatics or absorbed via venous outpouchings known as arachnoid granulations, situated within the subarachnoid space (Jessen, Munk et al. 2015). This facilitated CSF absorption into the venous sinuses usually occurs down a pressure gradient and can be limited in conditions such as venous sinus thrombosis where this gradient may be reversed, or where previous subarachnoid haemorrhage or infection (meningitis), results in occlusion of these arachnoid projections (Damkier, Brown et al. 2013).

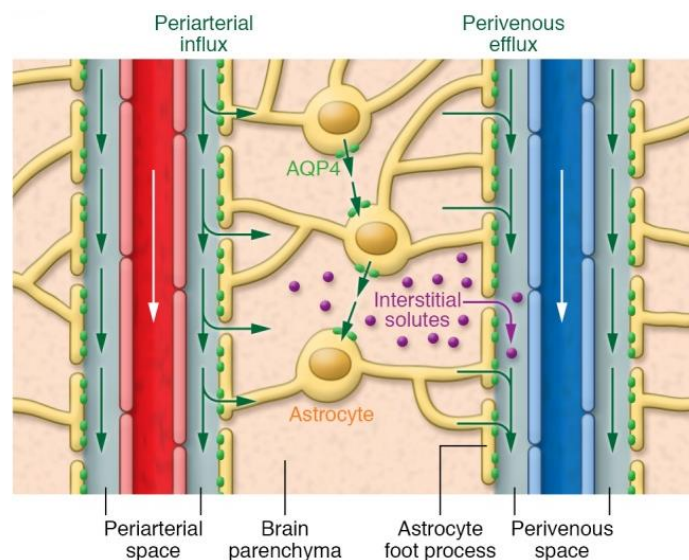


Figure 5.1 Perivascular flow of CSF through the glymphatic system.

CSF flow from the subarachnoid space enters the perivascular space following arterioles as they penetrate the pia. Aquaporin 4 (AQP-4) facilitated CSF-interstitial fluid exchange occurs via the astrocyte foot processes as shown. Figure from (Louveau, Plog et al. 2017)

The embryological development of the choroid plexus neuroepithelium begins within the fourth week and functions at expected capacity shortly after the closure of the neural tube in week 9 of gestation. The total volume of CSF circulating around the brain and spinal cord increases with age. In newborns, approximately 2ml/kg of CSF is reported, while in adults approximately 125-150 ml of CSF are contained in the subarachnoid space at any one time (Greenberg and Arredondo 2001, Damkier, Brown et al. 2013)

In comparison to plasma pH of 7.35-7.45, CSF pH is centred on pH 7.33 with the same osmolality as plasma in physiological conditions. CSF is constituted of 99% water with electrolytes and solutes in the approximate concentrations as indicated below (Table 5.1).

Table 5.1 Comparison of electrolyte content of CSF and plasma.

	CSF	Plasma
Sodium (mEq/L)	138	138
Potassium (mEq/L)	2.8	4.5
Chloride (mEq/L)	119	102
Calcium (mEq/L)	2.1	4.8
pO₂ (mmHg)	43	104
pCO₂ (mmHg)	47	41
pH	7.33	7.35-7.45

As we are interested in the matrix metalloproteinases circulating within the cerebrospinal fluid, the ratio and number of white blood cells present in the CSF, which could be the potential source of the MMPs, would necessitate some consideration (Table 5.2). As per current clinical standards, we adapted the accepted physiological cellular CSF constituents of: 0 polymorphonuclear leucocytes (PMN) which are acute phase immune cells and 0-5 monocytes. We expected clear, colourless CSF to be obtained from paediatric patients following atraumatic lumbar punctures, but accepted that the resulting colour could be influenced by trauma during lumbar puncture, recent surgery or concurrent intrathecal therapy.

Table 5.2 Expected cellular counts in cerebrospinal fluid (Termini, Neman et al. 2014).

Age group	WBC/mm ³	RBC/mm ³
Newborn	7-8	0
Infants 1-12 months	5-6	0
1-2 years	2-3	
Young child	2-3	0
Child 5-15 years	2-3	0
Adolescent & adult	3	0

Where available, this data was collated (Table 5. 3) to ensure that increased MMP-2 or MMP-9 signal was likely to originate from the circulating tumour cells or exuded by the tumour itself, as opposed to the potential MMP secretion by other immune cells within the subarachnoid space.

As discussed in the methodology section of this thesis, cerebrospinal fluid sampling was performed via lumbar puncture in all patients approximately two weeks post-operatively. Briefly, the patient would be positioned in the left lateral foetal position and the posterior superior iliac spine palpated to localise the interspace of interest: L3/4 or L4/5. In children, the latter would be preferred as the spinal cord ends at the L2 vertebral level. Once the back is thoroughly cleaned with an antiseptic solution and a sterile field applied, the entry point is once again confirmed and local anaesthetic infiltrated into the skin and subcutaneous tissues in the midline of the L3/4 interspace. A spinal needle is then advanced and CSF obtained and collected in sterile universal containers. The volumes of CSF samples collected are determined by the patient's age and their ability to tolerate the procedure. The needle is withdrawn and pressure applied to reduce the risk of creating a spinal haematoma. The sample is then sent to the laboratory for urgent sampling and cell cytology, with a short period of refrigeration if a short delay to analysis is expected.

Published literature suggests that increased sampling volumes of cerebrospinal fluid, repeated sampling and sampling of CSF closer to the regions of interest could result in higher yield of the biomarker (Weston, Glantz et al. 2011). To investigate the effect of sampling closer to the tumour site, we collected cerebrospinal fluid on dural entry following craniotomy for further tumour resections in a subset of the paediatric patients included in this study. It is also clinically accepted that, as cerebrospinal fluid is a poor incubatory medium, the time to analysis can

drastically affect the specificity and sensitivity of CSF cytology. This can however be slightly reduced with refrigeration of the sample for a short period if a delayed transport of the sample is expected (Bonner, Bornhorst et al. 2018). For some of the CSF samples examined, it was not possible to determine the duration between the lumbar puncture and the processing of the samples prior to their storage at -80°C, following sampling and analysis in the usual clinical fashion. Table 5. 3 shows the macroscopic and microscopic assessment of the patient cerebrospinal fluid samples used in this study. Informed consent for the study was obtained from each patient's parent or their respective adult with parental responsibility and the study protocols ethically approved by the National Research Ethics Service Committee East Midlands-Nottingham 2.

5.4 Results

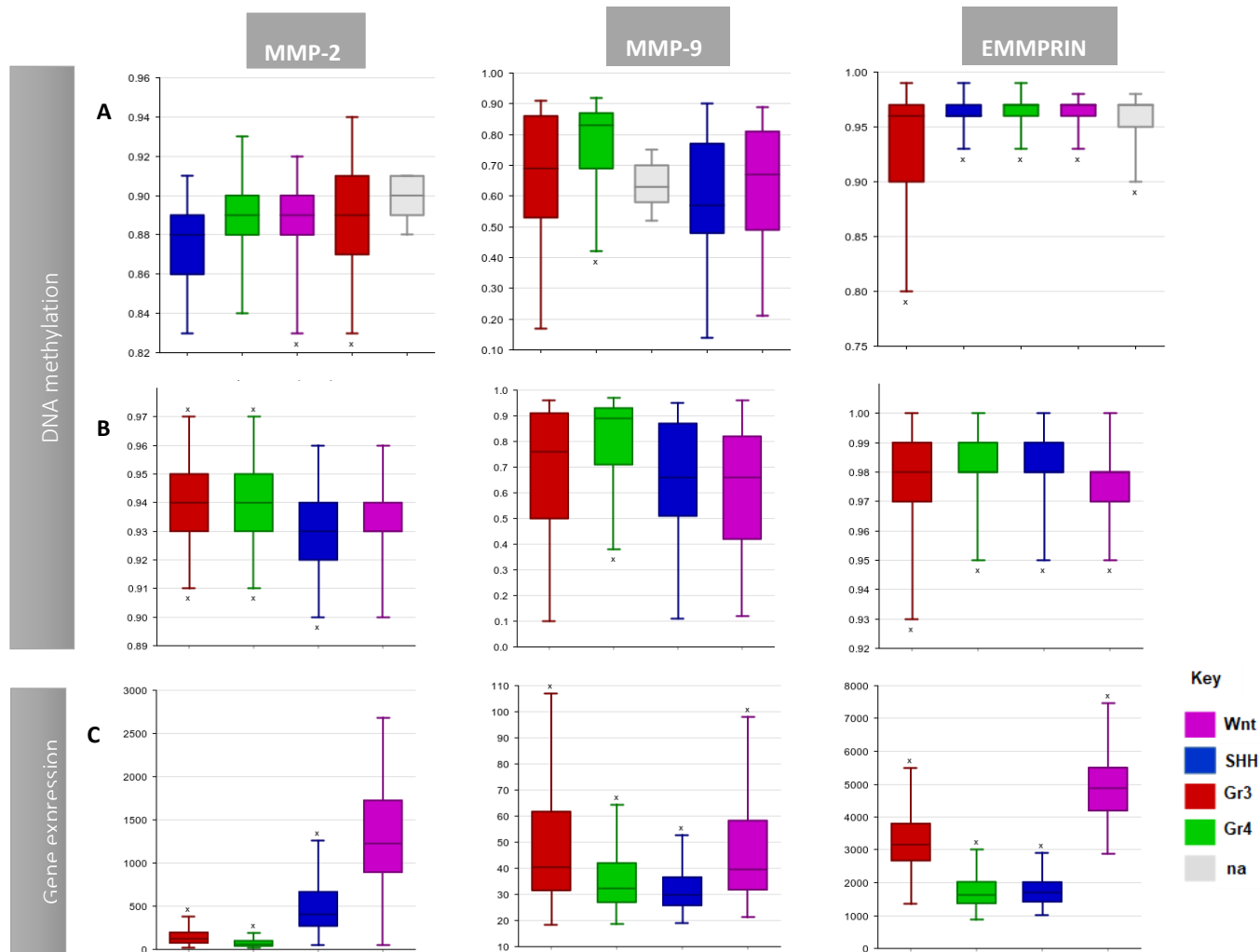
5.4.1 Investigating the epigenetic and genetic landscape of matrix metalloproteinases and their inhibitors

DNA methylation represents one of the epigenetic modifications of gene expression. Other forms of epigenetic regulation include chromatin remodelling and histone modifications. In many cancers, the addition of a methyl group to promoter regions of the gene, often leads to suppression of the gene in question. If this occurs in a tumour suppressor gene, this can trigger a cascade of mechanisms that may culminate in oncogenesis (Roussel and Stripay 2018). As MMPs are extracellular matrix proteins involved in many physiological processes such as cellular proliferation and remodelling of the extracellular matrix in response to injury, it is perhaps not surprising that MMP-2 for example, is constitutively expressed at higher levels in infancy and childhood (Ayoub, Cai et al. 2005). It therefore follows that epigenetic regulation of MMP-2 gene expression could be the level most implicated in tumorigenesis.

To explore this further, analysis of the DNA methylation and gene expression data of MMP-2, MMP-9 and EMMPRIN from fresh frozen and formalin-fixed paraffin embedded normal cerebellum controls and primary medulloblastoma patient samples within the Hovestadt dataset, was performed (Hovestadt, Remke et al. 2013, Hovestadt, Jones et al. 2014, Cavalli, Remke et al. 2017). As shown in Figure 5.2, the DNA methylation of MMP-2 in WNT, SHH, Group 3 and Group 4 MB are slightly lower in comparison to that in normal cerebellum. This relative

hypo-methylation of the MMP-2 gene in all the molecular MB subgroups appears to translate into reduced MMP-2 gene expression. Notwithstanding the considerable variation within the molecular subgroups, the comparison of methylation between the normal cerebellum and the MB subgroups is statistically significant ($p=0.027$). While analysis of MMP-9 DNA methylation revealed higher mean levels of methylation in Group 3, Group 4 and WNT tumours in comparison to normal cerebellum and SHH, the pattern of resulting gene expression was more complex than that for MMP-2. Mean levels of DNA methylation were observed to be highest in Group 4 tumours with resulting gene expression much lower than in Group 3 or WNT tumours, while SHH tumours with similar methylation levels to WNT, exhibited lower gene expression of MMP-9, suggesting subgroup specific differences in the effects of DNA methylation of MMP-9 exist.

Extracellular matrix metalloproteinase inducer (EMMPRIN) stimulates MMP release from tumour cells and the stromal cells in their proximity and has been correlated with poorer prognosis in MB (Chu, Chen et al. 2011). For this reason, its DNA methylation and gene expression were examined in the same manner as for MMP-2 and MMP-9. As shown in Figure 5.2, DNA methylation levels in EMMPRIN in all four MB subgroups were very similar to that observed in normal cerebellum tissue. Correlation of the two within the Cavalli dataset performed on the R2 Genomics Analysis and Visualisation platform suggested that hypermethylation of EMMPRIN results in its reduced gene expression.



The DNA methylation profiles and gene expression of the main MMP-2 and MMP-9 inhibitors, the tissue inhibitors of metalloproteinases TIMP-1 and TIMP-2 (Figure 5.3), were also examined. DNA methylation levels of TIMP-1 was observed to be lowest in the Wnt subgroup, with a resulting higher gene expression in the same. However, in Group 4 MB that exhibited the highest mean DNA methylation pattern, its TIMP-1 gene expression was the lowest of all the MB subgroups, suggesting that DNA methylation of the TIMP-1 gene inversely correlates to its gene expression.

While in the case for the TIMP-2 gene (Figure 5.2), both its DNA methylation profile and gene expression followed a similar pattern where both were observed to be highest in the Wnt subgroup, followed by Group 4 and Group 3, with SHH being the exception to the rule.

This data suggests that while epigenetic regulators of genes coding for MMPs and their inhibitors can inform our understanding of the pathogenesis of MB and inform our prognostication in some cases, the endpoint of their gene expression, gene transcription, protein translation and their secretion as functionally active enzymes, may provide better, measurable biomarkers of metastasis.

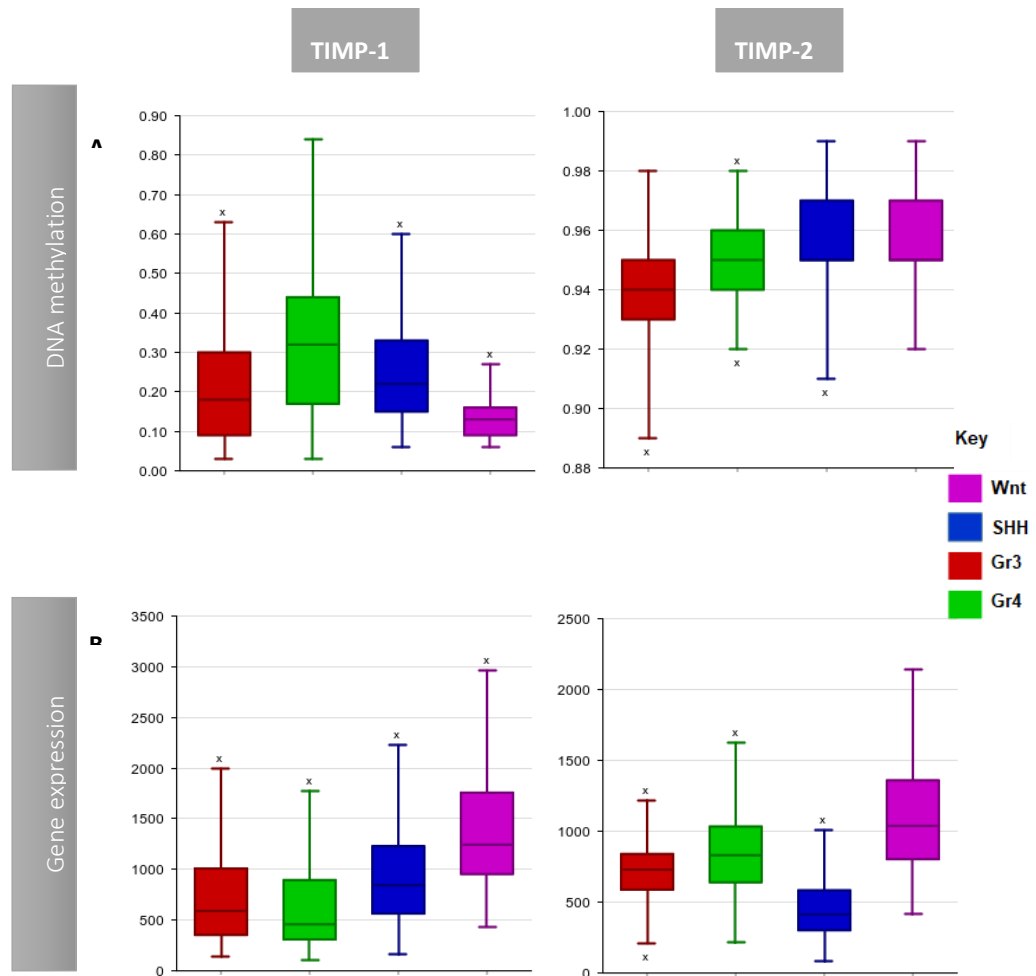


Figure 5.3 Correlation of DNA methylation patterns of TIMP-1 and TIMP-2 with their resulting gene expression in MB patients from the Cavalli dataset, as analysed on the R2 Genomics and Visualisation platform.

While there appears to be a correlation of TIMP-1 hypermethylation to increased TIMP-1 gene expression, this relationship is less clear for TIMP-2, where the pattern of methylation largely resembles that of its gene expression. However, there does appear to be a clear difference in the levels of hypermethylation of TIMP-2 in comparison to TIMP-1.

5.4.2 Gelatin zymography of cerebrospinal fluid from patients with primary and recurrent medulloblastoma

Characteristics of the cerebrospinal fluid samples obtained from the paediatric MB patients in our pilot study are demonstrated in Table 5. 3.

Table 5. 3 Characteristics of CSF sampled from paediatric patients with medulloblastoma							
Patient ID/ CSF source	Age at sampling	Primary/ recurrence	Volume received	Macroscopic appearance	Cell counts /μl	Cytology results	Documented concurrent systemic/ neurological infection
1[1] Lumbar	7 years old	Primary	10mL	Clear colourless fluid	RBC 340 PMN 0 Lymph 4 Mono 0 No organisms	Neoplastic cells seen	No
1[2] Lumbar	7 years old	Residual	4ml	Clear, straw coloured	No counts available	no neoplasia	No
2[1] Lumbar	20 years old	Recurrence	5mL	Clear fluid	No counts available	no neoplasia	No
2[2] Lumbar	20 years old	Relapse	12 ml	Clear colourless fluid	RBC 114 PMN 0 Lymph 1 Mono 0	No neoplasia	No
3[1] Lumbar	5 years old	Recurrence	10mL	Clear pale yellow fluid	No counts available	No convincing evidence of disseminated medulloblastoma	No
3[2] Subdural	6 years old	Relapse	Theatre sample	Clear colourless fluid	No counts available	no neoplasia	No
4[1] Subdural	13 years old	Primary	Theatre sample	Clear colourless fluid	RBC 6 WBC 0	No atypical cells	No
4[2] Lumbar	13 years old	Recurrence	5mLs	Clear colourless fluid	No counts available	No diagnostic evidence of neoplasia	No

Table 5.3 continuation: Characteristics of CSF sampled from paediatric patients with medulloblastoma

5[1] Lumbar	7 years old	Relapse	4mls	Clear colourless fluid	No cell counts available		No
6[1] Lumbar	12 years old	Primary	8mls	Clear colourless fluid	No cell counts available	no neoplasia	No
6[2] Lumbar	14 years old	Recurrence	5mls	Clear colourless fluid	No cell counts available	No viable cells	No
6[3] Ventricular	14 years old	IT chemo monitoring	4mls	Clear colourless fluid	RBC 285 WCC 0	No neoplastic cells	No
6[4] Ventricular	14 years old	IT chemo monitoring	5mls	yellow colourless fluid	PMN 1	No atypical cells	No
6[5] Ventricular	14 years old	IT chemo monitoring	5mls	yellow colourless fluid	No cell counts available	No neoplastic cells	No
6[6] Ventricular	14 years old	IT chemo monitoring	5mls	yellow colourless fluid	No cell counts available	No neoplastic cells	No
6[7] Subdural	14 years old	Theatre sample	-	Clear colourless fluid	No cell counts available	No neoplastic cells	No

Patient 1

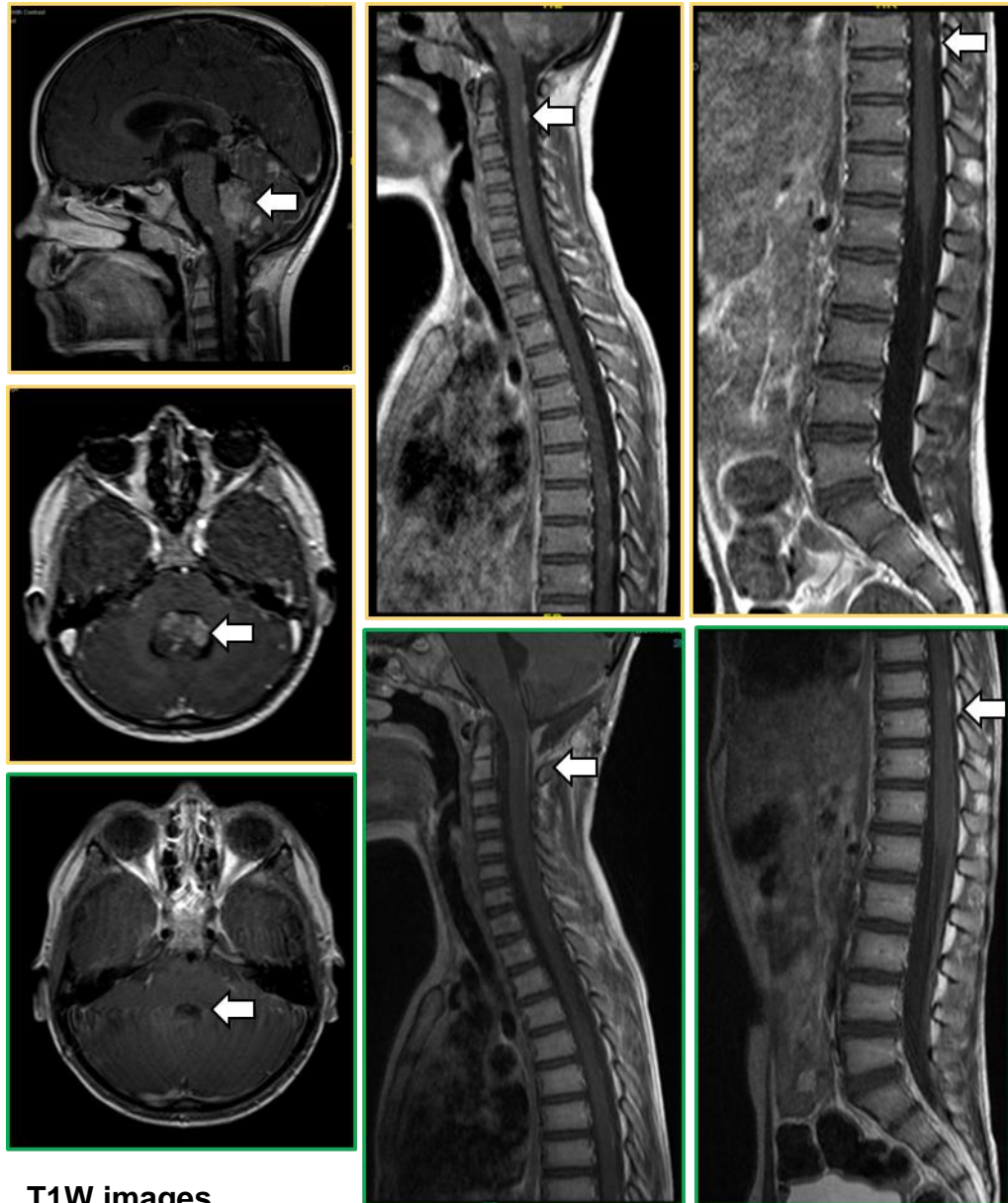
Patient 1 was a 7-year-old previously fit and well boy, who presented following a three-week history of progressive, intermittent vomiting associated with frontal headaches and unsteadiness on his feet. Initial contrast enhanced magnetic resonance imaging showed a 2.7 X 2.4 X 3 cm lesion arising from the cerebellar vermis, causing obstructive hydrocephalus. (Fig. 1) Neuroaxial imaging also demonstrated multiple enhancing nodules throughout his spine down to the cauda equina. He underwent an emergency posterior fossa craniotomy for resection of his midline cerebellar tumour and placement of an external ventricular drain (later revised to a ventriculoperitoneal shunt) for hydrocephalus management. Histological examination confirmed an anaplastic medulloblastoma. A small enhancing residuum in the inferior 4th ventricle and extensive leptomeningeal disease was evident on his post-operative imaging (Fig.5.2) As his CSF cytology obtained via lumbar puncture 2 weeks post-operatively was positive for clusters of neoplastic cells, his disease was staged as M3 and an intensive course of craniospinal irradiation (39.6Gy in 22 fractions with a total dose of 55.8Gy in 31 fractions to the 'boost zone' or resection cavity and possibly other areas of metastatic disease) and chemotherapy according to St. Jude's protocol was commenced(Thompson, Ashley et al. 2020).

Unfortunately, patient 1's tumour seemed to be chemo-resistant as follow-up MRI imaging performed 6 weeks later, showed increased abnormal leptomeningeal enhancement; most marked within the spine

where there were more confluent areas of enhancement. Interestingly, a further cerebrospinal fluid biopsy obtained at this point was devoid of neoplastic cells and therefore deemed negative. While gelatin zymography of his cerebrospinal fluid at initial operation was weakly positive, in keeping with the cytology result (see sample 1(1)), the CSF sample at recurrence (fig sample 1(R2)), demonstrated a 72.3% increase in levels of functionally active MMP-2 and a 100% increase in detectable levels of functionally active MMP-9, despite the negative CSF cytology result.

Radiotherapy was then initiated, with good treatment response demonstrated on imaging performed 2 months after. He however required further surgery to improve his response to RT and underwent a subtotal resection of the residual cerebellar mass and nodular enhancing lesion in his left cerebellopontine angle.

Patient 1's leptomeningeal disease responded well to the intensive radiotherapy regime, with no evidence of convincing intracranial or intraspinal disease seen at imaging 4 months after. He unfortunately developed panhypopituitarism and periventricular cavernomas due to his RT but remains stable with surveillance 4 monthly MR-imaging.



T1W images

Figure 5.4 Patient 1: T1 weighted (T1W) post-contrast pre-operative (yellow-outlined) and post-operative (green-outlined) magnetic resonance imaging.

Patient 1 pre-operative MRI with contrast imaging demonstrating a midline posterior fossa mass avidly enhancing with contrast. Spinal imaging shows nodular enhancement in the upper cervical cord. Post-operative imaging showing residual tumour (indicated by white arrow) surrounding 4th ventricle in Patient 1 cranial MRI head with contrast axial T1W slice and contrast enhanced spinal MRI with contrast (sagittal views) showing reduced leptomeningeal enhancement in upper cervical and thoracic spine following irradiation of the neuroaxis.

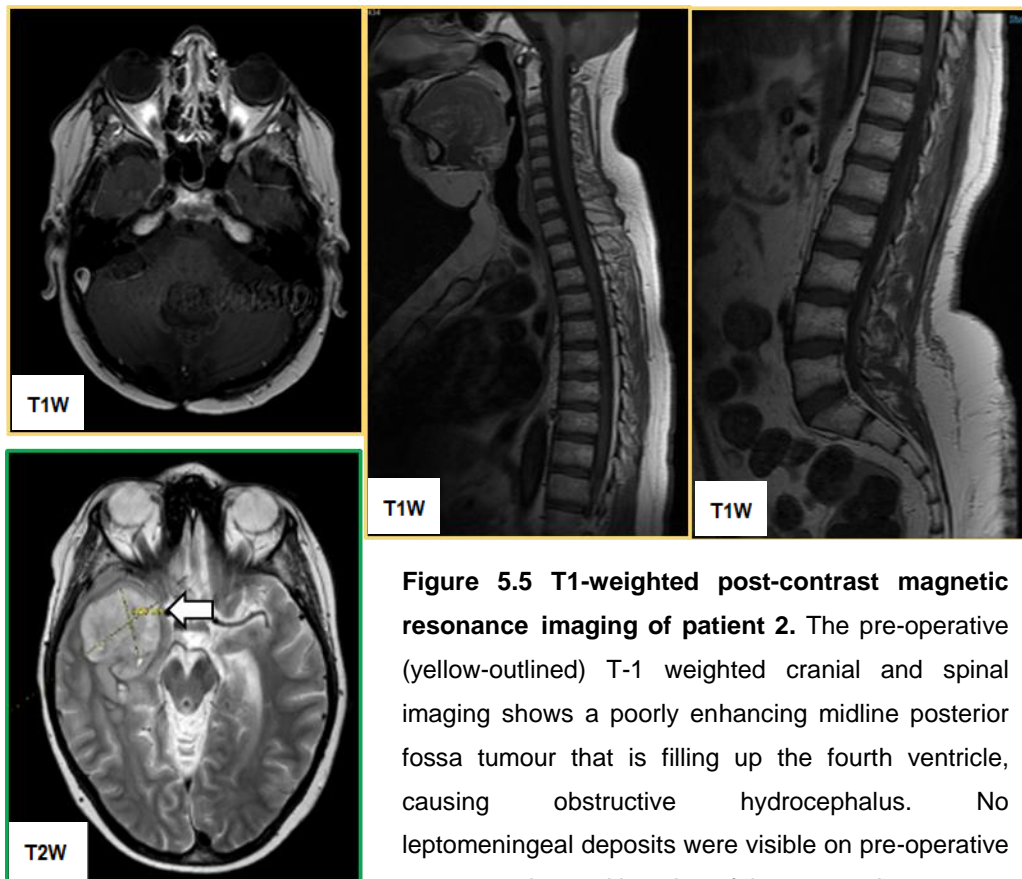
Patient 2

Patient 2 first presented at 11 years of age with a 3-month history of early morning headaches and vomiting, followed by a few days of ataxic gait. Computer tomography imaging revealed a posterior fossa space occupying lesion causing obstructive hydrocephalus, for which he initially underwent debulking surgery via a posterior fossa craniotomy and a third ventriculostomy. Residual disease was seen in the foramina of Luschka. Histological diagnosis confirmed a classical medulloblastoma and metastasis was excluded on the basis of negative post-operative imaging and cerebrospinal fluid cytology. Patient 2 therefore commenced adjuvant chemoradiotherapy (POG 9031).

His disease unfortunately relapsed 4 years later at which time he was treated with combination chemotherapy of oral and intrathecal Etoposide, Irinotecan and Temozolomide. Recurrence of patient 2's disease 3 months following completion of chemotherapy was detected on follow-up magnetic resonance imaging, which demonstrated enhancing foci with associated restricted diffusion in the right anterior temporal lobe and right lateral ventricle. This prompted further surgical debulking of his cerebellar disease and adjuvant Temozolomide/Cyclophosphamide chemotherapy. Despite these measures, patient 2's intracranial disease progressed further to multiple enlarged leptomeningeal deposits, the largest in the right temporal lobe and the right lateral ventricle. These deposits continued to grow

alongside a new radiotherapy associated meningioma. He was therefore palliated and succumbed to his disease soon after.

Interestingly, patient 2 never had definitive radiological evidence of enhancing disseminated spinal disease, which may explain why all his cerebrospinal fluid cytology results were negative in the face of obvious intracranial disease progression. Zymography of his cerebrospinal fluid detected persistent levels of functionally active MMP-2 and MMP-9 with progression of his disease, despite negative cerebrospinal fluid cytology.



T2-weighted MR imaging at recurrence (green-outlined) showing a large temporal tumour that grew from 3.6X3cm to 4.25X3.4cm (shown) over a period of 3 months. In addition to further leptomeningeal deposits in the spine and right lateral ventricle, discovery of this tumour contributed to the patient's poor prognostication resulting in his palliation.

Patient 3

Patient 3 was a 4-year-old boy who presented with a 4-week history of headaches, vomiting and unsteadiness. On admission, he was increasingly drowsy but rousable with a left 6th cranial nerve palsy. Pre-operative imaging revealed a midline posterior fossa tumour with patchy contrast enhancement and avid diffusion restriction, causing obstructive hydrocephalus for which he had emergent placement of an external ventricular drain (later converted to a ventriculoperitoneal shunt). He subsequently underwent subtotal resection of the cerebellar tumour, which was confirmed to be a Group 4 medulloblastoma. Magnetic resonance spectroscopy performed on this occasion demonstrated a marked choline peak with no identifiable N-acetyl aspartate peak. Of note, the post-operative imaging did not confirm presence or absence of residual or metastatic disease due to the poorly enhancing nature of the primary tumour following contrast administration. For this reason, Patient 3's follow-up imaging was repeated 1 month post-operatively and revealed a mildly T2/FLAIR sequence nodular enhancing lesion in the midline posterior fossa measuring 2.1X 2.2 cm, which was likely residual disease. He was therefore initiated on craniospinal irradiation and combination chemotherapy (Vincristine, CCNU and Cyclophosphamide). Despite this, his residuum progressively enlarged until its growth plateaued. At this point the neuro-oncology multidisciplinary team recommended further surgery and patient 3 underwent a further craniotomy and debulking of his residual disease which was confirmed to be completely excised on post-operative imaging with no evidence of

spinal disease. He continued his adjuvant chemoradiotherapy, but unfortunately developed tumour recurrence within 14 months of his second surgery culminating in further surgery for this and adjuvant chemoradiotherapy.

Once more, cerebrospinal fluid (CSF) cytology assessed throughout his recurrent disease was negative on all except one occasion, when it was reported as indeterminate with cells showing striking atypia which could not conclusively be ruled out as a minor population of neoplastic cells. At the point of his last surgery (Figure 5.10, sample 3[2]), his CSF cytology was negative despite the demonstrably increased levels of MMP-2 and MMP-9 following gelatin zymography of the same samples.

Following an intensive course of adjuvant craniospinal irradiation, Patient 3 has remained clinically well, with no radiological detection of recurrence of his disease to date.

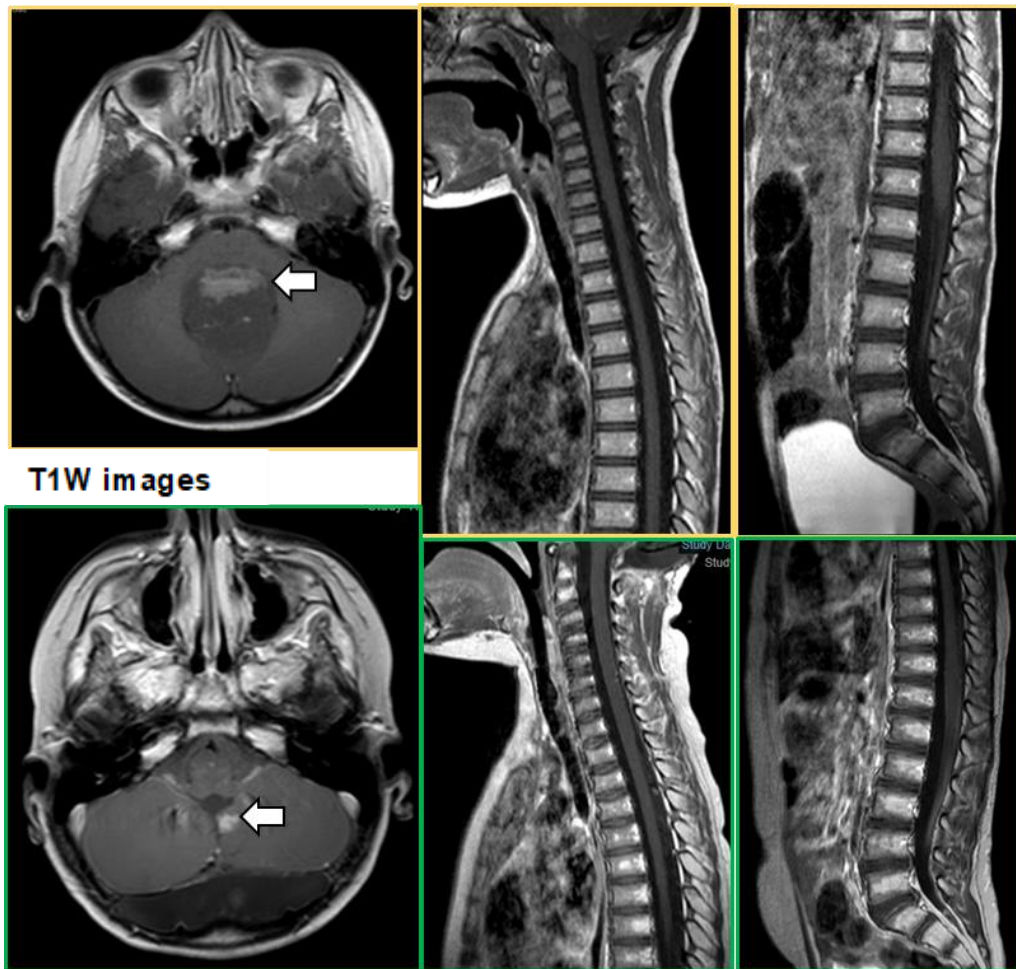


Figure 5.6 T1-weighted post-contrast magnetic resonance imaging of patient 3. Patient 3's pre-operative (yellow-outlined) T1-weighted MRI with contrast cranial imaging showing a midline posterior fossa mass with patchy enhancement. Spinal imaging was clear of leptomeningeal disease. At patient 3's 2nd relapse (green-outlined), T1-weighted contrast-enhanced cranial imaging showed a midline posterior fossa mass with patchy enhancement. Spinal imaging remained clear of leptomeningeal disease.

Patient 4

Patient 4 was a 13-year-old boy who presented with a 2-week history of frontal headaches, ataxia and papilloedema on examination. His imaging on admission showed a 4X3.8cm midline heterogeneous lesion within the 4th ventricle compressing the brainstem with patchy contrast enhancement and mild diffusion restriction. Magnetic resonance spectroscopy demonstrated a marked choline peak with minimal NAA elevation. Patient 4 underwent a posterior fossa craniotomy (and had subsequent placement of an external ventricular drain) for complete resection of his disease. No metastatic dissemination was detected on postoperative imaging. Histological analysis confirmed a Group 4 medulloblastoma and no evidence of viable tumour cells on post-operative CSF cytology or follow-up imaging. As such, patient 4 was commenced on standard risk MB craniospinal radiotherapy followed by chemotherapy. He unfortunately developed posterior fossa syndrome with marked limb weakness, swallowing and speech difficulties necessitating intensive neurorehabilitation, with no obvious cause exhibited on post-operative imaging.

Patient 4's initial cerebrospinal fluid samples were obtained at diagnosis in theatre (sample 4(1)) and following lumbar puncture 6 weeks after (sample 4(2)). While the cytology was negative, we obtained 2.5X higher levels of functionally active MMP-2 in the recurrent sample compared to that taken previously as shown in table 1.

Patient 4 remains clinically stable to date with no evidence of recurrence on follow-up imaging.

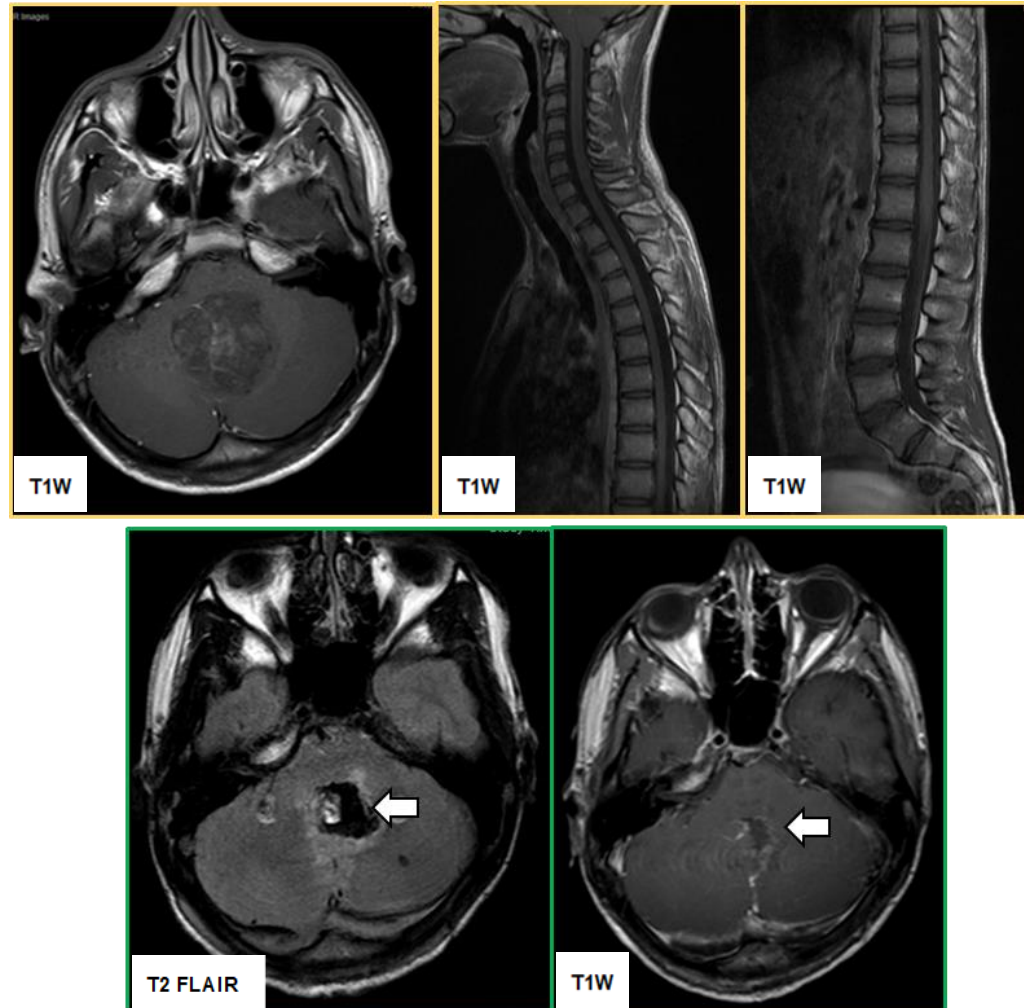
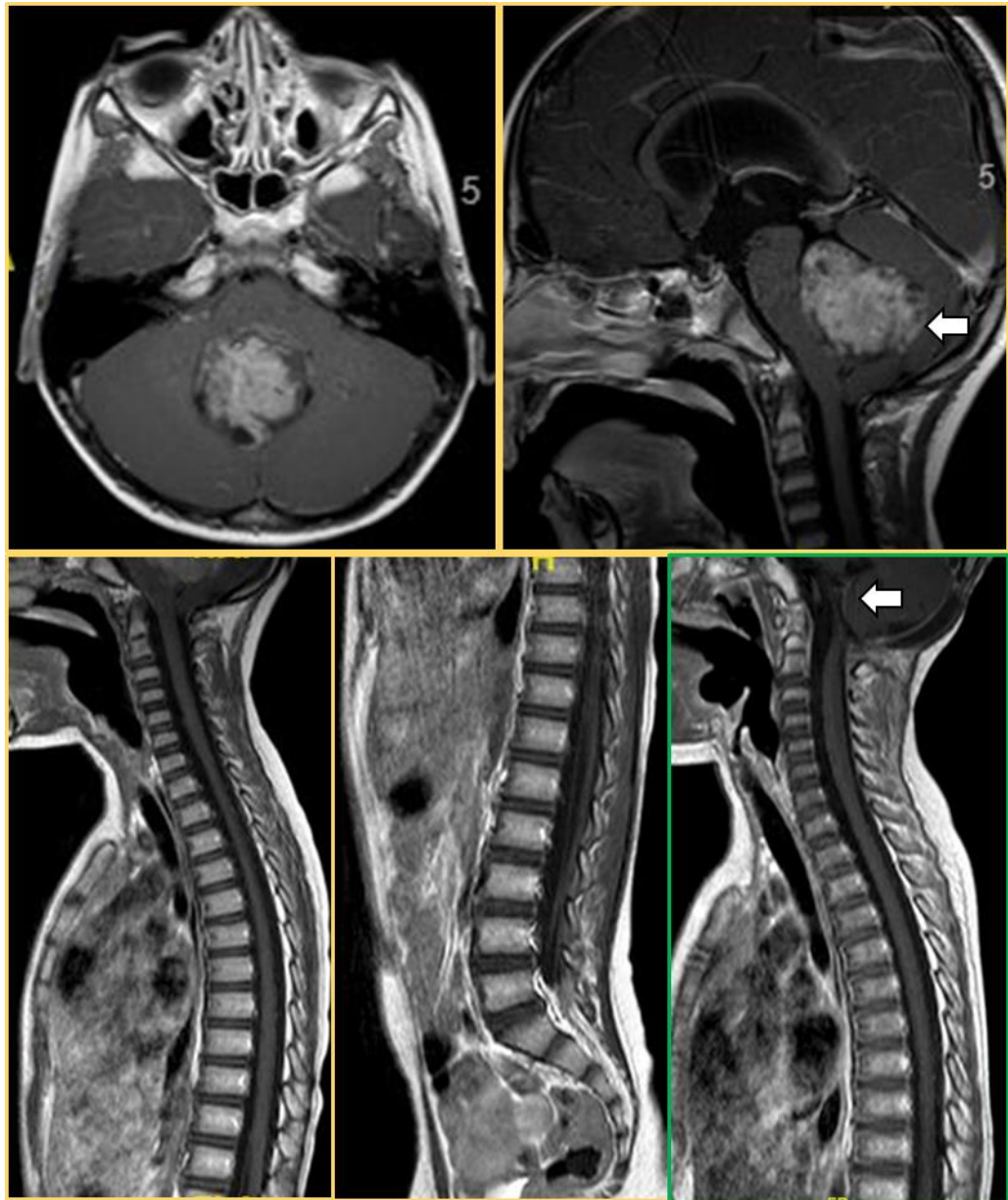


Figure 5.7 T1-weighted post-contrast magnetic resonance imaging of patient 4. Patient 4's pre-operative (yellow-outlined) MRI with contrast imaging of Patient 4 demonstrating a 4 cm lesion within the 4th ventricle with solid and cystic components resulting in patchy enhancement, with no evidence of spinal disease. Patient 4 required repeated post-operative MRI (green-outlined) with contrast due to the residual enhancement on the T2 FLAIR sequence (bottom left image), suspected to be residual disease. The bottom right image shows repeated T1W MRI head with contrast performed 4 weeks later, which confirmed residual enhancement, necessitating repeated cerebrospinal fluid cytology.

Patient 5

Patient 5 was 5 years old at his initial diagnosis with medulloblastoma, having presented with a 3-4 month history of occasional headaches. He underwent macroscopic complete resection of his 4th ventricular tumour, followed by adjuvant craniospinal irradiation and Cisplatin/Etoposide combination chemotherapy that was later changed to Cyclophosphamide and Vincristine, due to patient's intolerance of the previous regime. As a consequence of his treatment, he later required growth hormone and thyroid hormone replacement but remained disease free for over a year. He was unfortunately found to have relapsed disease on surveillance gadolinium enhanced magnetic resonance imaging, which demonstrated a 3mm focal enhancing nodule with associated diffusion restriction at the right lateral aspect of the 4th ventricle, 28 months after his initial diagnosis. Patient 5 therefore had a further surgery for resection of the enhancing nodule in the right lateral 4th ventricle via an occipital craniotomy. Complete resection was confirmed on post-operative imaging and his post-operative CSF cytology was also devoid of neoplastic cells. Of note, this sample remained strongly positive on gelatin zymography as shown in figure 5.10. (Patient 5[1]).

He therefore went on to have stereotactic radiosurgery and unfortunately developed a radiation-associated tumour-a frontal osteosarcoma at age 9, which required further surgery. He remains on active surveillance imaging with no evident recurrent disease so far.



T1W images

Figure 5.8 T1-weighted post-contrast magnetic resonance imaging of patient 5.

Axial and coronal imaging at Patient 5's initial presentation (yellow-outlined) demonstrating an enhancing large 4th ventricular tumour and no evidence of spinal leptomeningeal disease. He had complete macroscopic resection of his primary tumour, 2 years prior to his recurrence 28 months later. The recurrence is demarcated by the white arrow shown in the imaging outlined in green.

Patient 6

Patient 6 presented with a 5-week history of headaches and vomiting at 12 years old. Initial MR imaging showed a posterior fossa minimally enhancing tumour, causing obstructive hydrocephalus. Marked elevated choline peaks and absent NAA/lipid peaks were demonstrated on MR spectroscopy. Neuroaxial imaging excluded disseminated disease and patient 6 therefore underwent macroscopic resection of his tumour and adjuvant standard risk chemoradiotherapy. Histology confirmed classical medulloblastoma and his post-operative CSF cytology showed no diagnostic evidence of neoplasia. Patient 6 remained well until 20 months post-operatively; when new multiple non-enhancing lesions were detected in the left superomedial cerebellum in addition to bilateral periventricular diffusion-restricting lesions. He then underwent stereotactic radiosurgery and placement of an Ommaya reservoir for intrathecal etoposide therapy. Initial follow-up imaging showed progressive enlargement of the periventricular lesions but 5 months after initiation of treatment for his relapsed disease, MR imaging demonstrated complete resolution in 2 of 3 lesions with ongoing improvement. Cerebrospinal fluid samples for this patient were collected at initial (Sample 6[1]) and subsequent operation as well as opportunistically via the Ommaya reservoir, prior to administration of intrathecal chemotherapy. In both samples from his primary operation and at the insertion of the Ommaya reservoir, CSF cytology was negative despite radiologically proven metastatic deposits. Of note, gelatin zymography

was sensitive enough to detect changes in his disease response following consecutive intrathecal administrations as shown in Fig 1.

He thereafter had further surgery for resection of the residual lesion, on which occasion we collected and analysed a cerebrospinal fluid sample on dural entry (sample 6[6]). Patient 6 has since remained well with no evidence of disease recurrence on surveillance imaging.

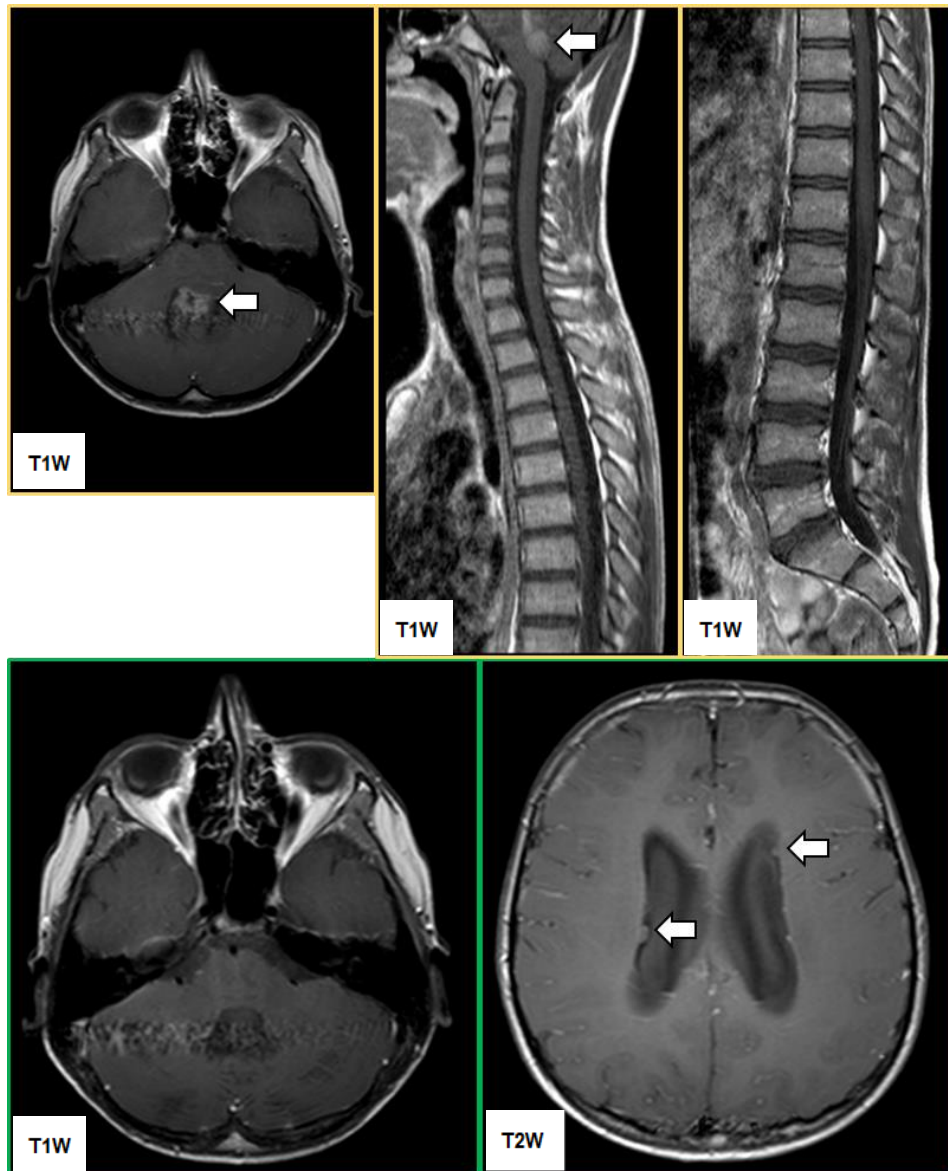


Figure 5.9 T1-weighted post-contrast magnetic resonance imaging of patient 6.

Patient 6's imaging at first presentation (yellow-outline) demonstrating a minimally enhancing posterior fossa lesion (indicated by white arrow) with no detectable lesions on spinal imaging. The green-outlined contrast imaging (left) and T2W imaging (Zeltzer, Boyett et al.) at relapse 24 months post-operatively showed that while no disease recurrence was detectable at the primary site, 3 sites of recurrent subependymal disease were detectable in the lateral ventricles. 2 of these are demonstrated by the white arrows. These lesions responded well to intrathecal etoposide chemotherapy.

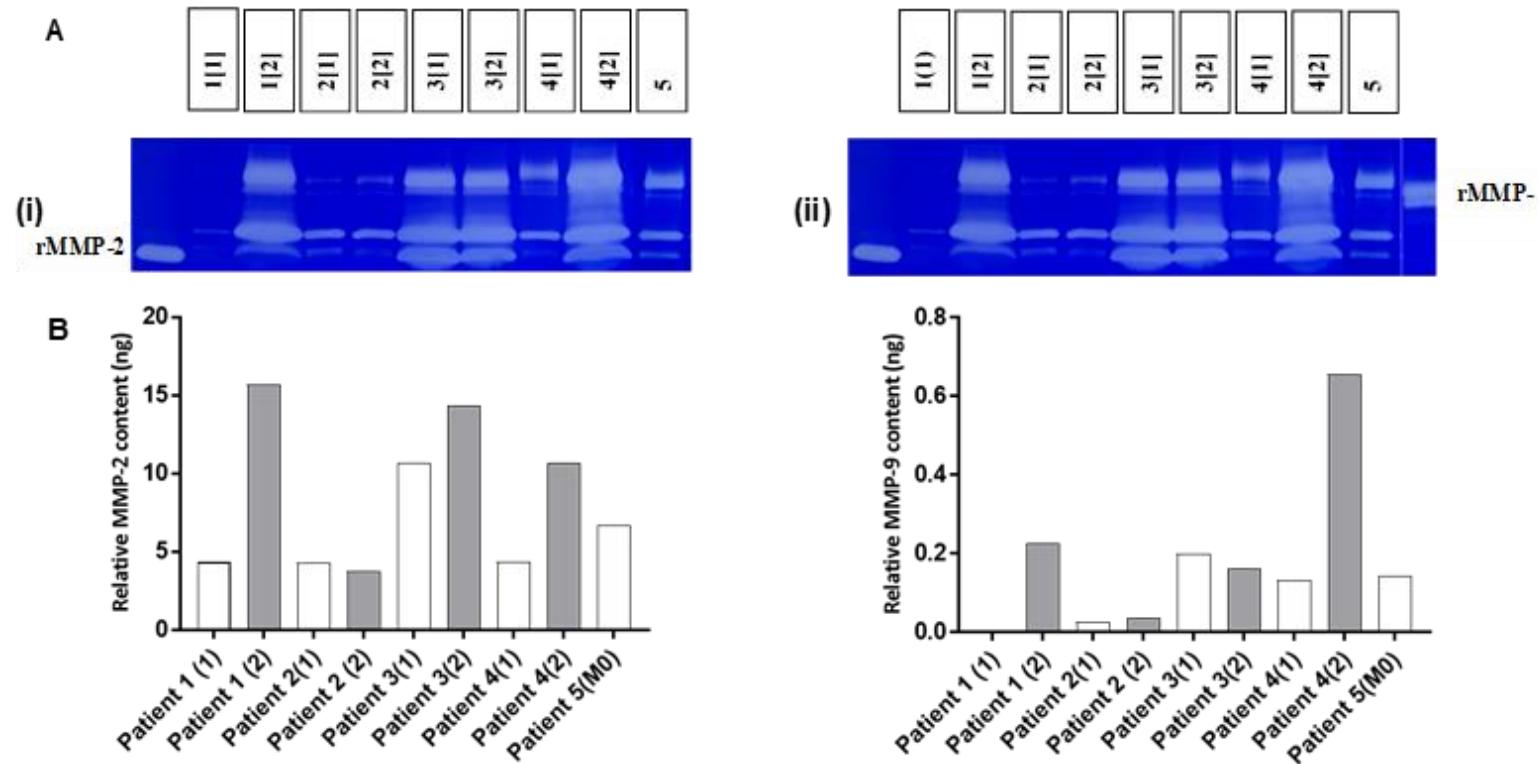


Figure 5.10 Levels of functionally active MMP-2 and MMP-9 within cerebrospinal fluid from matched primary and recurrent MB paediatric patients.

A. Gelatin zymography of cerebrospinal fluid samples obtained from patients with matched primary and recurrent medulloblastoma (Patients 1-4, 6) and relapsed medulloblastoma in patient 5. **B.** Image J Densitometry demonstrating the content of functionally active MMP-2 and MMP-9 in the primary and metastatic samples, relative to the loaded recombinant MMP-2 and MMP-9 controls. As shown, in patients 1, 3 and 4 the levels of functionally active MMP-2 were higher at recurrence, while the levels of MMP-9 were increased in all recurrent samples.

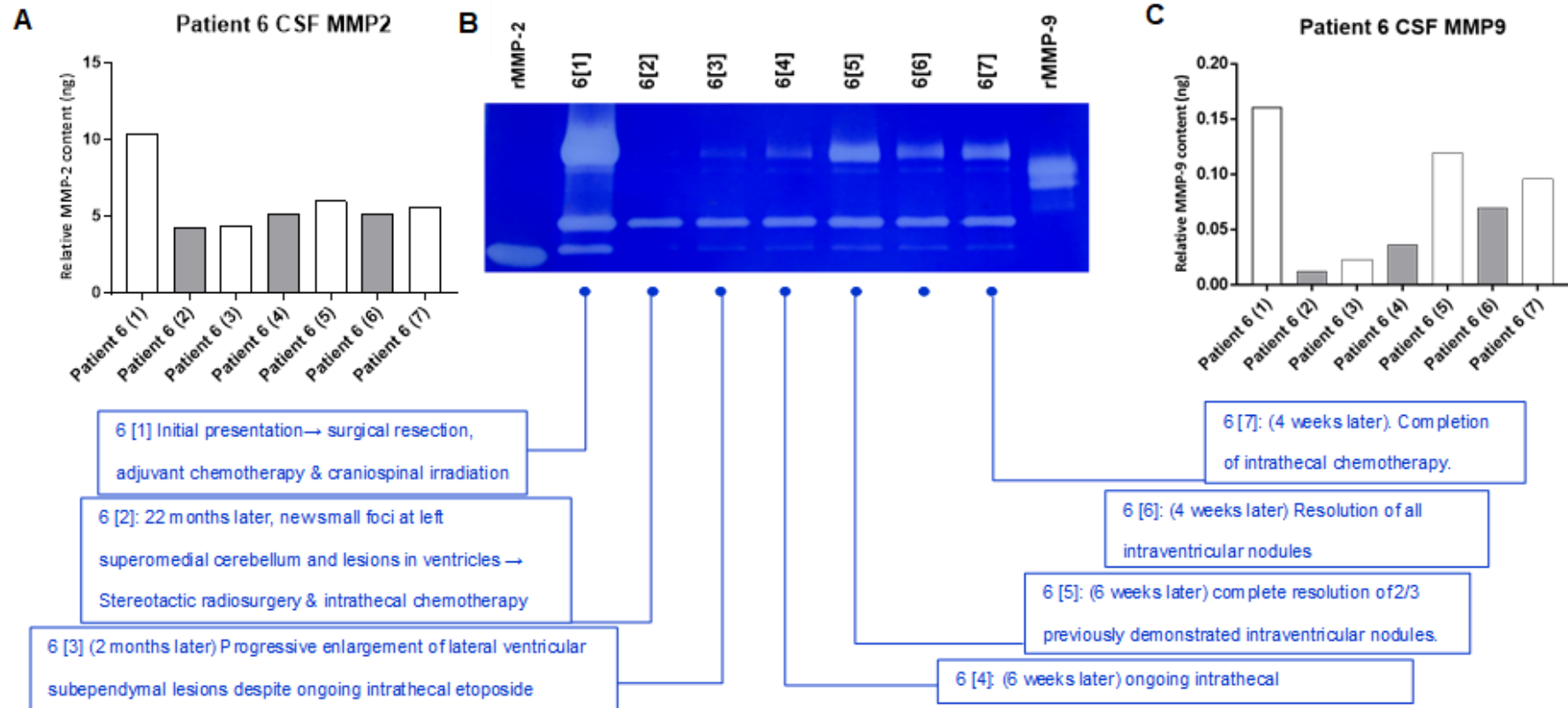


Figure 5.11 Serial cerebrospinal fluid samples from Patient 6 in whom surgical resection of his primary tumour was performed prior to sample 6 [1] and recurrence detected at 6 [2]. B. Gelatin zymography of his CSF samples demonstrated stepwise increased signal intensity of functionally active MMP-2 and MMP-9 from detection of the recurrent tumour from 6[2] to 6[5] and reduction in signal intensity with ongoing treatment from 6[5] to 6[7]. A and C demonstrate MMP-2 and MMP-9 densitometry determined using Image J.

Table 5.4 Characteristics of paediatric medulloblastoma patients.

Patient	Primary/ Recurrence	Gender	Age at presentation	Time to recurrence (months)	Imaging	Extent of resection	Histology	Lumbar CSF cytology	Molecular subgroup	Chang's staging
Patient 1	Primary	Male	8 years	N/A	Midline cerebellar vermis tumour with multiple leptomeningeal enhancing nodules in the posterior fossa and spinal surface.	Subtotal resection	LCA	Positive		M3
	Residual			N/A		N/A		Negative		
Patient 2	Recurrence	Male	11 years	24 months	Multiple new/enlarged leptomeningeal deposits on R. inferior temporal lobe	Subtotal resection	Classical	Negative	Not performed	M2
	Relapse			12 months	Right anterior temporal lobe lesion+ foci in tight superior cerebellar peduncle	Subtotal resection		Negative		M2
Patient 3	Recurrence	Male	4 years		Posterior fossa midline space occupying lesion	Gross total resection of residual midline cerebellar tumour	Classical	Negative	Group 4	M0
	Relapse			14 months	Mildly T2/FLAIR hyperintense lesion at site of previous tumour	Maximal safe resection	Classical	Theatre sample		M3

Patient 4	Primary	Male	13 years	N/A	4 th ventricular lesion with solid and cystic components & patchy enhancement	Gross total resection	Classical	Negative	Group 4	M0
	Recurrence			2 months	Recurrent 4 th ventricular nodule	Gross total resection	Classical, No MYC/MYCN/mon.6, No CTNNB1/tp53 mut.	Negative		
Patient 5	Relapse	Male	7 years	28 months	Enhancing nodule right lateral 4 th ventricular lesion	Gross total resection	Classical	Negative	Group 3	M0
Patient 6	Primary	Male	12 years	N/A	Posterior fossa tumour obstructing 4 th ventricle with very minimal enhancement	Gross total resection	Classical	Negative		M0
	Recurrence			24 months	New diffusion restricting ependymal lesions in the frontal horn and right lateral ventricle and anterior body of the left lateral ventricle. No evidence recurrence at primary site & spine clear.	N/A	-	Negative		M2

5.4 Summary

From these preliminary results, we can conclude that:-

- ❖ Epigenetic modification of the genes involved in the regulation of MMPs such as EMMPRIN, TIMPs and the MMPs themselves, occurs in all MB sub-groups in comparison to normal cerebellum. While these epigenetic changes influence the resulting MMP gene expression, it is more than likely that further modification at other levels of MMP regulation result in the increased levels of functional activity seen in the metastatic and recurrent MB samples.
- ❖ Cerebrospinal fluid cytology remains a grossly inaccurate method for the determination of leptomeningeal metastatic disease especially in the case of intracranial disease recurrence as demonstrated in the unfortunate outcome of Patient 2, who succumbed to his metastatic disease.
- ❖ Gelatin zymography of the paired cerebrospinal fluid samples was sensitive enough to detect serial changes in the levels of functionally active MMP-2 and MMP-9 between the primary and recurrent as well as the recurrent and relapsed patients. The preliminary data in patients with residual disease suggests that the levels of functionally active MMP-2 and MMP-9 remain persistently elevated, proposing its usefulness in determining tumour burden and patient response to therapy.
- ❖ Cerebrospinal fluid samples obtained in theatre at dural entry such as in Patient 3 sample 3[2] can give stronger prognostic indication

of likely recurrence, in the face of conflicting imaging and cytology results. While day 14 post-operative lumbar punctures are currently performed to determine the tumour burden of viable circulating tumour cells, theatre samples could be easily translated into clinical practice, to give more robust information regarding the patient's metastatic status at the time of diagnosis, without the complications of iatrogenic dissemination.

- ❖ As demonstrated in the pre-operative magnetic resonance contrast enhanced imaging of patients 2, 3, 4 and 6, poorly enhancing tumours present substantial difficulty in the diagnosis and detection of metastases as these often harbour similar imaging characteristics to the primary tumours. As such, the use of more sensitive MR compatible imaging biomarkers could give better diagnostic accuracy and reduce the need for repeat imaging as well as the risk of delays to life-saving escalation of therapy.

Chapter 6

**Towards the radiological characterisation
of matrix metalloproteinases in biological
samples using our
¹⁹Fluorine-MMP-MRI biosensor**

6.1 Chapter outline

Metastasis remains the leading cause of death in paediatric medulloblastoma, with a predilection for spread to the leptomeninges (Mata-Mbemba, Zapotocky et al. 2018). As such, its detection carries substantial prognostic implications for the patient, whose adjuvant therapy selection will be determined by the resulting risk stratification of their disease. While it is reported that approximately 1 in 3 paediatric MB patients present with disseminated disease at initial diagnosis, the actual figures are likely to be higher, given the published sensitivity of CSF cytology to be as low as 50% (Bennett, Ashmawy et al. 2017, Chamberlain, Junck et al. 2017, Torre, Lee et al. 2020). Thus to enhance the detection and monitoring of leptomeningeal spread, the preferential mode of metastasis in MB, radiological imaging of the entire neuroaxis is performed at diagnosis and disease surveillance.

While Gadolinium contrast-enhanced magnetic resonance imaging is widely advocated as the gold standard for diagnosis and surveillance of paediatric brain tumours, its diagnostic accuracy for leptomeningeal dissemination remains sub-optimal and observer-biased, with published sensitivity and specificity both approximating 76-77% (Torre, Lee et al. 2020). Though its excellent spatial resolution can identify micrometastases $<5\text{mm}^3$, this may also result in the misdiagnosis of physiologically-enhancing vascular artefacts as suspicious, thus necessitating specialist neuroradiology expertise for the accurate reporting of true leptomeningeal metastatic deposits.

In addition, while most aggressive solid tumours exhibit enhancement following administration of intravascular gadolinium contrast, medulloblastoma, particularly those from the molecular Group 4 subgroup, are often poorly or non-enhancing (Thompson, Hielscher et al. 2016). In these patients, their ensuing leptomeningeal metastases tend to share this radiological characteristic, which inevitably results in poor detection of spinal disease which could lead to administration of a reduced dose or omission of craniospinal irradiation, culminating in the unperturbed growth of their metastatic disease. Thus, more sensitive imaging techniques that can be easily translated into clinical practice could hold prognostic promise, in the personalised management of paediatric patients with medulloblastoma.

Molecular magnetic resonance imaging is an emerging field in which alterations in the tumour microenvironment such as cellular metabolism, acid-base changes and proliferation for example, could be detected in advance of established visible macrometastases (Haris, Yadav et al. 2015). This type of imaging could provide earlier prognostic and therapeutic information and opportunities to interrupt metastatic dissemination, by either rendering the pre-metastatic niches hostile with intrathecal chemotherapy for example, or definitively demonstrating evidence of leptomeningeal spread, thus indicating the need for aggressive therapy.

One such technique involves magnetic resonance imaging using exogenous enzymatic activatable MRI probes, which enable the

detection of specific biomarkers in the tumour proteome (Carril 2017). As previously shown in Chapter 5, the levels of functionally active MMP-2 and MMP-9 in cerebrospinal fluid, appear to give a better prediction of the patients' disease prognosis, in comparison to their CSF cytology given that the cytology was mostly negative. It was therefore investigated whether this finding would be translatable using a locally developed MRI-MMP-2/9 biosensor. Briefly, the biosensor is a ¹⁹F-fluorine moiety that is covalently linked to a gadolinium-III bound DOTA complex by a protein substrate specific to MMP-2/MMP-9. In the presence of functionally active or activated MMP-2 or MMP-9, the gelatine substrate is cleaved in a manner that is similar to the digestion of gelatine in our zymography experiments. Upon cleavage, the previously paramagnetically-shielded fluorine moiety emits a stronger ¹⁹F MR signal which can be detected and measured (Krupa 2016).

6.2 Objectives and Hypothesis

To determine whether our ^{19}F -MRI-MMP biosensor could be used as a prognostic imaging biomarker in metastatic medulloblastoma, we firstly investigated the conditions in which the biosensor is activatable, by designing experiments using Fluorescence Resonance Energy Transfer (FRET) assays (Lei, Jian et al. 2020). As Figure 6.1 illustrates, in FRET assays, which our biosensor is modelled after, a donor and acceptor fluorophore are linked in close proximity on a peptide substrate such as gelatin. Cleavage of the gelatin linking substrate by MMP-2/MMP-9 within our samples, increases the distance between the donor and acceptor fluorophore, augmenting emissions from the excited donor fluorophore at a rate proportional to the rate of substrate digestion.

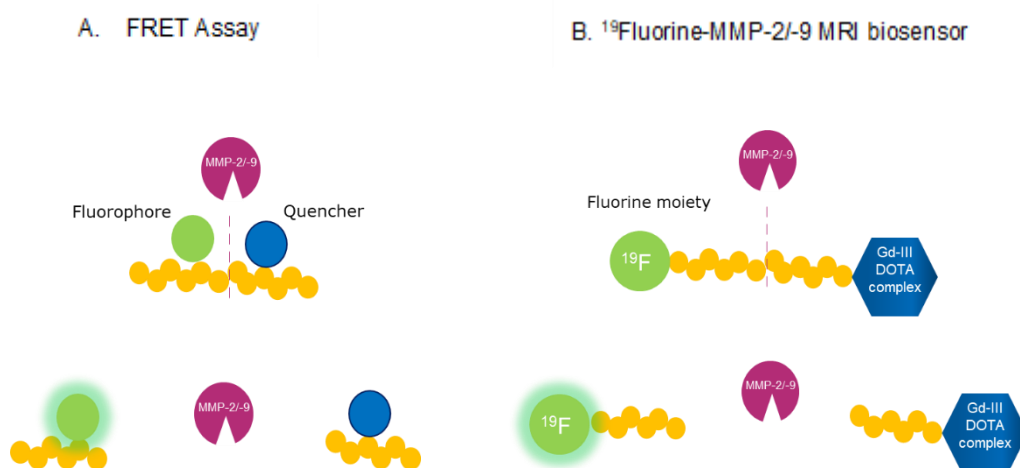


Figure 6.1 Representative diagram demonstrating the shared mechanisms of FRET assay (A) and our ^{19}F MRI MMP-2/MMP-9 biosensor (B).

As shown, the proximity of the quencher synonymous to the Gadolinium-III DOTA complex (Gd-III DOTA complex) is proportional to the fluorescence emitted by the fluorophore or ^{19}F Fluorine moiety.

Working towards the characterisation of the levels of functionally active MMP-2 and MMP-9 in biological samples using the biosensor, Fluorescence Resonance Energy Transfer (FRET) experiments were designed using recombinant proteins firstly, to simulate the specific conditions employed in the biosensor optimisation experiments as they offer a more economical alternative. These recombinant proteins were then substituted for concentrated primary and metastatic medulloblastoma cell line supernatants before investigating the cerebrospinal fluid from paediatric patients with medulloblastoma, to ensure its compatibility and stability with more physiological samples.

The hypothesis was that FRET would be able to detect differential levels of functionally active MMP-2 and MMP-9 in the samples tested ranging from recombinant proteins to concentrated cell line supernatants and cerebrospinal fluid. We believe that the biological samples with the highest levels of functionally active MMP-2/MMP-9 in gelatin zymography will also exhibit the highest levels of fluorescence in the FRET assays and with our fluorine biosensor.

As the FRET experiments are limited to ex-vivo analyses, the translation of this work using an MRI compatible MMP-2/MMP-9 biosensor, would enable real-time detection and quantification of metastases at diagnosis and disease surveillance, complimenting the gadolinium contrast enhancing capabilities of the tumour. In addition, the biosensor could hold promise as an intra-operative contrast agent that could enhance the maximal safe resection of aggressive MB cell performed.

6.3 Results

6.3.1 FRET Optimisation experiments

6.3.1.1 Concentration of medulloblastoma cell line supernatants

To strengthen the signal obtained in the biosensor experiments, the conditioned medulloblastoma cell supernatants obtained following 48 hour 2-D culture of 5×10^6 primary and metastatic medulloblastoma cell lines. These were concentrated using Vivaspin® 20 centrifugal concentrating columns. Cell line samples designated for each experiment were concentrated at the same time, using the same starting volume and conditions. To reduce the rate of protein denaturation, the samples were centrifuged at 4°C, which as per the manufacturer's advice, necessitated an increased centrifugation time. To recover both MMP-2 and MMP-9 from the samples, columns with membranes with molecular weight cut offs of 50,000 MWCO were used. Table 6. 1 below shows the resulting volumes of cell line supernatants following column concentration. Samples were normalised by dilution to the same volume prior to plate set-up.

Table 6. 1 Results from centrifugal column concentration of MB cell line supernatants

Cell line	Passage	Starting volume (µl)	Final volume (µl)	Concentration factor
DAOY	p18	7500	219	34.2
ONS-76	p29	7500	222.5	33.7
ONS-76 dnp53	p16	7500	215.5	34.8
UW228-3	p21	7500	190	39.5
CHLA-01-MED	d53	7500	198.5	37.8
CHLA-01R-MED	d52	7500	92	81.5
CHLA-01-MED	d49	9000	243	37.0
CHLA-01R-MED	d48	9000	178	50.6
D425-MED	p14	7500	200	37.5
D458-MED	p102	7500	238	31.5
HD-MB03	p60	7500	222.5	33.7
HD-MB03	p66	7500	200	32.0

6.3.1.2 The effect of acetonitrile concentration on FRET assays using recombinant MMP-2 and MMP-9

Due to the negligible background fluorine signal in the human body, the fluorine MRI signal after administration of exogenous fluorinated contrast agents is proportional to the concentration of fluorinated contrast administered (Tanifum, Patel et al. 2018).

While ^{19}F Fluorine MR imaging is highly specific, its sensitivity compared to hydrogen based MRI is poor, necessitating increased concentrations of the ^{19}F nuclei by saturation of the probe. However, this results in the decreased solubility of the probe in water due to increased concentrations of the hydrophobic, inert fluorine moiety. One way to circumvent this issue is by dissolving the probe in an organic solvent such as acetonitrile (ACN). As the MRI-MMP-2/-9 biosensor probe was found to be most stable and soluble in 10% acetonitrile, the effect that different concentrations of acetonitrile would have on the detection of known concentrations of recombinant MMP-2 protein ($0.61\text{ng}/\mu\text{l}$) was investigated. The same concentration of the same recombinant protein that had been used in the most recent biosensor optimisation experiments was employed here.

As shown in Figure 6.2, while the fluorescence signal of rMMP-2 0% acetonitrile solution gradually inclines, the fluorescence increments plateau in the 5% acetonitrile solution while the fluorescence signal in the 10% acetonitrile solution drastically declines with time. This suggests that in the presence of acetonitrile, the recombinant MMP-2 protein had precipitated out of the solution, resulting in reduced digestion of the DQ gelatin demonstrated as reducing fluorescence signal with time.

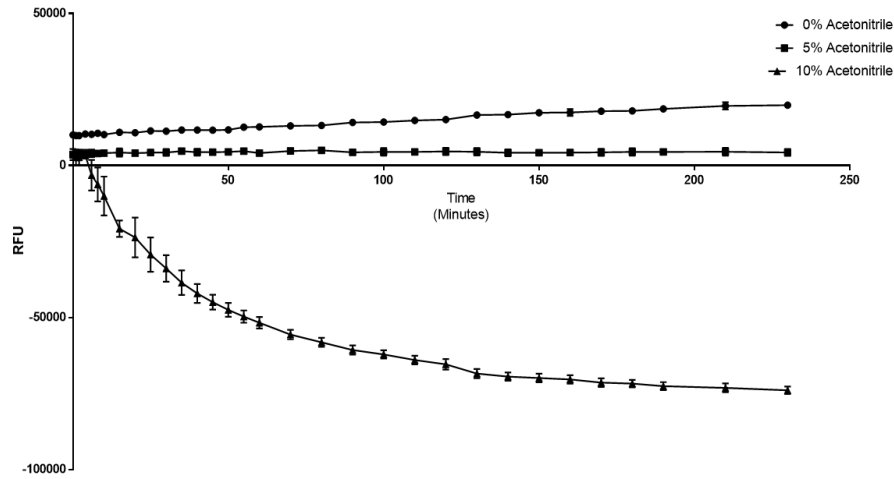


Figure 6. 2 FRET Assay of recombinant MMP-2 (0.61ng/μl) in Acetonitrile solutions.

The fluorescence signal measures as relative fluorescence units (RFU) only increases in the absence of acetonitrile while it plateaus in the 5% acetonitrile and declines in the 10% acetonitrile solutions.

To further investigate this effect and determine whether its impact could be negated by increasing the concentration of recombinant MMP-2 in the sample, similar experiments were repeated in 0%, 5%, 10% and 15% solutions of acetonitrile.

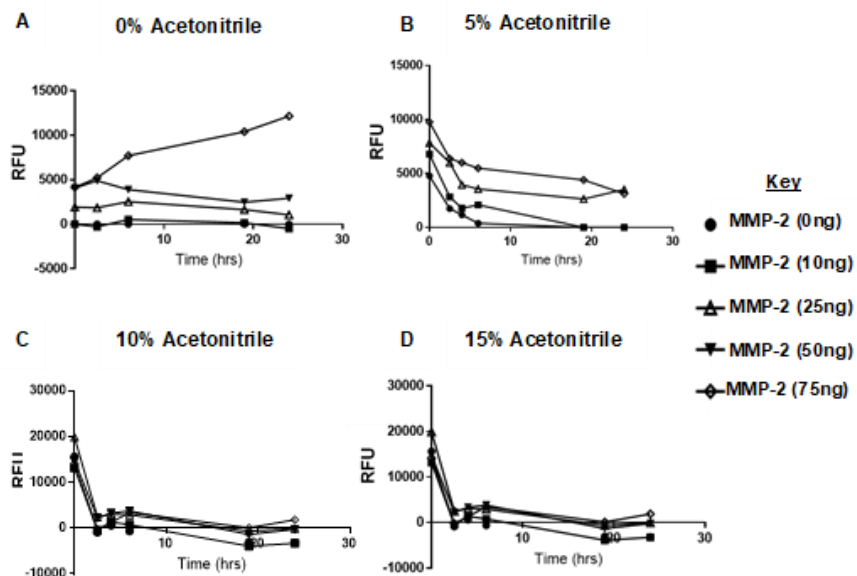


Figure 6.3 FRET assay of different amounts of recombinant MMP-2 protein (Peptotech) in different percentage concentrations of acetonitrile.

Serial fluorescence readings taken over 24 hours are graphically represented using GraphPad prism. The highest fluorescence signal from digestion of the DQ gelatin was observed in the 0% acetonitrile group (A).

As shown in Figure 6.3, where ACN was absent, the highest fluorescence signal was obtained in the solution with the highest MMP-2 content of 75ng, as expected. While in the 5% acetonitrile solution, the sample containing 75ng of rMMP-2 was the least affected though in all samples containing rMMP-2, there was a drastic decline in fluorescence from the beginning of the experiment. At the acetonitrile concentration of 10% at which the biosensor probe was most stable, the relative fluorescence units (RFU) drastically declined within 2 hours of the experiment.

While the synthesis of the probe was optimised to maximise the density of the fluorine moiety and thereby the fluorine signal obtained at MR imaging, this increased its hydrophobicity and necessitated its solution in the organic solvent, acetonitrile. Furthermore, to enable further characterisation of the probe, the precipitation of unwanted proteins would be an advantage prior to analysis in liquid chromatography and mass spectrometry. While re-synthesis of our ¹⁹F MMP MRI probe in a more physiological solvent was desirable, this was not achievable within the remaining period of this research. Further optimisation was therefore carried out, with this caveat in mind.

While the initial MRI MMP-2/MMP-9 biosensor optimisation experiments performed before the scope of this PhD had demonstrated specificity to MMP-2 and MMP-9, the DQ gelatine provided in the Enzchek® Gelatinase Assay Kit was also reported to be efficiently digested by both gelatinases. An experiment to determine whether this molecular probe

was equally digested by both rMMP-2 and rMMP-9 or preferentially digested by either protein. As shown in figure 6.4, even at a lower concentration, rMMP-9 appears to more efficiently digest the DQ gelatine when compared to that of r-MMP-2. We aim to repeat this experiment in the biosensor to ensure it has equal sensitivity to MMP-2 and MMP-9.

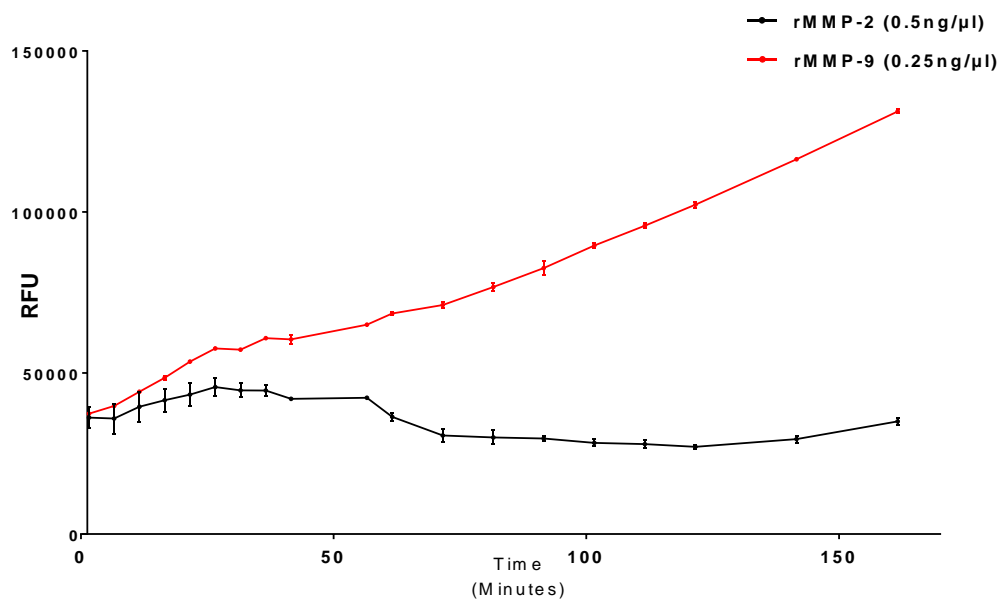


Figure 6.4 FRET assay of different amounts of recombinant MMP-2 protein (Peprotech) in different percentage concentrations of acetonitrile. Serial fluorescence readings taken over 24 hours are graphically represented using Graphpad prism. The highest fluorescence signal from digestion of the DQ gelatin was observed in the 0% acetonitrile group (A).

6.3.1.3 The effect of acetonitrile concentration on FRET assays of column- concentrated medulloblastoma cell line supernatants

Having determined that the FRET assay could be used to correlate the levels of functionally activatable recombinant MMP-2 protein, it was investigated whether it would reflect the differential levels of functionally active MMP-2/MMP-9 in concentrated medulloblastoma cell line supernatants.

To confirm that endogenous MMP-2 and MMP-9 would be affected by the presence of acetonitrile in a similar manner as with the recombinant protein, we performed a FRET assay of the same volume of column concentrated ONS-76 medulloblastoma cell line supernatant, in 0% and 10% ACN. As shown in Figure 6.5, the fluorescence from the supernatant without ACN gradually increased over time, while the fluorescence signal in the 10% ACN solution remained static, suggesting endogenous MMP-2/-9 are as vulnerable to precipitation as their recombinant counterparts.

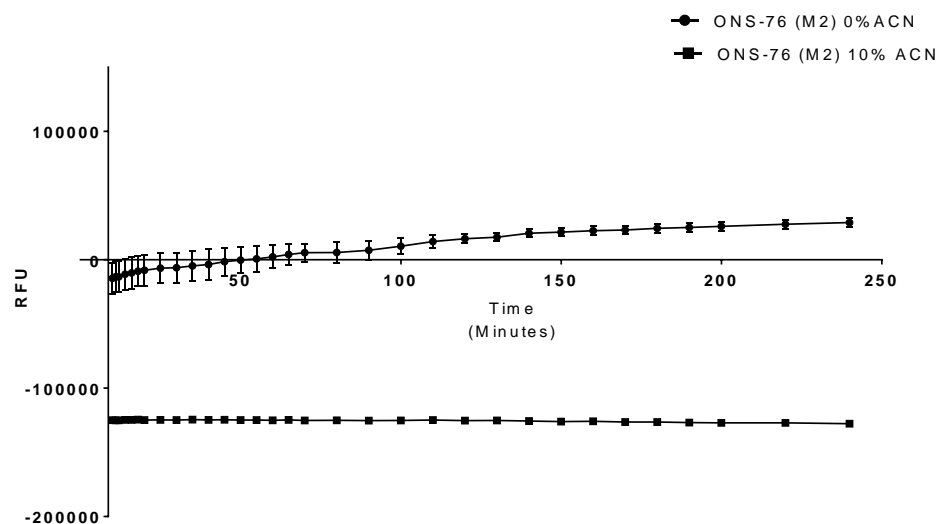


Figure 6.5 FRET assay of column concentrated supernatant from 48 hour culture of ONS-76 medulloblastoma cells.

As expected, reduced and static fluorescence signal was seen in the 10% ACN containing solution.

However, FRET analysis of the same experimental set-up with the substitution of HD-MB03 conditioned cell supernatant demonstrated an increase in the fluorescence signal even in the solution containing 10% ACN. As demonstrated in Figure 6.6, though the fluorescence intensity is lower in the ACN containing solution, its fluorescence signal continues

to increase with time in a near parallel fashion. It was postulated that this could be due to the increased levels of functionally active MMP-9 within this cell line, which seemed to be somewhat resistant to the precipitation effects of acetonitrile.

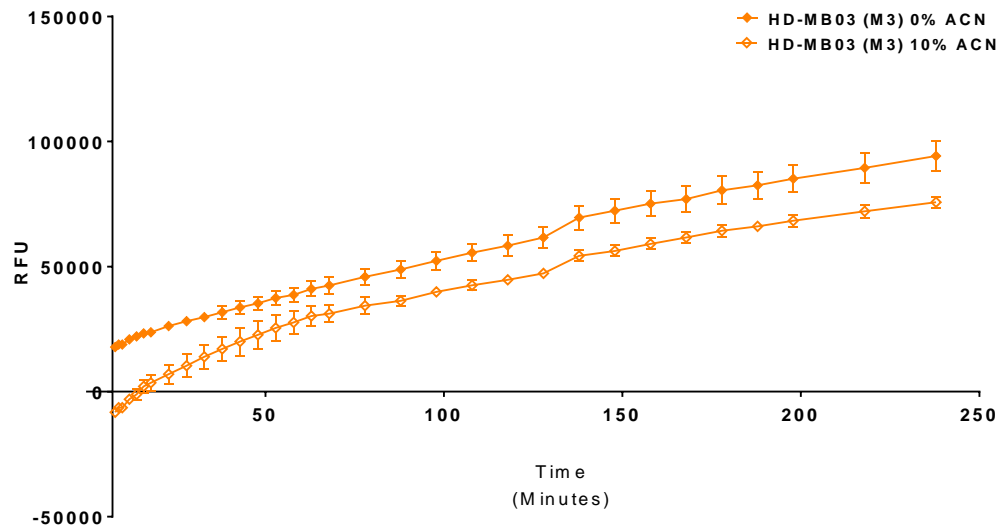


Figure 6.6 . FRET assay of column concentrated supernatant from 48 hour culture of HD-MB03 (Group 3 metastatic) medulloblastoma cells.

As demonstrated, the fluorescence signal of the 10% ACN containing solution increases in a parallel fashion to that of the solution without ACN.

6.3.1.4 FRET assays of column-concentrated paired medulloblastoma cell line supernatants

To determine whether FRET assays and by extension the biosensor, could detect differential levels of functionally active MMP-2 and MMP-9 in biologically paired samples, experiments using concentrated cell line supernatants from primary and metastatic MB cell lines were performed.

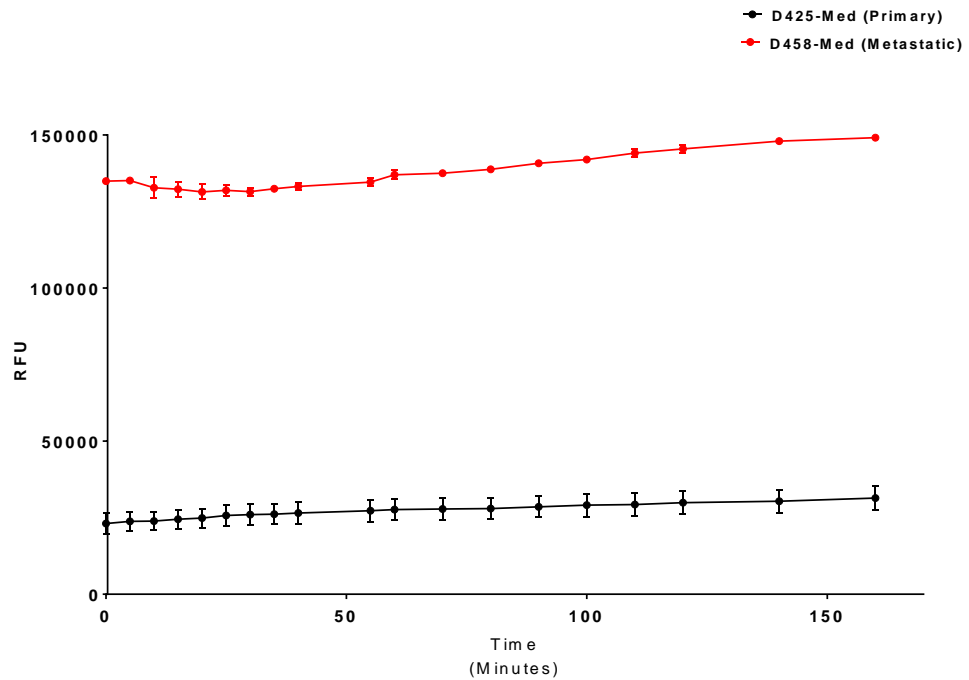


Figure 6. 7 FRET assay of column concentrated supernatant from 48 hour culture of paired Group 3 primary-D425-Med and metastatic D458-Med medulloblastoma cells. As shown, the levels of functionally active MMP-2 and MMP-9 are much higher in the metastatic cell line D458-Med.

As shown above in Figure 6.7, the levels of fluorescence slowly incline with time but begin at much higher fluorescence levels in the concentrated cell line supernatants of the metastatic line, D458-Med. As the D458-Med cell line was derived from cells that had metastasised to the cerebrospinal fluid of the patient, these cells exhibit higher levels of functionally active MMP-2 and MMP-9 which may have enabled their dissemination and survival in the CSF.

Repeating the same experiment in the paired Group 4 MB cell lines CHLA-01-MED (primary) and CHLA-01R-MED (metastatic), a higher level of fluorescence was depicted from the latter in Figure 6. 8,

suggesting its higher levels of functionally active gelatinases digested more of the DQ gelatine substrate.

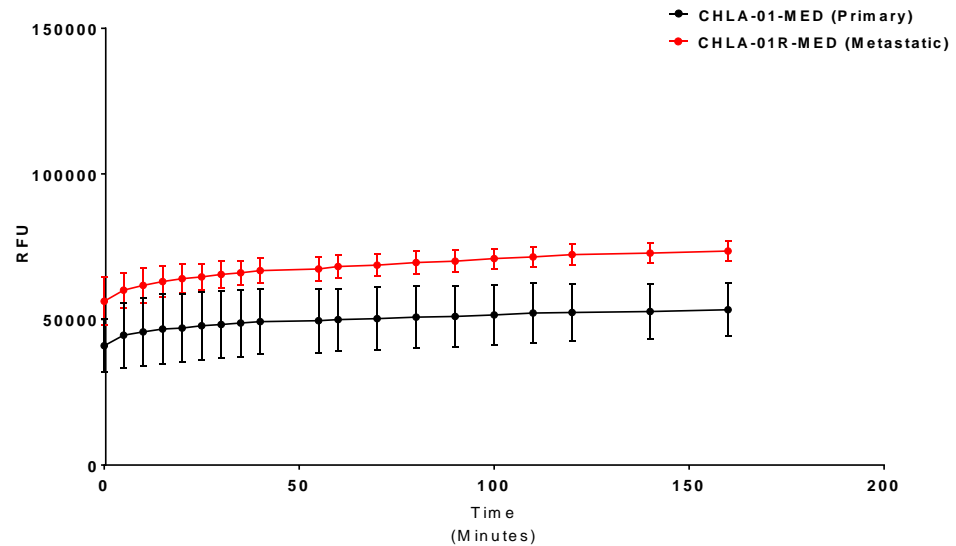


Figure 6. 8 FRET assay of column concentrated supernatant from 48 hour culture of paired Group 4 primary-CHLA-01-Med and metastatic CHLA-01R-Med medulloblastoma cells.

Though the difference is less striking when compared to the previous Group 3 pair, this experiment showed higher levels of fluorescence in the metastatic cell line.

To determine whether the FRET assay could detect differential levels of functionally active MMP-2 and MMP-9 between cell lines with differential metastatic potential, we examined the concentrated cell supernatants from the metastatic SHH cell line ONS-76 (*wt p53*) and its counterpart ONS-76 (*dnp53*). With a binding site within the promoter of the MMP-2 gene, p53 has been shown to exert transcriptional regulation of MMP-2. (Bian J, 1997) As shown in figure 6.9, the cell line with wild type functional p53 ONS-76 (*wt p53*), also demonstrates higher levels of fluorescence with increasing time, likely as a result of higher levels of functionally active gelatinases.

Thus the increased fluorescence signal in the preserved p53 ONS-76 cell line will likely contain higher levels of functionally active MMP-2 compared to its counterpart in which the p53 gene is non-functional.

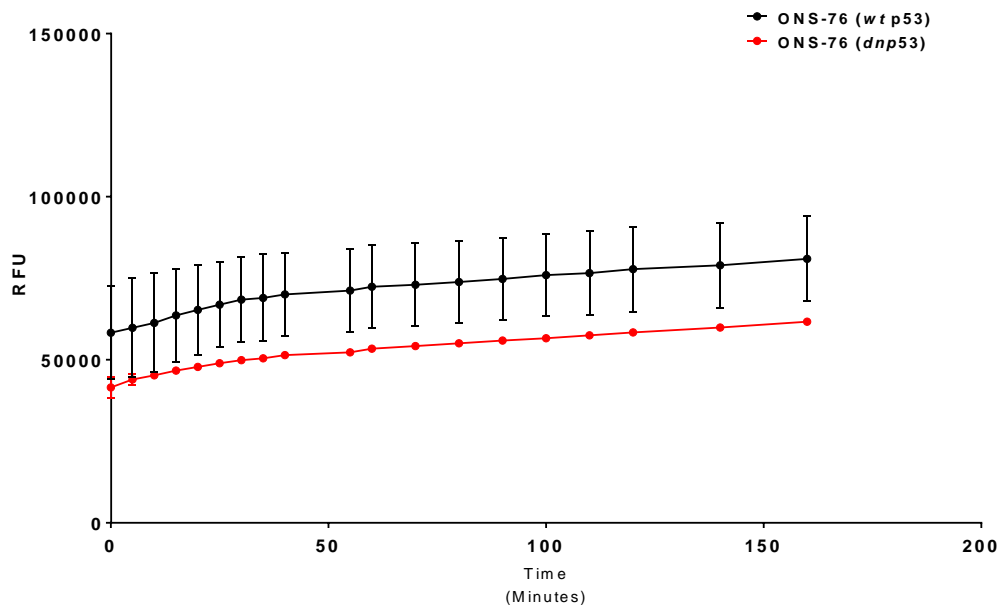


Figure 6. 9 FRET assay of the SHH MB cell line ONS-76 (wt p53) in black and ONS-76 (dnp53) in red.

This shows that the levels of functionally active MMP-2/MMP-9 are higher in the cell line in which the p53 is functionally intact.

6.3.1.5 The effect of using reaction buffer on FRET assays of column-concentrated medulloblastoma cell line supernatants

As the FRET assay was used to model the biosensor experiments, it seemed pertinent to investigate whether the reaction buffer provided within the Enzchek Gelatinase Assay Kit made a difference in the resulting fluorescence signal levels, as this reagent was not used in the biosensor experiments. The reaction buffer was supplied as a 10X

solution constituted of 50mL of 0.5M Tris-HCl, 1.5M NaCl, 50mM CaCl₂ and 2mM of sodium azide pH 7.6.

FRET experiments of ONS-76 (*wt p53*) concentrated supernatant without acetonitrile were performed, wherein neutral pH-phosphate buffered saline was used to substitute the reaction buffer. As depicted in Figure 6. 10, the resulting fluorescence signals are higher in the samples without reaction buffer at each given time point. This suggests that the depicted levels of functionally active MMP-2 and MMP9 would likely be higher in the biosensor, negating the need to add reaction buffer to the biosensor experiments.

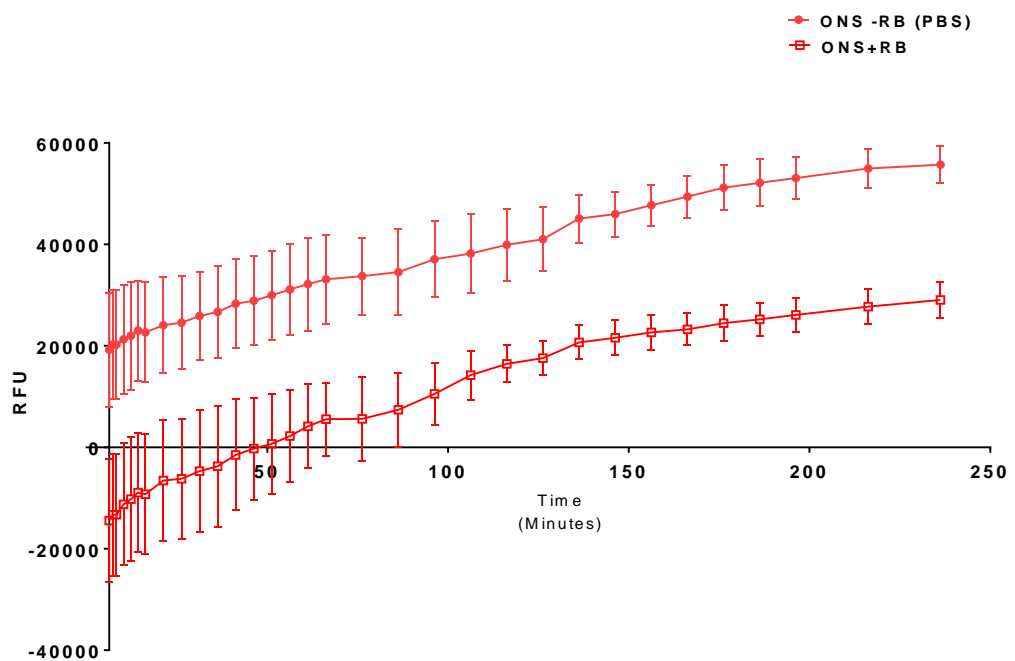


Figure 6. 10 FRET assay of column concentrated supernatant following 48-hour culture of ONS-76 medulloblastoma cells.

To determine the effect of the reaction buffer used for FRET assays on the levels of fluorescence from DQ gelatin digestion, ONS-76 supernatants were examined with and without (+PBS) reaction buffer. As demonstrated, the addition of reaction buffer appeared to reduce the resulting levels of fluorescence with increasing time.

6.3.1.6 FRET assays of cerebrospinal fluid from paediatric patients with primary and recurrent medulloblastoma

To determine whether the levels of functionally active MMP-2 and MMP-9 within naïve cerebrospinal fluid would result in a detectable fluorescence signal, CSF samples from the Patient 1-4 who presented with either primary and recurrent MB or recurrent and relapsed MB, were examined.

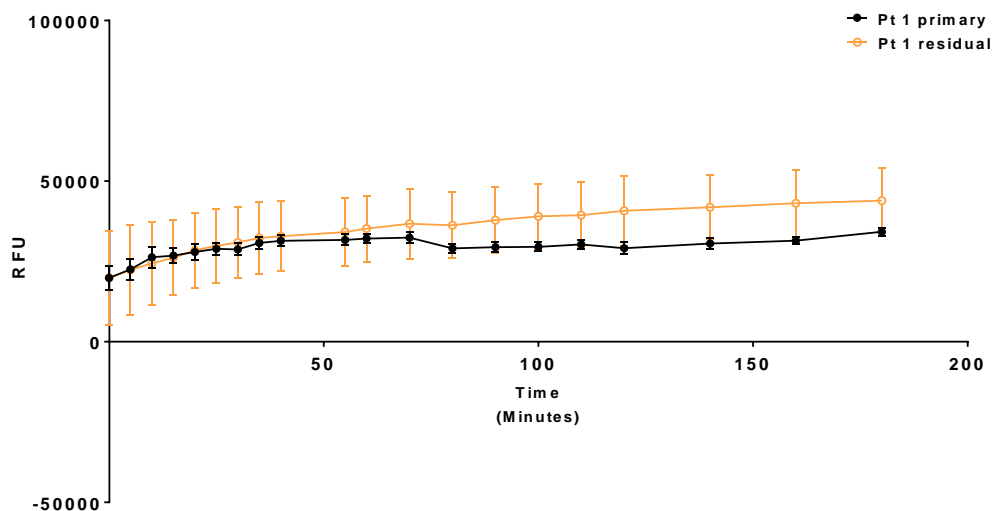


Figure 6. 11 FRET assay of naïve CSF samples from Patient 1 at their first presentation (primary) and following growth of the residual tumour.

As demonstrated, the levels of fluorescence are very similar suggesting that higher levels of functionally active MMP-2 and MMP-9 remained present within the CSF. This is confirmed in the gelatin zymography results of the same samples in Chapter 5.

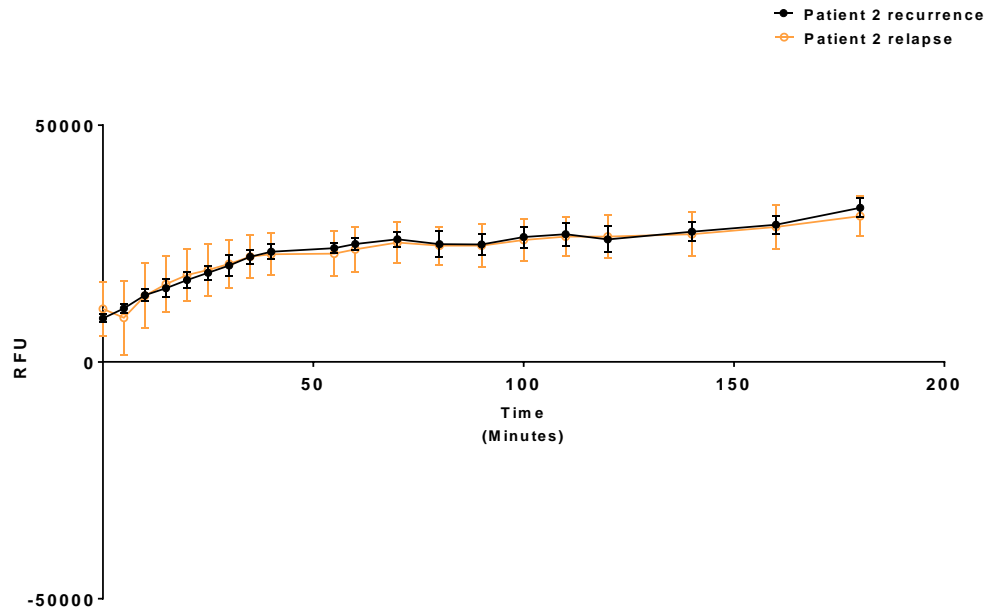


Figure 6. 12 FRET assay of naïve CSF samples from Patient 2 at the first recurrence of their MB (recurrence) and following relapsed MB.

Once more, the levels of fluorescence are incredibly similar suggesting similar levels of functionally active gelatinases within the cerebrospinal fluid.

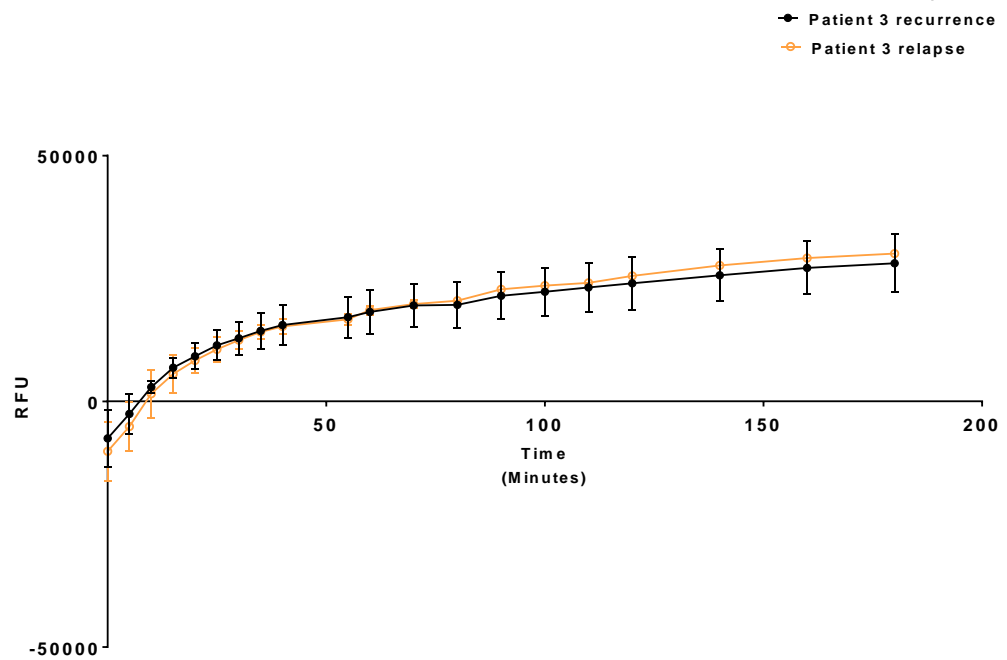


Figure 6. 13 FRET assay of naïve CSF samples from Patient 3 at recurrence of their MB (recurrence) and following relapsed MB.

Interestingly the levels of fluorescence detected in the CSF sampled at relapse mirrored the recurrence very closely in a similar manner as in the patient in Figure 6.12.

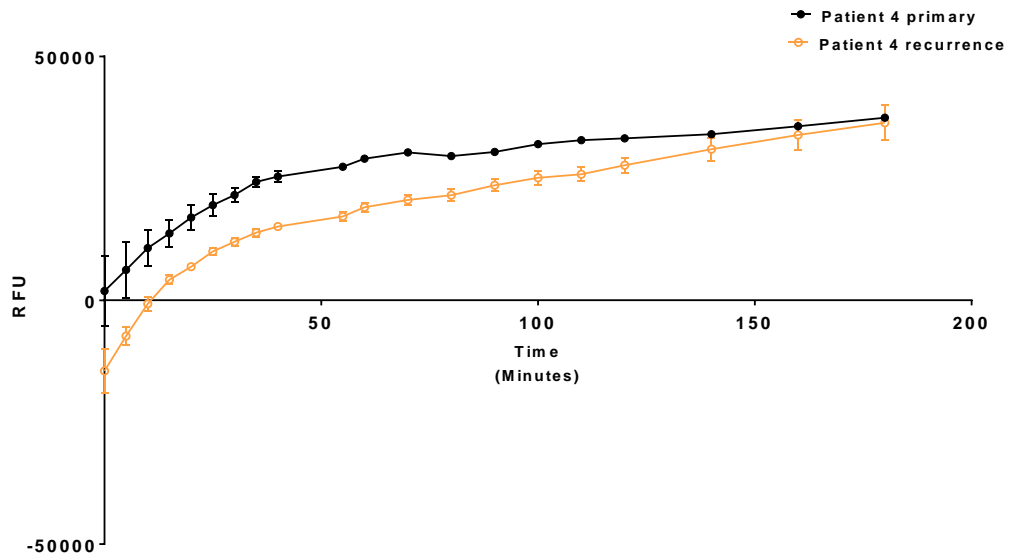


Figure 6. 14 FRET assay of naïve CSF samples from Patient 4 at his first presentation with MB (primary) and recurrence of their disease.

In a manner similar to that of Patient 1 who also presented with primary and recurrent MB, the fluorescence signal in the primary sample appears to be higher but begins to plateau by 100 minutes while the recurrent CSF fluorescence continues to increase.

Figures 6.11-6.14 demonstrate a striking similarity in the fluorescence signal from FRET assay experiments of cerebrospinal fluid samples, taken at either the primary and recurrent presentations (Figure 6. 11 and Figure 6. 14) of the patients' MB or at recurrence and relapse (Figure 6. 12 and Figure 6. 13) as specified in each figure. This suggests that the levels of functionally active MMP-2 and MMP-9 are detectable and comparable in both stages. Furthermore, the similarity in the levels of fluorescence between the primary and recurrent or recurrent and relapsed medulloblastoma, suggest that at the time these tumours are detectable as visible macrometastases, they are secreting similar levels of functionally active MMP-2 and MMP-9. This finding supports the hypothesis that the levels of functionally active MMP-2 and MMP-9, could be clinically relevant.

6.4 ¹⁹Fluorine MRI MMP-2/MMP-9 biosensor experiments

6.4.1 Biosensor optimisation experiments and proof of principle

To determine whether the biosensor would be responsive to functionally active MMP-2 and MMP-9, experiments using known concentrations of recombinant proteins were performed. As described in recently published work (Faas, Krupa et al. 2019), recombinant MMP-1, MMP-2, MMP-9 and MMP-12 were purchased from R&D systems (Minneapolis) and reconstituted to concentrations of 75µg/ml in a 0.05% Brij 35 developing buffer, pH 7.5. To ensure their maximal activity, these recombinant proteins were incubated in a 1mM solution of 4-aminophenylmercuric acetate (APMA) in DMSO. APMA is a well-established MMP zymogen activating agent, used to amplify MMP activity prior to molecular biology, organic chemistry and nuclear magnetic resonance imaging experiments. Interestingly, the recombinant MMP-2 only required 1 hour of incubation while MMP-9 required a 24-hour incubation period at 310K (37°C), following which they were and stored in aliquots at 193 K (-80°C) to preserve maximal activity and thawed immediately prior to use (Faas, Krupa et al. 2019)

The optimisation experiments were carried out in a Bruker Avance III 400 MHz (9.4 tesla) spectrometer and microimaging system which was tuned to 376.5 MHz. For each experiment, 600µl of 1.2mM of the ¹⁹-Fluorine MRI MMP-2/MMP-9 probe in 9:1 water: acetonitrile was used. To

determine the probe's sensitivity to MMP-2 and MMP-9, 5 μ l of 75 μ g/mL activated recombinant MMP-2 or MMP-9 were incubated in a 5mm NMR tube and placed within a receptacle in the 19 Fluorine coil. Due to the complexity of this imaging, these experiments were undertaken in the Sir Peter Mansfield Imaging Centre by Dr Henryk Faas, Professor Thomas Meersman and his team. Samples were imaged alongside controls without MMP for 12-18 hours and the spectroscopy analysed with Igor Pro 7. A representative 1 H-NMR spectra of the probe, as it is digested by the recombinant MMP-2/9 is shown below.

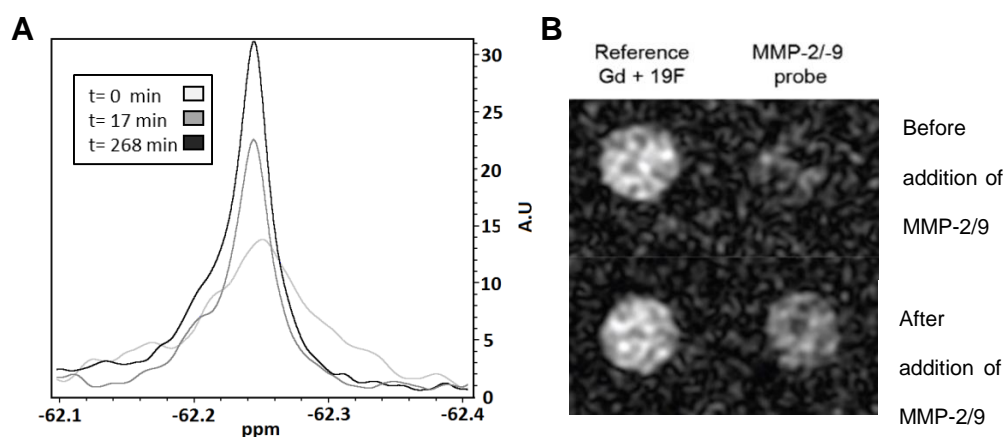


Figure 6.15 19 -Fluorine MMP2/MMP-9 biosensor optimisation experiments

A. Proton spectroscopy of the 19 -fluorine probe with increasing time of incubation with activated recombinant MMP-2/9. At time 0, the lowest peak visible shows a larger curve width which is synonymous with a higher concentration of the probe. As cleavage of the probe by MMP-2 or MMP-9 occurs, this linewidth continually diminishes with time. B. Representative diagram of fluorine signal change following biosensor incubation with activated recombinant MMP-2/9. As the probe is cleaved, increased distance between the fluorine moiety and the Gd-DOTA complex, results in an increasing fluorine signal with time.

Having demonstrated that the probe was digested by recombinant activated MMP-2 and MMP-9, similar experiments were designed and undertaken using the same concentrations of MMP-1 and MMP-12, to

ensure specificity of the probe. These experiments showed no similar changes in signal in the biosensor or fluorine signal, following when incubated with 5 μ l of 75 μ g/mL of activated MMP-1 and MMP-12 in comparison to the controls (Faas, Krupa et al. 2019).

As the most repeatable results were obtained in these conditions, they were taken forward and the biosensor deemed ready for experiments using biological samples of conditioned medium from medulloblastoma cell lines prior to planned experiments with patient derived cerebrospinal fluid samples.

6.4.2 Biosensor detection of functionally active MMP-2 and MMP-9 in concentrated cell supernatant

To maximise the signal obtained from the biosensor, concentrated supernatant from the most aggressive medulloblastoma cell line, HD-MB03, a group 3 metastatic cell line was selected. To reduce the dilution of the biosensor, 50 μ l of the supernatant was added to a 5mm diameter NMR tube containing 600 μ l of the biosensor, pH 7.5, temperature 293 Kelvin (20°Celcius). The NMR tube was placed in the centre of a microimaging Bruker head alongside a tube containing a similar volume of the negative control, i.e. no added supernatant or recombinant protein. The samples were then imaged by our team at the SPMIC using a fluorine coil with a ¹⁹-fluorine frequency of 564.6 megahertz and detected on a Bruker Avance III 400 megahertz spectrometer. As shown in figure 6.16, the NMR tube containing the supernatant revealed a loss

of gadolinium signal (synonymous with an increase in the fluorine signal) following digestion of the gelatin substrate linker within the biosensor, by the functionally active MMP-2 and MMP-9 within the supernatant.

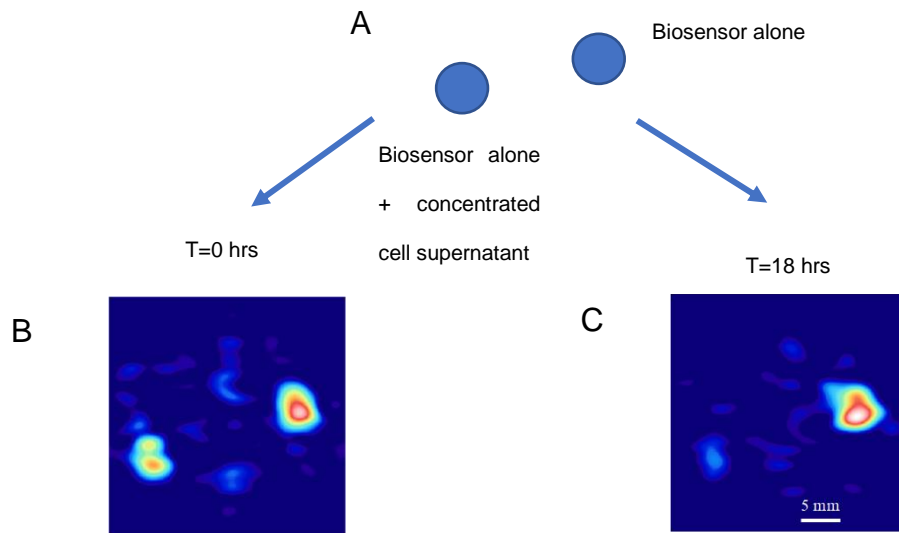


Figure 6.16 19-Fluorine MRI MMP-2/MMP-9 imaging of concentrated cell supernatant

A. Schematic diagram showing experimental set up. B. Spectral imaging performed at $t=0$ just after addition of concentrated HD-MB03 cell supernatant showing similar Gadolinium (Gd) signal compared to C where the Gd is substantially reduced after 18 hours of imaging.

6.4 Summary

The results presented suggest the following conclusions:

- ❖ Though the biosensor is constituted in 10% acetonitrile, we have shown through our FRET experiments that this organic solvent may cause the precipitation of our proteins of interest out of the samples, resulting in false negative results. For this reason, further work into the re-constitution of the biosensor in a more hydrophilic physiological solvent is under investigation.
- ❖ The FRET assay demonstrates similar levels of fluorescence in samples obtained at primary and recurrence of MB and recurrence and relapse of MB in paediatric patients. This confirms that the levels of functionally active MMP-2 and MMP-9 hold prognostic significance and are detectable using imaging modalities, suggesting they would be suitable imaging prognostic biomarkers. As the biosensor experiment showed a substantial reduction in the gadolinium signal following addition of the supernatant, it suggests that the biosensor will also be able to detect the levels of functionally active MMP-2 and MMP-9 in patient CSF. This will be the next step following synthesis of the Fluorine probe in a hydrophilic, physiological solvent.

Chapter 7. Discussion

7.1 Background and rationale

With a reported incidence of 5 cases per million children (Juraschka and Taylor 2019), medulloblastoma is considered a rare but devastating disease that constitutes nearly 20% of all paediatric brain tumours (Holgado, Guerreiro Stucklin et al. 2017). It is a highly malignant (WHO grade IV) embryonal tumour of the cerebellum, which presents with radiological or cytological evidence of metastasis at diagnosis in approximately one third of patients (Holgado, Guerreiro Stucklin et al. 2017).

The clinical presentation of paediatric patients with MB is dependent upon the patient age and concomitant hydrocephalus. MB in infants may manifest as increased head circumference, vomiting, irritability, failure to thrive and developmental delay, while older children and young adults may complain of headaches, nausea and vomiting, unsteady gait, incoordination and intellectual difficulties at school or university (Millard and De Braganca 2016).

While the multimodal therapeutic approach of maximal safe surgical resection, adjuvant chemotherapy, and irradiation of the tumour bed and neuroaxis in patients older than 3-5 years of age, have significantly improved survival, metastasis remains the predominant cause of mortality in paediatric medulloblastoma (Van Ommeren, Garzia et al. 2020). Building upon the pioneering study of craniospinal irradiation in medulloblastoma by Paterson et al. in 1953, the previously deemed 'hopeless' prognosis of medulloblastoma was transformed into a 3-year

60% survival (Paterson and Farr 1953). The subsequent introduction of adjuvant chemotherapy over the last 40 years culminated in the current 5 year survival of 70-80% in patients stratified in the average risk category, while in the less fortunate high risk patients, 5 year survival is given as 60-65% (Millard and De Braganca 2016).

The prognosis for paediatric patients with recurrent and relapsed (following previous recurrence) MB is poorer still and considered a predominantly pre-terminal diagnosis (Hill, Richardson et al. 2020). Owing to its preference for spread to the leptomeninges, the child with suspected MB will have diagnostic MRI brain and staging spinal scans for anatomical localisation of the tumour and exclusion of macroscopic metastases within the neuroaxis, as well as cerebrospinal fluid cytology from lumbar puncture ~ 2 weeks post-operatively (Dufour, Beaugrand et al. 2012).

Following discussion of the patient at a paediatric neuro-oncology MDT, the child would be risk stratified to guide their subsequent management. Factors traditionally considered for risk stratification of these patients include their age (to determine patient suitability for radiotherapy), the volume of residual tumour following maximal safe resection (high risk: $>1.5\text{cm}^3$; average risk: $<1.5\text{cm}^3$) and radiological (MRI of neuroaxis) or cytological determination of metastasis as defined by Chang's criteria (Dufour, Beaugrand et al. 2012).

While significant advances attained in the genomics and molecular subgrouping of MB have informed our prognostication of patients through

correlation of their MB subgroup and histological subtypes as defined by the revised WHO staging of MB (Louis, Perry et al. 2016), our methods of diagnosing disease dissemination lag behind.

Considering the serious prognostic implications associated with metastasis and recurrence of MB, current disease surveillance imaging at the magnetic field strength of clinical MRI scans (1.5-3 Tesla) may be too insensitive to detect pre-metastatic changes that herald macrometastases. Many scientists and clinicians postulate that this pre-macro-metastatic phase would be the ideal opportunity to intervene, as once established macrometastases are evident on radiological imaging, it may be too late. Furthermore, the inadequacy of CSF cytology and the vast array of confounding factors associated with its post-operative, lumbar puncture sampling in paediatric patients, limit its sensitivity as a prognostic marker of disseminated disease (Escudero, Llord et al. 2020).

Therefore to improve the accuracy of risk stratification of paediatric patients with MB and inform our provision of tailored multimodal treatment regimes, we sought to:-

- ❖ Discover a biomarker of increased metastatic potential in paediatric MB cell lines
- ❖ Determine and optimise a method for the robust detection of the biomarker that could be translated into clinical practice
- ❖ Work towards the translation of the prognostic biomarker into an imaging biomarker to promote the timely, dynamic diagnosis of MB metastatic dissemination at diagnosis and surveillance.

A model described by Dregely et al. 2018, for the development of imaging biomarkers in cancer was employed as a guideline.

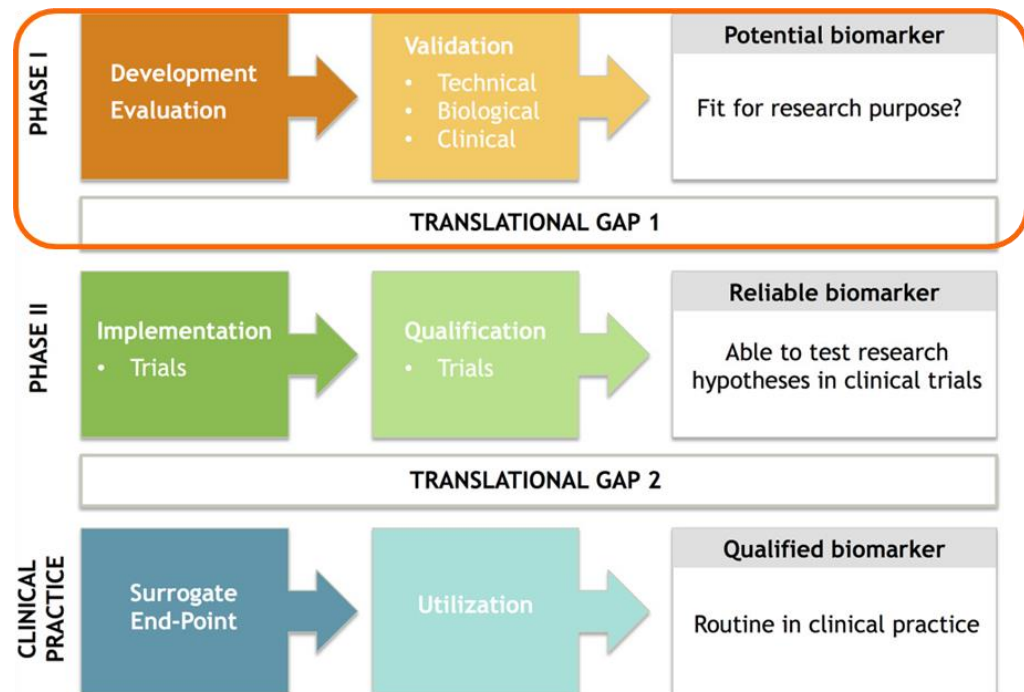


Figure 7.1 Schematic diagram of the stepwise development of an imaging biomarker

The above pathway was used to guide our development of an MRI compatible imaging biomarker, which would correlate the metastatic potential and behaviour of paediatric MB and delineate laminar and nodular leptomeningeal metastases that would otherwise be difficult to detect on conventional MRI imaging of the neuroaxis. Adapted image from (Dregely, Prezzi et al. 2018).

Guided by the schematic pathway depicted in Figure 7.1 as well as the ‘roadmap’ for imaging biomarkers in cancer (O'Connor, Aboagye et al. 2017), the elucidation of a biomarker expressed by all medulloblastoma (MB) subgroups, that could be used to predict the metastatic potential of the tumour of origin was performed.

7.2 The elucidation of a biomarker of increased metastatic potential in MB.

To streamline the potentially elusive search of a prognostic biomarker of metastasis in MB, the determination of differentially expressed proteins in matched pairs of subgrouped medulloblastoma cell lines, with known metastatic status was performed. Having been previously demonstrated to be enriched in the metastatic counterpart of a matched pair of Group 4 MB cell lines, genes involved in the extracellular matrix (ECM) were chosen as our starting point (Wu, Northcott et al. 2012).

Furthermore, given the increasing evidence of intra-tumoural biological heterogeneity between clones of the same MB tumour, it was postulated that differentially expressed proteases and protease inhibitors could help explain the diverse tumour microenvironments inhabited by the primary cerebellar MB and metastatic leptomeningeal deposits (Zou, Poore et al. 2020).

Conditioned supernatant from matched pairs of primary and metastatic Group 3 and Group 4 MB cell lines derived from male paediatric patients aged five and 8 years of age at initial diagnosis respectively, were examined using a protease and protease inhibitor array kit (Figure 3.1). The group 3 metastatic cell line D458-Med exhibited substantially higher expression of KLK5 (95% increase), MMP-3 (62.9% increase) and MMP-2 (56.9% increase) proteases in comparison to its primary counterpart (Table 3.1). Furthermore, there was a distinct decrease in the levels of protease inhibitors detected in the metastatic Group 3 cell line

supernatant as well a limited array of protease inhibitor analytes in comparison to the range demonstrated by its primary counterpart (Figure 3.2). The highly expressed proteases and downregulated protease inhibitors in the secretome of the metastatic Group 3 MB cell line could result in unchecked extracellular matrix degradation, which would likely be advantageous and conducive to the migration of the metastatic cells.

Review of the analytes detected in conditioned supernatant from the matched primary (CHLA-01-MED) and recurrent (CHLA-01R-MED) Group 4 cell lines (Figure 3.3), demonstrated the increased expression of MMP-2 in the latter's secretome (97.3% increase) in comparison to the former (Table 3.3). This result complemented the increased MMP-2 expression demonstrated in the proteomic analysis of the recurrent CHLA-01R-MED by Gu et al. 2017 (Gu, Chen et al. 2017). Once again, the array of protease inhibitors expressed by the metastatic Group 4 cell lines was limited in comparison to those secreted by the primary, echoing the pattern observed in the Group 3 MB cell lines (Figure 3.4).

While other proteases were highly expressed in both metastatic Group 3 and 4 cell lines, MMP-2 was selected as the foremost biomarker for further study, as it was highly differentially expressed in both the metastatic MB cell line supernatants and is well-correlated to higher grade, aggressiveness and staging in other cancers (Isaacson, Jensen et al. 2017). Its fellow gelatinase MMP-9, which has also been shown to be overexpressed in metastatic tumours including medulloblastoma, was also examined in further experiments, to gain a comprehensive overview

of the interactions of MMP-2 with MMP-9 and its endogenous tissue inhibitors of MMPs (TIMPs) which were also differentially expressed in the matched primary and metastatic MB cell lines.

7.3 Biological characterisation of MMP-2 and MMP-9 in 2-D cultured sub-grouped MB cell lines

Considering the multi-level regulation of MMPs, it was deemed necessary to investigate the expression of MMP-2 and MMP-9 at epigenetic, genetic, protein and functional activity levels. In addition to portraying a comprehensive landscape and determining which would be the most robust level for translation into clinical practice, it was postulated that the activation and inhibition of MMP-2 and MMP-9 would be the levels most highly implicated in the metastatic MB cell lines and patients.

To this end, a panel of 9 sub-grouped medulloblastoma cell lines were closely examined and cultured in their optimal cell culture medium in the manner described in the methodology section of this thesis. Matched, paired cell lines destined for the same experiment were cultured at the same time and cell pellets as well as conditioned supernatant obtained simultaneously. This was done to reduce the confounding effects from potential differences in the handling of samples destined for comparison, including factors such as ambient temperature, or slight differences in batch preparations of chemicals and serum, for example, that would be difficult to control.

Overall, at the gene level, MMP-2 was highly expressed in the MB cell lines with higher metastatic potential i.e. derived from MB tumours of higher 'M' grade or cell lines harbouring mutated p53 genes, the latter being well known markers of poor prognosis (Ramaswamy, Nör et al. 2016). As shown in Figure 3.5, MMP-2 gene expression was highest in the metastatic Group 4 cell line CHLA-01R-MED, which in comparison to its primary counterpart demonstrated statistical significance (ANOVA; $p=0.0215$) in comparison to expression levels from the remaining cell lines. While variation in the protein expression of MMP-2 from the panel of 9 MB cell lines prevented a statistically significant result, a trend towards higher MMP-2 protein expression was observed in the metastatic cell lines, compared to their primary counterparts within each subgroup (Figure 3.6)

While gene expression of MMP-9 was not feasible given technical difficulties with primer optimisation, this was thought to be due to the incredibly low levels of MMP-9 gene expression in MB. This theory is supported by the low levels of MMP-9 expression in MB patient samples from the Cavalli dataset (Cavalli, Remke et al. 2017), analysed on the R2 Genomics and visualisation platform (R2).

However, at the protein level, MMP-9 expression was highly variable with no results of statistical significance following western blotting of the MB cell lines. These experiments further reinforced the potential of MMP-2 rather than MMP-9 as the better biomarker of metastasis in MB.

Given the fundamental role of MMPs in both physiological and pathological circumstances, in the enzymatic remodelling of the extracellular matrix, the regulation of their functional activity was believed would best correlate the metastatic potential and behaviour of MB. As such, gelatin zymography was used to examine the levels of functional activity in 48-hour conditioned supernatant derived from the same panel of MB cell lines. These experiments demonstrated a statistically significant increase (ANOVA; $p=0.022$) in the levels of functionally active MMP-2 secreted by the metastatic group 4 MB cell line CHLA-01R-MED, in comparison to its matched primary (Figure 3.10). On the other hand, the highest levels of functionally active MMP-9 were detected in the supernatant from SHH and Group 3 cell lines with the highest metastatic potential (Figure 3.10).

ELISA experiments to determine the optimal storage of the MB cell line derived conditioned supernatant and later MB patient cerebrospinal fluid, showed a stepwise decline in the MMP-2 protein content with each week of storage at 4°C. All supernatant samples and cerebrospinal fluid samples obtained from theatre, were therefore stored at -80°C, to minimise protein degradation as much as possible.

Having established that the levels of functional activity best correlated with the expected metastatic potential of subgrouped MB cell lines cultured in 2-D, we explored whether this finding would be observed in subsequent experiments involving 3-D cultured MB, a step towards the clinical translation of this work.

7.4 Functional characterisation of matrix metalloproteinases in 3-D models of medulloblastoma

While 3-D models of MB do not mirror the exact nature of the *in vivo* metastatic tumour microenvironment, they present an opportunity to better interrogate specific conditions that play a role in the metastatic niche. This is invaluable, given the rarity of MB and subsequently, the limited access to metastatic patient samples, which further prevent the interrogation of the *in vivo* tumour microenvironment.

On the other hand, animal models are expensive to maintain, require expert licensing for their use and may perish prior to the establishment of disseminated disease. For these reasons, customisable 3-D models are preferable as they enable the recapitulation and interrogation of the *in vivo* tumour microenvironment, with improved biological relevance (Van Ommeren, Garzia et al. 2020).

Given our findings that 2-D cultured MB secrete functionally active MMP-2 and MMP-9 in levels that correlate with their metastatic potential, we sought to determine whether altering their tumour microenvironment would alter their levels of secreted MMPs. It was postulated that a 3-D microenvironment would better simulate the *in vivo* setting and thus better portray the influence of the primary (cerebellum) and metastatic (leptomeningeal for example) milieu upon the secretion of MMP-2 and MMP-9 from MB.

To best explore this, two forms of 3-D cell culture were used. A migration spheroid model that was previously optimised by a colleague Dr Sophie Roper (Roper S, 2019) for SHH MB and a 3-D invasion transwell assay, also optimised by another colleague Dr Macha Aldighieri (Aldighieri 2020). Schematic diagrams depicting these are shown in Figure 7.2.

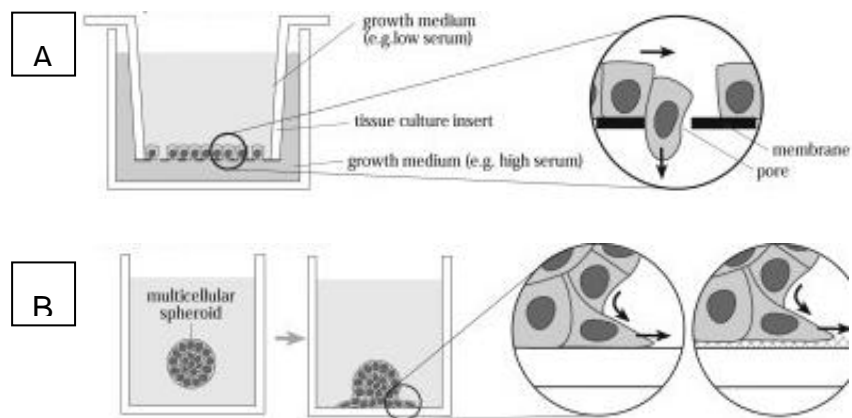


Figure 7.2 Schematic diagram of the 3-D models used.

A. Boyden chamber also known as the transwell assay in which a gradient across a semi-permeable membrane with an ECM component coating, enables the determination of a cell line's capacity to invade and metastasize. B. A multicellular spheroid model consisting of the same or a combination of different cell types can be used to study the migration patterns of 3-D MB spheroids across an ECM-like matrix. Image adapted from (Kramer, Walzl et al. 2013).

While initial spheroid model experiments included the Group 3 MB cell line HD-MB03, their lack of formation of tight spheroids introduced unacceptable variation when transferred between media or matrix coatings. While their looser cell aggregates may be a result of their highly metastatic nature, early apparent dissemination captured in photomicrographs at 24 hours, could have resulted from mechanical dispersion on landing onto the matrix (Figure 4.2).

To explore whether key components present within the primary MB microenvironment such as hyaluronan (recapitulating the cerebellar parenchyma) or collagen IV (enriched in the leptomeningeal metastatic milieu), spheroid migration assays over different matricellular protein combinations were performed. DAOY *mut* p53 (M0), ONS-76 *wt* p53 (M2) and UW228-3 *wt* p53 (M0) were seeded onto either a pure or factor-supplemented collagen IV matrix or a pure or supplemented hyaluronan matrix and allowed to migrate over 72 hours (Figure 4.5, Figure 4.6).

As the spheroids were generated from considerably lower cell numbers (range: 250-1500 cells) in comparison to those examined at 2D-culture (5×10^6 cells), the resulting low levels of secreted functionally active MMP-2 and MMP-9 proved difficult to detect at 24 and 48 hours. This necessitated further optimisation of the zymography protocol to maximise detection of the MMP-2 and MMP-9 signal. Even so, a trend towards increased levels of detectable functionally active MMP-2 and MMP-9 was observed at 48 hours in all SHH cell lines (Figure 4.3).

The spheroid migration experiments began with Day 4 SHH spheroids generated as previously described and seeded on top of a combination of modifiable hyaluronan-based matrices (Hystem[®]). This was found to result in highly statistically significant differences in the levels of functionally active MMP-2 (ANOVA; $p=0.0004$) and MMP-9 (ANOVA; $p=0.0333$) secreted by DAOY spheroids, seeded on top of pure hyaluronan or hyaluronan supplemented with collagen I, Laminin I, vitronectin, fibronectin or all 4 factors, in duplicate experiments (Figure

4.5). Photomicrographs of these experiments (Roper 2019) reportedly portrayed similar extents of migration of the DAOY spheroids across all matrix combinations.

Likewise, ONS-76 spheroids migrated equally well across all HA- based matrices as across the Collagen IV matrix. However, 72-hour migration across collagen IV appeared to result in lower secreted levels of functionally active MMP-2 and MMP-9 in comparison to migration across HA matrices. Interestingly, the levels of MMP-9 were most accentuated in ONS-76 spheroids cultured on top of HA/Laminin I and HA/vitronectin combinations (Figure 4.6).

Though not statistically significant, this data suggests that the notion of CD44-mediated, hyaluronan-dependent MMP-9 activation (Novak and Kaye 2000) may explain the pattern of MMP-9 secretion from ONS-76 spheroids cultured on hyaluronan-based matrices (Figure 4.6). Confirmation of their differential hyaluronan receptor expression revealed that while both DAOY and ONS-76 spheroids have been shown to express CD44 receptors at high levels by immunohistochemistry, their expression of the other, receptor for hyaluronan-mediated motility (RHAMM) was not determined (Roper 2019). As the UW228-3 SHH spheroids did not demonstrate any convincing migratory behaviour on any ECM coating, these spheroids were cultured alongside the other two as a somewhat negative control.

While it was postulated that encapsulation within the established 3-D ECM, would increase the secretion of MMP-2 and MMP-9 from DAOY

and ONS-76 spheroids, this was not proven as when initially embedded within hyaluronan based hydrogels, no invasive behaviour was observed.

However, embedding of single MB cells within a pure hyaluronan gel as performed by my post-doctorate fellow Dr F. Linke resulted in marked increases in the signals of MMP-2 and MMP-9 detectable by gelatin zymography (Fig. 4.8). As this screening experiment demonstrated that, the biophysical characteristics of the tumour microenvironment could alter the levels of functionally active MMP-2 and MMP-9, further optimisation of the embedding of older spheroids into hyaluronan-based hydrogels, is ongoing.

While modulating components of the interstitial matrix such as hyaluronan or collagen IV had quantifiable effects on the levels of MMP-2 and MMP-9 secreted by MB spheroids and cells, we wondered whether the presence of immune cells within the tumour microenvironment would result in higher levels of secreted MMP-2 and MMP-9.

To this end, DAOY and ONS-76 spheroids were co-cultured with varying numbers of macrophages and seeded on top of a collagen IV coating on Day 4. Following 72 hours of migration, conditioned supernatant from these spheroids demonstrated increasing levels of functionally active MMP-9 signal with concurrent increasing numbers of macrophages present. While preliminary, this data suggested that majority of the detectable MMP-9 likely emanates from the MB tumour's cellular microenvironment. However, as the zymography of conditioned

supernatant from 2-D cultured SHH also demonstrated their secretion of high levels of MMP-9, it may be that their serum-complemented media contained immune mediators such as complement proteins, that recapitulated the effects seen in SHH tumours *in vivo*. Immunohistochemical studies of SHH-MB have demonstrated high levels of MMP-9 at the tumour edges, as well as a predilection for immune cell infiltration (Margol AS 2015).

Further work in the co-culture of SHH spheroids with other cellular components such as astrocytes and microglia would be useful in the accurate characterisation of the interactions between MB and their specialised brain tumour microenvironments.

7.5 The effect of pharmacological inhibition of MMP-2 and MMP-9 on the patterns of migration and invasion of 3-D cultured MB

Having observed the unimpeded migration of DAOY (M0) and ONS-76 (M2) SHH spheroids across a combination of different ECM component coatings, we sought to determine whether pharmacological inhibition of their secreted MMP-2 and MMP-9, would alter the migration patterns or behaviour.

To more closely recapitulate the *in vivo* matricellular landscape, tissue inhibitors of MMPs (TIMPs) were used. To determine which inhibitors from the family of four would be optimal, DNA methylation and gene expression data from samples of normal cerebellum and MB patients

were analysed using the R2 Genomics and visualisation platform. We found that TIMP-1 DNA was hypomethylated relative to normal cerebellum, with statistically significant differences (ANOVA; $p=0.015$), in the methylation levels of the subgroups and cerebellum. Furthermore, Kaplan-Meier survival analysis of high versus low gene expression of TIMP-1 and TIMP-2 revealed a stark difference in the more favourable prognosis of MB patients with high levels of TIMP-1 gene expression compared to those with high levels of TIMP-2, while those for TIMP-3 and TIMP-4 did not demonstrate any significant survival advantage (Figure 4.14).

In addition, TIMP-1 gene and protein overexpression has been positively correlated with poorer outcomes in brain tumours as well as other cancers (Jackson, Defamie et al. 2017). Taken together, these findings suggest that TIMP-1 upregulation is an inducible regulatory step that is triggered in highly aggressive and metastatic tumour microenvironments. While TIMP-1 may function as a good biomarker of increased metastatic potential in other cancers, this may not be the case in MB, as demonstrated in our protease and protease inhibitor experiments of conditioned supernatant from matched primary and metastatic Group 3 MB, in whom levels of TIMP-1 and TIMP-2 were both decreased in the metastatic cell lines (Figure 3.4).

Conversely, TIMP-2 expression is reported to be 'equivocal' in most cancers (Jackson, Defamie et al. 2017). However, its seemingly contradictory role in activating MMP-2 by binding to MT-MMP-1, made

TIMP-2 a less optimal candidate inhibitor given the confounding effects it may cause (Jackson, Defamie et al. 2017).

Following treatment with recombinant forms of either TIMP-1 or TIMP-2 at 25 and 50nM concentrations, DAOY (M0), ONS-76 (M2) and UW228-3 (M0) SHH spheroids remained viable. Surprisingly, despite clear demonstration of inhibition of their 72 hour conditioned supernatant (Figure 4.16), there was little convincing evidence of restricted migration in all three cell lines (Figure 4.15). This suggests that MMP-2 and MMP-9 may not be essential for the migration of SHH-MB spheroids across an extracellular matrix. While examination of the photomicrographs of these experiments, suggested a possible alteration in the mode of migration, from collective to single cell migration (Figure 4.18, Figure 4.19), more experiments are needed to demonstrate this observation conclusively.

Therefore, to explore whether the invasive potential of MB would correlate to their secreted levels of functionally active MMP-2 and MMP-9, it was thought that transwell assays would be the best model. Having demonstrated statistically significant differences in the gene expression and functional activity of MMP-2 and MMP-9 between the matched primary and metastatic Group 4 MB cell lines, these and their Group3 matched pair counterparts were examined, after optimisation experiments using the highly aggressive Group 3 cell line, HD-MB03.

Their semi-adherent phenotype when cultured in 2-D made the transwell invasion assay a more suitable model for Group 3 and 4 MB cell lines in comparison to the spheroid model which is optimal for adherent cells.

This suggests that the 2-D phenotypes may correlate with the strength of the cell-cell interactions between the MB subgrouped samples, which may contribute to their respective predilection for dissemination to anatomically distant sites from the primary tumour (Kramer, Walzl et al. 2013).

Given that Group 3 and 4 MB predominantly metastasise to the leptomeninges, an optimised transwell model recapitulating invasion through the BBB was used (Aldighieri 2020). Using HD-MB03 cells for further optimisation, it was determined that a Collagen IV/laminin I barrier would best model the proteins most prevalent in the BBB (Figure 4.21). Following confirmation that recombinant TIMP-1 and TIMP-2 proteins at 10nM, 25nM, 50nM and 100nM would not be cytotoxic (Figure 4.22), we proceeded to treat 100,000 HD-MB03 cells with rTIMP-1 at 100nM for 48 hours prior to permitting their invasion for a further 24 hours.

Remarkably, this rTIMP-1 treatment did not have any effect on the invasive capacity of the cells as shown in Figure 4.23. This finding would support our previous suspicions that the TIMP proteins may promote modified migratory/invasive behaviour, promoting single rather than collective cell movement, which in the transwell invasion model, would be advantageous.

We therefore explored whether the differentially expressed MMP-2 and MMP-9 levels from the matched Group 3 and Group 4 MB cell lines would correlate with their expected differential invasive capacity. Replicated experiments (n=3) of the matched Group 3 and Group 4 MB correlated

surprisingly well with their levels of secreted functionally active MMP-2 and MMP-9 as depicted in Figure 3.10. Once again this finding was highly statistically significant for the Group 4 MB pair (t-test; $p < 0.05$), suggesting that the levels of functionally active MMP-2 would be a suitable biomarker for prognosis, especially in Group 4 MB.

This is especially significant, given that Group 4 MB are the least likely to demonstrate contrast enhancement in neuroaxial contrast-enhanced MR imaging, resulting in poorly detectable leptomeningeal deposits. We therefore progressed to examine a small cohort of available cerebrospinal fluid samples from paediatric patients, who received management at our centre.

7.6 Validation of MMPs as prognostic biomarkers in paediatric MB patient samples

To gain a balanced impression of the MMP landscape in paediatric patients with MB, DNA methylation and gene expression data of MB patient samples from the Hovestadt and Cavalli dataset were analysed on the R2 Genomics and Visualisation platform (Cavalli, Remke et al. 2017) . While it is widely postulated that epigenetic regulation and its resulting gene expression would serve as optimal levels for biomarker detection, we found that this was not always the case in MB.

In the Hovestadt dataset, whereas MMP-2 hypomethylation was observed in DNA from MB patient samples compared to normal cerebellum, the methylation pattern for MMP-9 varied around the mean levels detected in normal cerebellum, while it appeared to be stringently regulated in EMMPRIN at levels observed in normal cerebellar tissue (Figure 5.2). Conversely, the same analysis applied to the DNA methylation and subsequent gene expression of TIMP-1 revealed an inverse correlation between the levels of DNA methylation and its resulting gene expression in all subgroups, while a similar trend was observed for TIMP-2 in all MB subgroups except SHH (Figure 5.3). While reasons for these observations are difficult to decipher, review of the epigenetic modulation of MMP related genes demonstrated the difficulties associated with predictions given the likelihood of subgroup specific epigenetic regulations and their effects on subsequent gene expression.

Thus, the examination of cerebrospinal fluid from paediatric patients with MB was postulated to be the optimal medium from which to detect biomarkers of increased metastatic potential.

While the evidence of a glymphatic pathway of cerebrospinal fluid circulation along perivascular spaces of brain vasculature has led to its designation as the lymphatic pathway in the brain, it may also explain why it has been reported that sampling of cerebrospinal fluid close to a tumour improves the sensitivity of the cytology. This observation made by Weston et al. 2011 could compound the poor sensitivity of cytology

from cerebrospinal fluid obtained through lumbar punctures 14-days following surgical resection of the primary MB. Considering the likelihood of circulating tumour cells within the lumbar subarachnoid space would likely deposit in the thecal sac under gravity, CSF sampling above this level would more than likely return negative results.

Furthermore, factors associated with the sampling, delivery and storage of the CSF could result in erroneously negative results, even in the presence of radiologically proven leptomeningeal disease. These include a CSF sampling volume of less than 10 ml, delays of sample delivery to the lab for processing and cooling as well as inappropriate storage and handling of the samples. Given the less than ideal manner in which clinical samples may be handled in our current resource scarce NHS, these factors may result in the erroneous risk stratification of patients with high-risk metastatic disease, being labelled as average-risk, and prescribed sub-optimal therapy regimens. While this has obvious implications for the prognosis in the affected children, it also worryingly culminates in significant neurocognitive, health and psychosocial morbidity from therapies necessitated at disease recurrence or relapse.

Out of 10 CSF samples from lumbar puncture performed in six paediatric patients with MB who were treated at our centre, only one sample gave a positive result, in Patient 1 who presented with metastatic dissemination at diagnosis. This result is even more concerning given that the reported sensitivity of traditional CSF cytology results is

approximately 50% (Bennett, Ashmawy et al. 2017, Chamberlain, Junck et al. 2017).

Furthermore, in Patient 4 who returned with an intraventricular recurrence of his Group 4 MB, his CSF cytology remained negative while zymography of the same CSF samples demonstrated strong signals denoting the increased levels of functionally active MMP-2 and MMP-9 within the samples (Figure 5.10). Interestingly, surveillance CSF sampling from patient 6 obtained via an Ommaya reservoir, an indwelling catheter that sits within the lateral ventricles, demonstrated continually increasing levels of MMP-2 and MMP-9 on zymography, preceding the radiological detection of his macrometastases.

While the levels of functionally active MMP-2 and MMP-9 could be attributed to tumour or implant-associated inflammation, the cellular characteristics of the cerebrospinal fluid samples in Table 5.3 suggest otherwise. This finding further supports the validity of the detection of levels of functionally active MMP-2 within patient CSF as a robust biomarker of dissemination that could be used to improve prognostication of patients as well as enable earlier detection of recurrent disease and treatment response on surveillance. Furthermore, the sensitivity of gelatin zymography appears to be better than that CSF cytology as demonstrated by the CSF samples obtained in theatre for Patient 4[1] that was strongly positive in comparison to the sample from lumbar puncture 2 weeks later (sample 4[2]). While the sample size of this proof of principle pilot study is a limitation, we demonstrated that zymography

of cerebrospinal fluid samples obtained at the point of dural entry in theatre, and subsequent expedited delivery to a lab for processing and storage at -20°C at least, would improve the diagnosis of disease dissemination in paediatric patients with MB. Furthermore, these pragmatic and attainable improvements are likely to be easily translated into clinical practice, with little specialised equipment required. While ELISA or protease and protease inhibitor assays could also be argued to give similarly quantifiable results, these methods incur substantial financial costs of the kit and equipment required.

However, to further improve the accuracy or radiological detection of metastatic dissemination, the use of an MRI compatible MMP-2/-9 biosensor administered as intrathecal or intravenous contrast could prove a promising tool in our quest to improve the risk stratification of paediatric patients with MB.

7.7 Improving the risk stratification of paediatric patients with MB using our ¹⁹Fluorine-MMP-MRI biosensor

Metastatic dissemination is arguably the most powerful determinant of a medulloblastoma patient's prognosis. However, our current clinical methods used to detect it have a reported sensitivity of 50-76% (Bennett, Ashmawy et al. 2017), resulting in suboptimal management and culminating in death and morbidity in these high-risk patients.

While MRI is the designated gold standard tool for the identification of neuroaxial disease in the paediatric patient with MB, the subtle appearances of leptomeningeal disease can prove incredibly difficult to diagnose, especially without specialist neuro-radiology expertise or in the case of non-enhancing MBs as is often observed in Group 4 MB (Figure 7.3). As the most commonly occurring and the second most likely subgroup to metastasise to its preferred leptomeningeal and sanctuary sites, the poor contrast uptake of Group 4-MB renders the diagnosis of their metastatic deposits incredibly difficult (Holgado, Guerreiro Stucklin et al. 2017).

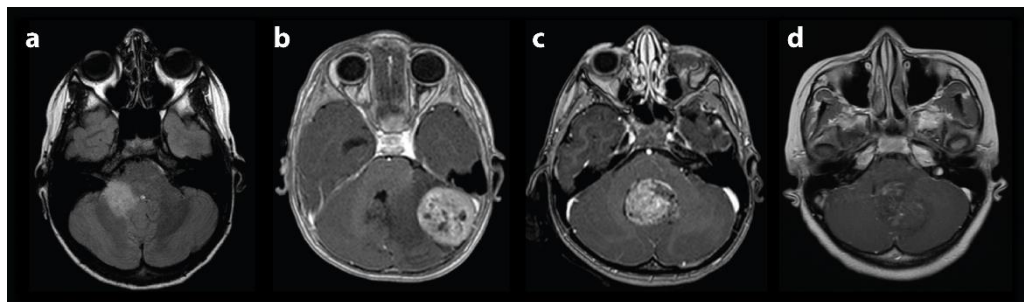


Figure 7.3 Typical MRI appearances of the four MB subgroups

A. WNT-MB commonly arise in the cerebellopontine angle and demonstrate avid enhancement with gadolinium contrast. B. SHH-MB, which typically arise in the lateral cerebellar hemispheres. C. An avidly enhancing midline cerebellar tumour is most likely to be a Group-3 MB. D. The characteristic appearance of the poorly enhancing Group 4 midline MB. Image reproduced from Holgado et al. 2017.

Therefore to determine whether our locally synthesised 19 Fluorine-MMP/MRI biosensor could be used to translate the levels of functionally active MMP-2 and MMP-9 into prognostic imaging biomarkers, FRET assays were used to examine the conditioned MB cell line supernatant, as it was felt that it best recapitulated the biosensor.

Having demonstrated the strongest correlation of increased levels of functional gelatinases with the differential metastatic potentials of the matched primary and recurrent Group 4 cell lines, 48 hour conditioned supernatant was centrifuged, column-concentrated and stored at -80°C. These measures ensured the maximal retention of their enzymatic activity, which would be crucial for the working of the biosensor. While the FRET assays nicely demonstrated stark differences in the levels of fluorescence emitted by the quenched digested gelatin, the experiments also suggested that the 10% acetonitrile (ACN) solvent used in the biosensor synthesis, precipitated proteins out of the solution, resulting in decreasing levels of fluorescence in the presence of ACN. This highlighted the importance of using physiologically compatible solvents, to develop radiological contrast agents. While our biosensor contains a Gadolinium moiety, its administration would incur a less overall volume of contrast, which is preferential especially in allergic patients.

While the biosensor experiments proved its immense value for potential application as an imaging biomarker, further optimisation is required to improve its sensitivity and hence, enable the dynamic, detection of endogenous MMP-2 and MMP-9 as successfully as has been accomplished with their recombinant protein forms. Once established, this imaging modality could improve the detection of metastasis at diagnosis, during intra-operative MB resection with use of the intra-operative MRI to maximise safe resection, as well as during surveillance, to detect molecular changes that herald disease dissemination.

7.8 Proposals for future work

Given our current findings, focussed efforts in the following domains would advance our mission to improve our risk stratification of MB patients and improve our provision of personalised, patient-centred care.

- ❖ The development of more complex 3-D culture models that would better recapitulate the *in vivo* tumour microenvironment including both cellular and ECM components of the specialised brain tumour milieu, as well as incorporation of immune cells.

- ❖ Streamline and standardise the clinical methods employed in the diagnosis and detection of MB dissemination. This may involve enforcing the RANO criteria for the radiological assessment of the neuroaxis; improving the methods of CSF biopsy by undertaking clinical trials to:
 1. Establish whether the sensitivity of CSF cytology is improved when CSF is sourced at dural entry in theatre, in comparison to lumbar puncture 2 week's post-operatively;
 2. Determine whether analysis of patient CSF levels of functionally active MMP-2 and MMP-9 using gelatin zymography, ELISA or FRET techniques, would result in more accurate diagnosis of MB metastasis culminating in robust risk stratification of patients and timely initiation of appropriate adjuvant therapy.

- ❖ Continue optimisation of the MRI compatible MMP-2/9 biosensor to increase the sensitivity of its detection of endogenous MMP-2 and MMP-9. Ensuring that the biosensor is stable and soluble in a physiological solvent, will facilitate its safe translation into animal models and patients alike.

7.9 Concluding statement

Having demonstrated the biological validity of MMP-2 as a biomarker of poorer prognosis in MB, we aim to translate it into an MRI compatible imaging biomarker. This would enable accurate determination of a patient's risk of metastasis at first presentation with MB as well as on disease surveillance. With further optimisation, the biosensor could also be used as an adjunct, to improve the extent of maximal safe resection when given pre-operatively and imaged using the intraoperative MRI. While further work to improve the biosensor imaging is required, we have shown that liquid biopsy of patient cerebrospinal fluid at operation would likely improve the sensitivity of CSF cytology, without the confounding factor of iatrogenic dissemination associated with post-operative CSF sampling. Furthermore, streamlining the storage and handling of CSF samples, would be paramount to enhancing sensitivity and specificity of any CSF-based detection of circulating tumour cell DNA, protein or biomarkers and is thus, worth refining.

References

(<http://r2.amc.nl>). "R2 Genomics Analysis and Visualisation platform."

Abbott, N. J., et al. (2006). "Astrocyte–endothelial interactions at the blood–brain barrier." Nature reviews neuroscience **7**(1): 41.

Aldighieri, M. (2020). Identifying factors that control medulloblastoma cell migration using a model of brain-CSF dissemination. Medicine, University of Nottingham. **Doctor of Philosophy**.

Ayoub, A. E., et al. (2005). "Developmental expression of matrix metalloproteinases 2 and 9 and their potential role in the histogenesis of the cerebellar cortex." Journal of Comparative Neurology **481**(4): 403-415.

Bauvois, B. (2012). "New facets of matrix metalloproteinases MMP-2 and MMP-9 as cell surface transducers: outside-in signaling and relationship to tumor progression." Biochimica et Biophysica Acta (BBA)-Reviews on Cancer **1825**(1): 29-36.

Bennett, J., et al. (2017). "The clinical significance of equivocal findings on spinal MRI in children with medulloblastoma." Pediatric Blood & Cancer **64**(8): e26472.

Bhoopathi, P., et al. (2011). "MMP-2 mediates mesenchymal stem cell tropism towards medulloblastoma tumors." Gene Ther **18**(7): 692-701.

Bian, J. and Y. Sun (1997). "Transcriptional activation by p53 of the human type IV collagenase (gelatinase A or matrix metalloproteinase 2) promoter." Molecular and cellular biology **17**(11): 6330-6338.

Blüml, S., et al. (2015). "Molecular subgroups of medulloblastoma identification using noninvasive magnetic resonance spectroscopy." Neuro-oncology **18**(1): 126-131.

Boire, A., et al. (2019). "Brain metastasis." Nature Reviews Cancer: 1-8.

Boire, A., et al. (2020). "Brain metastasis." Nature Reviews Cancer **20**(1): 4-11.

Boire, A., et al. (2017). "Complement component 3 adapts the cerebrospinal fluid for leptomeningeal metastasis." Cell **168**(6): 1101-1113. e1113.

Bonner, E. R., et al. (2018). "Liquid biopsy for pediatric central nervous system tumors." NPJ Precis Oncol **2**: 29.

- Borgono, C. A. and E. P. Diamandis (2004). "The emerging roles of human tissue kallikreins in cancer." Nat Rev Cancer **4**(11): 876-890.
- Cacho-Diaz, B., et al. (2020). "Tumor microenvironment differences between primary tumor and brain metastases." J Transl Med **18**(1): 1.
- Carril, M. (2017). "Activatable probes for diagnosis and biomarker detection by MRI." J Mater Chem B **5**(23): 4332-4347.
- Cavalli, F. M., et al. (2017). "Intertumoral heterogeneity within medulloblastoma subgroups." Cancer Cell **31**(6): 737-754. e736.
- Chamberlain, M., et al. (2017). "Leptomeningeal metastases: a RANO proposal for response criteria." Neuro-oncology **19**(4): 484-492.
- Chamberlain, M., et al. (2014). "Leptomeningeal metastasis: a Response Assessment in Neuro-Oncology critical review of endpoints and response criteria of published randomized clinical trials." Neuro Oncol **16**(9): 1176-1185.
- Chu, T., et al. (2011). "Extracellular matrix metalloproteinase inducer is a negative prognostic factor of pediatric medulloblastoma." Pathol Oncol Res **17**(3): 705-711.
- COG, C. s. O. G. (2018). Long-Term Follow-up Guidelines for Survivors of childhood, adolescent and young adult cancers, Children's Oncology Group.
- Damkier, H. H., et al. (2013). "Cerebrospinal fluid secretion by the choroid plexus." Physiological reviews.
- Dauth, S., et al. (2016). "Extracellular matrix protein expression is brain region dependent." J Comp Neurol **524**(7): 1309-1336.
- Dong, Y., et al. (2014). "Metastasis of ovarian cancer is mediated by kallikrein related peptidases." Clinical & experimental metastasis **31**(1): 135-147.
- Dregely, I., et al. (2018). "Imaging biomarkers in oncology: Basics and application to MRI." J Magn Reson Imaging **48**(1): 13-26.
- Dufour, C., et al. (2012). "Metastatic medulloblastoma in childhood: Chang's classification revisited." International journal of surgical oncology **2012**.
- Escudero, L., et al. (2020). "Circulating tumour DNA from the cerebrospinal fluid allows the characterisation and monitoring of medulloblastoma." Nature communications **11**(1): 1-11.

Faas, H. M., et al. (2019). "Accelerated (19)F.MRI Detection of Matrix Metalloproteinase-2/-9 through Responsive Deactivation of Paramagnetic Relaxation Enhancement." Contrast Media Mol Imaging **2019**: 4826520.

Ferro, M. P., et al. (2020). "Materials for blood brain barrier modeling in vitro." Materials Science and Engineering: R: Reports **140**: 100522.

Friedberg, M. H., et al. (1998). "Specific matrix metalloproteinase profiles in the cerebrospinal fluid correlated with the presence of malignant astrocytomas, brain metastases, and carcinomatous meningitis." Cancer: Interdisciplinary International Journal of the American Cancer Society **82**(5): 923-930.

Ganji, P. C. N., et al. (2011). "siRNA-mediated downregulation of MMP-9 and uPAR in combination with radiation induces G2/M cell-cycle arrest in Medulloblastoma." Molecular Cancer Research **9**(1): 51-66.

Gerarduzzi, C., et al. (2020). "The Matrix Revolution: Matricellular Proteins and Restructuring of the Cancer Microenvironment." Cancer Res **80**(13): 2705-2717.

Goo, H. W. and Y.-S. Ra (2017). "Advanced MRI for pediatric brain tumors with emphasis on clinical benefits." Korean Journal of Radiology **18**(1): 194-207.

Greenberg, M. S. and N. Arredondo (2001). "Handbook of neurosurgery."

Gu, S., et al. (2017). "Proteomic profiling of isogenic primary and metastatic medulloblastoma cell lines reveals differential expression of key metastatic factors." J Proteomics **160**: 55-63.

Haris, M., et al. (2015). "Molecular magnetic resonance imaging in cancer." J Transl Med **13**: 313.

Hill, R. M., et al. (2020). "Time, pattern, and outcome of medulloblastoma relapse and their association with tumour biology at diagnosis and therapy: a multicentre cohort study." The Lancet Child & Adolescent Health.

Holgado, B. L., et al. (2017). "Tailoring medulloblastoma treatment through genomics: making a change, one subgroup at a time." Annual review of genomics and human genetics **18**: 143-166.

Hovestadt, V., et al. (2014). "Decoding the regulatory landscape of medulloblastoma using DNA methylation sequencing." Nature **510**(7506): 537-541.

Hovestadt, V., et al. (2013). "Robust molecular subgrouping and copy-number profiling of medulloblastoma from small amounts of archival

tumour material using high-density DNA methylation arrays." Acta neuropathologica **125**(6): 913-916.

Isaacson, K. J., et al. (2017). "Matrix-metalloproteinases as targets for controlled delivery in cancer: An analysis of upregulation and expression." Journal of Controlled Release **259**: 62-75.

Ivanov, D. P., et al. (2016). "In vitro models of medulloblastoma: choosing the right tool for the job." Journal of biotechnology **236**: 10-25.

Jabarkheel, R., et al. (2020). "Molecular correlates of cerebellar mutism syndrome in medulloblastoma." Neuro-oncology **22**(2): 290-297.

Jackson, H. W., et al. (2017). "TIMPs: versatile extracellular regulators in cancer." Nat Rev Cancer **17**(1): 38-53.

Jessen, N. A., et al. (2015). "The glymphatic system: a beginner's guide." Neurochemical research **40**(12): 2583-2599.

Junseo Oh, D.-W. S., Tere Diaz, Beiyang Wei, Yvona Ward, Jill M. Ray, Yoko Morioka, Shuliang Shi, Hitoshi Kitayama, Chiaki Takahashi, Makoto Noda and William G. Stetler-Stevenson (2004). "Tissue Inhibitors of Metalloproteinase 2 Inhibits Endothelial Cell Migration through Increased Expression of RECK." Cancer Research **64**(24): 9062-9069.

Juraschka, K. and M. D. Taylor (2019). "Medulloblastoma in the age of molecular subgroups: a review: JNSPG 75th Anniversary Invited Review Article." Journal of Neurosurgery: Pediatrics **24**(4): 353-363.

Justus, C. R., et al. (2014). "In vitro cell migration and invasion assays." JoVE (Journal of Visualized Experiments)(88): e51046.

Kessenbrock, K., et al. (2010). "Matrix metalloproteinases: regulators of the tumor microenvironment." Cell **141**(1): 52-67.

Kool, M., et al. (2014). "Genome sequencing of SHH medulloblastoma predicts genotype-related response to smoothed inhibition." Cancer Cell **25**(3): 393-405.

Kralik, S., et al. (2017). "Radiological diagnosis of drop metastases from paediatric brain tumours using combination of 2D and 3D MRI sequences." Clinical radiology **72**(10): 902. e913-902. e919.

Kramer, N., et al. (2013). "In vitro cell migration and invasion assays." Mutation Research/Reviews in Mutation Research **752**(1): 10-24.

Krupa, J. L. (2016). "Design, Synthesis and Evaluation of MRI Ligands for in Vivo Imaging of Protease Activity." University of Nottingham.

Kumar, R., et al. (2020). "Medulloblastoma genomics in the modern molecular era." Brain Pathology **30**(3): 679-690.

Kumar, V., et al. (2017). "Challenges and recent advances in medulloblastoma therapy." Trends in pharmacological sciences **38**(12): 1061-1084.

Laronha H, C. I., Portugal J, Azul A, Polido M, Petrova KT, Salema-Oom M, Caldeira J (2020). "Challenges in matrix metalloproteinases inhibition." Biomolecules **10**(5).

Lei, Z., et al. (2020). "Biosensors and bioassays for determination of matrix metalloproteinases: state of the art and recent advances." J Mater Chem B **8**(16): 3261-3291.

Li K, T. F., Yiu CK. (2020). "The past, present and future perspectives of matrix metalloproteinase inhibitors." Pharmacology & Therapeutics. Mar **1**(207).

Louis, D. N., et al. (2007). "The 2007 WHO classification of tumours of the central nervous system." Acta neuropathologica **114**(2): 97-109.

Louis, D. N., et al. (2016). "The 2016 World Health Organization classification of tumors of the central nervous system: a summary." Acta neuropathologica **131**(6): 803-820.

Louveau, A., et al. (2017). "Understanding the functions and relationships of the glymphatic system and meningeal lymphatics." The Journal of clinical investigation **127**(9): 3210-3219.

Manias, K. A., et al. (2017). "Magnetic resonance imaging based functional imaging in paediatric oncology." European Journal of Cancer **72**: 251-265.

Margol AS, R. N., Gnanachandran J, Hung LT, Kennedy RJ, Vali M, Dhall G, Finlay JL, Erdreich-Epstein A, Krieger MD, Drissi R. (2015). "Tumor-associated macrophages in SHH subgroup of medulloblastomas." Clinical cancer research **15**;21(6): 1457-1465.

Massimino, M., et al. (2016). "Childhood medulloblastoma." Critical reviews in oncology/hematology **105**: 35-51.

Mastorakos, P. and D. McGavern (2019). "The anatomy and immunology of vasculature in the central nervous system." Science immunology **4**(37).

Mata-Mbemba, D., et al. (2018). "MRI Characteristics of Primary Tumors and Metastatic Lesions in Molecular Subgroups of Pediatric Medulloblastoma: A Single-Center Study." AJNR Am J Neuroradiol **39**(5): 949-955.

McCord, M., et al. (2017). "Targeting WNT Signaling for Multifaceted Glioblastoma Therapy." Frontiers in Cellular Neuroscience **11**(318).

Menyhart, O., et al. (2019). "Molecular markers and potential therapeutic targets in non-WNT/non-SHH (group 3 and group 4) medulloblastomas." J Hematol Oncol **12**(1): 29.

Menyhárt, O. and B. Györffy (2020). "Molecular stratifications, biomarker candidates and new therapeutic options in current medulloblastoma treatment approaches." Cancer and Metastasis Reviews: 1-23.

Millard, N. E. and K. C. De Braganca (2016). "Medulloblastoma." Journal of child neurology **31**(12): 1341-1353.

Morad, G. and M. A. Moses (2019). "Brainwashed by extracellular vesicles: the role of extracellular vesicles in primary and metastatic brain tumour microenvironment." J Extracell Vesicles **8**(1): 1627164.

Northcott, P. A., et al. (2017). "The whole-genome landscape of medulloblastoma subtypes." Nature **547**(7663): 311-317.

Northcott, P. A., et al. (2012). "Medulloblastomics: the end of the beginning." Nature Reviews Cancer **12**(12): 818-834.

Northcott, P. A., et al. (2019). "Medulloblastoma." Nature Reviews Disease Primers **5**(1): 1-20.

Novak, U. and A. H. Kaye (2000). "Extracellular matrix and the brain: components and function." Journal of clinical neuroscience **1**(7(4)): 280-290.

O'Connor, J. P., et al. (2017). "Imaging biomarker roadmap for cancer studies." Nat Rev Clin Oncol **14**(3): 169-186.

Ö., Ö., et al. (2004). "Expression of matrix metalloproteinases and their inhibitors in medulloblastomas and their prognostic relevance." Clinical cancer research **15**(10(14)): 4746-4753.

Olson, O. C. and J. A. Joyce (2015). "Cysteine cathepsin proteases: regulators of cancer progression and therapeutic response." Nature Reviews Cancer **15**(12): 712-729.

OpenStaxCollege (2013). Circulation and the Central Nervous System Connexions, Connexions.

Orr, B. A. (2020). "Pathology, diagnostics, and classification of medulloblastoma." Brain Pathology (Zurich, Switzerland) **30**(3): 664.

Panigrahy, A. and S. Blüml (2009). "Neuroimaging of pediatric brain tumors: from basic to advanced magnetic resonance imaging (MRI)." Journal of child neurology **24**(11): 1343-1365.

Paterson, E. and R. Farr (1953). "Cerebellar medulloblastoma: treatment by irradiation of the whole central nervous system." Acta radiologica **39**(4): 323-336.

Pavelic, S. K., et al. (2011). "Metastasis: new perspectives on an old problem." Molecular cancer **10**(1): 22.

R2. R2: Genomics Analysis and Visualization Platform <http://r2.amc.nl>.

Rae, C. D. (2014). "A guide to the metabolic pathways and function of metabolites observed in human brain 1 H magnetic resonance spectra." Neurochemical research **39**(1): 1-36.

Raeeszadeh-Sarmazdeh M, D. L., Hritz BG. (2020). "Metalloproteinases and Their Inhibitors: Potential for the Development of New Therapeutics." Cells **9**(5).

Ramaswamy, V., et al. (2016). "p53 and Medulloblastoma." Cold Spring Harbor perspectives in medicine **6**(2): a026278.

Ramaswamy, V., et al. (2016). "Risk stratification of childhood medulloblastoma in the molecular era: the current consensus." Acta neuropathologica **131**(6): 821-831.

Ramaswamy, V., et al. (2013). "Recurrence patterns across medulloblastoma subgroups: an integrated clinical and molecular analysis." The Lancet Oncology **14**(12): 1200-1207.

Ramaswamy, V. and M. D. Taylor (2017). "Medulloblastoma: from myth to molecular." Journal of Clinical Oncology **35**(21): 2355-2363.

Richard, S. A., et al. (2020). "The Pivotal Novel Pathogenic Roles of Hyaluronic Acid and its Receptors in Gliomas." Advances in Bioscience and Clinical Medicine **8**(2): 1-9.

Roper, S. (2019). "Development of three-dimensional spheroid models for the analysis of medulloblastoma drug response and metastatic dissemination." University of Nottingham.

Roussel, M. F. and J. L. Stripay (2018). "Epigenetic Drivers in Pediatric Medulloblastoma." Cerebellum **17**(1): 28-36.

Sawlani, V., et al. (2020). "Multiparametric MRI: practical approach and pictorial review of a useful tool in the evaluation of brain tumours and tumour-like lesions." Insights into Imaging **11**(1): 1-19.

Schulz, M., et al. (2019). "Microenvironmental Regulation of Tumor Progression and Therapeutic Response in Brain Metastasis." Frontiers in Immunology **10**(1713).

Sharma, T., et al. (2019). "Second-generation molecular subgrouping of medulloblastoma: an international meta-analysis of Group 3 and Group 4 subtypes." Acta neuropathologica **138**(2): 309-326.

Shay, G., et al. (2015). "Moving targets: Emerging roles for MMPs in cancer progression and metastasis." Matrix biology **44**: 200-206.

Shimoda, M. and R. Khokha (2017). "Metalloproteinases in extracellular vesicles." Biochimica et Biophysica Acta (BBA)-Molecular Cell Research **1864**(11): 1989-2000.

Steeg, P. S., et al. (2011). "Brain metastases as preventive and therapeutic targets." Nature Reviews Cancer **11**(5): 352-363.

Stetler-Stevenson, W. G. (2008). "Tissue inhibitors of metalloproteinases in cell signaling: metalloproteinase-independent biological activities." Science signaling **1**(27): re6-re6.

Taylor, P. D., et al. (2018). "Diagnostic and prognostic biomarker potential of kallikrein family genes in different cancer types." Oncotarget **9**(25): 17876.

Tanifum, E. A., et al. (2018). "Hydrophilic fluorinated molecules for spectral 19 F MRI." Scientific Reports **8**(1): 1-8.

Termini, J., et al. (2014). "Role of the neural niche in brain metastatic cancer." Cancer Research **74**(15): 4011-4015.

Thompson, E. M., et al. (2020). "Current medulloblastoma subgroup specific clinical trials." Transl Pediatr **9**(2): 157-162.

Thompson, E. M., et al. (2016). "Prognostic value of medulloblastoma extent of resection after accounting for molecular subgroup: a retrospective integrated clinical and molecular analysis." The Lancet Oncology **17**(4): 484-495.

Thompson, E. M., et al. (2017). "The role of angiogenesis in Group 3 medulloblastoma pathogenesis and survival." Neuro Oncol **19**(9): 1217-1227.

Toole, B. P. (2020). "The CD147 - HYALURONAN Axis in cancer." The Anatomical Record **303**(6): 1573-1583.

Torre, M., et al. (2020). "Integration of rare cell capture technology into cytologic evaluation of cerebrospinal fluid specimens from patients with

solid tumors and suspected leptomeningeal metastasis." Journal of the American Society of Cytopathology **9**(1): 45-54.

Touboul, C., et al. (2013). "Mesenchymal stem cells enhance ovarian cancer cell infiltration through IL6 secretion in an amniochorionic membrane based 3D model." Journal of Translational Medicine **11**(1): 28.

Van Ommeren, R., et al. (2020). "The molecular biology of medulloblastoma metastasis." Brain Pathol **30**(3): 691-702.

Vandenbroucke RE, L. C. (2014). "Is there new hope for therapeutic matrix metalloproteinase inhibition?" Nature reviews Drug discovery **13**(12): 904-927.

Vihinen, P. and V. M. Kahari (2002). "Matrix metalloproteinases in cancer: prognostic markers and therapeutic targets." Int J Cancer **99**(2): 157-166.

Vince, G. H., et al. (2001). "Medulloblastoma displays distinct regional matrix metalloprotease expression." Journal Of Neuro-Oncology **53**(2): 99-106.

Vinje, V., et al. (2020). "Intracranial pressure elevation alters CSF clearance pathways." Fluids and Barriers of the CNS **17**: 1-19.

Weston, C. L., et al. (2011). "Detection of cancer cells in the cerebrospinal fluid: current methods and future directions." Fluids Barriers CNS **8**(1): 14.

Wu, X., et al. (2012). "Clonal selection drives genetic divergence of metastatic medulloblastoma." Nature **482**(7386): 529-533.

Yeo, K. K., et al. (2019). "Prognostic significance of molecular subgroups of medulloblastoma in young children receiving irradiation-sparing regimens." Journal Of Neuro-Oncology **145**(2): 375-383.

Yu, C.-F., et al. (2017). "Dual roles of tumour cells-derived matrix metalloproteinase 2 on brain tumour growth and invasion." British journal of cancer **117**(12): 1828-1836.

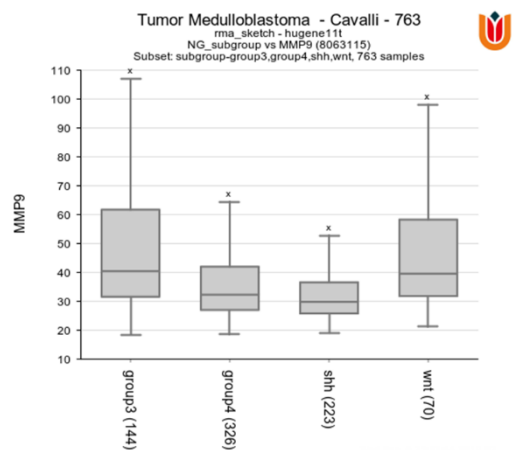
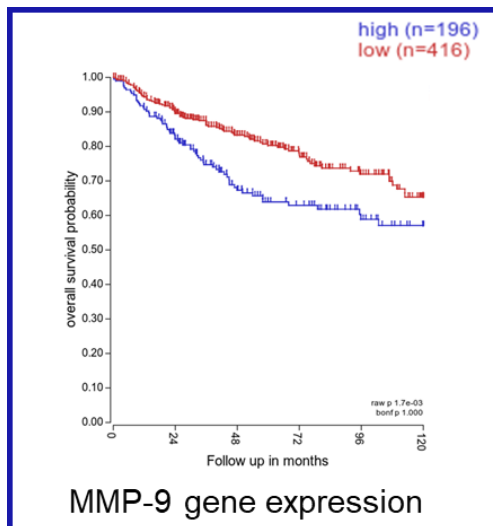
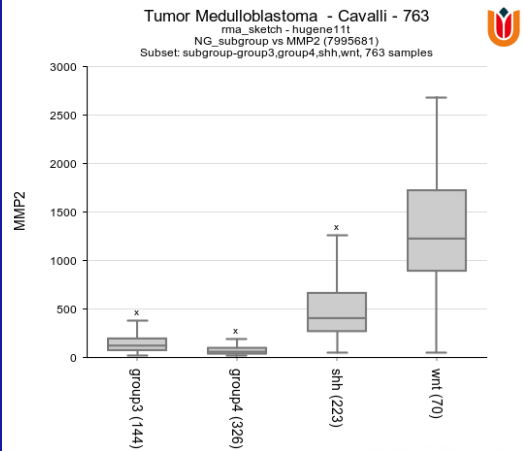
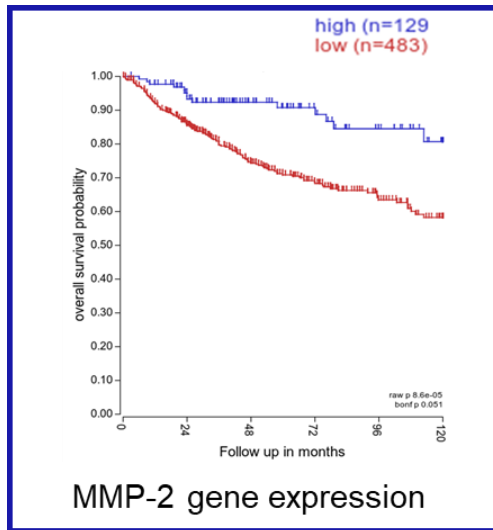
Zapotocky M, M.-M. D., Sumerauer D, Liby P, Lassaletta A, Zamecnik J, Krskova L, Kyncl M, Stary J, Laughlin S, Arnoldo A. (2017). "Differential patterns of metastatic dissemination across medulloblastoma subgroups." Journal of Neurosurgery: Pediatrics. **21**(2): 145-152.

Zeltzer, P. M., et al. (1999). "Metastasis stage, adjuvant treatment, and residual tumor are prognostic factors for medulloblastoma in children:

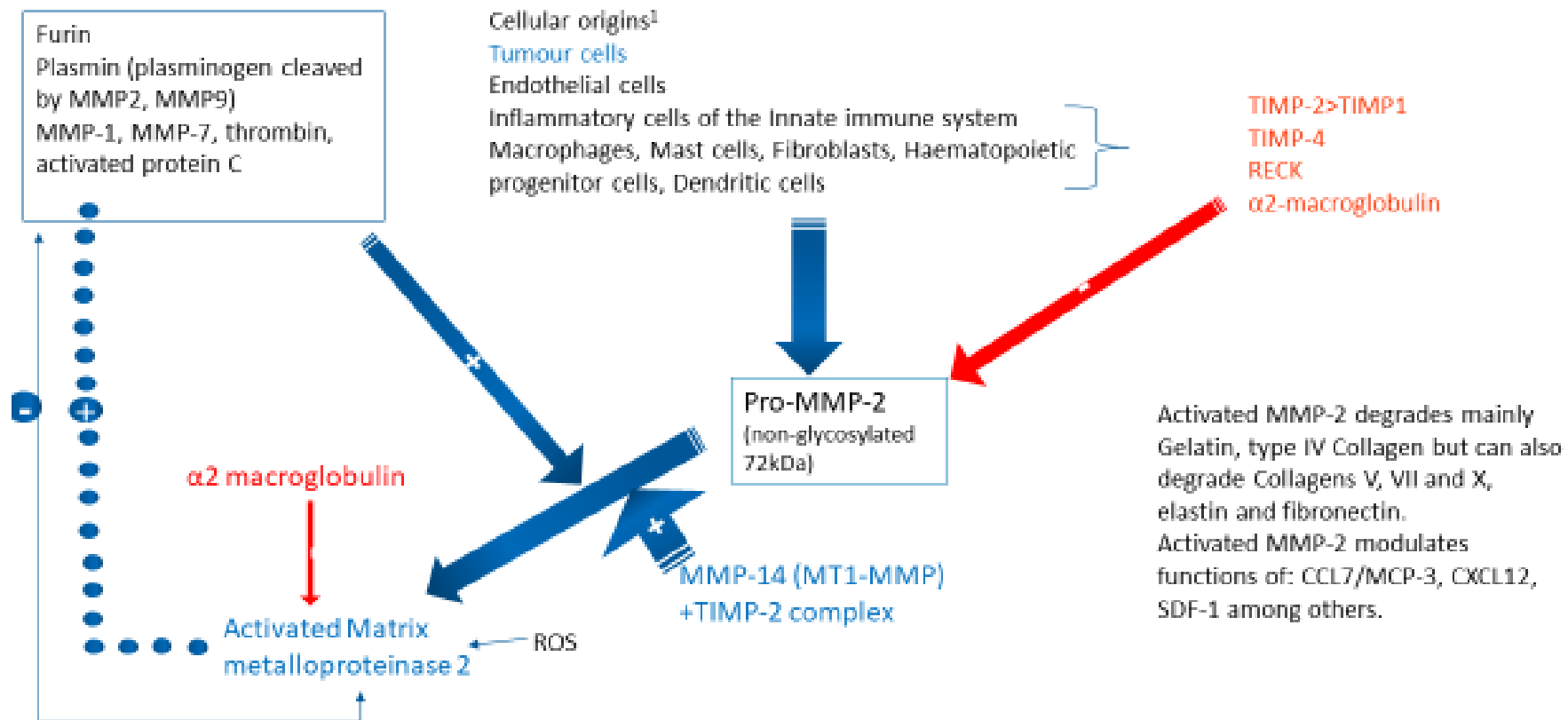
conclusions from the Children's Cancer Group 921 randomized phase III study." Journal of Clinical Oncology **17**(3): 832-832.

Zou, H., et al. (2020). "Molecular Heterogeneity and Cellular Diversity: Implications for Precision Treatment in Medulloblastoma." Cancers **12**(3): 643.

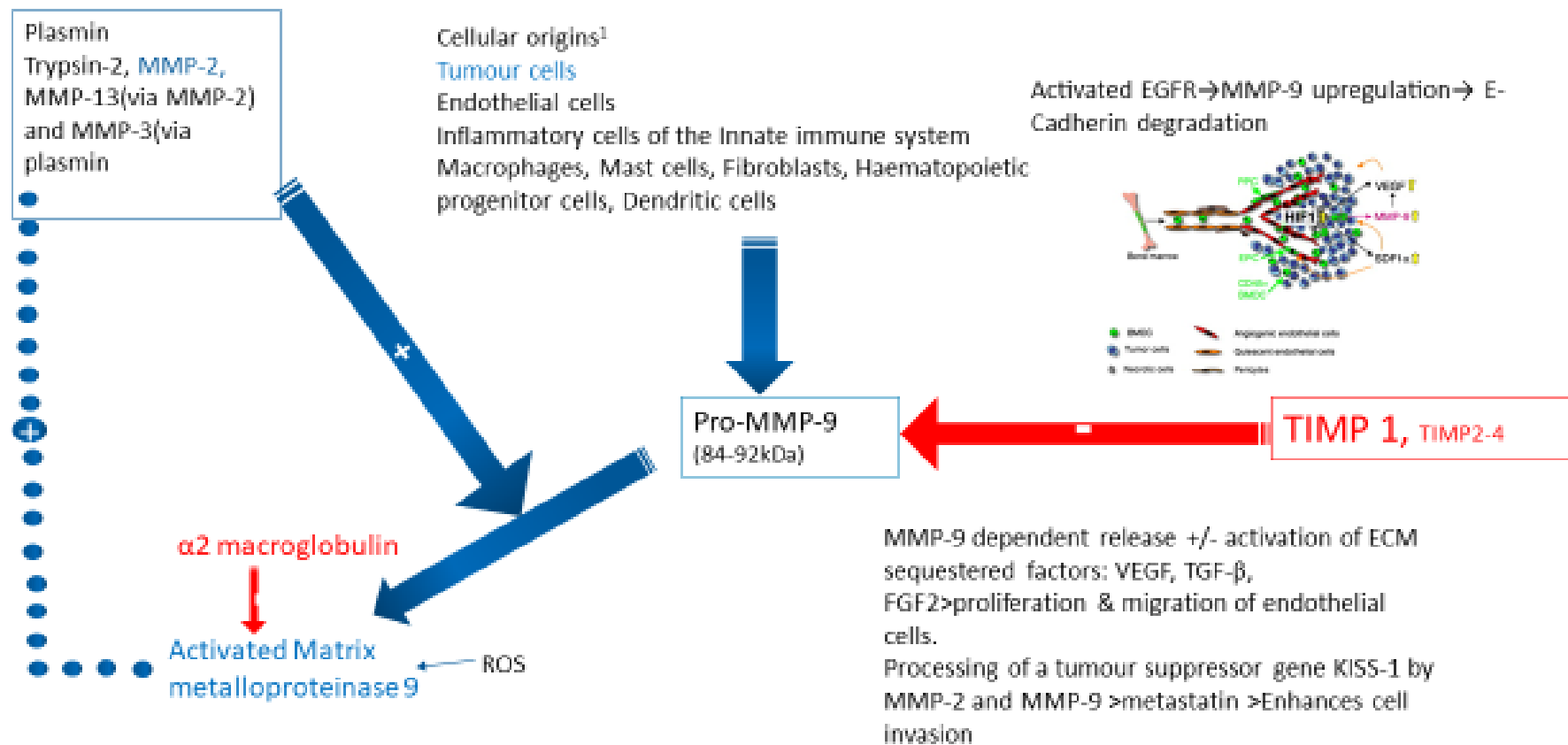
Appendices



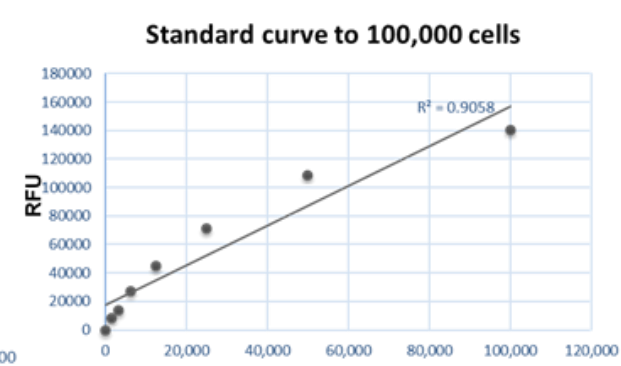
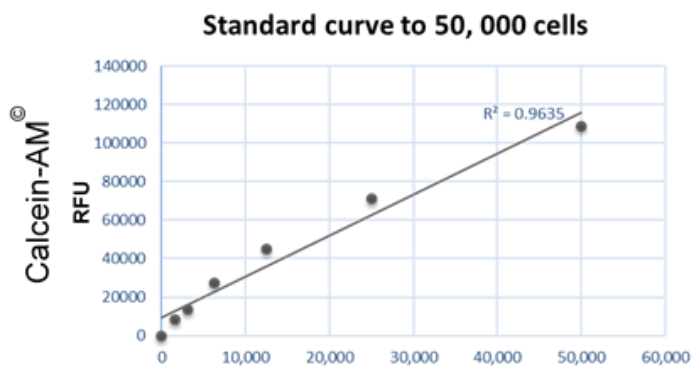
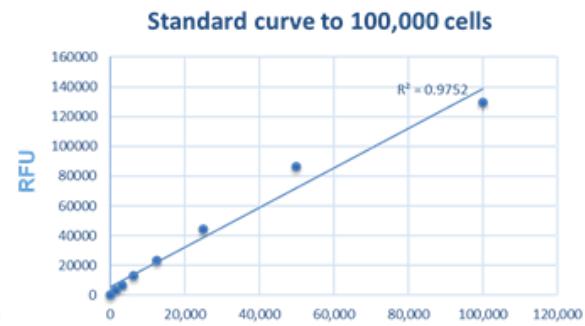
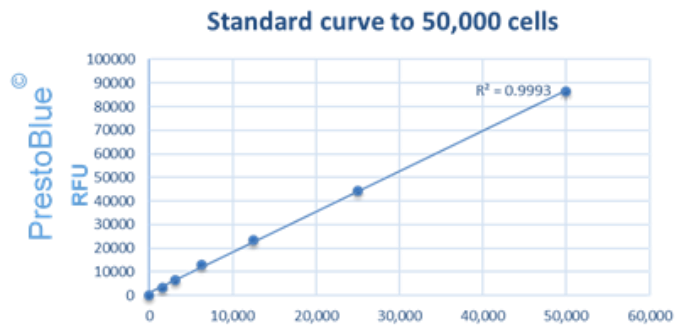
Appendix Figure 1 Cavalli dataset differential gene expression in MB subgroups and survival analysis for MMP-2 and MMP-9 gene expression in MB (<http://r2.amc.nl>)



Appendix figure 2: MMP-2 flow chart diagram (Kessenbrock, Plaks et al. 2010, Bauvois 2012)



Appendix figure 3: MMP-9 flow chart diagram (Kessenbrock, Plaks et al. 2010, Bauvois 2012)



Appendix figure 4: Optimisation of fluorescence cell detection methods

Spheroid macro written by Dr Ivanov and modified by Dr Roper:

//This macro aims to automate spheroid size measurement in three-dimensional cell culture. It requires input and output folders with images only, processes the images, records a file with spheroid measurements (Area, Ferret max, Ferret min, etc.) and writes an image with the outline/s of the determined spheroid/s.

//The spheroid detection and size determination function to be repeated for every image is defined below

```
function action(inputFolder,outputFolder,filename) {
open(inputFolder + filename);

//sets scale to predetermined values from calibration slide
run("Set Scale...", "distance=1360 known=1000 pixel=1 unit=µm global");
run("16-bit");

//run("Brightness/Contrast...");
run("Enhance Contrast", "saturated=0.35");

//Uses Yen thresholding algorithm
setAutoThreshold("Yen");
setOption("BlackBackground", false);
run("Convert to Mask");

//Gets the ratio between black (spheroid) and white (background) pixels. If we assume a
single spheroid, the ratio between black and white pixels would allow us to estimate the size
of the spheroid.
getHistogram(0,hist,256);
ratio = hist[255]/hist[0];

//If there are more pixels detected as spheroid(black) than background(white) then the
spheroid has not been detected due to variations in background
if (ratio>1) {
    // closes the image, reopens it, subtracts the background and proceeds as normal
    close();
    open(inputFolder + filename);
    run("16-bit");

    // Subtract Background is not used in the default function because it can lead to
merging of spheroids and debris or it can remove the core of the spheroid leaving a very
thin interrupted edge. In certain cases where the edges of a spheroid are very bright
removing the background can give better results.
    run("Subtract Background...", "rolling=50 light");
    setAutoThreshold("Yen");
    setOption("BlackBackground", false);
    run("Convert to Mask");
    run("Remove Outliers...", "radius=15 threshold=0 which=Dark");
    getHistogram(0,hist,256);
    ratio = hist[255]/hist[0];
}
```

//The strategy here is to act differently according to spheroid size. The general pattern is to expand and then shrink back the spheroids in order to include all cells on the edges. Then a series of functions are used to remove noise and the Watershed function separates fused or superimposed particles. The Analyze particles function is targeted to the specific spheroid size according to the black/white pixel ratio.

```
if (ratio<0.001) {
    run("Maximum...", "radius=8");
    run("Fill Holes");
    run("Minimum...", "radius=8");
    //small spheroids require a more "gentle" function to clean up noise
    run("Median...", "radius=2");
    run("Maximum...", "radius=25");
    run("Minimum...", "radius=25");
    run("Fill Holes");
    run("Watershed");
    run("Analyze Particles...", "size=4000-Infinity circularity=0.20-1.00 show=[Overlay Outlines] display exclude include summarize");};
if (ratio >=0.001 && ratio<0.01) {
    run("Maximum...", "radius=8");
    run("Fill Holes");
    run("Minimum...", "radius=8");
    //slightly bigger spheroids and a more rigorous function to remove noise
    run("Remove Outliers...", "radius=10 threshold=0 which=Dark");
    run("Watershed");
    run("Analyze Particles...", "size=10000-Infinity circularity=0.20-1.00 show=[Overlay Outlines] display exclude include summarize");};
if (ratio>=0.01 && ratio<0.2) {
    run("Maximum...", "radius=8");
    run("Fill Holes");
    run("Minimum...", "radius=8");
    run("Remove Outliers...", "radius=15 threshold=0 which=Dark");
    run("Median...", "radius=4");
    run("Watershed");
    run("Analyze Particles...", "size=20000-Infinity circularity=0.20-1.00 show=[Overlay Outlines] display exclude include summarize");};
if (ratio>=0.2 && ratio<1) {
    //Very big spheroids generally do not need to be expanded much to fill up the edges.
    run("Maximum...", "radius=3");
    run("Fill Holes");
    run("Minimum...", "radius=3");
```

```

//Outliers and noise are removed rigorously
run("Remove Outliers...", "radius=50 threshold=0 which=Dark");
run("Minimum...", "radius=30");
run("Maximum...", "radius=30");
run("Watershed");
run("Analyze Particles...", "size=50000-Infinity circularity=0.20-1.00 show=[Overlay
Outlines] display exclude include summarize");
if (Overlay.size > 0) {
//Sends particles detected to the ROI manager
run("To ROI Manager");
close();
//Reopens the original image and pastes the outlines of the determined particles onto it
open(inputFolder + filename);
run("From ROI Manager");
outputPath = outputFolder + filename;
save(outputPath);
close(); }
else {
close();
};
call("java.lang.System.gc");
};
call("java.lang.System.gc");
run("Clear Results");
inputFolder = getDirectory("Choose the input folder!");
outputFolder = getDirectory("Choose the output folder!");
//Delete the next line if you want to see how the macro works on the images. However that
will reduce processing speed.
setBatchMode(true);
images = getFileList(inputFolder);
//Sets the measurements that are recorded for each spheroid
run("Set Measurements...", "area centroid shape feret's display add redirect=None
decimal=1");
//That is the cycle that runs through all images
for (i=0; i<images.length; i++) {
action(inputFolder,outputFolder,images[i]);
showProgress(i, images.length);
};

```

```
//Writes in the Results and Summary windows and saves the data.  
selectWindow("Results");  
saveAs("Measurements", "" + outputFolder + "Results.txt");  
selectWindow("Summary");  
saveAs("Text", "" + outputFolder + "Summary.txt");  
setBatchMode(false);
```

Macro for Image J analysis of protease and protease inhibitor microarrays

A publically available Image J macro for the analysis of protease and protease inhibitor microarray was used to perform densitometry on the digital images (.TIFF) following chemiluminescence of the microarrays (<https://imagej.nih.gov/ij/macros/toolsets/Protein%20Array%20Analyzer.txt>). The image below demonstrates the manner in which the microarrays were analysed. The macro coded for the subtraction of the background from each analyte. The resulting densitometries were then normalised to the mean of the reference points giving each analyte's relative signal strength.

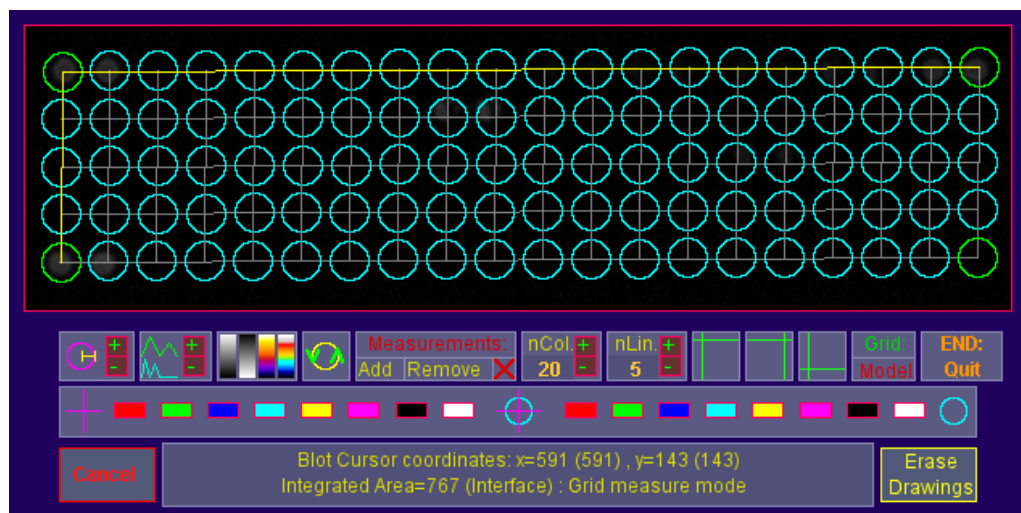
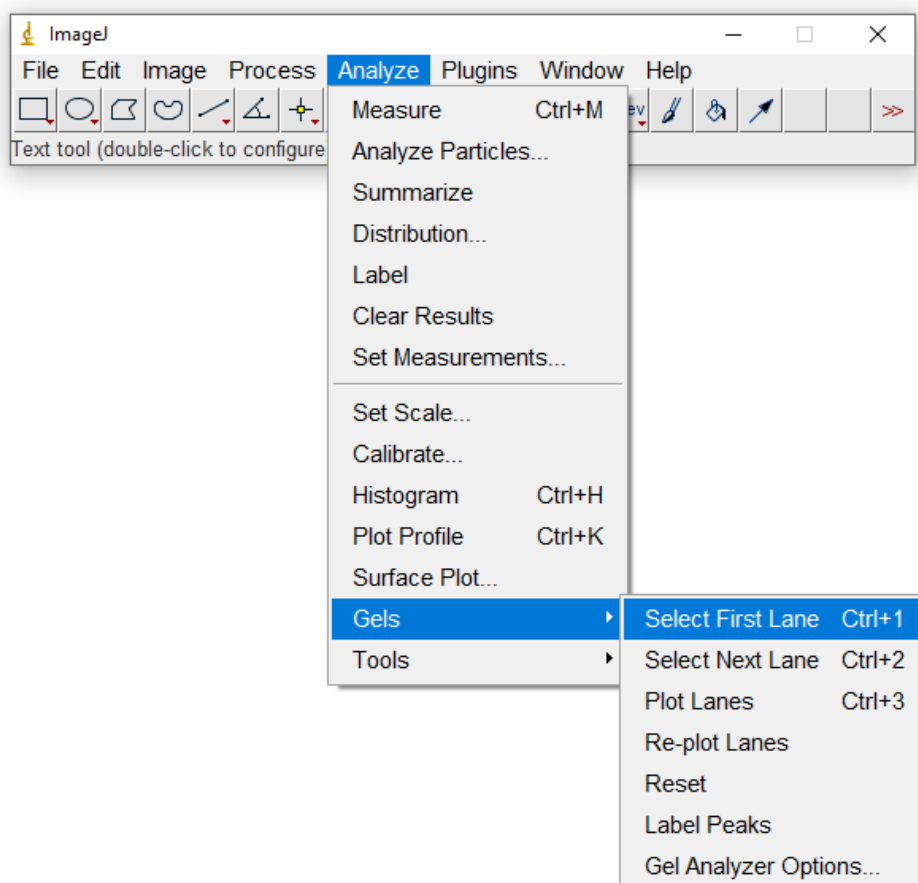


Image J densitometry of western blot membranes and zymograms

Following chemiluminescence of each membrane using our machine (LAS 4000 mini Biomolecular imager, GE Healthcare), the images saved as TIFFs were imported into Image J software. Photographs of each zymogram was taken with a 14MP phone camera and saved as digital files as well (.tiff). Densitometric analysis was performed as shown below.

1. Open Image J software after downloading from NIH website.
<https://imagej.nih.gov/ij/download.html>
2. Highlight the rectangular left sided button and select Analyze and follow as below to gels then choose 'select first lane' as shown below.



3. This will highlight the first lane as shown. This is your region of interest (ROI). You can drag this box horizontally without changing its dimensions to each lane to improve validity between your measurements.



4. Once an ROI is selected, press 'ctrl+M' or select 'Measure' under the Analyse section.

5. Ensure to measure an ROI area of background which can be subtracted from the densitometry of each sample.

6. Once all the measurements are complete, export these to Excel and normalise them to the volumes of protein lysate loaded for each sample. Lastly, ensure to normalise them to their respective GAPDH densitometries.

PhD Project outputs

Conferences

Society of British Neurological Surgeons	April 2021
International Symposium on Paediatric Neuro-Oncology	June 2018
British Neurosurgical Research Group	March 2018
European Society for Magnetic Resonance in Medicine and Biology	October 2017
Red Hot Fluorine Magnetic Resonance Imaging	October 2017
Consensus on Cerebellar Mutism Workshop	May 2017

Published conference abstracts

Mitoko C, Linke F, MacArthur D, Faas H, Coyle B. Using sensitive magnetic resonance imaging techniques to improve the risk stratification of patients with metastatic medulloblastoma. June 2018 Neuro-Oncology 20(suppl_2)i138-i139

Mitoko C, Linke F, MacArthur D, Faas H, Coyle B. Developing imaging biomarkers to improve our risk stratification of metastatic medulloblastoma. British Neurosurgical Research Group Meeting, March 8th-9th 2018, Sheffield, UK. Abstract number: 58.

Post-graduate prizes

The Graduate School Travel Prize: University of Nottingham April 2018

The Alder Hey 2018 International Society for Paediatric Neuro-Oncology
International Traveling Fellowships Award Program March 2018

The University of Nottingham School of Medicine funding grant from the
Doctoral Programmes Committee March 2018

Award of Haydn Green International scholarship: as a full-time
International PhD student August 2016

Presentations

Oral Presentations

International

Mitoko C, Linke F, Zamberlan F, Krupa J, Thomas NR, Philp C, Pavlovskaya G, Meersmann T, Bray J, Macarthur D, Coyle B, Faas H. Characterisation of Cellular Expression of Matrix Metalloproteinases using MMP Biosensor Magnetic Resonance Imaging. European Society for Magnetic Resonance Imaging in Medicine and Biology (ESMRMB) 34th Annual Scientific Meeting. 19th-21st October 2017, Barcelona, Spain. Abstract number: 1091. Presentation number 411. Lightening talk and poster presentation.

National

Mitoko C, Linke F, MacArthur D, Faas H, Coyle B. Improving prognostication in paediatric metastatic medulloblastoma. Society of British Neurological Surgeons spring meeting April 2021.

Mitoko C, Linke F, MacArthur D, Faas H, Coyle B. Developing imaging biomarkers to improve our risk stratification of metastatic medulloblastoma. British Neurosurgical Research Group Meeting, March 8th-9th 2018, Sheffield, UK. Abstract number: 58.

Poster Presentations

Mitoko C, Linke F, MacArthur D, Faas H, Coyle B. Using sensitive magnetic resonance imaging techniques to improve the risk stratification of patients with metastatic medulloblastoma. International Symposium on Paediatric Oncology. 29th June-3rd July 2018, Denver, Colorado. Abstract number: MBRS-49.